The Micro-thermal Analysis of Polymers

by

David Brian Grandy

A doctoral thesis

submitted in partial fulfilment of the requirements

for the award of

the degree of Doctor of Philosophy of Loughborough University

2002

Supervisors: Dr. M. Reading and Professor D.J. Hourston

Institute of Polymer Technology and Materials Engineering

Acknowledgements

Abstract

This study is concerned with the development of micro-thermal analysis as a technique for characterising heterogeneous polymers. It is divided into two main parts. In the first part, the use of miniature Wollaston wire near-field thermal probes mounted in an atomic force microscope (AFM) to carry out highly localised thermal analysis (L-TA) of amorphous and semi-crystalline polymers is investigated. Here, the temperature of the probe sensor or tip is scanned over a pre-selected temperature range while in contact with the surface of a sample. It is thereby used to heat a volume of material of the order of several cubic micrometres. The effect of the glass transition, cold crystallisation, melting and degree of crystallinity on L-TA measurements is investigated. The materials used are poly(ethylene terephthalate), polystyrene and fluorocarbon-coated poly(butylene terephthalate). The primary measurements are the micro- or localised analogues of thermomechanical analysis (L-TMA) and differential thermal analysis (L-DTA). The effect of applying a sinusoidal modulation to the temperature of the probe is also investigated.

In the second part, conventional ultra-sharp inert AFM probes are used, in conjunction with a variable-temperature microscope stage, to conduct variable-temperature mechanical property-based imaging of phase-separated polymer blends and copolymers. Here, the temperature of the whole sample is varied and the temperature of the probe tip remains essentially the same as that of the sample. The primary AFM imaging mode is pulsed force mode (PFM-AFM). This is an intermittent contact (IC) method in which a mechanical modulation is applied to the probe cantilever. The methodology is demonstrated on a model 50:50 blend of polystyrene and poly(methyl methacrylate) (PS-PMMA) and three segmented polyurethane (SPU) elastomers containing different chain extenders. In doing so, it is shown that PFM-AFM imaging can be carried out successfully over a temperature range of −50°C, or lower, to above 250°C. The adhesion-dependent pull-off force signal is found to be far more sensitive to local variations in mechanical properties than the local compliance-dependent indentation force signal.

Finally, the principle of using a high resolution micro-fabricated thermal probe in pulsed force mode is established. PFM-AFM images acquired with the probe at room temperature and 150°C are presented. A similar transformation is evident in the pull-off force image of the PS-PMMA blend as is obtained by changing the temperature of the whole sample while using an inert probe.

Contents

Tables and Figures

Abbreviations and Symbols

Micro-TA	Micro-thermal analysis
L-TA	Localised thermal analysis
L-TMA	Localised thermomechanical analysis
L-DTA	Localised differential thermal analysis
AFM	Atomic force microscope / atomic force microscopy
SFM	Scanning force microscope / scanning force microscopy
SPM	Scanning probe microscope / scanning probe microscopy
STM	Scanning tunnelling microscope / scanning tunnelling microscopy
SThM	Scanning thermal microscopy
TASM	Tomographic analysis for scanning microscopy
IC-AFM	Intermittent contact AFM
NC-AFM	Non-contact AFM
PFM-AFM	Pulsed force mode atomic force microscopy
PDM	Phase detection microscopy
LFM	Lateral force microscopy
FMM	Force modulation microscopy
FDC	Force distance curve
LI	Layered imaging
SLAM	Scanning local acceleration microscopy
HFM	Heterodyne force microscopy
DSC	Differential scanning calorimetry
MTDSC	Modulated temperature differential scanning calorimetry
T_g	Glass transition temperature
T_m	Melting temperature
GC-MS	Gas chromatography-mass spectrometry
L-EGA	Localised evolved gas analysis
(TGA)-GC-MS	Thermogravimetry-gas chromatography-mass spectrometry
FT-IR	Fourier transform infra-red spectroscopy
SAXS	Small angle X-ray scattering
SALS	Small angle light scattering
TEM	Transmission electron microscopy
NMR	Nuclear magnetic resonance

PS	Polystyrene
PMMA	Poly(methyl methacrylate)
SPU	Segmented polyurethane
M_w	Weight average molecular weight
M_n	Number average molecular weight
c_p	Heat capacity
k	Thermal conductivity
μ	Thermal diffusivity
ρ	Density
L	Thermal diffusion length
F	Force
E	Young's Modulus
ω	Angular frequency
φ	Phase shift / lag
k_c	Elastic constant
k_s	Stiffness
Q	Quality factor
a_c	Contact area

Chapter 1

Introduction

1. Micro-thermal analysis using a thermal probe

1.1.1 Introduction

The term *micro-thermal analysis* (micro-TA) encompasses techniques or combinations of techniques that use a method of highly localised material property characterisation carried out at the micrometre or sub-micrometre scale, on a sample subjected to a controlled temperature regime. In its broadest sense, micro-TA could therefore include hot-stage optical microscopy. It is generally accepted, however, that the term is used to describe methods that exploit a combination of atomic or scanning force microscopy (AFM, SFM) and one or more of the following techniques: thermomechanical analysis or thermomechanometry (TMA), dynamic mechanical analysis (DMA), differential thermal analysis or differential scanning calorimetry (DTA, DSC), spectroscopy or analytical pyrolysis. In a sophisticated arrangement, it is possible to combine all these techniques in a single "bench-top" instrument. These are all well established materials characterisation methods which, through the introduction of AFM, can now be carried out on pre-selected parts of a sample typically a few cubic micrometres in volume or smaller. The atomic force microscope is used to acquire topographic and other types of image of a surface and/or to position accurately a near-field probe at a particular location on that surface. Control over the temperature of a sample is provided by the use of a thermally-active electrically resistive probe (thermal probe) and/or a variable temperature microscope stage (temperature stage). If the latter is being used, practically any type of probe normally available for AFM may be mounted in the microscope. A thermal probe may function as a thermometer as well as a heat source. This enables a further type of micro-TA to be carried out, in which heat is applied to the sample from an external energy source (infrared radiation, for example) and the probe is used to sense the resulting change in temperature of the material. This enables spectroscopy to be carried out with a spatial resolution that is, in theory, better than the diffraction limit.

Using the established *"macro"* forms of these characterisation methods, typically carried out on a minimum of a few cubic millimetres or milligrams of material, it is often possible to deduce that a particular sample is heterogeneous, a polymer blend, for example, to assign thermal transitions to different components, and perhaps to identify the constituents and in what proportion they are present. However, no information on the size, shape and spatial distribution of phases is acquired. The development of micro-TA significantly enhances the utility of these techniques by enabling variations in properties or composition to be mapped at the microscopic level. This will increase

their usefulness in the field of materials science and technology, which is becoming ever more concerned with the control of material structure and hence properties at the *micro-* and, increasingly, the *nano-*scale.

1.1.2 The atomic force microscope

The invention of the atomic or scanning force microscope (AFM, SFM) in 1986 by Binnig *et al.* has been a major factor in enabling the development and commercialisation of micro-thermal analysis. Prior to its development, the scanning probe microscopes (SPM) available were restricted to use on electrically conductive samples. This is because they utilised the tunnelling current between a surface and a conductive near-field probe or, more specifically, the dependence of its magnitude on
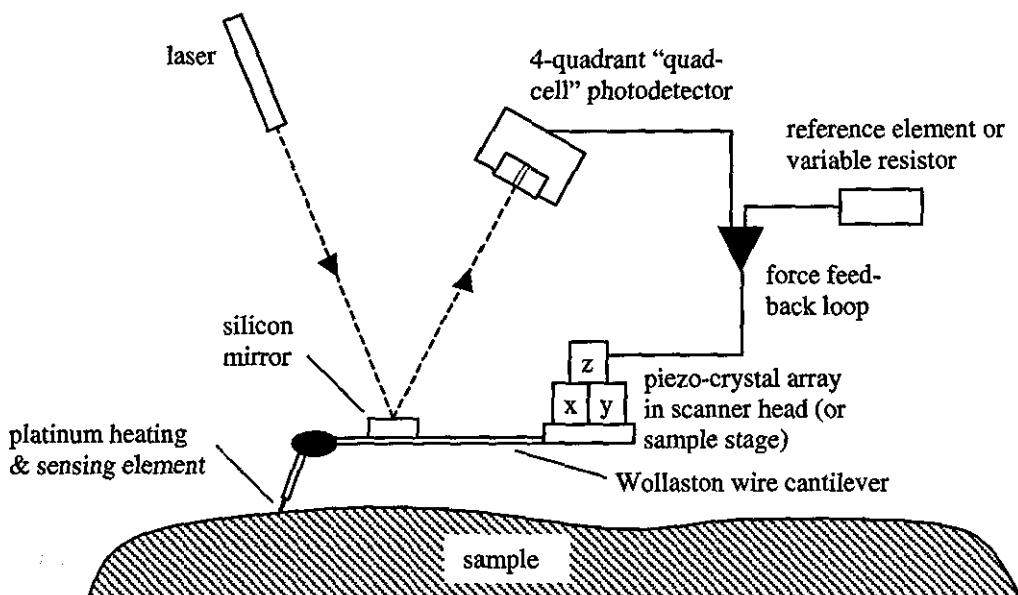
Figure 1.1. Schematic diagram of a typical atomic force microscope.

the probe tip-sample distance. This technique, developed by Binnig and Rohrer in 1982,[2] is known as scanning tunnelling microscopy (STM) and can be used to acquire extremely high resolution elevation maps or topographic images of a surface down to the atomic scale. The operation of the AFM, on the other hand, depends on the nature of the short-range repulsive or attractive forces that exist between all solids in close proximity. Its use, therefore, is not restricted to conductive materials. The microscope provides the mechanism by which a near-field probe can be positioned and/or raster-scanned, with *nanometre*-level accuracy on or across a surface, whilst maintaining a controlled contact force. Fig. 1.1 is a schematic diagram of a typical AFM with a

thermal probe installed (see section 1.1.5 for a detailed description of thermal probe technology). At its heart are two independent but inter-connected mechanisms. The first is a piezo-electric scanner, which controls and measures the position of the fixed end of the probe *cantilever* in three dimensions. In certain instruments an additional height measurement is made by a strain gauge bonded to the surface of the z-piezo actuator. The second is an optical lever, in which laser light is shone onto the reflective top surface of the cantilever (or, in the case the thermal probe illustrated, a discrete but integral probe mirror) and collected in a four-quadrant photodetector. The vertical position of the laser spot on the detector is a measure of the degree of bending of the cantilever and, therefore, the normal force acting between the tip and sample. This is calculated from the signal arriving at the top two quadrants minus that detected at the lower two (sometimes referred to as the T–B signal). Similarly, the horizontal position of the laser spot is a measure of cantilever twist and hence frictional forces. In the simplest AFM scanning mode, the average normal force is kept constant by means of a feedback signal from the photodetector to the scanner. The response of the scanner is to raise or lower the fixed end of the cantilever to accommodate the effects of surface topography on the normal force. In this manner, a three-dimensional topographic map of the sample surface is obtained. In certain applications, this may be all that is required. Usually and often more usefully, images can be acquired simultaneously that are constructed from variations in some physical property across the surface of the sample. These may be mechanical, electrical, magnetic or, when using a thermal probe, thermal properties. A detailed description of the various imaging modes that can be used in micro-thermal analysis is given below.

1.1.3 Scanning thermal microscopy

Scanning thermal microscopy (SThM) enables the acquisition of images of the surface of a sample constructed from spatial contrast in one or more thermal properties of the material. In constant temperature mode, the thermal probe is held at a fixed temperature by means of a thermal feedback loop as it is raster-scanned across the surface of the sample. The AFM force-feedback mechanism holds it at a constant contact force. The vertical movement of the AFM scanner required to maintain constant force is used to construct a topographic image. The power supplied to the probe to maintain it at the selected temperature is recorded and used to construct the "thermal conductivity image". The instrument software assigns each measurement to a pixel in the image, coloured or shaded according to its magnitude. The ratio of the sampling

rate to the image-resolution (here, this simply means the total number of pixels required) determines the number of measurements per pixel. When multiple measurements are used to construct a single pixel, the average value is calculated and the pixel shaded accordingly. Areas of relatively high thermal conductivity will result in more power being supplied to the probe than neighbouring areas with lower conductivity. By convention, areas with relatively high or low conductivity appear, respectively, as relatively bright or dim areas in the resulting image. In a multiphase material then, providing there is sufficient contrast in thermal conductivity between phases, the spatial distribution, shape and size of phases will be mapped. As all materials conduct heat, a significant amount of information in the image will originate from the sub-surface structure of the material. Most other AFM modes, such as mechanical property based imaging, are generally restricted to measuring the response of the material in the immediate vicinity of the surface. The ability of SThM to carry out sub-surface imaging can therefore provide a significant advantage. Often the microstructure at the surface of a material is unrepresentative of that of the sub-surface region, or the sample may be a multi-layer film or contain a buried structure. On the other hand, it may well be that the immediate surface region of a sample is of most interest and the greater effective sample volume provided by SThM is an unnecessary complication. However, by applying a modulation (usually sinusoidal) to the temperature of the probe, typically a few kelvin in amplitude and at a frequency in the kilohertz range, a degree of control may be exerted over the effective sample depth. This is because, assuming a one-dimensional sample, the rate of attenuation with distance from the heat source, z, of the thermal wave penetrating into the material is dependent on the factor $\exp(-z/L_1)$, where L_1 is the thermal diffusion length. L_1 is proportional to $\sqrt{(\mu f)}$, where μ and f are, respectively, the thermal diffusivity of the material and the frequency of temperature modulation.[3] [$\mu = k_c/(\rho c_p)$, where k_c is the thermal conductivity of the material, ρ is its density and c_p the specific heat capacity]. The response of the sample to the modulated or AC heating therefore results, in principle, in an image being acquired based on variations in the local thermal diffusivity over a sample depth controlled by the frequency of modulation, usually in the range 5 – 20 kHz. For a typical polymer, L_1 is of the order of 5 μm at a modulation frequency of 10 kHz. This model does not take into account the three-dimensional nature of the heat flow into the sample and in practice L_1 is significantly greater than the maximum effective depth of a real sample. The modelling of an accurate three-dimensional space envelope for the sample is fraught with difficulties, not least because the area of

contact between the probe and surface is unknown. Nevertheless, the ability to detect the presence of a sub-surface structure, inclusion or void without necessarily being able to measure accurately its depth and dimensions, is a useful one. Furthermore, AC imaging has already been used successfully to study spatial variations of thermal diffusivity in real materials.[4-6] Some progress has also been made by Smallwood *et al.*,[7] using finite element methods (FEM), in modelling the effective size, shape and depth of features within the effective space envelope of the sample. This can be seen as an initial step in the possible development of AC thermal imaging into a three-dimensional tomographic technique — thermal impedance tomography or TASM (Tomographic Analysis for Scanning Microscopy). This is an adaptation of the recently established medical imaging technique of electrical impedance tomography.[8] Recent work has also been carried out by Depasse *et al.*[9-12] to describe quantitatively the nature of the coupling between an AC-heated probe and a sample. This has been used to model the image obtained from discrete buried inclusions having a thermal conductivity different from that of the continuous matrix. This work takes into account factors such as the temperature gradient along the sensing element of the thermal probe.

In practice, two AC thermal images are acquired. One is constructed from the phase lag between the temperature modulation induced in the sample and the excitation signal supplied to the probe and the other from the amplitude of the sample response relative to the amplitude of the input signal. These images are acquired simultaneously with the DC thermal conductivity image, extracted from the averaged signal. Hence it is possible, in a single experiment, to sample two layers of different thickness. In addition, new developments in thermal probe technology and the use of more sophisticated electronic control systems will enable the simultaneous acquisition of images constructed from spatial contrast in local mechanical properties (thermomechanical imaging). This is discussed in more detail in the section describing variable-temperature AFM.

The modelling of the nature of the probe-air-sample interactions in the DC case is less complex, but still not straightforward. An attempt has been made by Hammiche *et al.*[13] to model the heat flow into a sample consisting of one or two simple structures buried in a semi-infinite matrix having a different thermal conductivity. The results are compared with those from a real sample. It is reported that a number of factors affect the accuracy and sensitivity of depth detection, the maximum depth at which structure can be detected and the minimum resolvable distance between adjacent buried

structures. These principally include the instrument's temperature resolution and its minimum detectable heat flow. Assuming these are otherwise optimised, the major influence here is the contact area between probe and sample — see section 1.1.4 for a detailed description of thermal probes and their limits of resolution. It is concluded that the rate of degradation of resolution with depth is considerable, falling by around half an order of magnitude at a depth of several micrometres.

As well as the considerable difficulties inherent in modelling the real three-dimensional nature of the sample, there is a more straightforward and perhaps more fundamental difficulty in the interpretation of both DC and AC thermal images acquired by SThM. This is because the power required to maintain the probe at constant temperature is strongly affected by the surface topography proximal to the probe at any given point in the scan. Indeed, the *deconvolution* of topographic effects, so-called *topographic artefacts*, from images constructed from the measurement of a physical property is a problem common to many AFM imaging modes. Conversely, and usually less importantly, variation in mechanical properties can disturb the topographic image. The nature of this effect in SThM is illustrated in Fig. 1.2. When the probe is at or near
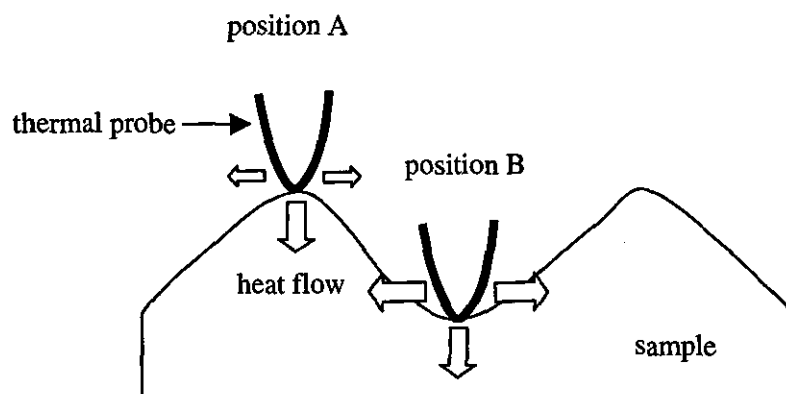
Figure 1.2. An illustration of the effect of sample topography on the heat flux from a thermal probe to its surroundings.

the summit of a relatively high feature (position 'A') it is surrounded predominantly by air, whereas at or near to the bottom of a hole or valley (position 'B') the effective volume of the sample is larger. This is due both to the absolute increase in probe-sample *contact area* and, if radiative heat transfer is significant (see below), to the greater amount of material in close proximity to the probe. Variation in contact area is the most common cause of topographic artefacts amongst AFM imaging techniques. In this case, the relatively high thermal conductivity of the solid means that more heat is

transferred from the probe at position 'B' and so more power has to be supplied to the probe to maintain constant temperature. This appears in the resulting thermal image as a region with a different shade or colour (by convention, brighter) from the region around position 'A'. Hence, even a thermally-homogeneous material, unless it is perfectly smooth, gives rise to thermal image-contrast. This means that a careful comparison of the corresponding topographic and thermal images must be made before concluding that features in the thermal image are indeed due to genuine spatial variations in thermal conductivity. On the other hand, the effects of topography may act to mask or considerably reduce the degree of contrast in thermal images from multiphase materials in which exist otherwise detectable variations in thermal conductivity. This is because raised features with relatively high thermal conductivity may cause the probe to consume a similar amount of power as low areas with relatively low conductivity. An extreme case of this would be a binary mixture or blend in which occluded high conductivity domains were raised above a surrounding higher conductivity continuous phase. Such samples are rare and it could be argued that in cases where systematic topographic variation exists between different phases, the thermal conductivity image becomes, to an extent, superfluous. In practice it is usually the case that, for a given sample, the local topography in some areas will act to increase the apparent thermal contrast and in other areas to reduce it.

There are several methods which may be employed to aid interpretation of thermal images. The simplest is a careful visual comparison of the topographic and thermal images to determine how closely the location, size and shape of features in one image are reflected in the other. The success of this qualitative approach is dependent on the experience and judgement of the experimenter, as well as on the complexity of the sample. A somewhat more robust method is to compare the shape of the *intensity histograms* extracted from both images.[13] Each element of an image histogram contains the number of pixels occurring at each measurement value [14] (in this case, height for the topographic image and probe power consumption for the thermal image). If the shapes of the two distributions are a close match or, possibly, near to a mirror image of each other, there is probably a powerful topographic influence on the thermal image. On the other hand, if the shapes of the distributions are substantially different, any contrast present in the thermal image is probably caused by real differences in material properties. For a binary polymer blend this could manifest itself in a substantially monomodal or perhaps random height distribution and a bimodal thermal conductivity distribution. Eventually, it is likely that the strategies described above to

develop methods to model the three-dimensional structure of the sample detected by the thermal probe, will also lead to progress in solving the topography deconvolution problem. A less fundamental but potentially more practical approach, is the development of neural net based algorithms that can "learn" to recognise the influence of topography on thermal conductivity data sets. The initial step would be to use "ideal" samples, consisting of domains with well-differentiated thermal properties and relatively simple topography, whose behaviour could be used as a basic input into the model. If these approaches are successful, they could be applied to similar problems encountered both in AFM in general and in a range of other applications.

A further imaging mode provided by SThM exploits spatial variations in the coefficient of thermal expansion. This is a development of a previously–reported technique known as Scanning Joule Expansion Microscopy[15] which exploits AC heating of a conductive sample and a standard AFM to detect differences in the local (modulated) thermal expansion. The equivalent technique using a thermal probe, which can be applied to non-conductive materials, has been termed Scanning Thermal Expansion Microscopy (SThEM).[16] It is potentially a more sensitive technique than SThM for differentiating between phases. This is because thermal transitions in most polymeric materials, notably the glass transition, produce a significantly greater percentage change in the coefficient of thermal expansion than in thermal conductivity or heat capacity. Therefore, in the case of an immiscible binary polymer blend, imaging with the thermal probe at a temperature intermediate to the glass transition temperatures of the component polymers should produce superior phase contrast to that in the equivalent thermal image. The use of previously-determined transition temperatures to dictate the probe and/or sample temperature is, in fact, a powerful strategy adopted in micro-thermal imaging, either when employing an active thermal probe or a standard inert AFM probe.

1.1.4 Localised thermal analysis

Localised thermal analysis (L-TA)[17-19] exploits the ability of the AFM, in conjunction with a suitable microscope stage having x-y translation, to place a thermal probe at any point on the surface of a sample. This may be done with or without first having carried out SThM on that surface. If an image (topographic and/or thermal) has been acquired previously, the probe can be directed to any feature of interest within the image (the maximum scan area available is normally of the order of 100 µm × 100 µm). With the probe tip or sensor in position on the surface and exerting a predetermined downward

force (or more precisely, a fixed T–B set point, which is proportional to force), a temperature ramp can be applied to the sample via the probe. This is usually a linear heating program or linear heating followed by linear cooling. Heating and cooling may be set at different rates. Essentially, two signals are acquired simultaneously. These are (a) the vertical deflection of the probe and (b) the power required by the probe to maintain the temperature ramp. The measurement of probe deflection with temperature is the micro- (or localised) analogue of thermomechanical analysis (micro-TMA, L-TMA), used on bulk samples. Similarly, the measurement of probe power consumption is the micro-analogue of differential thermal analysis (micro-DTA, L-DTA). Both these techniques have long been used widely in the study of thermal transitions in polymers and other materials.[20-22] The information on thermal properties garnered from such studies need not be an end in itself and is indeed used more often as a tool for understanding material structure and processes. Their micro-analogues enable similar results to be acquired but with the additional benefit of the information being spatially-resolved.

Once the probe is in contact with the surface and the temperature program is initiated, the force-feedback mechanism is disabled. This is to prevent the probe being driven continuously into a soft or molten sample, as the z-axis actuator would move the fixed end of the probe downwards in an attempt to maintain constant contact force. Instead, for a given material and heating rate, the depth to which the probe penetrates is controlled by the initial contact force (see chapter 2 for a discussion of the effects of heating rate). Hence, the contact force steadily increases as a relatively hard sample expands, or decreases as the probe tip sinks into a soft material; the fixed end of the cantilever remaining at constant height throughout. Before a particular probe is used, the relationship between the degree of bending of the cantilever (i.e. contact force) and the vertical displacement of the tip or sensor must be calibrated. This is a rapid procedure included as part of the instrument control software.

For a material which undergoes no thermal transitions over the temperature range of the experiment, the probe deflection with temperature will be essentially linear and upwards as the sample beneath the probe heats and expands. Under a fixed set of instrument parameters, the rate of upward deflection will depend on the coefficient of thermal expansion, thermal conductivity and heat capacity of the material. The heating of the probe element will itself cause some movement of the cantilever, but for the relatively massive Wollaston wire thermal probe (see section 1.1.5) this effect should be minimal. Providing a baseline subtraction procedure is carried out (acquired from a
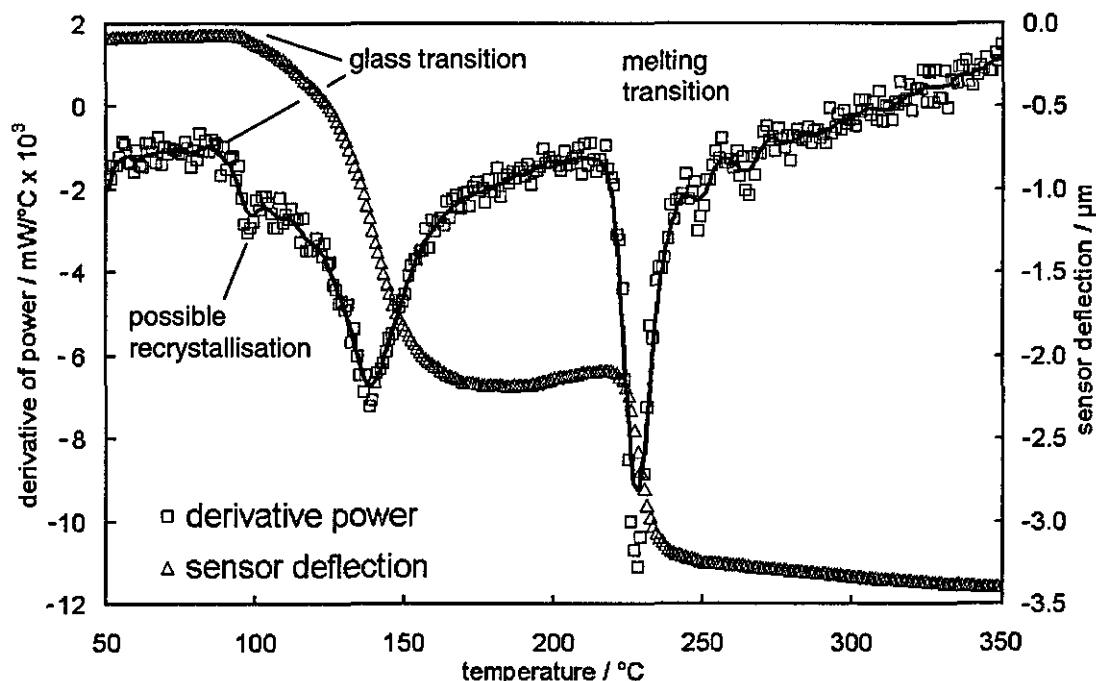
Fig. 1.3. Micro-TMA and micro-DTA curves for amorphous poly(ethylene terephthalate).

run with the probe in free air), the rate of power consumption of the probe over the duration of the same experiment should remain constant. When heating a polymer or other material that may undergo one or more transitions over the temperature range of the experiment (a glass transition, softening, cold crystallisation, curing, melting or degradation), the response of the micro-TA signals will be very different, as illustrated in Fig. 1.3. This shows typical micro-DTA and micro-TMA results for a crystallisable, initially-amorphous polymer. It is conventional to plot the first derivative of power with respect to temperature. In doing so, the melting transition is converted from a step-change to a peak, just as in conventional DTA results. It can be seen that the glass and melting transitions are readily detected in both signals, the latter as an endothermic peak in the micro-DTA signal and as a precipitous downward deflection in the micro-TMA signal. The glass transition is detected as a change in slope in both signals. There is also a weak exothermic peak in the power signal at around 110°C, which is possibly a consequence of cold crystallisation. A more detailed discussion of this and other localised thermal analysis results is given in chapter 2.

A beneficial consequence of the small mass of the sample (of the order of a few micrograms compared with several milligrams), is that heating (and cooling) rates can be much higher than in conventional thermal analysis techniques. Currently, the maximum heating rate available in the commercial instrument is $25°Cs^{-1}$, compared

with $10°Cmin^{-1}$ typical of conventional experiments. This allows many more experimental runs to be carried out in a limited time, which may be of particular benefit to the industrial user. Another benefit is that multiple runs can be carried out on samples that are available in a very limited quantity. In certain cases, samples can only be produced in a form unsuited to conventional TA, but which is readily amenable to L-TA ; a thin film on an inert substrate, for example. In work to be published, Tian *et al.*[23] have demonstrated the detection of the melting transition of polyethylene in the form of an ultra-thin (ca. 11 nm) layer using micro-TA. This shows that, after a careful temperature-calibration procedure has been performed (see below), it is now possible to measure the melting temperature of single crystals and to study directly the effects of, for example, lamellar thickness on the crystalline melting temperature. L-TA can be used to study differences between surface and bulk properties through the use of suitable sectioning techniques.[59] Indeed, because the volume of material heated during a run is so small, several L-TA experiments can be carried out on the surface of, for example, an individual polymer granule without unduly affecting the results from a conventional TA experiment conducted subsequently on the same sample.

As with SThM, AC heating may be applied to the thermal probe. This produces a fixed temperature modulation in the range $±1°C$ - $±10°C$, although it is usually confined to $±2°C$ - $±5°C$. This may be seen as analogous to the relatively recent development by Reading and co-workers[24, 25] of modulated temperature differential scanning calorimetry (MTDSC). In this technique the response of the sample to the modulated and underlying heat flows can be separated using a deconvolution program. The former is sensitive to the reversible changes in the heat capacity of the material, associated with molecular vibrations and the latter detects changes due to irreversible (over the range of the temperature modulation) kinetically-controlled processes. An obvious advantage of this technique is its ability to characterise heterogeneous samples in which different types of transition occur over the same temperature range. In the case of L-TA, a lock-in amplifier is used to extract two signals (AC signals) that are dependent on the response of the sample to the modulated heating. The first is the phase lag between the response of the sample and the input signal to the probe. The second is the amplitude of the response of the sample compared with the input amplitude. Acquisition of both signals normally requires the use of a differential technique in which the response of the sample probe is compared with the response of a near-identical reference probe or suitable reference resistor. Theoretically, the use of AC heating offers similar advantages to those of MTDSC over conventional DSC and it has been

shown that the AC signals may be particularly sensitive to transitions that produce a relatively large change in heat capacity for a small heat input.[26] Examples of typical AC L-TA results are discussed in chapter 2.

It will be noted that the use of the L-TA power signal has previously been named micro-DTA and not micro-DSC. This is because, as discussed in section 1.1.3, the volume and hence the mass of the heated sample is unknown and its calculation at present presents a formidable challenge. Hence it is argued that the technique cannot be described as a form of calorimetry, because it cannot measure the heat capacity of a material or the enthalpies associated with particular transitions. This is a major disadvantage. However, the ability of the technique to detect transitions occurring in a sample at the micrometre scale and to measure the temperature range over which those transitions occur is a powerful one. Furthermore, results are presented in chapter 2 which show that, providing calibration is first carried out using an absolute technique, variation in the area under micro-DTA melting peak can be used to study spatial variations in melting enthalpy and hence degree of crystallinity.

In order to measure the temperature of local transitions, a robust temperature-calibration of the thermal probe must first be carried out. This usually involves carrying out L-TA experiments on two or more substances whose melting temperature (T_m) is well known from the literature. These may be relatively low molecular weight organic crystals with narrow well-defined melting temperatures, such as biphenyl, benzoic acid and 2-chloroanthraquinone (T_m = 69.3°C, 122.4°C and 209.6°C, respectively). The preparation of relatively smooth samples consisting of large crystals from such compounds can, however, be problematic. For this reason, it is often more convenient to use polymer films whose melting point has previously been measured using DSC or another technique and can be shown to be spatially invariant. The melting transition of polymers is much broader than for low molecular weight substances and it is usual to use the onset T_m as the datum. The reason for this is that it is much more likely that at least some of the crystallites with the lowest T_m in the sample will be present at its surface. On the other hand, there is no guarantee that the peak T_m of the surface and bulk will coincide. Once two or more calibration points have been obtained which substantially cover the intended temperature range of subsequent experiments, a calibration curve of temperature versus probe resistance is generated and stored by the control software. The subject of temperature calibration has been addressed comprehensively by Blaine et al.[27] For applications in which the probe is being used as a thermometer, a suitable method of calibration is to use a calibrated microscope hot

stage to vary the temperature at which the probe enters thermal feedback. The onset temperatures obtained can then be correlated with the stage temperature.

An extension of TMA is dynamic thermomechanical analysis (DMA, DTMA), in which an oscillating stress (tensile, compressive, bending or shear) is applied to a clamped sample, subject to a controlled temperature program. [20-22] This technique can detect the large change in modulus (tensile, compressive, bending or shear) that usually accompanies a thermal transition in a polymer. Its sensitivity to the glass transition, for example, is far higher than that of DSC. A localised analogue of this has now been demonstrated and is termed dynamic localised thermomechanical analysis (DL-TMA). [19, 28, 84] In this technique, a thermal probe is brought into contact with a sample, to which a low amplitude oscillation is applied. Both in-plane and normal oscillations have been used. In order to minimise lateral frictional forces that would otherwise cause twisting of the cantilever, the preferred direction of oscillation is parallel to its longitudinal (i.e. stiffest) axis. The temperature of the probe is then scanned (which as before, disables the force-feedback control). The signals acquired are the DC lateral force, and the phase and amplitude of the AC lateral force. This technique can be used, amongst other things, to study the effect of oscillation frequency on the glass transition temperature (T_g).

Although the measurement of heat capacity and enthalpies of transitions is not yet possible using L-TA, some progress has been made in the measurement of absolute thermal conductivity (k_c) at the micrometre scale. This may well be of particular value in the electronics industry, where a major challenge is the dissipation of heat produced by devices such as microprocessors. The ability to quantify the variation in thermal conductivity at different measurement scales is crucial in the development of models that would allow the thermal performance of a new device to be optimised at the design stage. The potential accuracy of such measurements is dependent on the ability to predict the nature and relative importance of the possible heat transfer mechanisms between probe and sample. These will include, radiation, conduction, and convection through the air gap between them or through any adsorbed aqueous contamination layer present on the surface and direct solid-solid conduction. In principle, any aqueous layer could be removed by making measurements with the probe at a temperature above 100°C. In two studies, Dransfield et al.[29, 30] concluded that radiative heat transfer at this scale could be neglected compared with conduction through the probe-surface gap in all but high vacuum. The importance of direct probe-sample (solid-solid) conduction is dependent on the area of contact, the thermal

conductivity of the sample and, to some extent, the heat capacity of the probe. Although the Wollaston wire probe has a relatively large heat capacity compared with that of the thermocouple probes used in early studies, it is thought that direct conduction only becomes significant for metallic samples.[29,30] The other major difficulty in making such measurements using a thermal probe is in quantifying the probe/sample contact area and, therefore, the heat flux entering the sample and that dissipated to the surrounding air. The approach adopted by Ruiz et al.[33] was to measure the heat loss from a Wollaston probe (see below) in air and subtract this baseline value from measurements made with the probe in contact with a range of (hard) materials of known (macro-scale) conductivity. This calibration must be carried out for each probe used. The resulting plot of measured value against k_c shows excellent linearity. Its slope is compared with that predicted by the approximation describing the effect of contact area on the thermal impedance of the junction:

$$\Delta Q/\Delta T = k_c \pi r_c \qquad (1.1)$$

where Q is the heat flux, ΔT is the difference in temperature between probe and sample and r_c is the radius of contact. This relationship holds provided the time taken for an individual measurement , $t >> r_c^2/4\mu$ (where μ is the thermal diffusivity) and r_c is greater than a theoretical limiting value, below which the effects of contact geometry begin to dominate the effects of thermal conductivity. It will be noted that as the thermal mass and, therefore, the thermal time constant of the probe become smaller, t will also be decreased. This will be offset, however, by the reduction in contact radius. This approach was used to measure the local thermal conductivity of chemical vapour-deposited (CVD) diamond-like nanocomposite films with an accuracy of ±15%. A more accurate model of the probe/sample heat flow has been adopted by Gorbunov et al.[32,34] Firstly, the increase in heat flux was measured as the probe/sample separation decreased. They then used these data to verify the linearity of equation 1.1. A theoretical model, which takes into account the effect of the thermal resistance of the air gap, was used to predict the conditions under which linearity held true. Measurements were then carried out on samples of known thermal conductivity and a plot of $\Delta Q/\Delta T$ against k_c obtained. Such a plot could be used as the basis on which localised measurements of k_c in a thermally-heterogeneous material could then be made. To optimise the technique, the materials used to construct the curve should have a comparable hardness and be in a form having a surface roughness similar to the samples to be studied. It was shown that the sensitivity of the measurement,

estimated at 0.2 $Wm^{-1}K^{-1}$, was generally insufficient to distinguish between different polymers. An additional difficulty with relatively soft materials is that there will be significant variation in contact radius with probe force. The shape of an individual probe tip (see below) will also be more significant for polymers. Difficulties may be encountered with thin films, in that it is important for the contact radius to be significantly lower than the thickness of the sample. This is not always possible when using a relatively large Wollaston probe. Other workers [12, 35] have challenged the validity of the linear relationship between heat flow and thermal conductivity shown in equation 1.1. A factor of particular importance cited is the variation with k_c of the heat flow from the probe tip into the adjoining probe structure,[12, 36] as such variation will affect the validity of the measurement of the baseline heat dissipation.

Some of the limitations of the approach described above to the measurement of the local thermal conductivity are overcome by studying the response of the sample to the AC heating of the probe. The so-called "three-omega" (3-ω) method is widely accepted as being a robust method of modelling a system that uses a combined heat source and temperature sensor.[37, 38] The term refers to the relatively weak third harmonic of the alternating current. Using Ohm's law to describe the relationship between voltage (*i.e.* probe temperature signal), current and impedance, it can be shown that the amplitude of the current is the only variable that affects the amplitude of the third harmonic term. Furthermore, this signal is unaffected by temperature gradients present in the probe or sample. Moon *et al.*[39] have used this approach on a macro-scale to study the thermal conductivity of sapphire (used widely as a calibration material in thermal analysis) and polypropylene. Fiege *et al.*,[40] on the other hand, have applied the technique to the measurement of the local thermal conductivity of a CVD diamond film using a Wollaston probe.

1.1.5. Modes of scanning thermal microscopy, thermal probe design and spatial resolution

A number of different types of probes have been used for SThM, but not all are suitable for L-TA. In a development concurrent with that of AFM, Williams and Wickramasinghe [41] first used thermal probes as a means of imaging electrically insulating materials and thus overcame the major limitation of STM. The probe consisted of a miniaturised coaxial thermocouple which was mounted in a SPM. The probe was heated electrically and the sample could be heated either electrically or by using a laser. As the probe was raster-scanned in the near-field of the surface, the

magnitude of the heat flow across the gap was monitored. This signal was fed to the scanner control system and the z-actuator raised or lowered the probe to keep the heat flow constant and hence the gap between probe and sample. In this manner, thermal feedback control was exploited to acquire a topographic image of the surface, in the same way that the AFM uses force-feedback control. The spatial resolution of the system was of the order of tens of nanometers. The device was also used in its passive mode as a thermometer to map spatial variations in temperature across the surface of a heated sample to an accuracy of approximately 10^{-3} °C.[42] In a later development,[43] thermal imaging of an electrically conductive sample was achieved by bringing a conductive probe within tunnelling distance of the surface, the tip and sample acting as the junctions of a thermocouple. Nonnenmacher and Wickramasinghe [44] used a similar approach, this time with a laser-heated probe, to carry out sub-surface imaging of electrically conductive samples. Thermal imaging was carried out by exploiting the powerful temperature dependence of the probe/sample contact potential. A simplified design of thermocouple probe was used in passive mode by Majumdar et al.,[45] under force feedback control to obtain, independently, topographic and temperature maps of a surface. A miniature gold-Constantan thermocouple probe was used by Oesterschulze et al.[4] to obtain DC and AC thermal images of a chromium-doped grid on a silicon substrate and CVD diamond-like films.

A somewhat different approach is provided by the use of bi-material cantilevers.[46, 47] Here, the probe cantilever is coated with a second material having a different coefficient of thermal expansion. As the probe is scanned over a heated sample, changes in temperature resulting from thermal anisotropy in the sample, will produce variable bending of the cantilever. The degree of bending is then sensed in the usual way via the laser-optics of the microscope and the data processed to produce a temperature map. However, this must be separated from the effects of topography. A related development is the use of a cantilever that incorporates an integral thin film temperature sensor.[48] Another method is provided by scanning near-field optical microscopy (SNOM, NSOM).[49, 50] This can be used to exploit the temperature-dependence of the optical properties of a material, namely the reflectance. For this reason it is called reflectance thermometry.[51]

Despite the success of all these approaches, most SThM is now carried out using near-field electrical resistance thermometry and this has been the method adopted in the work reported in this dissertation. This is because miniaturised resistive probes have the considerable advantage that they can be used both in passive mode as a
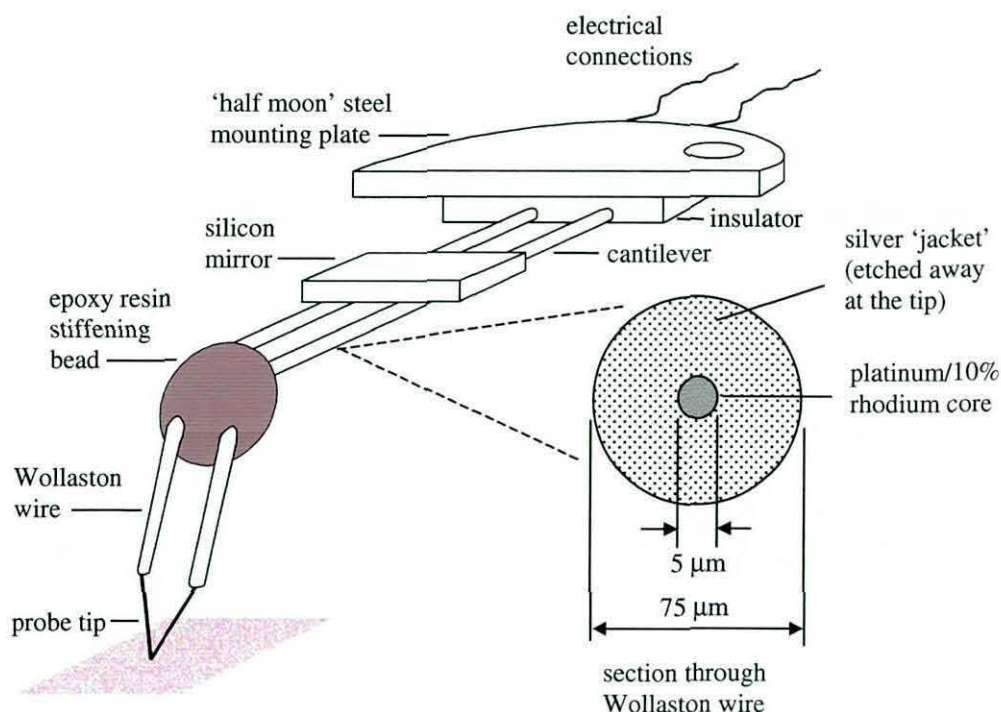
Fig. 1.4. A Wollaston resistive thermal probe (not to scale), including a section through Wollaston process wire. Fig. 1.1 is a schematic diagram of such a probe mounted in an AFM.

thermometer and as an active heat source. This enables L-TA to be carried out as well as SThM. At present the most common type of resistive probe available is the so-called Wollaston or Wollaston wire probe, developed by Dinwiddie, Pylkki and West [52, 53] and first used by Balk et al.[5] and Hammiche et al.[18, 19] A diagram of the construction details of this probe is shown in Fig. 1.4. A loop of 75 μm diameter coaxial bimetallic Wollaston wire is bent into a sharp 'V' shape loop. The wire consists of a central 5 μm diameter platinum/10% rhodium alloy core surrounded by silver. The loop is stabilised with a small bead of epoxy resin deposited approximately 500 μm from its apex. The probe tip or sensor is made by etching the outer silver wire in the immediate vicinity of the apex of the loop. This exposes the 5 μm platinum alloy over a length of approximately 50 μm. Because the wire at the tip is so much thinner than the rest of the wire in the loop, this is where most of the electrical resistance in the probe circuit is concentrated (typically 2–3 ohm). Hence, when a current is passed through the probe, heating is substantially restricted to this element (usually known as the probe *tip*). The other end of the loop is fixed, via an insulator, to a "half-moon" steel mounting plate compatible with the AFM scanner magnetic chuck. A silicon mirror is bonded to the top side of the loop to allow operation of the laser optics. The loop is bent downwards between the epoxy bead and the apex, typically at an angle of 45°-70° to what is now the cantilever.

The precise angle is determined largely by the shape of the bead, which is somewhat variable. Some variability also exists in the length of the exposed tip and the bend radius of the loop. The minimum bend radius of the apex of the platinum loop is determined by the overall diameter (and formability) of the Wollaston wire, so it is considerably larger than would be possible by bending a 5 μm wire independently. This has a considerable effect on the minimum spatial resolution of the probe — see below for a fuller discussion on resolution and related issues. The variability imparted by the manufacturing process on the precise shape of the tip means that imaging and L-TA capabilities may vary from probe to probe. In a L-TA experiment this may take the form of variation in the shape of a melting peak in the derivative power signal, for example. A discussion of the effect of probe geometry on L-TA results is given in chapter 2. Once an experiment is complete, the probe can readily be removed from the sample, by simultaneously heating to above the T_m or softening point of the material and moving the z-actuator vertically upwards. The tip can be decontaminated between runs by heating; for most materials 400°C for a few seconds is sufficient. They can withstand temperatures considerably higher than this, which makes them suitable for localised pyrolysis (see below). Wollaston probes have proved themselves to be very robust and, in the hands of an experienced operator, capable of enduring several hundred individual L-TA cycles.

The Wollaston probe is a relatively massive structure compared with most inert probes used in other forms of AFM. These usually incorporate hard ultra-sharp tips, made from silicon or silicon nitride, whose contact radius may be as small as 10 nm or so, mounted at the end of a relatively simple stiff elastic cantilever. The spatial resolution of such probes is therefore far superior to that of the Wollaston probe, whose high and variable spring constant (5–20 Nm⁻¹) and complexity also render it unsuitable for all but the *contact-mode* imaging described above (various alternative AFM imaging modes are described below). These disadvantages have led to recent efforts at Glasgow University [54-56] to develop a micro-fabricated thermal probe, having a smaller tip-sample contact area, less manufacturing process variability and a more versatile cantilever geometry. This is shown in Fig. 1.5. Semi-conductor manufacturing techniques — photo and electron beam lithography and potassium hydroxide etching — are used to batch-produce the probes from a parent wafer. Palladium conductors are vapour-deposited along the underside of the cantilever and meet on the flattened 2.5 μm × 2.5 μm apex of the pyramidal probe tip. A narrow neck, typically 100 nm wide, is produced in the conductor as it crosses the apex, thus forming a resistive element
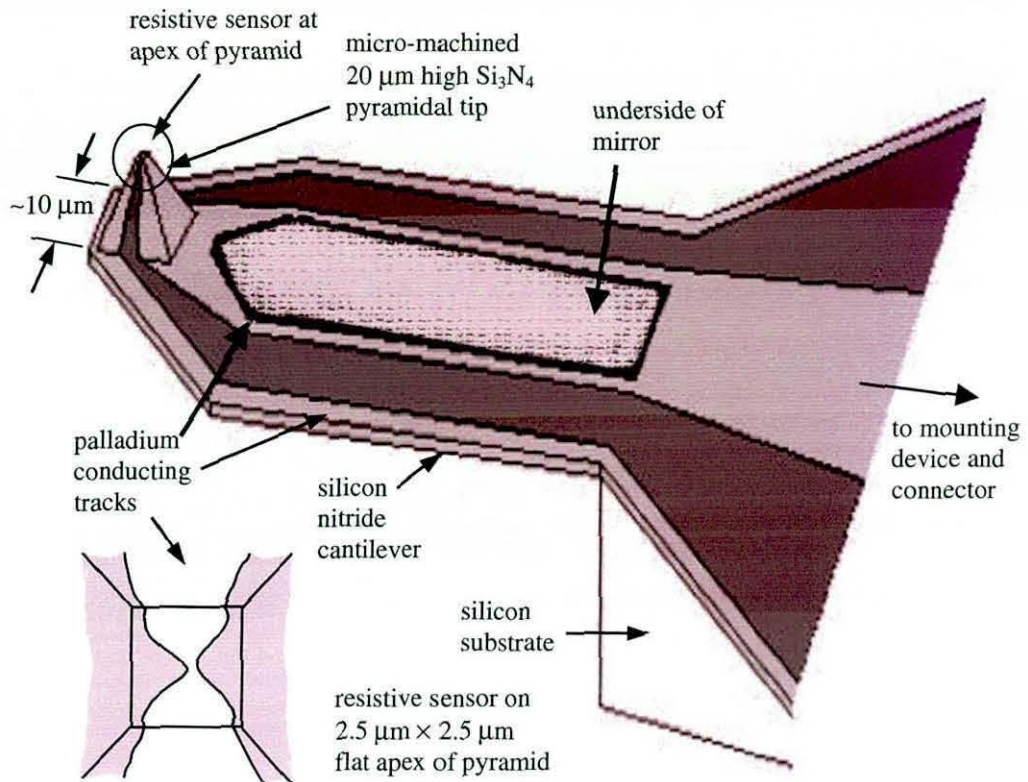
Figure 1.5. Micro-machined thermal probe viewed from the underside of the cantilever, including a plan view of the apex of the pyramid showing the active "bowtie" sensor.

with a nominal resistance of 75 Ω or 125 Ω, depending on the track-width. The conductor has a characteristic "bowtie" shape in this region and so these probes are commonly known as bowtie probes. Apart from its improved resolution compared with that of the Wollaston probe, the bowtie probe has a further advantage in that the mechanical properties of its cantilever are much more akin to those of a standard AFM probe. This makes it much more amenable to use in intermittent contact imaging, including pulsed force mode AFM (see below). The major disadvantage is that it can be used only for SThM and not for L-TA. This is because the heater is relatively small compared with the size of the pyramidal tip. This means that once the probe has indented, for example, a thermoplastic sample, the pyramid is effectively welded in place and cannot be heated to facilitate its removal. The conducting tracks are also somewhat vulnerable to damage. Hammiche et al.[57] have demonstrated the superior resolution of the bowtie probe compared with the Wollaston probe by imaging across the interface in a sectioned polyester-acrylic laminate, using both types of probe.

A development in thermal probe technology that promises to overcome the limitations of the bowtie probe for L-TA, has recently taken place at IBM Research

Division and Stanford University.[58-60] The probes have been designed for use in thermomechanical recording devices for data storage purposes.[61-63] Here, *multiple parallel* micro-machined thermal probes are used to imprint arrays of pits in films of polycarbonate or poly(methyl methacrylate) (PMMA) and then to read the resulting pattern. It can readily be appreciated that such a technology should be able to be *adapted for use in micro-thermal analysis.* The major advantage that this design of probe has over the bowtie probe is that the conductors are produced by doping a thin (100 nm) layer with boron or phosphorus, thus allowing the whole of the surface of the *pyramid to be heated and therefore removed from a sample. A further* advantage is that the conductors, being an integral part of the surface, should be more robust. The spatial resolution of these probes in SThM should also be superior to that of the bowtie probe, because the pyramid has a higher aspect ratio (see below) *and its apex is not* flattened.

As discussed above, the spatial resolution of a particular probe design depends largely on the size of the probe tip or, more specifically, the contact area between tip *and sample. This will gradually increase with tip-wear.* When considering resolution, we take into consideration both the smallest topographic feature that can be detected (the detection limit), how accurately its size and shape is measured and the minimum *distance between adjacent features that allows them to be revealed as distinct* entities (spatial resolution). With a thermal probe the spatial resolution of a topographic image may well differ from the *thermo-spatial* resolution in the corresponding DC and/or AC thermal image. Furthermore, the sub-surface resolution of the thermal *image will* degrade with depth. Besides contact area, other more subtle factors may influence resolution; principal amongst these is the aspect ratio of the tip (length / projected area), as shown in Fig. 1.6. This demonstrates that, although all the probe tips *illustrated will detect* the surface feature shown, it is only the pyramidal tip with the higher aspect ratio that will map it accurately. Similar effects of tip geometry may readily be envisaged on the detection and mapping of narrow and/or steep-sided and/or deep holes *or valleys. This may have a powerful effect on the thermal image in* particular, if the sides of the tip are in contact with the walls of the valley while the apex remains out of surface contact. An additional effect caused by the shape of the Wollaston probe, is that its optimum spatial resolution occurs *in the direction* perpendicular to the plane of the tip loop. However, if the probe normal force is too high, distortion of the tip can take place most easily in this direction, leading to a deterioration in resolution and definition. Under normal scanner operation the plane of

a) Wollaston wire

b) low aspect ratio
pyramidal tip

c) high aspect ratio
pyramidal tip
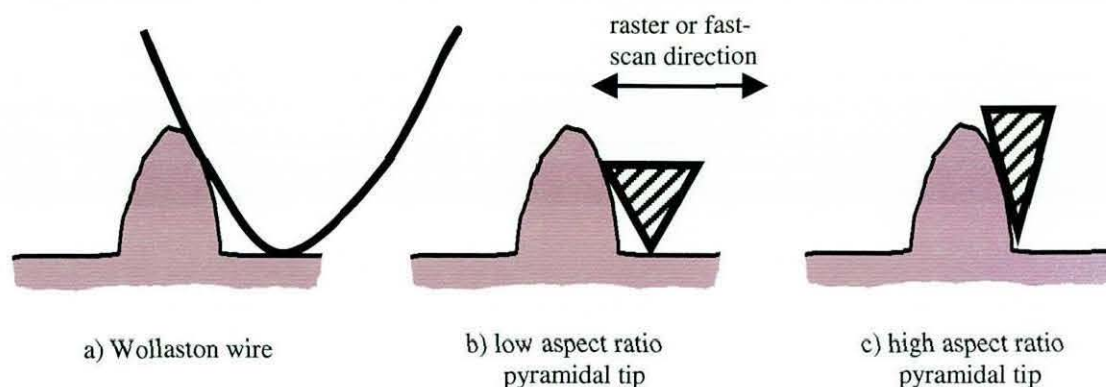
Figure 1.6. An illustration of the effect of the shape of the probe tip on spatial resolution.
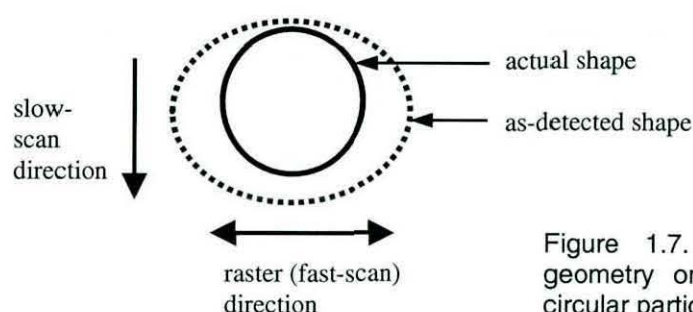
Figure 1.7. The effect of Wollaston probe geometry on the two-dimensional shape of a circular particle as acquired in the resulting image.

the loop is parallel to the raster or fast-scan direction. This is itself at right angles to the direction of probe advancement across the surface (slow-scan direction). Moreover, the edge of a particle or valley will be detected most accurately along the aspect of the feature facing the slow-scan direction. The effect of this on the as-detected shape of a relatively high circular feature is shown in Fig. 1.7. Such spatial distortion can be counteracted to some extent by varying the raster direction in successive scans of the same area and comparing the resulting images, but this is time-consuming. There may also be differences, caused by in-plane asymmetry of the loop, in the shape of the feature as detected in images acquired in the forward and reverse fast-scan directions, but these can be acquired concurrently.

Various papers have been published that give a good indication of the spatial and thermo-spatial resolution that may be expected from both Wollaston and micro-fabricated bowtie probes. Sub-micrometre spatial resolution has been demonstrated on polymer blends using Wollaston probes[18, 19, 64] and Balk et al.[5] have reported detection of features as small as a few tens of nanometres using AC imaging on a GaAs diode, although for most practical samples, such high resolution is unattainable. Work on an paracetamol tablet in the as-supplied condition has been reported by Price et al.[65, 72] in which the contrast in the thermal conductivity image is truly independent of surface

topography. Furthermore, the resolution obtained in a thermal image may be superior to that in the corresponding topographic image.[66] The resolution of the bowtie probe has been demonstrated on model samples of silica coated with a layer of PMMA.[67] Elongated rectangular discontinuities in the coating are detected in thermal images down to a width of 200 nm, but only when lying parallel to the raster direction. The resolution perpendicular to this is shown to be roughly a factor of two poorer. In another direct comparison of the two types of probe, Conroy et al.[68] have demonstrated the superior edge definition as well as absolute spatial and thermo-spatial resolution attainable with the micro-machined probe.

1.1.6   Localised chemical analysis

The techniques mentioned so far provide no direct spatially-resolved information on the chemical composition of materials. Various established analytical techniques, such as secondary ion mass spectrometry (SIMS), X-ray photoelectron spectrometry (XPS) and infrared (IR) and Raman micro-spectrometry can be used to carry out localised compositional studies. In the case of SIMS and XPS, the sample needs to be held in high vacuum, whilst in IR and Raman micro-spectrometry, the resolution is limited by the relatively large wavelength of the excitation radiation. Two developments of micro-thermal analysis have attempted to overcome these limitations. The first of these is localised evolved gas analysis (L-EGA) coupled with gas chromatography-mass spectrometry (GC-MS) [65, 69, 72] or directly with mass spectrometry.[70] This may be regarded as the micro-analogue of the established hybrid technique of thermogravimetry (TGA)-GC-MS, [71] in which the gases evolved from a sample heated in a thermobalance are analysed. The second technique is near-field photothermal infrared spectroscopy. [73-79]

In localised pyrolysis-MS or GC-MS, a Wollaston probe is used to volatilise or pyrolyse a small area (typically < 10 µm × 10 µm) of material by applying a rapid temperature ramp to the tip, typically to 600-800°C, while it is in surface-contact. The maximum depth of the resulting crater is of the order of a few micrometres. The volume of sample pyrolised is dependent on the maximum temperature, the rate of heating, the probe force and the nature of the material (for example, some materials will shrink away from the probe before pyrolysis occurs [69]). As before, the probe can be directed to any location of interest within a previously-acquired image and L-TA can be carried out if required. In the GC-MS configuration of the technique, the gases evolved are sucked into a tube packed with a suitable adsorbent material, such as Tenax or

Carbopak. The intake nozzle of the tube is placed in close proximity to the probe tip, by use of a micromanipulator. After pyrolysis, the tube is removed and placed in a thermal desorption (td) unit from which the resulting products are fed into the GC-MS set up. The advantage of using td-GC as a precursor to MS is that the analysis can be ion-specific, the disadvantage is that it is relatively slow; to build up a representative compositional map of a surface would take several hours. To overcome this, the evolved gases can be fed directly into the spectrometer through a fine capillary tube, with one end again placed in close proximity to the probe tip. The gases take a few seconds to travel the length of the transfer line.

The technique has been demonstrated by Price et al. [65, 69, 70] in the identification of poly(α-methyl styrene) contaminant in a sample of polystyrene and on a polyethylene-coated styrene-butadiene rubber film. In the latter application, successive pyrolysis runs were carried out at the same location to obtain depth-related information. It has also been shown that the Wollaston probe can be used to remove a small sample from the surface, by heating the material to a temperature sufficient to soften it, but too low to cause appreciable degradation.[70] The probe is pulled out of contact while the material is in the softened state, leaving a *nano-sample* on the tip. This method has the advantage that a much lower volume of material is sampled than in a local pyrolysis experiment, so the spatial resolution is potentially superior (provided there is sufficient material to be analysed). Furthermore, by removing the sample from the tip in a solvent wash, it could be subjected to other characterisation techniques, such as nuclear magnetic resonance spectroscopy (NMR). It is also possible to carry out micro-TGA with the sample on the tip, by using the AC power signals as a measure of heat capacity from which the weight-loss may be inferred.[72]

The spatial resolution of the technique is determined by the minimum volume of the heat-affected zone required to produce sufficient gas to be analysed. It is envisaged that the use of smaller probes with lower thermal time constants will enable resolution to be improved considerably to significantly better than micrometre level. This, in combination with the use of sensitive time-of-flight mass spectrometry and a synchronised gas sampling mechanism, should enable the technique to be used for high resolution real-time chemical imaging. Moreover, by carrying out repeated runs over the same sample area, it should be possible to carry out three-dimensional depth-resolved imaging and develop a form of chemical composition-based tomography.

In near-field photothermal infrared spectroscopy, infrared radiation from a conventional Fourier transform infra-red spectrometer (FT-IR) source is focused to a

spot, typically 500 μm in diameter, on the surface of the sample. A bespoke mounting stage enables an AFM to be located inside the sample cell of the instrument. A thermal probe or a conventional AFM probe can therefore be placed on the surface in the region of highest IR flux density within the spot. A thermal probe in its passive mode can be used to detect the change in temperature at the surface induced by the *photothermal effect*, whereas an inert probe can detect the resulting thermal expansion.[77-81] Using the latter approach Anderson [79] has produced an interferogram with a form similar to those obtained in conventional FT-IR. As yet, however, a spectrum has not been produced from the data. In the established (macro) form of photothermal spectroscopy,[80] the spatial resolution normally achievable is limited by the wavelength of the evanescent thermal wave induced in the sample by a laser beam and for polymers is of the order of tens of micrometres. No such limit exists when a near-field probe is used as the detector and, in principle for a given material, the resolution is determined by the spatial or thermospatial resolution of the probe itself.

As with many of the techniques described a modulation can be applied to the excitation signal, in this case in the amplitude of the of the infra-red radiation. This results in temperature (and volume) fluctuations in the sample. This modulated signal is amplified, fed through an analogue-to-digital (A-D) converter and converted into a spectrum by the standard FT algorithm provided as part of the instrument software. A number (tens) of co-additions are necessary in order to produce an acceptable signal-to-noise ratio. This typically takes several minutes. Hammiche *et al.*[73] have demonstrated the technique on a number of pure polymers and have acquired spectra that correlate well with those obtained by conventional FT-IR. Industrial samples, such as bilayer films, powders and liquids have also been studied with some success.

1.1.7 Practical applications of scanning thermal microscopy and localised thermal analysis

There is a growing body of work describing a broad range of applications of micro-thermal analysis. Results have been reported from work carried out both on model samples and in helping to solve real industrial problems. It can readily be envisaged that micro-TA, in addition to being a powerful research tool, could be used for quality control and testing, and in failure and forensic investigations. It is clear, therefore, that the range of micro-TA techniques, used independently or in concert with appropriate macro-methods, will find an increasing number of uses in the fields of polymeric materials, pharmaceuticals, semiconductors and biological materials.

Polymeric and composite materials provide probably the largest single area for potential applications; in materials development, quality control, diagnosis of production and in-service problems, and forensic applications. The ability of the technique to distinguish between surface and bulk properties, for example in the degree of crystallinity, should prove to be particularly useful.

In recent years, a rapidly growing area has been the development of binary or higher order polymer bends. The mechanical properties of such materials are largely controlled by their microstructure, the morphologies of which have been studied by a wide variety of characterisation techniques. These may consist of discrete, well-separated phases (an occluded or dispersed phase in a continuous phase, for example), an interpenetrating network (IPN), or, in the case of partially-miscible systems, may incorporate a mixed interphase. Such materials are not always amenable to established high resolution imaging methods, such as transmission and scanning electron microscopy (TEM, SEM) and, as discussed previously, conventional thermal analysis provides no spatially-resolved information. The process of phase separation can be studied in real-time using techniques such as light scattering, solid state and scattering NMR, to obtain information on important parameters, including diffusion coefficients and local concentration fluctuations. Such techniques, however, cannot be readily applied to mapping the changes in domain size and phase distribution with time. Furthermore, in higher order blends where a multiplicity of phases may be present, scattering results become very difficult to interpret. The possibility that micro-TA could be used both to obtain images of such microstructures and to carry out L-TA on individual phases is therefore an attractive one and a number of blends have been investigated. These include partially miscible polystyrene-poly(vinyl methylether) (PS-PVME),[64, 82] natural rubber-nitrile rubber (NR-NBR),[82] poly(vinyl acetate)-poly(vinyl butyrate) (PVAc-PVB),[83, 66] poly(methyl methacrylate)-chlorinated polyethylene (PMMA-CPE)[84] and PMMA-polycarbonate (PC).[85] In the case of the PS-PVME system, two studies have been carried out on blends prepared by spin-casting from solution in chloroform (60:40[64] and 50:50[82] by weight). The samples were then annealed at elevated temperature (105°C and 125°C respectively). SThM was then carried out at increasing annealing times in order to study the process of phase separation and subsequent growth of the dispersed phase. This was followed by L-TA[82] at selected locations as indicated by the resulting images, to identify the domains rich in PS and PVME and to plot the increase in T_g with annealing time. The morphology of rubber-rubber blends can be difficult to study using TEM, because the

different domains are very similar in electron density, even after staining with a powerful oxidising agent, such as osmium or ruthenium tetroxide. The fact that Song et al.[82] have used SThM to clearly elucidate the domain structure of a NR-NBR blend, shows that it could be a very useful tool in the field of rubber technology. In the case of the PVAc-PVB blend, the composition was unknown initially and a combination of MTDSC and micro-thermal analysis was used to characterise its morphology. MTDSC was carried out first to obtain a plot of the first derivative of heat capacity with respect to temperature against temperature. This produces a diffuse peak containing the individual responses of the component polymers as they undergo their respective glass-rubber transitions The method of curve fitting to the plot, developed by Song et al.[86] was used to separate this into individual peaks. This confirmed that the system was indeed phase-separated and allowed the T_g of each component to be identified, as well as the composition (70:30, by weight). SThM and L-TA was then used as before to complete the characterisation. With the advent of higher resolution thermal probes, it should be possible to study the much smaller-scale phase separation typical of more complex blends and to probe the segregated interphases (typically, tens of nanometers in width) that can exist in partially miscible systems.

Other heterogeneous polymer systems that may usefully be subjected to micro-thermal analysis include multi-layer films, coatings, composites and joints in adhesively-bonded and welded assemblies. Price et al.[87] have studied a four-layer packaging film, consisting of a thin poly(ethylene-vinyl alcohol) (PVOH) gas barrier sandwiched by high density polyethylene layers with a printing ink-compatible low density polyethylene (LDPE) outer layer. The utility of SThM and L-TA is clearly demonstrated, in being able to obtain, in this case, topographic images of the film in section to identify the number and thickness of the layers followed by L-TA to help identify the polymers from their respective melting temperatures. Similar results have been presented by zur Müehlen, in this case on a film containing a 2 μm polyamide-6 barrier layer.[88] Here, DC and AC thermal images were used to distinguish the individual layers. Also presented are DC and AC thermal images, acquired at high and low frequency, of a metallic paint film. The high frequency AC image reveals only the distribution of metallic particles present close to the surface, whilst the low frequency AC and the DC images clearly show the distribution of sub-surface particles. The use of L-EGA to characterise a PE-SBS film has already been mentioned.[70]

Welding (thermoelectric, ultrasonic or solvent) is routinely used to join thermoplastics (high pressure PE natural gas pipes and PVC pipes and extruded

sections, for example). The quality of such welds must be closely controlled by applying the correct temperature-time-pressure regime. If the temperature is too low or heat is applied for insufficient time, a lack of fusion will result. Conversely, if the temperature is too high, then degradation of the material may occur (crosslinking and consequent embrittlement, for example). Price et al.[89] have used micro-TA to examine the changes in softening temperature of PVC through a sectioned weld line and heat affected zone (HAZ). It is reported that, compared with the parent material, the softening temperature falls in the HAZ and then rises sharply to over 400°C in the weld bead itself.

In fibre-reinforced (FRP) or particle-filled composites, similar variations in T_g may be detected between matrix material remote from a fibre or particle and that in the immediate vicinity an interface. In a FRP, it is usually desirable to have strong bonding between fibre and matrix and for this reason, glass fibres are often treated with sizing or coupling agents. If this is the case, the T_g of the matrix may be expected to rise towards the constrained interface (although there may be a narrow region in which the T_g falls, due to the plasticising effect of the coupling agent itself). This phenomenon may be a consequence of the constraining effect of the high modulus fibre alone, or, in a system where the maximum crosslink density has not been attained in the matrix proper, due to an increase in crosslink density in the interfacial regions. If, on the other hand, efficient bonding has not occurred, then the T_g could fall at what is effectively a free surface. Micro-TA can therefore be used as a diagnostic tool to test the efficiency of the bonding between matrix and reinforcement. Häßler and zur Müehlen [26] carried out such a study of a glass fibre reinforced epoxy resin and were able to detect an increase in T_g towards an interface. A similar study has been reported by van Assche et al. [90] in which L-TA profiling was carried out in a silica-filled epoxy resin. In this case, a reduction in T_g was obtained within approximately 70 μm of the particle-matrix interface. This is attributed to adsorbed water diffusing from the surface of the silica particles into the curing resin and therefore hindering the crosslinking reaction and reducing the crosslink density.

A number studies have been carried out using micro-thermal analysis in the field of pharmaceutical science.[65, 72, 91-96] These fall into two general categories. The first of these is the identification and mapping of the spatial distribution of the active drug and other constituents, such as coatings and fillers (excipients), in compressed tablets. This is important, because it will affect the in-vivo release profile of the drug, which may require careful control. In more sophisticated controlled-release preparations, the

uptake of a drug may be delayed by using a controlled-thickness slow-dissolution coating or by distributing it within or on the surface of microspheres. The spatially resolved information provided by SThM and L-TA is, therefore, potentially of considerable benefit in understanding the effect of manufacturing process variables and storage time on the efficacy of such drug preparations. Results have been published for paracetamol (4-acetamidophenol),[65, 72, 91] which demonstrate the ability of SThM and subsequent L-TA to distinguish drug from excipient. The drug appears as a relatively low-conductivity (dark) area in the image and shows a well-defined melting transition starting at approximately 160°C, whereas the excipient remains unchanged up to 200°C. The structure is undifferentiated in the topographic image. Similar work has been carried out by Royall *et al.* on a controlled-release preparation of ibuprofen in a hydroxypropyl methyl cellulose (HPMC) matrix [93] and on a preparation containing polylactic acid microspheres.[94]

The second major pharmaceutical application is in the study of crystalline *polymorphs* of a drug (forms of the same chemical compound having different *crystalline structures*). Polymorphism is a major area of concern, because the *performance of one polymorph of a drug compound may differ greatly from that of another. Considerable effort is therefore spent in identifying the structure of the desired polymorph and in understanding the factors that may lead to the formation of an undesirable form during manufacture. Moreover, because the polymorph required may be metastable, its storage-stability must also be well understood.* Of increasing interest is the potential use of amorphous compounds which, *because of their tendency to* crystallise, has traditionally been avoided in drug preparations. *The ability of L-TA in* particular to distinguish between amorphous and crystalline materials *may be of* considerable value here. Polymorphs A and B of the drug cimetidine were *the subject* of a study by Sanders *et al.*[92] These were readily distinguished in an SThM conductivity image, due, it is thought, to the presence of adsorbed water in only one of the polymorphic forms.

In the electronics industry, micro-TA will find use in both the direct study of semiconductor materials and devices (where the use of AFM is already well established) and applications involving polymeric components, polymer coatings and metallic materials. In the former category, the study of heat flow and dissipation mechanisms should prove to be of particular interest. Indeed, thermocouple-type thermal probes have already been used to study surface variations in temperature in field effect transistors (FETs).[37] A Wollaston resistive probe has been used by Buck *et*

al.[97] to detect discontinuities in metal conductors beneath a polyimide coating, whilst Myers et al.[98] have used the same type of probe in both imaging and L-TA modes to study the effects of curing temperature on the properties of a dielectric polymer film on a silicon substrate. A similar application has been reported by Fryer et al.[99] in a study of the effects of film thickness and curing cycle on the T_g of crosslinked PS-PMMA photo-resist films. Interestingly, they report significant depression (10-20°C) of the T_g in coatings of the component polymers on silicon oxide when the thickness is less than 70 nm. This presumably implies that the constraining effect of the substrate is outweighed by the "free-surface effect". Light emitting diodes (LEDs) have also been the subject of recent work,[83] in which DC and AC imaging followed by L-TA at several locations were carried out. Different parts of the LED assembly were identified by variations in local thermal expansion detected in the L-TMA signal.

For biological samples, the great advantage of AFM over EM is that plant and animal organisms can be studied in their natural hydrated state and even, with care, while still alive. Indeed, specimens can be imaged while immersed in fluid to simulate the environment in which they live, although this may be impractical when using a thermal probe. As yet a limited number of studies have been reported. Price et al.[83] used micro-TA to measure the thickness (ca. 1 µm) and melting behaviour of water-retentive waxy coatings on the leaves of the succulent plant crassula argentea. In related work,[100] the leaf of the medicinal plant feverfew was subjected to SThM followed by localised pyrolysis-GC-MS, to detect the source and identity of the natural oil exuded by the plant. Imaging clearly identified sac- or nodule-like structures, which evolved gas analysis subsequently identified as containing camphor, which was not present elsewhere on the leaf.

1.2 Micro-thermal analysis using conventional AFM probes in conjunction with a variable-temperature microscope stage

1.2.1 Introduction

Variable temperature stage micro-TA can not only be used to study the effect of different temperature-time regimes on morphology, but also in the study of the morphology of materials that remain essentially unchanged between ambient temperature and the temperature at which the experiment is conducted. In the latter case, temperature is simply used as a variable to improve the sensitivity of the particular imaging technique with respect to the material being studied. For example,

the adhesion or viscoelastic properties of different domains within a heterogeneous material may be indistinguishable at room temperature, but at elevated temperature generate sufficient phase contrast to allow the microstructure to be characterised. Raising the temperature above the T_g of one phase but not the other is perhaps the most obvious strategy for achieving this. This may perhaps be regarded as analogous to conventional TMA, because it is the effect of temperature on a mechanical property (local viscoelasticity, modulus or adhesion) that is exploited, rather than the direct measurement of the thermal properties of the sample.

There are various advantages and disadvantages associated with the use of a variable temperature stage rather than a thermal probe. The most significant advantage is that, through the use of conventional ultra-sharp AFM probes, significantly higher resolution imaging is achievable. Moreover, the sample can now be cooled below ambient temperature (see chapter 3 for a discussion of the temperature limits and other practical considerations). This also enables L-TA to be carried out, using a thermal probe, from a sub-ambient initial temperature, so that low temperature transitions can be studied. The temperature stage can also be utilised in the study of temperature-dependent processes, such as crystallisation, and their effect over time on the structure of the whole sample.

The major disadvantage associated with heating the sample is that, if an irreversible process occurs, the whole of the specimen is transformed. This is evidently not the case with a thermal probe, as only that material in the immediate vicinity of the tip is heated. Different parts of the sample can therefore be subjected to different temperature regimes.

The size of discrete phases or domains present in many heterogeneous polymer systems is often at the nanometre scale. The spatial resolution of the Wollaston thermal probe, at around one micrometre, is therefore insufficient to enable the microstructure of such materials to be imaged and L-TA on individual phases to be conducted. Furthermore, its complex construction renders it suitable only for contact mode AFM (see below for a discussion of other imaging modes). These limitations are to a certain extent overcome by the smaller micro-fabricated bowtie probe. However, its limit of resolution, at around 100 nm, is still insufficient for many applications. For example, the average domain size present in phase-separated block copolymers is often less than 10 nm. Moreover, the design of the bowtie probe renders it unsuitable for L-TA. As has been mentioned, thermal probes developed for data storage applications could produce significant improvements in performance. At present,
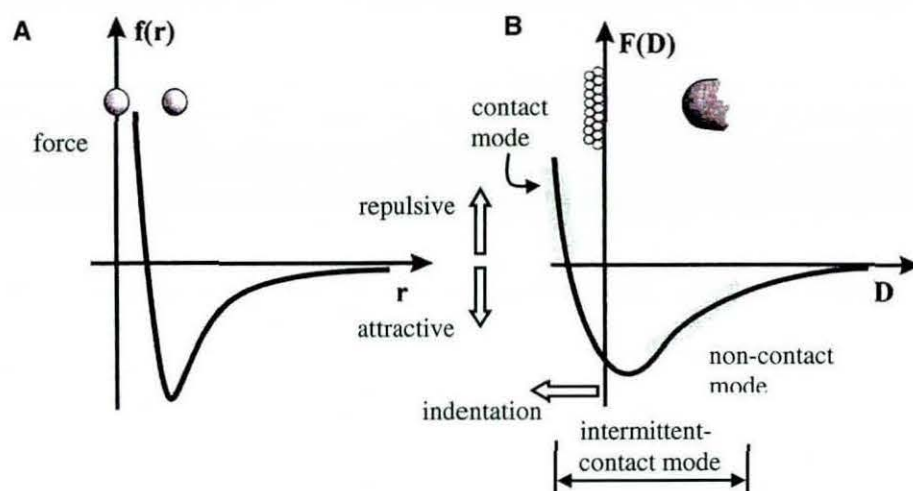
Fig. 1.8. The variation in force with distance acting between (A) two atoms and (B) an ultra-sharp AFM probe tip and a clean surface, assuming the probe normal force is sufficient to cause indentation of the sample surface (hard contact).[103]

however, the only way of carrying out micro-thermal analysis at a resolution comparable with that available in established forms of AFM, is through the use of a variable temperature microscope stage and conventional ultra-sharp probes.

1.2.2 AFM imaging modes

Up until now SThM has almost exclusively been carried out in *contact mode* with the probe held at a constant contact force. The tip-sample distance is in the repulsive regime of the van der Waals interatomic force-distance curve, within a few angstrom of the surface, as shown in Fig. 1.8. This is the simplest form of AFM imaging [107-110] and, if a conventional probe is used, produces only a topographic image, or, if the height is held constant, an image constructed from variations in force (cantilever deflection) caused by changes in sample height and perhaps local elastic modulus — see Fig. 1.9. The latter gives better results on relatively flat samples, as it is very sensitive to small steps and ripples. In practice, unless the scan speed is very low, the height image at constant force will contain a contribution from the tip deflection. This is because the response of the feedback control mechanism is neither instantaneous nor perfect. Moreover, if the probe force is sufficient to cause local elastic deformation of the sample, this will be reflected in the topographic image, particularly if the material is elastically heterogeneous. Therefore, by varying the probe force, the operator is able to enhance particular features in an image (high modulus fibres or particles in a softer matrix, for example [104]). This can be achieved by varying the set-point of the
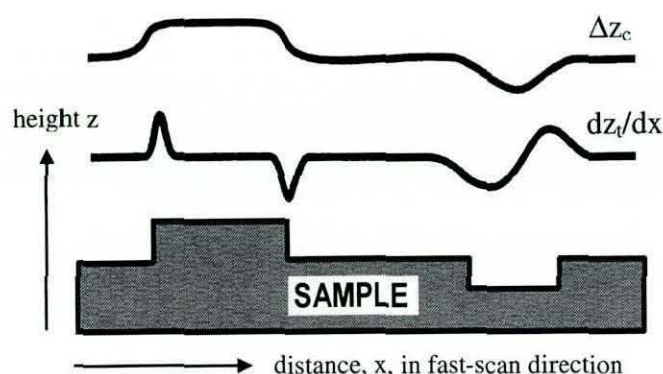
Fig. 1.9. Contact mode imaging. Variation in cantilever (scanner) height, z_c, at constant force ($\propto$ tip deflection, z_t) and variation in force at constant cantilever height (dz_t/dx).

photodetector signal or by using cantilevers of varying stiffness. The limit of detection of the optical lever arrangement towards bending of the cantilever is of the order of 1 nm. When a relatively low-stiffness cantilever is being used, this enables forces as low as 1 pN to be detected.[111] However, this is within the Johnson noise of the cantilever.

Under ambient conditions, a thin aqueous layer is present on the surface of most materials and this can produce a strong attractive capillary force, of the order of 10^{-8} N, between probe and sample, as a meniscus is formed around the tip. The magnitude of the capillary force is dependent on the tip-sample separation, the geometry of the tip and the material from which it is constructed. In contact mode the tip-sample separation remains constant and, provided the aqueous layer is uniform, the capillary forces should remain constant during a scan. Tips can be chemically or physically treated to modify capillary and other forces, or imaging can be carried out in vacuum or in liquid to eliminate the effects of the contamination layer altogether. In the absence of long-range attractive or repulsive electrostatic forces, the remaining major force exerted on the tip is that imparted by the cantilever, which acts as a spring. The magnitude of the cantilever force is determined by the degree of bending and its spring constant. The total downward force acting on the sample can be as low as 10^{-8} N, with the cantilever in its neutral position, to a more typical value in the range 10^{-7}-10^{-6} N, with the cantilever bent in a convex curve towards the sample surface.[106] As has been mentioned, in the repulsive regime, the tip-sample distance is largely independent of the normal force. This is because, rather than pushing the tip closer to the surface, high cantilever forces result in a compressive stress large enough to cause elastic distortion of the sample surface, which therefore moves away from the tip. In polymers and other compliant materials (having a shear modulus less than around 1 GPa), the lateral forces imparted by the tip in the fast-scan direction on anything but a perfectly flat specimen are easily sufficient to cause local plastic deformation and hence damage to the surface. This has been a major factor in the development of intermittent contact modes for imaging polymers.

Integrated tip and cantilever assemblies are commonly available in two standard design formats, according to the geometry of the cantilever itself. The most popular for contact mode imaging is the 'V'- shape or double cantilever (see Fig. 1.10). These are relatively soft in the horizontal plane, but have a high torsional stiffness. For intermittent (IC-AFM) and non-contact (NC-AFM) modes, where a modulation is applied to the cantilever (see below), single "diving board" types are used most often. Cantilevers range from 100-500 µm in length, 10-50 µm in width and 0.3-2.0 µm in thickness. Spring constants vary accordingly, from a few mNm^{-1} to tens of Nm^{-1}. In IC and NC-AFM, the resonant frequency of the assembly is of critical importance and this ranges from several kilohertz to a few hundred kilohertz. Under most imaging conditions, probes for these modes are required to have a single, relatively high-frequency, narrow dominant resonance peak with a minimum of lower-order harmonic peaks.
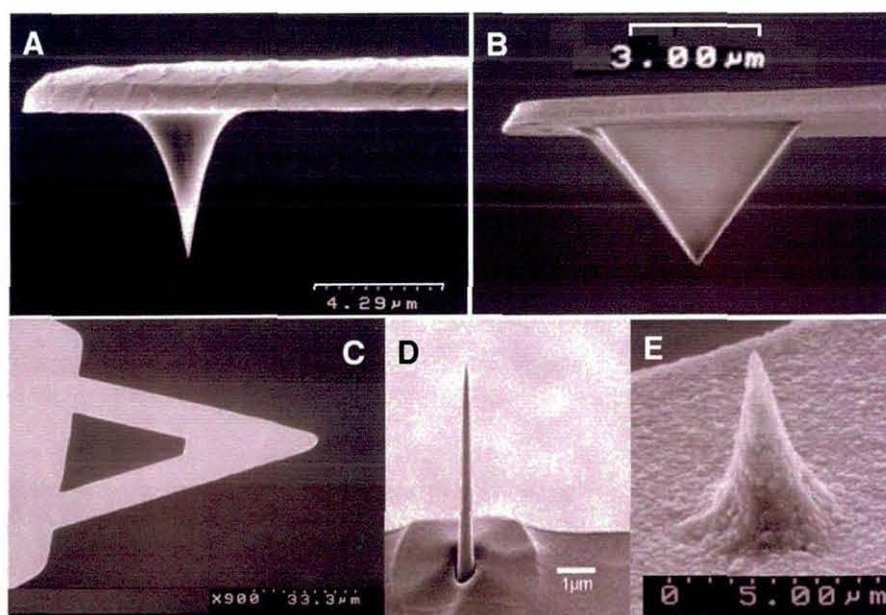
Fig. 1.10. Examples of integrated tip and cantilever assemblies. A) Conical silicon tip on single cantilever. B) Pyramidal silicon nitride tip. C) 'V'-shape cantilever. D) Ion beam-sharpened tip. E) CVD diamond-coated conical tip. *Courtesy of TM Microscopes Ltd.*

As with thermal probes, the lateral spatial resolution achievable at a given scanner resolution (step size) is dependent on the radius of the tip. This may vary according to the scan direction, because no tip will be exactly symmetrical. With a sharp tip, the best lateral resolution achievable in AFM is 1-2 nm. This is sufficient for imaging atomic-scale features, but unlike STM, AFM does not achieve true atomic resolution. This is because interactions between several tip and sample atoms contribute to the overall force, whereas in STM the instantaneous current between two single atoms dominates.

The *vertical* spatial resolution is unaffected by this and can be sub-angstrom in each case. *Tips are available in three basic geometries: conical, pyramidal and tetrahedral.* Examples of conical and pyramidal tips are shown in Fig. 1.10. Silicon tips are usually conical and sharp, with tip radii of the order of 10 nm routinely achieved. Moreover, the cone angle is relatively shallow (high aspect ratio), making them suitable for imaging deep, narrow valleys. This does, however, render them relatively fragile and subject to bending under high lateral forces. Pyramidal and tetrahedral tips are usually made from silicon nitride, which is harder and therefore less prone to wear than silicon. These tips have a lower aspect ratio, which makes them mechanically robust, but less suitable for imaging deep valleys and holes. In some imaging modes, notably lateral force microscopy (see below), it may be preferable to sacrifice lateral spatial resolution by using a blunter tip to increase the contact area.

Silicon tips can be doped to render them electrically conductive, in order to prevent the build up of electrostatic forces between tip and sample, as these can have a deleterious effect on the results. In extreme cases, electrostatic forces can be so powerful that other interactions are swamped and it can become extremely difficult to carry out other modes of imaging. Alternatively, a metallic coating, such as cobalt, can be applied. Other coatings, notably CVD diamond, are available to improve properties such as wear resistance. In more specialised applications, a surface treatment may be applied that is wholly dictated by the properties of the particular sample. These include, for example, non-polar (hydrophobic) or polar (hydrophilic) surfactant coatings. Such treatments may act to reduce or increase overall adhesive forces or "activate" a tip towards one particular component in a multiphase system. In applications where spatial resolution may be of secondary importance, it is possible to replace a sharp tip with, amongst other things, a polymer microsphere or even a living biological cell. Again, this is to increase or decrease the affinity of the probe towards certain materials or, in the case of the biological sensor, to detect interactions between, for example, a cell wall and a variety of biological molecules. It is even possible to dispense with a tip altogether and simply use an activated cantilever as a highly sensitive chemical detector.

Although the underlying morphology of a heterogeneous material may affect the topography of a surface, it is usually the case that the size, shape and distribution of domains or phases cannot be gauged from topography alone. This is a major reason why imaging methods have been developed that generate phase contrast from local variations in a physical property, be it mechanical, thermal, electrical, optical or

excitation or driving signal

uncorrected cantilever modulation
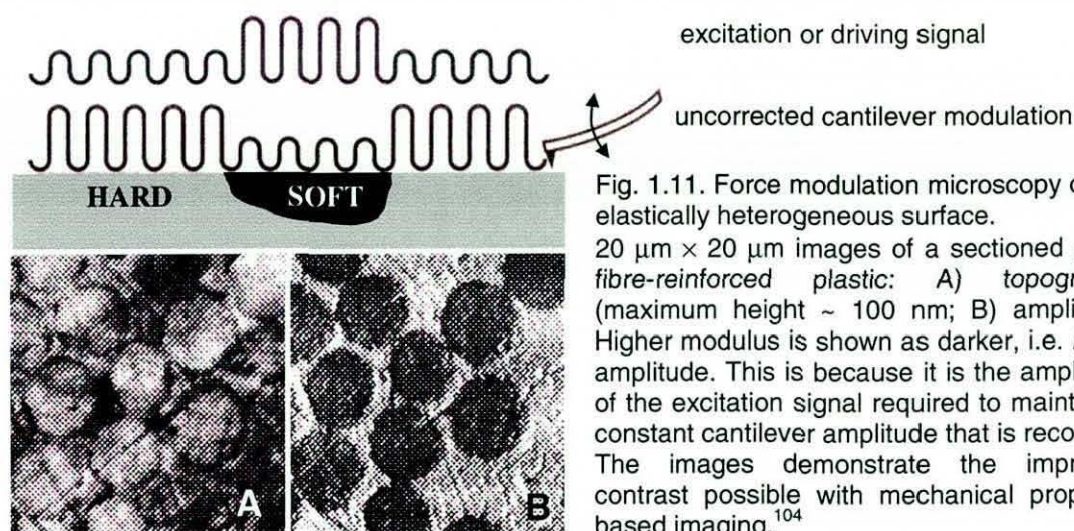
Fig. 1.11. Force modulation microscopy on an elastically heterogeneous surface. 20 μm × 20 μm images of a sectioned glass fibre-reinforced plastic: A) topography (maximum height ~ 100 nm; B) amplitude. Higher modulus is shown as darker, i.e. *lower* amplitude. This is because it is the amplitude of the excitation signal required to maintain a constant cantilever amplitude that is recorded. The images demonstrate the improved contrast possible with mechanical property-based imaging.[104]

magnetic. It is possible to generate mechanical property-based contrast in contact mode by applying a sinusoidal modulation to the cantilever or to the sample. This is known as force modulation microscopy (FMM) and was introduced in 1991 by Maivald *et al.*[112] The operating principle is illustrated in Fig. 1.11. The amplitude of the modulation is of the order of 10 nm at a frequency generally in the range 5-20 kHz, which is well below the resonant frequency of most cantilevers. This is too high for the z-piezo crystal to be able to respond to individual cycles via the force-feedback loop, so the modulation does not disturb the acquisition of a topographic image. The amplitude of the cantilever modulation varies according to the elastic properties of the surface and so can be used to construct simultaneously a *force modulation image*. For polymers, phase sensitive detection (see below) can be used to monitor and construct images from the in-phase (elastic) and out-of-phase (viscous) components of the sample's response to the tip modulation.[113, 114] This is analogous to the measurement of storage and loss moduli in DMA.[20-22] FMM has found a number of applications in the surface characterisation of heterogeneous polymers, including block copolymers,[115] polymer blends[116, 117] and nanocomposites.[118] A recent trend in FMM has been towards the use of increasingly high modulation frequencies and lower amplitudes. In scanning local acceleration microscopy (SLAM),[119] the sample is oscillated at around 1 MHz. At this frequency, the probe can no longer follow the oscillatory deformation of the sample and its response becomes independent of the cantilever stiffness and is proportional to the so-called contact stiffness and inversely proportional to the mass of the cantilever. The probe force is substantially reduced and is in the μN range which results in the elastic deformation of the sample becoming increasingly localised, improving the lateral spatial resolution of the technique. In heterodyne force microscopy (HFM),[118] an
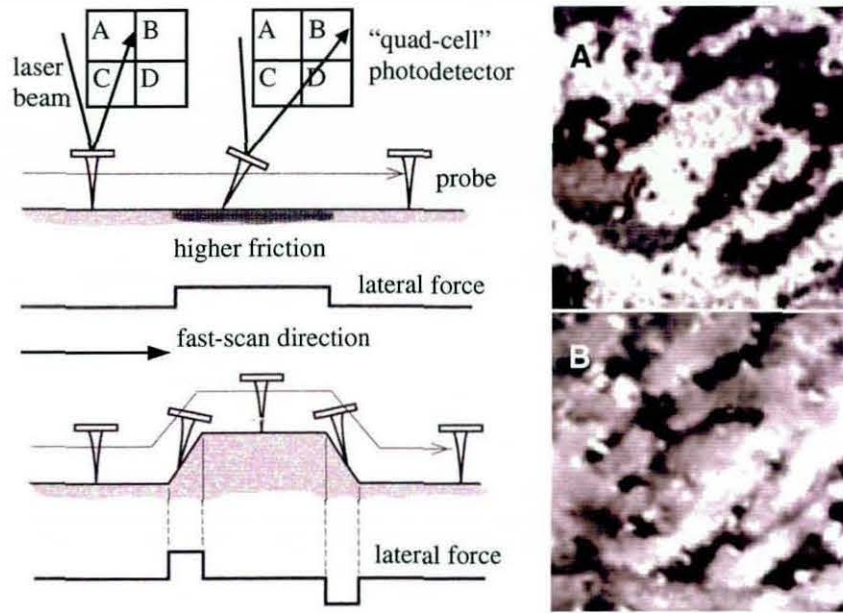
Fig. 1.12. Lateral force microscopy. Changes in lateral deflection of the laser spot at the photodetector [(B+D)-(A+C)] caused by variations in surface friction (top left) and topography (bottom left). The latter effect produces enhanced edge-definition. Also shown are the corresponding 5 μm × 5 μm lateral force (A) and topographic (B) images of a rubber-rubber blend. High friction areas are revealed as bright features in the lateral force image. Note the different shapes of the features revealed at the same location in each image. This shows that topography does not reflect the true phase-separated morphology of the material.[104,106]

ultrasonic vibration, in the MHz range, is applied to the sample to achieve a similar result.

Another method of generating a mechanical property-based image in contact mode is by monitoring the variation in the degree of twist of the cantilever. On a perfectly flat sample this is determined by the local lateral or frictional forces acting between tip and sample. This method is therefore known as lateral force microscopy or friction force microscopy (LFM, FFM).[111, 120-122] In practice, the total lateral force contains contributions from local adhesion, viscoelastic deformation and roughness. In the field of *nanotribology*, the use of calibration techniques[123-126] enables quantitative or semi-quantitative measurements of localised friction and wear properties to be made, although most studies have been made on metals and ceramics.[127-130] The operating principle and examples of lateral force and corresponding topographic images are shown in Fig. 1.12. LFM can also be useful in the imaging of mechanically-homogeneous samples, because the variations in cantilever twist, that inevitably occur as a result of changes in local gradient, produce enhanced edge-definition of discrete features which may merge relatively gradually into the contiguous land. This is because

the signal produced by the lateral deflection of the laser at the photodetector is much greater than that detected by z-actuator. This is illustrated in the lower schematic diagram in Fig. 1.12. In a development analogous to that of FMM, a lateral modulation can be applied to the probe or the sample. In this case, lateral force images can be acquired that are constructed from the amplitude or phase lag of the sample response relative to the excitation signal.[131]

A relatively limited number of LFM studies of polymeric materials have been reported, including some variable-temperature work. Recently, Dinelli et al.[132] have examined the effect of the lateral speed of the tip and the probe force on the glass transition detected in thin polymer films. Vansco et al. have used hot stage LFM and ambient temperature LFM to study the local thermal expansion [133] and the tribological properties [134] of thin films of poly(tetrafluoroethylene) (PTFE).

As has been mentioned, contact mode imaging can be unsuitable for relatively compliant materials and can produce excessive tip-wear and a degree of lateral bending of the tip. All of the above variations of contact mode suffer from this disadvantage. To overcome these problems, non-contact mode imaging was developed.[134-163] Here, a relatively stiff cantilever is vibrated at its resonant frequency (typically, 100-500 kHz) with an amplitude ranging from a few nanometres to several tens of nanometres. As the tip approaches the sample surface, the forces exerted between the tip and sample cause damping of the oscillation and a shift in the resonant frequency. At a fixed average cantilever force, the magnitude of the instantaneous damping or frequency shift is strongly-dependent on the tip-sample separation. This is indicated by the gradient of the van der Waals' curve in the non-contact region shown in Fig. 1.8B. In practice, the AFM feedback and scanner system is used to move the fixed end of the cantilever towards or away from the surface, so as to keep either the amplitude or phase lag between the response of the sample and the driving signal (see below) constant, or in some cases, the resonant frequency of the cantilever. The vertical movement of the z-actuator is used to construct a topographic image. The average force acting on the tip during a cycle is of the order of 10^{-12} N, which is several orders of magnitude lower than in contact mode imaging. This, together with the fact that a stiffer cantilever is used, means that the detected signal is much smaller and necessitates the use of a highly sensitive AC detection system. Besides being useful for imaging compliant materials, NC-AFM is often used in semi-conductor applications in which tip-to-sample material transfer must be avoided.

A major disadvantage of NC-AFM compared with contact mode, is that the topography of any surface contamination layer will be imaged, rather than that of the underlying substrate. Furthermore, it can be difficult to achieve stable feedback conditions, because electrostatic and capillary forces can significantly affect the oscillatory motion of the cantilever. In the worst case, the tip can penetrate the meniscus of a liquid droplet lying on an abrupt raised feature and be pulled into surface-contact by capillary forces.

Intermittent contact imaging combines, to a certain extent, the advantages of contact and non-contact modes. As in NC-AFM, a relatively stiff cantilever is vibrated at its resonant frequency, but this time with the fixed end of the cantilever sufficiently close to the sample (see Figs. 1.8B and 1.13) to bring the tip into contact with the surface at the lowest extent of an oscillation. The duration of the contact or "tap" is sufficiently short to render lateral forces negligible. IC-AFM is often referred to in the literature as "tapping mode"™. The amplitude of vibration can be as large as 100 nm in order to overcome adhesive forces that occur during the contact period. The phase lag (at constant amplitude) or amplitude shift (at constant phase lag) between the sample response and the driving signal can be used to construct so-called phase or amplitude images. The magnitude of the acquired signal is dependent on the viscoelastic nature of the sample. Highly viscoelastic materials will produce higher phase or amplitude shifts than more elastic samples and this can be exploited to produce mechanical property-based phase contrast of heterogeneous surfaces. This is known as phase detection microscopy (PDM) or simply as *phase imaging*. Again, the amplitude or phase of the vibration is kept constant in order to acquire the topographic image and as before either a phase or amplitude image can be acquired simultaneously. In phase detection mode, the actual amplitude of vibration, and therefore the average tip-sample separation, is fixed at a percentage (typically 40-60%) of that of the free oscillation. In amplitude detection imaging, the same goal is achieved by adjusting the set point as a percentage of the maximum
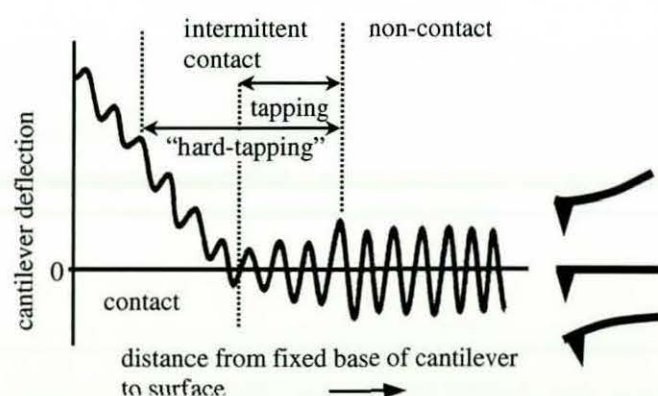
Fig. 1.13. Variation in cantilever deflection as the z-actuator brings the fixed end of a vibrating cantilever towards the sample surface.

downward deflection of the cantilever (and hence maximum downward force) during a cycle. In general, phase detection is used for optimum sensitivity and amplitude detection is used when a large amplitude is required to maximise tip-sample interaction. The choice of mode and optimisation of the set-point value and other operating parameters is largely a process of trial and error for each new sample.

As a consequence of the more intimate interaction between tip and sample, the sensitivity of the technique is far superior to that of NC-AFM, with respect to the detection of variations in mechanical properties across a surface. Moreover, the frequency of vibration is sufficiently high to substantially minimise the viscous or time-dependent contribution to the total viscoelastic response of a polymer. The powerful dependence on measurement frequency of the mechanical properties of a viscoelastic material subject to dynamic testing is a well known phenomenon [20-22] and is a consequence of the macromolecular structure of such materials. On first consideration minimising the viscoelastic response may appear to be a disadvantage, but the technique is so sensitive that saturation of the phase or amplitude signal would be a problem were it otherwise. This would mean that polymers with a wide range of mechanical properties would not be able to be differentiated. Measurement at high frequency also increases the T_g of a polymer, which makes it easier to achieve sub-T_g imaging of materials that are rubbery at ambient temperatures (an in-depth discussion of the practical aspects of sub-ambient temperature and hot-stage AFM is offered in chapter 3). The sensitivity and stability of IC-AFM imaging mean that it has become an almost ubiquitous method in the study of heterogeneous polymer systems and other soft materials by AFM.

In the work reported in this dissertation, unless SThM was being carried out, the contact modes discussed above were used infrequently compared with IC-AFM. For this reason, a more detailed analysis of the mechanisms governing the dynamics of tip-sample interaction and the origins of mechanical property-related phase contrast follows. The description is qualitative and follows the approach taken by Lantz *et al.*[128] *This is because a mathematical analysis of tip-sample interactions in IC-AFM is* complex and, furthermore, a comprehensive model has not yet been developed. More importantly perhaps, the ability to interpret phase and amplitude images is more dependent on a qualitative understanding of the technique and its potential pitfalls. The complexity of the probe-sample interaction during a single measurement cycle arises partly from the fact that the damping force exerted on the cantilever continuously varies with time and changes from repulsive, close to the surface, to attractive further away,

as illustrated in Fig. 1.8. The damped vertical motion of the tip can be approximated by a second order non-linear differential equation of the form:[135-142]

$$m\frac{dz^2}{d^2t} = -k_c z - \frac{m\omega_0}{Q}\frac{dz}{dt} + F_{ts}\left(z_c, z\right) + F_0 \cos(\omega t) \qquad 1.2$$

Where $\omega_0 = 2\pi f_0$ and f_0, k_c and Q are, respectively, the resonance frequency, elastic constant and quality factor of the cantilever; ω is the contact frequency; the driving signal is described by the term $F_0\cos(\omega t)$ and F_{ts} is the tip-sample interaction force, dependent on the equilibrium tip-sample separation, z_c and instantaneous separation, z.

At a fixed lateral scanner displacement, the cantilever deflection and its amplitude of vibration will vary with tip-sample separation in the manner depicted in Fig. 1.13. In the non-contact regime, the cantilever vibrates at constant amplitude. As the tip approaches the surface, the positive force gradient effectively reduces the spring constant of the cantilever and, over a short distance, the amplitude increases. Closer in, this oscillation becomes unstable and the attractive forces are sufficient to pull the tip into momentary contact. At this stage, the kinetic energy of the probe is sufficient to pull the tip out of contact and the cycle is repeated. This is the intermittent contact regime and as the probe moves closer to the surface, the amplitude will decrease accordingly. At some distance determined by the initial amplitude, set-point and stiffness of the cantilever, the probe will have insufficient energy to pull free and the tip becomes trapped in contact. The presence of significant attractive or repulsive electrostatic forces may render it impossible to achieve a stable IC regime. If the cantilever has a high initial amplitude, it may have sufficient energy to cause significant local elastic deformation and still escape from surface-contact some way inside what is normally considered the contact regime. This is known as "hard-tapping" or "hammering" mode. Aside from the inherent complexity of this dynamic system, the construction of a rigorous model is hampered by factors analogous to those discussed for a thermal probe. The most important of these is again the topographic variation in contact area from cycle to cycle, as this will profoundly affect the magnitude of the forces acting on the probe. Moreover, the precise tip and cantilever geometry will vary from probe to probe, causing variation in tip-sample interaction forces with each probe used. Lateral forces, although small, are not completely eliminated in IC-AFM and their contribution is also difficult to factor into any complete model. Their magnitude will depend on the oscillation frequency, which, for a given sample and set of operating

conditions, controls the contact time. The longer the contact time, the greater will be the contribution of lateral forces to the total tip-sample interaction. It has been estimated that the contact time represents 10-30% of the total measurement cycle.[136] This means that over a typical driving frequency range of 100-300 kHz, the contact time is of the order of 0.1-3.0 μs. For a heterogeneous sample consisting of a hard elastic phase and a compliant viscoelastic phase, the contact time will be higher at locations containing the compliant phase. The angle of tilt of the vertical axis of the tip relative to the sample surface at a particular location will also affect lateral forces. It will be noted that, for a given probe and mechanically-homogeneous sample, the number of cycles contributing to a pixel in the acquired image will depend on the required image resolution, the scan area and the scan speed. Assuming that the contact time is 30% of the total cycle time, for a 1 μm × 1 μm scan carried out at a resolution of 300 × 300 pixel at a scan speed of 1 μm s^{-1} with the tip running at 100 kHz, the number of contacts per pixel is 333. The number of actual measurements contributing to a pixel will be determined by the sampling rate of the instrument.

We now consider the origin of the signals required to produce phase and amplitude images in a stable IC regime. Fig. 1.14(a) shows the damped oscillation amplitude (A) and the variation in phase shift, φ, as a function of time at a fixed lateral tip position. Fig. 1.14(b) illustrates the dependence of A and φ on ω. Here z_c is fixed by the set-point ratio (A_{sp}/A_0) and the angular frequency is swept through ω_0. The direction of the amplitude and phase shifts is dependent on the regime of the tip-sample interaction. A net force in the repulsive regime results in an upward shift in the resonance frequency, giving a positive phase shift, (a shift of $\pi/2$ radian corresponds to the free cantilever oscillation). Conversely, in the attractive regime, the resonance frequency decreases and the phase shift is negative. The positive shift of the amplitude peak in Fig. 1.14(b) is typical of compliant materials, such as polymers.[142] Energy dissipation during the tip-sample interaction produces an effective decrease in the quality factor of the probe, resulting in a broadening of the amplitude peak. For materials with a high elastic modulus, the amplitude peak will become narrower and the phase shift will decrease. Under certain combinations of cantilever, sample, driving amplitude and set-point, two stable amplitudes can co-exist at the same frequency. In such cases, the system can flip between the two states, giving rise to the phenomenon of contrast inversion or reversal. An example is shown in Fig. 1.16. A similar effect can occur in the phase image by varying the free amplitude or set-point ratio when operating in the IC-NC transition region, shown in the insets in Fig. 1.14(d).[143-146] This

(a)

(b)

(c)

(d)
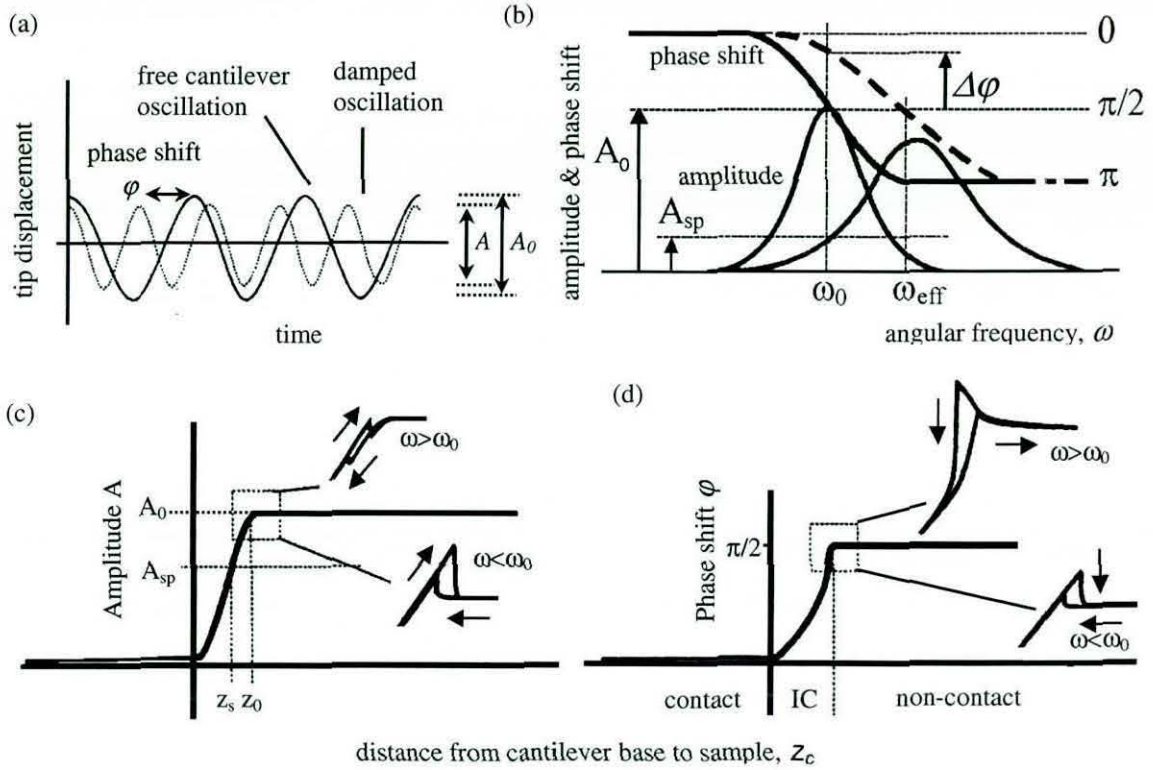
Fig. 1.14. (a) Oscillation of a free and damped $[A = A_0\cos(\omega t+\varphi)]$ cantilever at a fixed lateral location. (b) The variation of amplitude and phase shift with oscillation frequency obtained in the *frequency sweep* mode in the repulsive regime. (c) and (d) show, respectively, the variation in amplitude and phase shift with tip sample separation. The insets depict the hysteresis obtained between the approach and retraction parts of a cycle in the transition zone between the IC and NC regimes and its dependence on frequency.[128]

illustrates the caution the experimenter must adopt when assigning relative phase or amplitude shifts in an image to relative differences in mechanical behaviour. Assuming only a single stable state exists and the operating parameters fall well within the IC regime, the magnitude of the phase or amplitude shift will depend on a combination of local modulus, viscoelasticity [106,145,146] and adhesion.[147-149] The variation in phase shift with Young's modulus and amplitude are depicted in Fig. 1.15(a) and (b) respectively.[135] The data for the elastic modulus were derived using a numerical solution of the equation of motion of the cantilever, assuming energy loss due to local adhesive or capillary forces. Above a modulus value of about 10 GPa, the phase shift becomes independent of stiffness. In the absence of energy dissipation due to adhesion or viscoelastic effects, i.e. the tip-sample interaction is purely elastic, the phase shift remains constant with modulus as indicated by the broken line. The curve of phase shift versus amplitude shows that the highest phase shift is obtained at low and high amplitudes and goes through a minimum at moderate values.
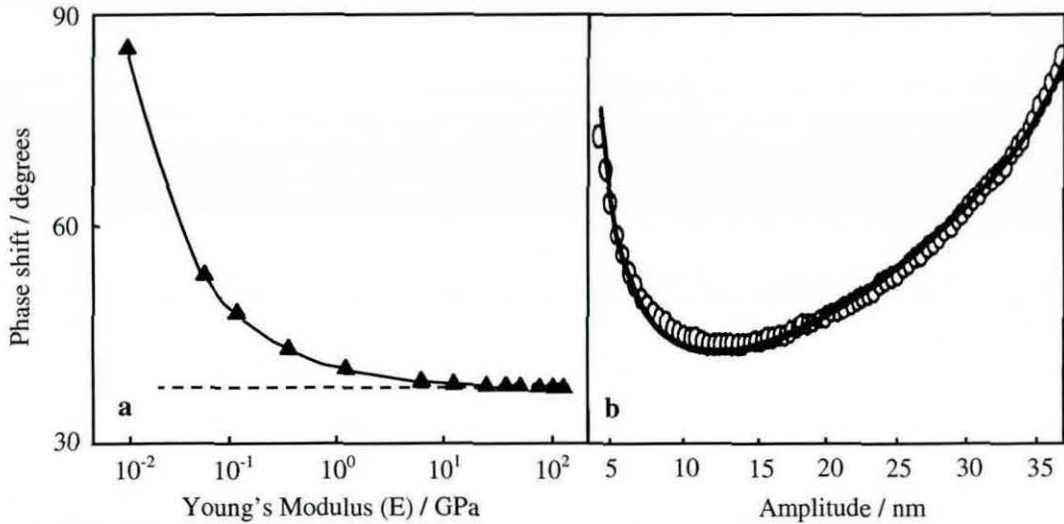
Fig. 1.15. *The dependence of phase shift in IC-AFM on (a) elastic modulus and (b) probe oscillation amplitude.*[135]

Good examples of topographic, amplitude and phase images acquired in IC mode are shown in Fig. 1.16. They were acquired from different scans carried out at room temperature on the same area of a segmented polyurethane elastomer. The utility of *imaging based on micro-mechanical properties is clearly demonstrated, in that the* phase-separated microstructure is by no means obvious from inspection of the topographic image alone. In the two phase images, on the other hand, there is excellent mechanical property-based image contrast which reveals clearly a two-phase morphology. This is reinforced by the shape of the intensity histogram for the images. In both cases there is a completely separated bimodal distribution. The magnitude of the phase contrast in the amplitude image is somewhat reduced and, although the histogram still shows a bimodal distribution, the two populations show considerable overlap in amplitude shift. This shows that the phase shift measurement is more sensitive than the amplitude measurement. The height histogram, on the other hand, is an approximately Gaussian monomodal distribution. In a case in which the images themselves were more ambiguous, such an observation could help confirm that any contrast in the mechanical property image was genuine and not topographic in origin. The significance of the shape of intensity histograms is discussed in detail in chapter 3. As mentioned above, contrast reversal is a potential pitfall in IC-AFM. A good illustration of this phenomenon is shown by images (c) and (d). These are both phase images of the same sample, but acquired under different operating parameters. In image (c), obtained at a lower amplitude and a 50% set-point ratio, the occluded phases are dark (low phase shift), which implies they are less compliant than the more viscoelastic continuous phase. In image (d), obtained at higher amplitude and a 60%
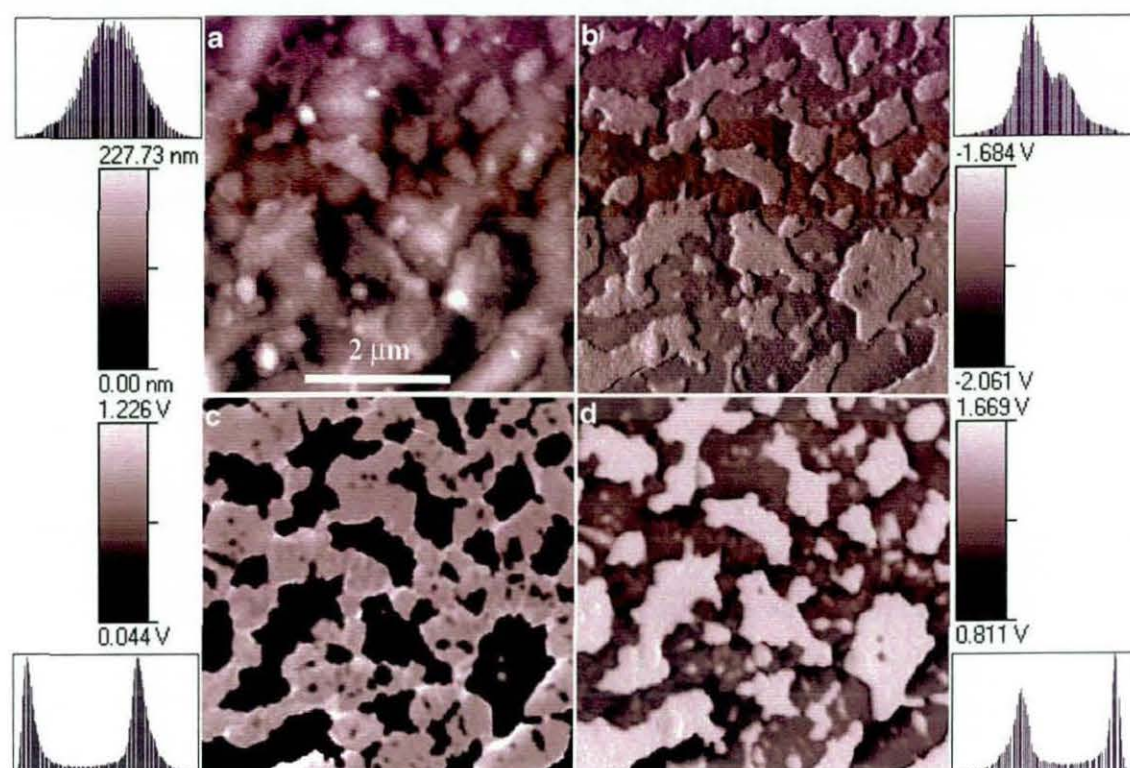
Fig. 1.16. 5 μm × 5 μm images of the same area of a segmented polyurethane elastomer: (a) Height; (b) amplitude; (c) phase shift at moderate amplitude (0.1V) and 50% set-point ratio; (d) phase shift at high amplitude (0.2V) and 40% set-point ratio. The measurement scales and the image intensity histograms of number of pixels (y-axis) against the height, amplitude or phase shift (x-axis) are shown next to the relevant image.

set-point ratio, the opposite is the case. Pulsed force imaging (see below) of the same sample confirmed that the true picture is shown in image (c). The absolute value of the phase shift has not been derived, because here only its relative magnitude across the surface is of interest.

Despite the relative complexity of the probe-sample interaction in IC-AFM and the difficulties that this may cause in the interpretation of images, a substantial number of studies of heterogeneous polymers using the technique have been reported. These range from the imaging of semicrystalline morphology, on a scale of tens of micrometres, to the visualisation of lamellar crystals, lattice structure and microphase-separation at the nanometre scale. In a significant proportion of this work, phase or amplitude imaging is used as a pseudo-topographic surface mapping technique. This is because the lateral sensitivity is superior to that of the height signal in the detection of small steps and other features. This produces better edge-definition than that revealed in the equivalent topographic image, in the same manner as illustrated in Fig. 1.12 for LFM. On the other hand, several workers have attempted to use a more rigorous semi-

quantitative approach in equating the magnitude of phase and amplitude shifts with the mechanical properties of the bulk material. The majority of studies, however, fall somewhere between these two extremes, in that phase or amplitude images are used to obtain qualitative information concerning spatial variation in relative mechanical properties across a surface and this is used to identify the different domains revealed in the image.

Crystallisation and melting, the growth of spherulites and resulting semicrystalline morphology have been the subject of several studies using both contact mode- (for sufficiently hard materials) and IC-AFM.[150-158] The majority of these have been on systems that crystallise relatively slowly after quenching from the melt to room temperature, or after casting from solvent. Increasingly though, the advent of variable-temperature AFM sample stages has facilitated real-time imaging of the development of crystalline order at elevated temperature (further aspects of variable-temperature work are discussed below and in chapter 3). Vansco et al.[150,151] have used ambient temperature and moderate temperature-hot stage AFM (ca. 50-70°C), in both contact and IC mode, to study crystallisation and melting in poly(ethylene oxide) (PEO), poly(ϵ-caprolactone) (PCL), β-isotactic polypropylene (β-IPP) and blends of PEO and PMMA. Depending on the sample, images are presented that clearly show the development of lamellar crystals, hedrites and spherulites and the post-impingement secondary crystallisation of spherulites. Ivanov and co-workers have used post-heat treatment ambient temperature contact mode AFM [152-154] and time-resolved hot stage contact mode AFM [155] to study crystallisation in semicrystalline-amorphous blends of poly(aryl ether ether ketone) (PEEK) and poly(ether imide) (PEI) and in the parent polymers. Magononv et al. have used IC-AFM phase detection to observe the real time crystallisation of ultra-thin layers of low density polyethylene (LDPE)[157] at temperatures up to 130°C and sub-ambient temperature phase transitions in polysiloxanes (silicones).[158] Height images are used to obtain information on large scale structure, such as corrugations, whereas phase images reveal finer structural detail.

IC-AFM is increasingly being used to study the morphology of polymer blends and copolymers. Bar et al.[159] have used IC phase detection to study the effect of blending history on the microstructure of blends of polystyrene-block-poly(ethene-co-but-1-ene)-block-polystyrene (SEBS) triblock copolymer with atactic and isotactic polypropylene. More recently,[160] they have reported similar work carried out on blends of two elastomers; cis-1,4-butadiene rubber (BR) and styrene-co-butadiene rubber (SBR) containing silica filler particles. In the latter study, the importance of considering the tip

indentation depth when interpreting phase images is stressed. At a fixed set-point ratio, the softer BR domains give a larger phase shift than the harder filled SBR, whereas at a fixed indentation depth, the reverse is the case. McLean and Sauer [161] have carried out similar work on SEBS and other copolymers and on segmented polyurethanes (SPUs). Of particular interest are the images for the SPU, which reveal phase *separation into hard and soft segment domains on the scale of 5–10 nm. As discussed* in more detail in chapter 3, such results are difficult to obtain by any other means. They also show that for very smooth (cast) films of phase-separated polymers, height contrast in IC mode may result almost entirely from compliance-related contrast in indentation depth. Further examples of phase and other IC images are presented in chapter 3.

The difficulties of relating property-related AFM results, such as IC-mode phase shifts, to actual mechanical properties have been mentioned previously. However, the AFM can be used to perform quasi-static highly localised indentation or compression tests, the results of which are somewhat more amenable to quantification. This is sometimes referred to as *force* or *point spectroscopy*, in which a force versus distance curve [163, 164] (*force-distance curve* or *FDC*) can be obtained from any location of interest in a previously-acquired image. The principle of operation is illustrated in Fig. 1.17. The conversion of the cantilever deflection measurement into an absolute force value requires a robust probe calibration procedure. This includes both the measurement of the spring constant of the cantilever and the tip radius. This is because even probes fabricated from the same parent wafer can differ substantially, both in the stiffness of the cantilever and the shape of the tip. The spring constant can be estimated from the resonant frequency, measured in NC mode, finite element methods and so-called spring-against-spring measurements, in which FDCs are obtained from a range of hard elastic materials for which surface deformation is minimal during tip-sample contact.[165–167] In this case all the probe deflection can be attributed to "pure" bending of the cantilever while the position of the tip apex remains fixed. The maximum tip-surface force at the downward limit of travel of the z-actuator occurs at point C in Fig. 1.17. This can be varied and is generally of the order of 10 nN. On a hard elastic sample this typically produces negligible penetration and a contact radius of the order of 0.1 nm. For a compliant viscoelastic polymer, on the other hand, the compressive stress may be sufficient to cause indentation, δ, to a depth of 10–100 nm[106] ($\delta = z_c - z_t$). If the elastic constant of the cantilever is known, the force, F, between tip and sample can be calculated and plotted against δ. *If the deformation is elastic (i.e. at small values of*
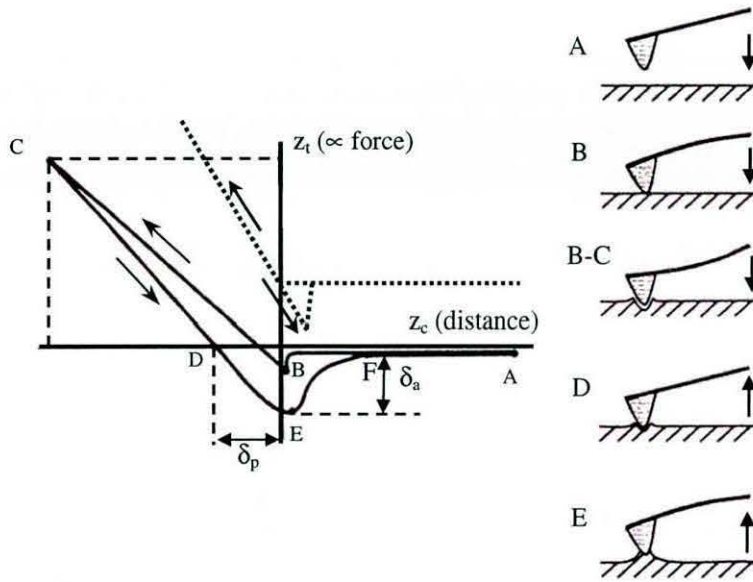
Fig. 1.17. A force-distance curve acquired from a typical viscoelastic polymer during a single slow (ca. 1 Hz) approach and retraction cycle. It shows the vertical deflection or bending of the cantilever (z_b) as a function of the displacement of the fixed end of the cantilever or z-actuator (z_c). The dotted curve, shifted along the force axis for clarity, is a typical result of an equivalent experiment conducted on a hard elastic material, such as glass.

δ), the contact radius may be assumed to be small and constant. The increase in compressive stress is therefore linear. Under these conditions, the stiffness of the sample, k_s, ($= F/\delta$) is proportional to Young's modulus, E, which, if the contact area, a_c, has been calibrated, may be calculated from the relationship $E = k_s/a_c$. It must be stressed, however, that the application of classical mechanics on the nanometre scale is at best an approximation. Reasonable agreement between has, nevertheless, been obtained for bulk and nanoscale values for a range of high modulus materials.[128]

The intercept, D, of the unloading (retraction) curve with the distance axis gives the permanent plastic deformation, δ_p, imparted on the sample, whilst the adhesion force, F_a is approximated by the product of the maximum negative deflection, δ_a (at point E) and the apparent sample stiffness, k_r, during unloading. This is known as the *pull-off force*. This is, in fact, a measure of a combination of adhesive forces and cohesive forces caused by deformation of material adhering to the tip. For low molecular weight materials, it has been shown that the pull-off force is closely related to the adhesive force.[168] At a given strain rate, the magnitude of the upwards stretching of the sample is determined by the thermodynamic balance between the work of adhesion and the cohesion energy of the sample material. In certain cases, a material may yield before adhesive failure occurs.[129] The form of the unloading curve between D and F may,

therefore, be somewhat complex. For a chemically neutral silicon dioxide tip, the pull-off force has been shown to be greater with hydrophilic samples than hydrophobic ones. [169,170]

It would be useful if the localised stiffness and adhesion measurements made possible by the acquisition of FDCs could be used to construct images. Such images should, in theory, be simpler to interpret than, for example, phase images. This is achieved in a technique known as *layered imaging* (LI) or *force-volume imaging*. [171-176] Here, a complete FDC is digitised and stored for each pixel in the final image. A "slice" or *layer* is then selected through the data set at a fixed value of force or distance to produce a two-dimensional property map and these can be added to together to build the 3-d layered image. The major drawback of this approach is the long acquisition time for a single experiment (typically several hours). Furthermore, the computer memory and processing power required to store the data and construct the final image are somewhat large. The maximum number of layers that can be stored reduces dramatically with increasing x-y image resolution; at 50×50 pixel, 200 layers can typically be stored, compared with 25 at 200×200 and 11 at 300×300 pixel. [177] Because of these limitations, LI has not been widely used as a practical technique. Chen et al.[175] have employed LI with protein-coated probes to produce 2-d adhesion maps of polymer surfaces exposed to the same protein. Areas of high adhesion are assumed to correspond to areas of adsorbed protein. Tsukruk and Huang[176] have used LI at different sample temperatures to study the spatial variation with temperature of elastic modulus and adhesion in PS-poly(butadiene) films. The lateral resolution of their images is, however, somewhat low (32×32 pixel).

In an effort to obtain more direct mechanical mapping of surfaces than PDM whilst overcoming the limitations of LI, Marti et al. have introduced pulsed force mode AFM (PFM-AFM).[177-183] This is an intermittent contact mode, in which the probe is subjected to a relatively low-frequency modulation, in the range 100–2000 Hz at an amplitude of 10-500 nm. The operating frequency is at least an order of magnitude less than the resonant frequency of the soft (single) cantilevers generally used in the technique and can therefore be two orders of magnitude less than the operating frequency in PDM. The operating principle is illustrated in Fig. 1.18. At the beginning of a measurement cycle, the tip is well above the sample surface and outside the attractive force regime. When the tip is sufficiently close to the surface, attractive forces pull it into contact (point A). The z-piezo crystal continues to push the fixed end of the cantilever towards the surface and the repulsive force acting on the tip increases to a user-determined
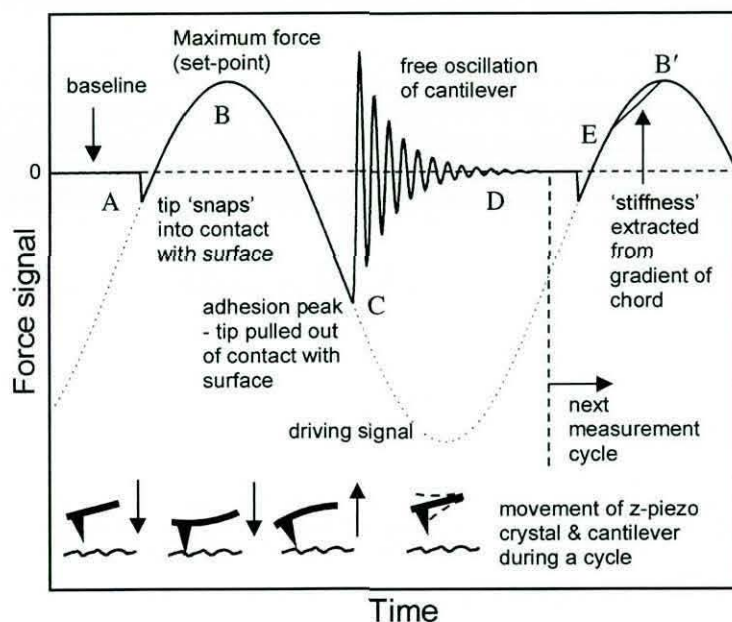
Fig. 1.18. Operation of pulsed force mode AFM. The solid line shows the variation of force with time during a single measurement cycle (ca. 500 Hz). The dotted sinusoidal trace shows the underlying driving voltage applied to the cantilever. The direction of movement and bending of the cantilever during the main phases of a cycle are also depicted.

For clarity, the contact time (A-C) has been exaggerated with respect to the time spent out of contact (C-D).

maximum (point B). Beyond this, the cantilever begins to move upwards and the force decreases towards the baseline (zero) value. At this point the cantilever is in its neutral position. The driving signal continues to move the cantilever upwards and the total normal force imparted by the sample on the tip becomes attractive. At some point (C), the upward force exerted by the bending of the cantilever on the tip will exceed the downward attractive force. When this *pull-off force* is reached, the tip jumps out of contact with the surface and the cantilever undergoes a period of free oscillation, damped towards the baseline (D). The cycle is then repeated at the next lateral location.

As with resonant frequency IC-AFM imaging, the number of measurements per pixel of image is determined by the ratio of the driving frequency to the desired lateral image resolution, the scan area and the scan speed. The much lower driving frequency means that the number of tip-sample contacts per scan is commensurately lower in PFM-AFM. This is not necessarily a disadvantage, because, as mentioned above, the sampling rate of the instrument is a limiting factor. Of greater concern, is the fact that the contact time per cycle is of the order of fractions of a millisecond rather than the microsecond level typical of phase or amplitude imaging. It may be expected, therefore, that PFM-AFM will induce greater shear forces in the surface, thus increasing the risk of permanent deformation being induced in the sample. Gómez-Herrero et al.,[184, 185] who refer to PFM as *jumping mode*, have carried out comparative imaging of delicate samples such as DNA strands and carbon nanotubes[185] using both PFM-AFM and PDM. They conclude that PFM-AFM does indeed induce permanent deformation in

such samples, whereas PDM does not. However, the contact time they used was 10 ms, which is much higher than usual for the commercially-available instrument used in the study reported in this dissertation. The likelihood of the occurrence of such damage to samples, albeit less delicate ones, is a factor considered in chapter 3. The different phases of the force regime are comparable with those undergone by a probe during the acquisition of a force distance curve. In LI, the whole of the force curve is digitised, but in PFM the analogue control electronics extract only a limited number of measurements. Firstly, the baseline is determined. This may vary from cycle to cycle, due to variation in long-range electrostatic forces. All other measurements are made relative to the baseline. If required, variation in the position of the baseline can be used to map variation in surface charges. The (constant) maximum force is recorded and, as in other AFM modes, used as the feed-back parameter to control the height of the z-actuator from which a topographic image is constructed. The AFM set point ratio is used to set the value of the maximum force relative to the baseline. The pull-off force (force at C minus the baseline) is stored for each cycle and is used to build a pull-off force or adhesion map of the surface. The sampling point 'E' shown in the repulsive part of the second cycle in Fig. 1.17 is selected by the operator before scanning commences. The gradient of the chord between this point and the force maximum is used to construct an image related to local stiffness. This is usually referred to as the "stiffness" or "indentation" image. Areas in the sample with relatively high modulus will produce a steeper curve and *vice versa*.

The fact that only this limited number of data points are recorded for each cycle, means that the demands made on the electronic control unit (ECU) and the computer system are much more modest than in LI. Hence scan speeds of the order of 1 Hz or faster (depending on the scan area) are possible. Acquisition times are therefore comparable with those possible in NC- and IC-AFM. Moreover, the pull-off force and indentation measurements should, in theory, be more directly related to definable localised mechanical properties than the phase or amplitude images acquired in IC-AFM (a direct comparison between PFM-AFM and IC-AFM carried out on the same sample areas is shown in chapter 3). As in point spectroscopy, the magnitude of the pull-off force obtained by PFM-AFM of viscoelastic materials is dependent on a number of factors, not adhesive forces alone. These include compliance, elasticity and under certain conditions, rheological properties. These effects are summarised in Fig. 1.19. In case (d), if the sample is able to wet the tip, capillary forces will pull the material up its surface, causing a substantial increase in contact area. If the tip-sample adhesion is
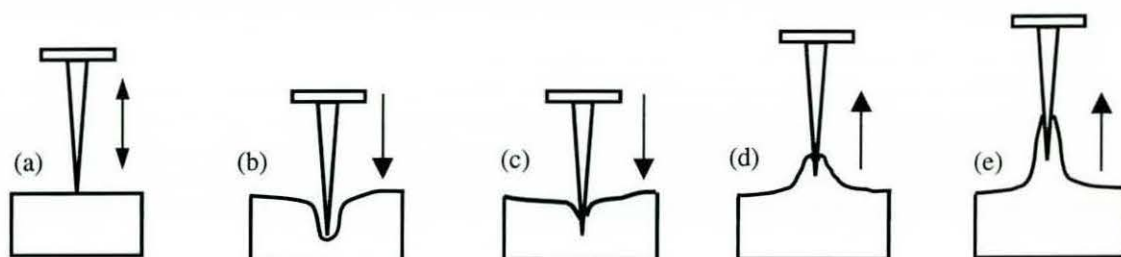
Fig. 1.19 Tip-sample interactions in PFM-AFM. (a) A hard elastic material shows minimal sample distortion and adhesion. (b) An elastic sample during indentation at high normal force. (c) A compliant viscoelastic material during indentation. As the tip indents, it will cause an increase in contact area with a consequent increase in tip-sample interaction forces. (d) A compliant viscoelastic material during retraction. The pull-off force required to pull the tip out of contact is dependent on a combination of the work of adhesion and the tensile elasticity of the sample. The adhesive forces will be critically dependent on the maximum indentation depth, because this largely determines the contact area. If adhesion is low, frictional forces may also contribute. (e) A low viscosity viscoelastic material, e.g. a molten polymer or an amorphous polymer substantially above its T_g. In this case, if the viscosity is sufficiently low, capillary forces may cause the material to "wick" up the tip, thus increasing contact area.

greater than the cohesion in the sample itself, the material will fracture before disbonding occurs, producing contamination of the tip. At the other extreme, if the material has a sufficiently high elongation at break, at low amplitudes the cantilever could reach the upper limit of its oscillation without the material fracturing. This would lead to a steady increase in adhesion and eventual signal saturation as the amount of material clinging to the tip increased with each measurement cycle.

PFM-AFM is a relatively recent development, so its use is not yet widespread and only a limited number of published studies are available in the literature.[13, 177-194] The utility of the technique is demonstrated by Fig. 1.20. This shows a pull-off force (b) and associated topographic image (a) of a rubber-toughened epoxy resin. The occluded circular dark domain is the rubber phase which has a lower pull-off force than the surrounding epoxy matrix. The relatively low adhesion of the rubber phase results from the fact that it is reinforced by a significant volume fraction of silica *nanoparticles* whose diameter is of the order of tens of nanometres. Clusters of these particles are discernible as the relatively dark areas (arrowed) in the 200 nm × 200 nm "zoom" pull-off force image (c). Although the pull-off force could be displayed in units of force (in the nN range), the scale has been left as a voltage. This is because, without carrying out a rigorous force calibration procedure for the cantilever as discussed above, readings in force carry no more information than the raw voltage signal. Inset into images (a) and (b) respectively, are the topographic and adhesion intensity histograms. The surface topography shows an approximately Gaussian monomodal height distribution, whereas the pull-off force has a well-differentiated bimodal distribution. As
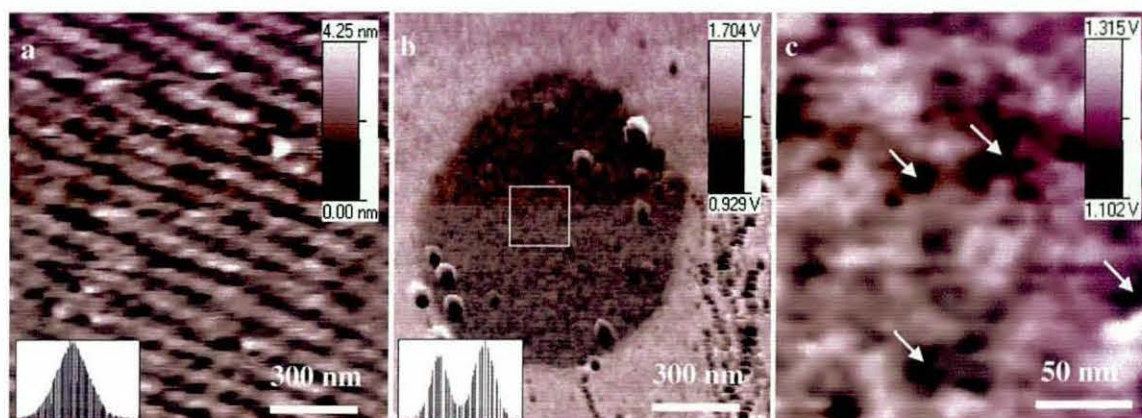
Fig. 1.20. PFM-AFM images of an epoxy-rubber-silica nanocomposite. (a) A 1.3 μm × 1.3 μm topographic image. A maximum height difference of 4.25 nm over 1300 nm reveals the sample to be very smooth. (b) The equivalent pull-off force image. Note that the scale is in volts, because no force or contact area calibration procedure has been carried out. The image intensity histograms of number of pixels (y-axis) against the height or pull-off force signal (x-axis) are inset in each case. (c) A 200 nm × 200 nm "zoom" pull-off force image of the marked area in image (b). The dark, relatively low adhesion domains (arrowed) are thought to be agglomerations of hard silica nanoparticles.

with the PDM results shown in Fig. 1.16, if the images themselves were more ambiguous, this would help confirm that any contrast in the pull-off force or indentation image was genuine and not topographic in origin. The most striking feature of this result is that the phase-separated morphology of this so-called *hybrid nanocomposite* is completely undetected in the topographic measurement. This is another good illustration of the utility of mechanical property-based imaging. The results described by Marti *et al.* are from experiments carried out on different types of "model" sample, designed to demonstrate the utility of the technique and its potential advantages and limitations compared with other AFM modes.[177-183] These include applications in the fields of polymers, semiconductors, electrochemistry and electrostatics carried out in air, vacuum and liquid. Immiscible PS-PMMA blends of varying composition, spun-cast onto silicon have been studied.[182] It was shown that the adhesion-dependent pull-off force measurement is sufficiently sensitive to distinguish between PS and PMMA layers formed as a consequence of their differing affinities for the glass substrate. The images and their interpretation are somewhat different to those offered in chapter 3 of this dissertation, in which results from a more comprehensive study of a similar PS-PMMA blend are presented (some of which have already been published [13]). Results showing the effect of temperature on the pull-off force of PS are also shown. They again differ substantially from the temperature-dependent results for PS presented in

chapter 3. The major difference is that a step increase in pull-off force is detected at temperatures of 50–55°C, which is substantially below the T_g (104°C).

A comparison between force-distance curves and PFM-AFM adhesion measurements carried out on poly(4-methyl-pent-1-ene) (PMP) at different temperatures has also been made.[182] A plot of pull-off force versus temperature in each case shows an increase with temperature above the T_g, although the relationship between measurement frequency and the glass transition means that the increase in adhesion detected by PFM-AFM is delayed until a somewhat higher temperature compared with that obtained by FDC measurements. A carbon black-reinforced natural rubber has been examined.[179] Pull-off force and indentation images are shown to be able to distinguish between the relatively soft high adhesion rubber matrix and the low adhesion harder carbon particles (average diameter ca. 70 nm) when the topography cannot. The pull-off force measurement has been shown to be able to distinguish between amorphous and crystalline areas in a PP spherulite, thus resolving the spherulitic morphology in greater detail than the equivalent topographic image.[182] The amorphous regions are shown to exert a higher force on the tip than crystalline areas, despite the latter having higher surface energy. The explanation offered for this observation is that the greater concentration of relatively mobile free chain ends at an amorphous surface means that greater interaction occurs between the tip and sample. The validity of this conclusion is perhaps questionable, because the amorphous regions between the 30-50 nm thick lamellae are somewhat narrow at 10-20 nm. They are also lower than the crystalline regions which is probably a consequence of them being more compliant. This combination could lead to an apparent increase in adhesion due to an increase in tip-sample contact area. The increase could, therefore, be a topographic artefact. Whatever the generating mechanism, a considerable amount of fine detail is resolved in the adhesion image.

The use of chemically-functionalised tips to carry out chemical force microscopy in pulsed force mode has been reported.[183, 187, 188] Here, a chemical treatment is carried out to produce an adsorbed layer of functional groups on the tip surface. The treatment is tailored towards the particular sample, so as to distinguish between chemically-discrete regions on the surface. Krotil et al.[183] have used silane-treated probes to distinguish, in the pull-off force image, between adsorbed layers of different silanes on a silicon substrate. Fujihira et al.[192, 193] have deployed a similar methodology in using tips treated with an agent terminated with either non-polar hydrocarbon or polar carboxylic acid groups. They have studied printed self-assembled monolayers (SAMs)

AFM tip
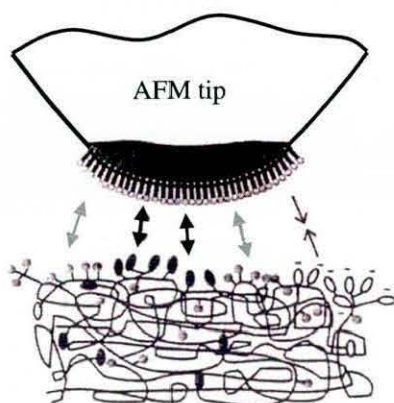
Fig. 1.21. Schematic diagram of a functionalised tip and interactions with a sample surface.[199]

on gold films, in air and water. In air, the highest adhesion occurred between COOH pairs and the lowest between CH_3 pairs. The reverse was the case in water. An illustration of the forces acting between a chemically modified tip and a sample surface is shown in Fig. 1.21.

Despite various workers reporting success, using PFM-AFM in a liquid environment can be problematic, as significant hydrodynamic damping of the cantilever oscillation will inevitably occur. This may be more significant than in resonance IC-AFM, because the oscillation frequency is much lower. Chen et al.[191] have developed a computer simulation to predict the effect of imaging in a liquid (in this case water) and have compared the results with those obtained from real samples. They conclude that the contribution to the tip deflection caused by induced liquid oscillations may exceed that originating from tip-sample interactions. Dickson and Berg[194] have used PFM-AFM and LFM to study the effect on adhesion and friction and, therefore, the surface distribution of a hydrophobic sizing agent (alkenyl succinic anhydride - ASA) when applied to cellulose films. A wide distribution of adhesion levels is reported except at the highest concentration of sizing treatment. In a similar application Leijala and Hautojarvi[186] have used PFM-AFM to study the surface distribution of antistatic, hydrophobic and hydrophilic surface treatments on polypropylene fibres. They found that an oil-like wetting agent could be imaged successfully with PFM, but was too soft for contact mode imaging.

Zhang et al.[189, 190] have studied the structure of mixed aggregates of two different polyphenylene dendrimers deposited on mica surfaces, using NC-AFM (primarily to obtain height information) and PFM-AFM to discriminate between the two components using pull-off force imaging, as well as to study the localised stiffness and adhesion properties of individual dendrimers.

The use of PFM-AFM to map the distribution of surface electrostatic charges, both in air and in water, has been investigated.[177, 180, 183] A patterned sample of Al_2O_3 and SiO_2 with different isoelectric coatings and opposite charges was prepared by Miyatani et al.[177] and subsequently imaged in water. The lateral resolution with which the electrical double layer could be used to discriminate between the different materials was found to be of the order of 30 nm. A similar study has been carried out at different

coupling solution pH values.[180] In the last example, Krotil *et al.*[183] constructed an ideal sample from gold foil laid on a glass substrate with a 25 μm wide gap cut in the film. The tip was negatively charged and the sample acted as a capacitor and, in one scan, both sides of the sample were earthed and in a second scan, one side was earthed and the other subjected to a ±2 V oscillating potential. The effect of relative potential between tip and sample could therefore readily be studied. Low contrast is shown for the earthed sample, whilst high contrast is demonstrated when the sample is positively charged with respect to the tip.

1.2.3 Variable temperature atomic force microscopy

As has been mentioned, work using a variable temperature stage has already been reported for both tapping mode and PFM-AFM. An in-depth consideration of the practicalities of both sub- and above-ambient temperature imaging in both modes is given in chapter 3. Some of the possible reasons for carrying out variable temperature work have also been outlined previously, as well as the advantages and disadvantages of varying the temperature of the whole sample rather than using a thermal probe. However, a brief summary of other variable temperature work and a consideration of more general aspects and problems of using a hot or cold stage in AFM is given here.

Variable temperature AFM sample stages were first developed for contact mode imaging. One of the first hot stage designs reported in the literature is described by Musevic *et al.*[196] This exploited resistive stage heating regulated by a custom-built feedback controller. This was coupled to a commercial instrument in which the sample rather than the probe was raster-scanned. Heat transfer from the hot stage to the piezo electric scanner in the sample mounting stage is reported as being a problem. At elevated temperatures the voltage-length characteristic of the piezo crystals is perturbed, resulting in image distortion. The use of a similar design has been reported by Baekmark *et al.*,[197] in which the scanner was insulated from the hot stage by a thin glass slide. They present distortion-free atomic resolution images of graphite acquired at a stage temperature of 52°C. In a further refinement, Sikes and Schwartz[198] used Peltier-cooling of the scanner to avoid thermal distortion and obtained excellent high resolution images at 95°C. Godovsky and Magonov report the use of a hot stage in which the sample is mounted in a ceramic cup heated by an embedded platinum foil.[157] The temperature of the sample is checked by a thermocouple in contact with its surface. In the absence of an *in-situ* sample thermocouple or other method of temperature measurement, calibration of the sample temperature versus the stage

temperature must be carried out, to account for thermal gradients between the heater and sample surface. Such a procedure is discussed in chapter 3. The use of a microscope that incorporates active probe scanning rather than sample stage scanning significantly ameliorates the problem of distortion due to heating of the piezo-electric scanner. This is simply because the vulnerable scanner components are further away from the heat source and are usually mounted well inside the microscope housing, which has a high thermal mass. This is the case for the TM Microscopes Explorer AFM (formerly Topometrix and then ThermoMicroscopes) used in the work reported in this thesis. The variable temperature stage used in conjunction with this microscope is described in chapter 3.

A problem common to all variable temperature AFM work is spatial *drift* of the sample relative to the scanner, due to thermal expansion or contraction in the mounting stage and sample. It is important, therefore, that scanning is not commenced before significant movement of the sample has ceased. Usually, the image distortion resulting from sample drift is relatively easy to recognise. The effect becomes more significant at higher image resolutions, because of the longer acquisition times this entails. The problem is also more significant for small scan areas (higher magnifications), although for a somewhat different reason. Absolute thermally-induced sample drift may, in fact, be less of a problem, because the scan frequency can usually be increased over small areas, thus reducing image acquisition time. However, in variable temperature work, it is often desirable to be able to scan precisely the same area at different temperatures. This is in order to be certain that any changes in the image are thermally-induced rather than a consequence of scanning a different location. If the scan area is very small, it can be very time consuming to relocate it after the sample has been heated or cooled. The usual way of solving this problem is to scan somewhat larger area than required and use "landmarks" within the resulting image to locate a smaller area of interest at different temperatures. This is not always possible when using a higher resolution scanner, as these have a limited maximum scan area (typically a few micrometres square) and if the temperature change is large enough, the scanned area can move outside the scanning envelope of the instrument. To relocate a small area by moving the sample relative to the scanner can be difficult and sometimes impossible, within a reasonable time limit.

In tapping mode there is an additional problem to be considered, in that varying the sample temperature will result in a shift in the resonance frequency and vibration amplitude of the cantilever. This means that the driving frequency must be re-tuned at

each temperature, thus introducing another variable into the experiment. This problem is not encountered in PFM-AFM, as the driving frequency is usually fixed. The amplitude of vibration will, however, be affected and the experimenter must judge whether the effect of this on the acquired images is significant. Re-tuning of the driving amplitude to ensure an invariant cantilever oscillation waveform at different temperatures is not straightforward with the instrument used in this study. The results reported in chapter 3 would, however, seem to indicate that the effects of the small temperature-induced changes in amplitude are negligible. Another factor is that, as discussed above, relatively small perturbations to the machine variables in PDM can lead to contrast reversal or the loss of a stable imaging regime altogether. However, in other respects it is possible that IC-phase imaging is more suited to variable temperature, particularly sub-ambient, work. This is because it operates at a higher frequency, which means that the T_g of a polymer is higher than that detected in an equivalent PFM-AFM experiment. Therefore, when the minimum temperature achievable by the cold stage is relatively modest, PDM will allow sub-T_g imaging of a greater range of materials. The higher stiffness of the probes typically used in tapping mode results in another potential advantage, in that temperature gradients between the sample surface and scanner will have proportionately less effect on the mechanical properties of the cantilever. In both of these modes there is a potential conflict between the requirements of producing the best possible image at each temperature (in terms of signal-to-noise ratio, definition and contrast) and keeping the machine parameters fixed in order to reduce the number of variables. The operator must therefore decide on the best strategy for each different study. If the effects of temperature on the absolute values of, for example, phase lag or pull-off force are the primary interest, then changes to machine variables must be minimised. On the other hand, for experiments in which the morphology of a material at different temperatures is being studied, then the parameters (such as amplitude and set-point ratio) should be optimised at each imaging temperature in order to obtain the best possible image quality.

In NC- and IC- AFM, the use of a hot stage can have a much greater impact on machine parameters and image quality than in contact mode. This is not just because of the changes in the vibration characteristics of the cantilever, but also because the signal produced is much smaller. This means that thermal effects in the piezo crystals will have a proportionately greater effect on the acquired signals. Better thermal insulation between scanner and heater is therefore required. A hot stage design suitable for IC-AFM using a stage scanner is described by Prilliman et al.[199] The

heating element is a film of indium-tin-oxide deposited on a 6.4 mm thick glass slide. Thermal insulation between the heater and scanner is provided by a 5 mm thick balsa-epoxy-balsa laminate. They report that no distortion was obtained in 5 µm × 5 µm images of a gold calibration grid acquired in tapping mode up to 100°C. Godovsky and Magonov [157] used their hot stage to carry out IC-AFM imaging of the crystallisation of polyethylene at a maximum temperature of 90°C down to a scan size of 300 nm × 300 nm.

Sub-ambient temperature imaging has received somewhat more attention than elevated temperature work.[200-209] The principal reason for this is that at temperatures substantially towards absolute zero, atomic or molecular motion relative to the tip becomes insignificant over the acquisition time of an image. This is clearly important if very high definition images are required at atomic scale resolution. Low temperature work shares some of the problems of hot-stage AFM. If cooling of the piezo-actuators occurs during a scan this will change their voltage-length relationship. Sample drift or non-uniform dimensional changes elsewhere in the equipment may be induced and the mechanical characteristics of the probe will change if there is a temperature gradient between the sample and scanner. There are additional problems in isolating the sample from vibrations caused by turbulence in the coolant system and, unless imaging in vacuum or a suitable low-melting point liquid, in preventing icing of the sample. It may also be desirable to be able to change the probe or sample while the apparatus is at low temperature and/or under vacuum. Several designs of ultra-low temperature instruments have been reported for STM, AFM (including NC-AFM) and magnetic force imaging (MFM). However, these are usually integrated instruments in which cooling apparatus and in some cases the microscope are custom-built. In many cases the instrument is installed in a high-mass anti-vibration mounting arrangement. Such instruments are therefore, of necessity, complex and therefore expensive. Almost invariably, such designs allow imaging to take place with the sample and microscope held in high or ultra-high vacuum. Images obtained at temperatures in the millikelvin range have been presented,[205] acquired using a liquid helium-cooled instrument. More often, though, with this type of cooling, the lowest temperature reported is 4.2 K.[201, 204, 208] Most designs avoid the use of a laser-based optical lever system and instead incorporate either an optical fibre interferometer[202, 204, 205] or piezoelectric tuning forks[208] to achieve tip-sample distance control. The focus of the low temperature work reported thus far has generally been on instrument development through the imaging of

inorganic crystals, such as NaCl [206] and KBr,[201] intermetallic compounds, such as InAs,[210] highly oriented pyrolytic graphite (HOPG) [201, 210] and xenon.[210]

The combined cold and hot stage used in the work discussed in chapter 3 is, by contrast, relatively simple, inexpensive and portable. It was designed for use with the TM Microscopes Explorer AFM and has an operating temperature range of approximately −70-250°C. This is sufficient to enable meaningful variable-temperature studies of a wide range of polymer systems, which, as mentioned above, often involves imaging the same sample above and below its T_g. It also clearly facilitates sub-ambient temperature imaging of, amongst other things, water-based emulsions and pastes and biological samples, which can be too soft at room temperature to allow even NC-AFM to be carried out. The effect of freezing of the aqueous phase on the morphology of such materials naturally requires careful interpretation. The major disadvantage of this stage is that the time available for imaging at low temperature is limited by the rather rapid loss of the nitrogen coolant. Replenishment of the coolant flask cannot be carried out with the microscope *in situ*, although at the time of writing modifications are planned to facilitate this.

1.3 Objectives of research

The primary goal of all the work reported in this thesis was one of practical technique development. Micro-thermal analysis is a recent addition to the range of materials characterisation methods and a thorough understanding of its strengths and limitations is therefore required before it can be considered a mature technology.

The work falls into two general categories designed to develop and evaluate different approaches to micro-TA. The first of these is localised thermal analysis (L-TA) using a Wollaston thermal probe. The main objective here was to study the ability of L-TA to characterise relatively well understood polymer systems, for which a considerable body of conventional thermal analysis and other characterisation data were available. Principal amongst these was poly(ethylene terephthalate) (PET). This polymer was chosen because it was well known that it could be prepared in both an amorphous form, that readily crystallises above its T_g, and in samples having a wide range of degrees of crystallinity. Moreover, PET is frequently used as a "model sample" in thermal analysis, notably DSC and MTDSC, therefore its bulk glass transition, cold crystallisation, melting and crystallisation behaviour are well documented. It therefore seemed a logical choice of material with which the form and reproducibility of the

　
various signals could be evaluated, over a large number of experimental runs, on both amorphous and a range of semi-crystalline samples.

The relative sensitivity of the L-TMA and the DC and AC L-DTA signals in detecting the glass transition and cold crystallisation in samples with varying degrees of crystallinity was another area of primary interest. The relative signal-to-noise ratio achievable in these signals was to be assessed. The effect of various machine variables on the results was then to be studied. These variables were to include the probe-sample contact force, heating rate, the particular probe used and the resistance of the reference probe or variable resistor. The dependence of the AC phase and amplitude signals on modulation frequency and amplitude was also to be evaluated.

Once the operating parameters had been optimised, a comparison was to be made between the trend in degree of crystallinity, as measured by bulk DSC, and any associated trend in L-TA results acquired through the melting transition. In the event of a close correlation being found between the data, the ability of L-TA to detect spatial variations in crystallinity across a surface and, if possible, between surface and bulk was to be evaluated. One of the few established techniques with the ability to measure localised crystallinity is micro-Raman spectroscopy. A comparison was therefore to be made between the ability of this technique and that of L-TA, in terms of the detection limit and the sensitivity to spatial variations in crystallinity.

The second part of the study was designed to assess the possibility of carrying out micro-TA using conventional high resolution AFM probes in conjunction with the variable temperature stage. The primary imaging technique used was to be pulsed force mode. This is because it was thought that any variation in results with temperature would be more amenable to interpretation than in the phase detection mode, used most widely in polymer science. Furthermore, it is a more recent technique, for which there is a much smaller body of literature. It was hoped, therefore, that the work would make a considerable contribution to its development in the field of polymer characterisation. The effect of temperature on the topography, indentation and pull-off force images produced in PFM-AFM was to be thoroughly investigated on at least two different types of sample, between them requiring the use of both high temperature and sub-ambient temperature imaging. Subsequently, the effect of temperature on images acquired in resonance IC-AFM was also to be investigated on at least one of the samples. The results for the two imaging modes would then be compared and an assessment made of the relative effectiveness of the techniques for this type of work.

The first objective was to determine the operating temperature range over which imaging could be routinely carried out. It was thought likely that deterioration in image quality could be caused by factors such as sample-drift relative to the tip, changes in the vibrational characteristics of the cantilever, or temperature-induced disturbance of the characteristics of the piezo-scanner itself. The avoidance of icing of the sample at low temperatures and the impact of noise generated by turbulence in the coolant reservoir was also to be investigated. As has been mentioned, the design of the temperature stage used in this work prevents the reservoir from being filled with the microscope *in-situ*. This means that only a limited time is available at sub-ambient temperatures before the sample has to be heated to above 0°C, the microscope removed and the flask replenished. The lowest temperature that could be reached while still allowing sufficient time for a scan to be carried out at reasonable image resolution and scan-speed was, therefore, another important factor to be evaluated.

Once strategies for obtaining reasonable images over a wide temperature range had been developed, a comprehensive variable temperature PFM-AFM study was to be carried out on at least two heterogeneous polymer systems. The results of previous conventional thermal analyses were to be used to direct the temperature range over which AFM was to be carried out (above and below a glass transition, for example). In studying samples that had been bulk-characterised it was hoped that, if necessary, the identity of any phases or domains revealed in AFM images could be established based on independent corroboration. The first material chosen for this part of the study was a 50/50 (by weight) blend of polystyrene (PS) and poly(methyl methacrylate) (PMMA). The reasons for this were that it was well known that it is a completely immiscible system and forms a phase-separated microstructure that remains stable over a wide temperature range. Furthermore, the domain size was thought to be too small to be able to obtain satisfactory images with SThM using a Wollaston probe, even if the difference in the thermal conductivity of the polymers was sufficient to be detected. The use of a 50/50 blend meant that it would not be clear from the image alone, even if there was good phase contrast, which material was which. The T_g of both polymers is around 100°C, which meant that high temperature imaging would be required. Furthermore, the similarity of their glass transition temperatures meant that imaging could not readily be carried out at a temperature intermediate to the T_g of each component. This is the most obvious initial strategy to adopt when attempting to distinguish between the phases in a blend. It was hoped, however, that the

investigation of the response of the individual polymers to variable temperature PFM-AFM would perhaps provide a method by which the phases could be identified.

The second class of materials to be studied were the segmented polyurethanes (SPUs). The main reason was that it was known that these copolymers have a phase-separated morphology consisting of so-called hard and soft segment domains which, it was hoped, would be amenable to discrimination by probing their relative adhesion and compliance by PFM-AFM. The T_g of the soft segment-rich rubbery phase is typically around -50°C and that of the hard segment is substantially above room temperature, necessitating low or high temperature imaging (lower than in any previous PFM-AFM work). It was hoped that scanning the same area above and below the T_g of the soft segment would unequivocally identify the spatial distribution of the two phases and at the same time provide a rigorous test of the low temperature capabilities of the instrument. An additional incentive was provided by the fact that the morphology of these materials is not revealed by conventional transmission electron microscopy (TEM), as the two domains are very similar in electron density, even after staining.

It was hoped that thermal probes with higher lateral resolution than the Wollaston probe would become available during the course of the work. If this proved to be the case, the possibility was to be investigated of using such a probe in pulsed force mode whilst simultaneously controlling the temperature of the tip. The results could then be readily compared with those generated by changing the global temperature of the sample.

Chapter 2

Localised thermal analysis using a Wollaston wire resistive thermal probe

2.1 Introduction

The commercial instrument with which the work in this study was carried out was based on the concept and prototype developed jointly by the Advanced Thermal Methods Unit (A.T.M.U.) headed by Dr. M. Reading of the Institute of Polymer Technology and Materials Engineering at Loughborough University and Professor H. Pollock's team at the School of Physics and Chemistry at Lancaster University. In early development work, the ability of the equipment to detect, for example, glass and melting transitions in polymers and to produce images of surfaces based on contrast in local thermal conductivity was proven. The overall aim of this subsequent study was to build on this early work and gain a much better understanding, based on a much more substantial body of data, of the utility of the technique in the characterisation of polymers. Of particular interest were the form that transitions take in the output of the various signals, the relative sensitivity of the different measurements and the run-to-run reproducibility that could routinely be achieved. This study was to be carried out on a typical highly crystalline polymer, an amorphous polymer that would remain amorphous during heating and an amorphous polymer that would readily crystallise during an experiment.

Once a thorough understanding of the performance of the instrument had been established, it was planned to investigate the feasibility of using localised thermal analysis as a semi-quantitative method of measuring the local degree of crystallinity in semi-crystalline polymers at the micrometre scale. If it proved possible to develop such a method, it was thought that it would represent a considerable advance in the state of the art in the characterisation of semi-crystalline polymers.

2.2 Experimental

2.2.1 Localised thermal analysis (L-TA) and scanning thermal microscopy (SThM)

L-TA and SThM were carried out using a TA Instruments (TAI) 2990 Microthermal Analyzer. This incorporates a TM Microscopes Explorer AFM, modified to enable electrical connections to be made to the sample and reference probes. In the first implementation of the instrument, the reference probe used was another Wollaston probe, but this has subsequently been replaced, for reasons discussed below, by a 1-10 ohm variable resistor. The AFM is operated under software-control via a personal computer coupled to an electrical control unit (ECU). Fig. 2.1 is a schematic diagram of the instrument set-up.
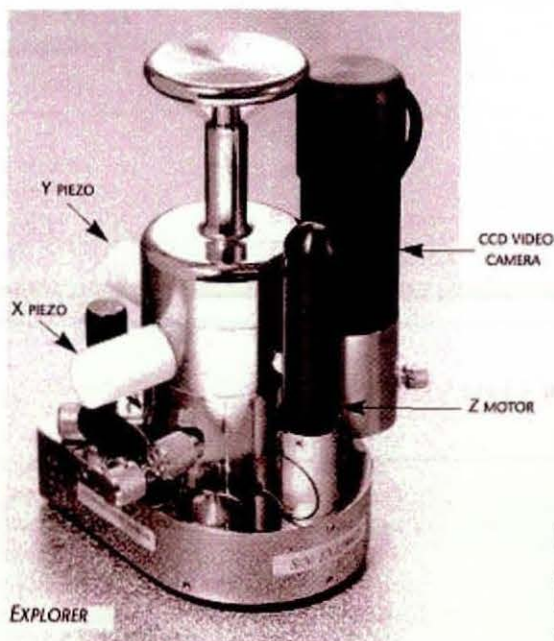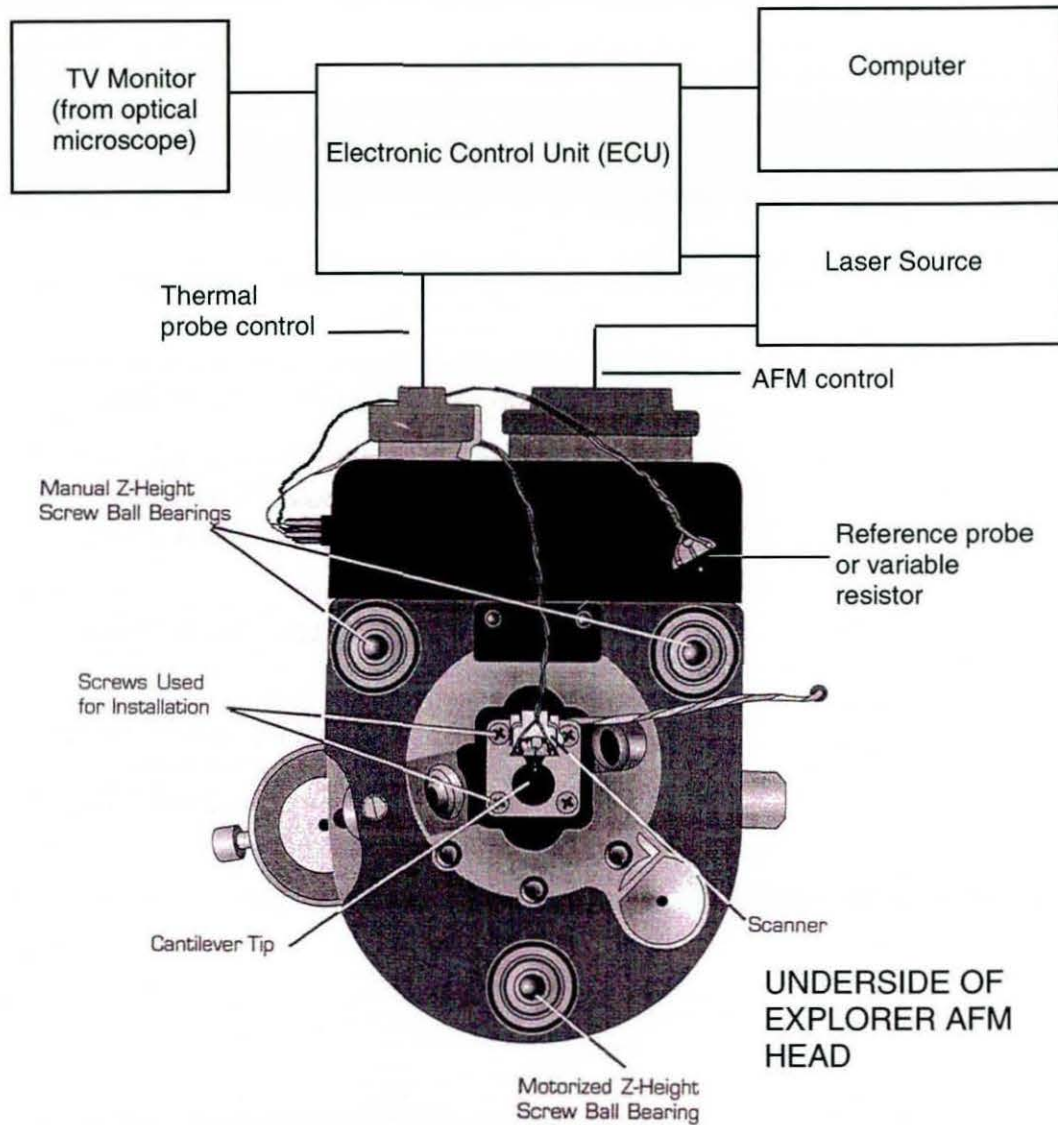
Fig. 2.1. TA Instruments 2990 Microthermal Analyzer incorporating a TM Microscopes Explorer AFM. *Courtesy of TA Instruments and TM Microscopes.*

Each Wollaston probe has its own unique relationship between electrical resistance and temperature. This is a consequence of the inherent variability of the manufacturing process, which produces probes in which the resistance of the 5 µm diameter sensing tip can vary considerably as a proportion of the resistance of the whole probe circuit. This means that a careful temperature-versus-resistance calibration procedure must be followed each time a new probe is installed.

The first step after a new probe is installed in the microscope is to ascertain, using the instrument's default temperature calibration, at what probe current thermal feedback is achieved at ambient temperature. In order to prevent possible overload of the probe, this is carried out by setting the initial nominal probe temperature (as indicated in the software display) close to absolute zero and increasing it in 50°C steps. The onset of thermal feedback is indicated by the probe beginning to consume power. Once this happens, the first calibration point can be obtained by scanning the temperature of the probe from, say, 50°C below to 50°C above this nominal probe temperature. The onset (knee) point in the power versus time trace, that indicates the onset of thermal feedback, is then set to the measured ambient temperature and stored as the first calibration point. Further calibration points can then be obtained by melting several organic crystalline substances, whose range of melting temperatures substantially covers that required by the subsequent experiments. This can be difficult to achieve in practice, as such solids are usually rough and therefore non-reflective. The position of the probe relative to the calibrant surface is therefore often difficult to judge via the TV monitor, which increases the risk of it sustaining damage during coarse positioning of the probe or sample height. For this reason smooth reflective polymer films are often used, despite their somewhat broad melting range. The onset melting temperature [$T_{m(onset)}$] is preferred as a datum, as there is no guarantee that the peak melting temperature in the surface region will be the same as that of a bulk sample. Although it is possible that the onset of melting can be different at the surface compared with the bulk, it is likely that at least some of the lowest melting temperature crystallites in the material will be present at the surface. This is particularly true of polymer films for which the fastest cooling occurs at the exposed surface of the film.

An alternative approach is to use a variable temperature microscope stage. The stage used in this study was developed specifically for the instrument by the A.T.M.U. and Linkam Ltd. Photographs of the stage are shown in Fig. 3.1.The temperature of the heated copper sample stub, after factory-calibration using a platinum resistance thermometer, is guaranteed to be within ±1.0°C of that indicated by the electronic

controller. Independent verification of the stage temperature was carried out in the laboratory using a surface-mounting thermocouple and digital thermometer and by the *melting of crystalline solids of known T_m.*

At each stage temperature the probe tip is lowered towards the heated plate using coarse (but careful) manual control of the z-motor. Contact is indicated by upward deflection of the internal sensor signal in the oscilloscope displayed in the µTA Lab™ software interface. The probe is then backed off until just out of surface contact. If the probe is left in contact, the apparent resistance of the tip will be altered slightly by conduction into the copper stub. The probe temperature is then scanned from 50°C below to 50°C above the stage temperature. The feedback onset temperature is then set to the stage temperature and stored. When a standard Wollaston probe is being used it is not generally recommended that the stage is taken above 150°C, because loss of structural integrity of the probe can occur. For the purposes of this study, however, the temperature was taken to 200°C.

A comparison between the two approaches is shown in Fig. 2.2. The solid line is the calibration curve derived from runs conducted on standard solids. The broken line was obtained using the temperature stage. It is apparent that there is a considerable discrepancy between the two results. This reaches a maximum of approximately 40°C. The most likely reason for this is that, when the tip is in contact with a sample, a somewhat higher current must be supplied to the probe to achieve the required temperature at the apex of the loop. In other words, the calibrant material acts as a heat sink, whereas in the case of calibration using the temperature stage, insulating air surrounds the tip. This is supported by the fact that, with the probe held in free air and subjected to a high temperature cleaning cycle, it is only the region proximal to the apex of the loop that incandesces. In that case, the main 75 µm diameter un-etched Wollaston wire acts as a heat sink whilst the air surrounding the tip acts as an insulator. A temperature gradient therefore exists between the apex of the loop and the junction of the loop with the Wollaston wire proper. It must be concluded therefore, that to allow accurate determination of, for example, transition temperatures, calibration must be carried out using standard calibrants. On the other hand, if the probe is being used to measure the temperature of the surface of a sample on the variable-temperature stage, it should itself be calibrated using the stage.

Calibration drift can be a problem with the instrument, as Fig. 2.3 demonstrates. The results of ten consecutive runs on highly crystalline PET conducted over a period of approximately 30 minutes are shown. During this time the measured T_m shifts by

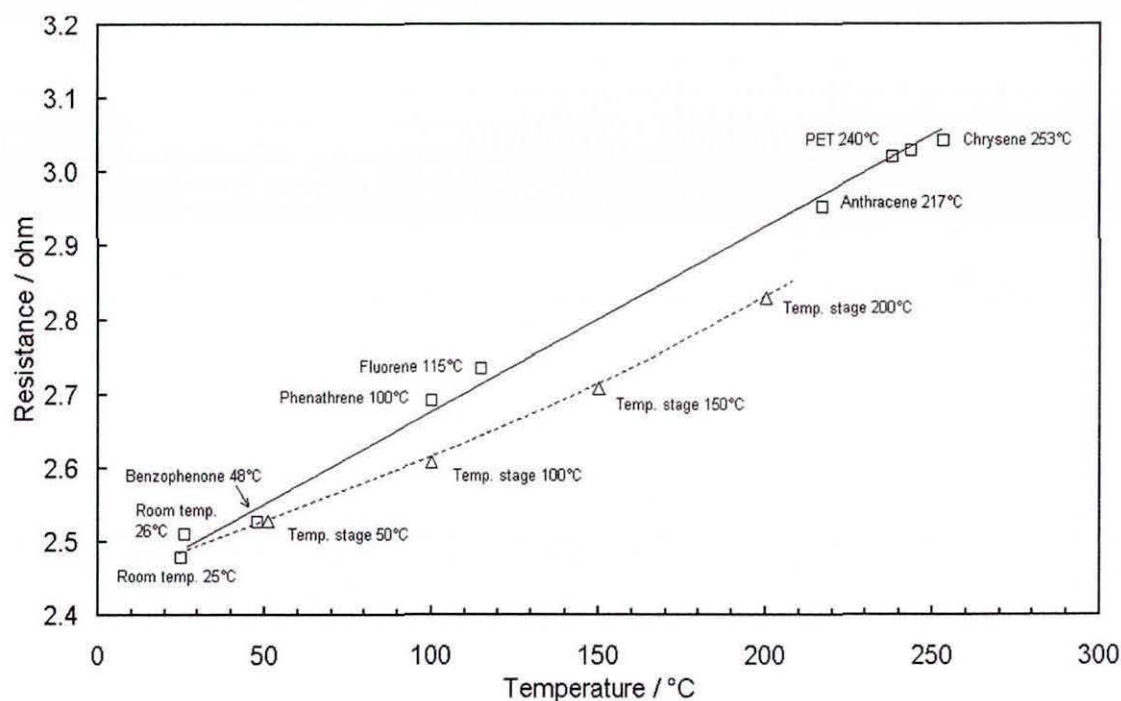Fig. 2.2. Wollaston thermal probe temperature calibration curves. The solid line was constructed by melting organic crystals of known T_m. The broken line was constructed by holding the probe just out of contact with the variable temperature stage at various temperatures.
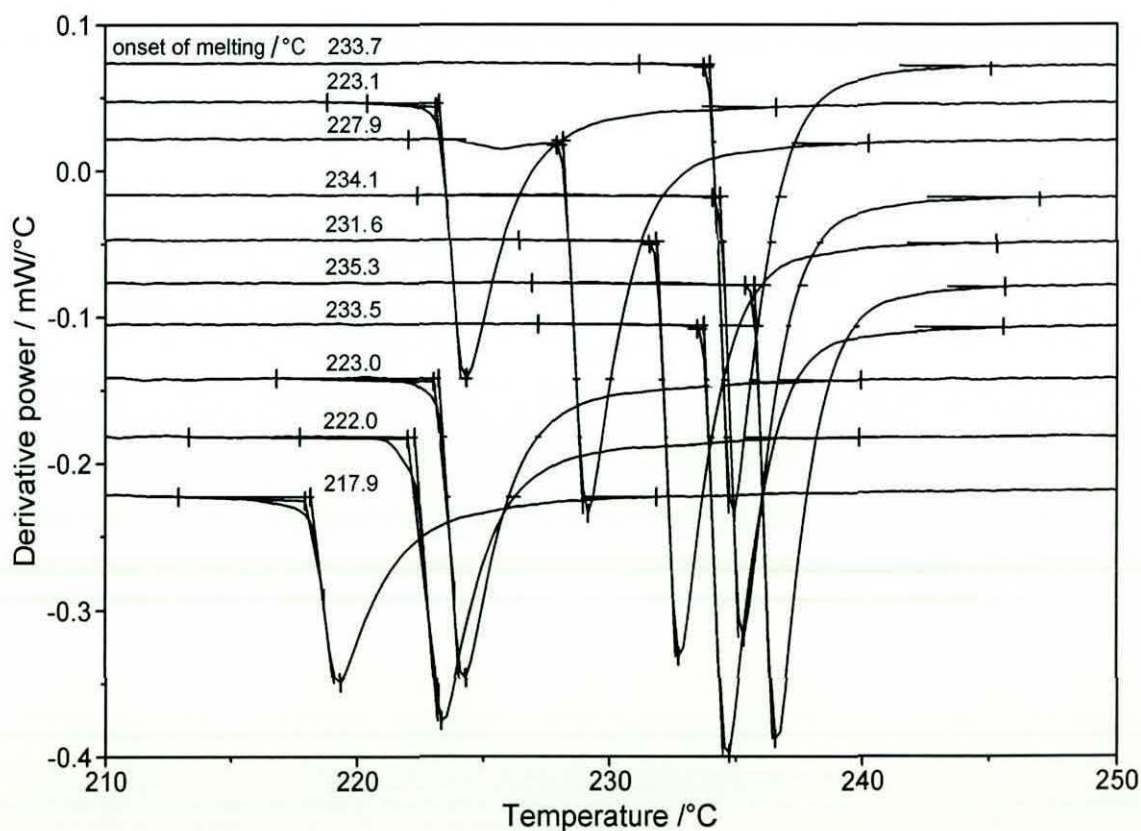
Fig. 2.3. Thermal probe temperature calibration drift obtained over a period of approximately 30 minutes when melting highly crystalline PET.

16°C from 234°C to 218°C. This drift tends to be an intermittent phenomenon which demands vigilance from the operator. The accuracy of the probe calibration must therefore be checked at regular intervals during each set of experiments. In the experiments reported here, if the measured T_m drifted more than $\pm 2°C$ from the known value, the calibration curve was recalculated. This was achieved by checking the onset of feedback at room temperature (with the probe in contact with a sample) and melting benzoic acid and a semi-crystalline polymer of known melting temperature.

Unless otherwise stated, the following conditions were used for L-TA: a heating rate of $10°Cs^{-1}$; a probe "force" of 15 nA; a modulation frequency of 5 kHz and an amplitude of 6°C. A discussion is given below as to how and why these operating parameters were decided upon. Baseline subtraction was used in all the measurements for which results are presented. This is achieved automatically by carrying out a run with the probe held in free air over the same temperature range and at the same heating rate as the subsequent experiment.

In this part of the study the only imaging carried out was using a Wollaston probe in contact mode to acquire topographic images of, for example, craters made by L-TA measurements. Thermal conductivity (or diffusivity) images of the samples have not been presented here, because, even if the contrast in thermal conductivity was large enough, the spatial resolution of the Wollaston probe is insufficient to reveal structural detail of the amorphous and crystalline material in samples of this nature. A contact "force" of approximately 10 nA and a scan frequency in the range 0.5-1.0 Hz were used. Unless otherwise stated, the image resolution was 300×300 pixels.

2.2.2 Differential scanning calorimetry (DSC) and modulated temperature differential scanning calorimetry (MTDSC)

A TAI 2920 instrument was used to carry out DSC and MTDSC on samples of amorphous and semi-crystalline PET. For DSC, the heating rate used was $10°C$ min^{-1}, for MTDSC the heating rate was $2°C$ min^{-1} with a modulation period of 60 s and amplitude of 1°C. The mass of the sample was 7-10 mg in each case and sealed aluminium crucibles (pans) were used. The furnace was purged with nitrogen. To correct for the effects of the sample crucibles, a baseline was constructed from a run carried out with an empty pan, as close as possible in weight to that of that of the sample pan, installed on the sample sensor.

2.2.3 Micro-Raman spectroscopy

Raman spectroscopy is an established technique for studying the morphology of polymers.[210] In its "micro" form it is one of the only methods for measuring variations in crystallinity with high spatial resolution, both two-dimensional and depth-resolved. Measurements were made on samples of PET of differing degrees of crystallinity using a Renishaw S1000 microprobe with 514.5 nm laser excitation. These were the same samples that had been previously studied by L-TA (and identical to those characterised by MTDSC) and the aim of this part of the study was to compare the limits of detection of crystallinity achievable by the two techniques. The instrument was operated in confocal mode allowing micro-Raman spectroscopy to be carried out on very small volumes with a lateral spatial resolution of one micrometre and a depth resolution of about two micrometres.

2.2.4 Materials

The primary material used was Du Pont Melinex 175 poly(ethylene terephthalate) (PET). This is a 175 μm thick biaxially oriented semi-crystalline film. It was used both in its as-supplied state and as the starting material in the preparation of amorphous polymer and samples having a range of degrees of crystallinity. The values of weight and number average molecular weight (M_w and M_n) were determined by gel permeation chromatography (GPC) to be 22,500 and 11,300 respectively (conducted by Rapra Technology). The amorphous material was prepared by melting a 50 mm × 50 mm piece of film on top of a thin woven PTFE sheet placed on a hot-plate at 300°C. A glass microscope slide was used as a doctor blade to squeeze out any air bubbles from the melt. When a reasonably uniform film was achieved, the PTFE film and PET were lifted from the plate and plunged into iced water. The resulting amorphous PET film was then peeled off the PTFE backing. The surface that had been in contact with the PTFE reflected its woven texture, whilst the free surface appeared smooth and glossy to the naked eye. The thickness of the film varied from approximately 50–125 μm. Each piece was cut into 10 mm × 10 mm squares for subsequent analysis or conversion to a semi-crystalline form. The latter was achieved by annealing in an oven at 110°C for times ranging from 1 to 60 minutes. It was ensured that the glossy surface was placed uppermost in the oven in each case and this was the surface subjected to L-TA. To avoid systematic errors arising from batch variations, each starting batch used to prepare samples over the whole range of annealing times and experiments on the different starting batches were randomised.

In order to investigate further the relationship between the L-TMA and L-DTA results produced by the instrument, a component consisting of a thin fluorocarbon coating on a poly(butylene terephthalate) (PBT) substrate was studied. This component was supplied by a third party and the details of its construction and the precise grades of material and coating process used are confidential. For the purposes of this study, such information is, however, not required.

2.3 Results and discussion

2.3.1 Typical L-TA results

Fig. 2.4 shows DSC results from the as-supplied and amorphous PET. The curve for the amorphous sample displays a T_g at approximately 70°C, an exothermic cold-crystallisation peak between 115°C and 140°C and a melting peak between 220°C and 265°C. The as-received material, on the other hand, reveals no evidence of a glass transition or crystallisation peak and has a somewhat narrower melting range whose onset temperature is some 3°C above that of the re-crystallised material. The gradual onset and the broad range of the melting peaks is typical of semi-crystalline polymers and is a consequence of the dependence of melting temperature range on the lamellar thickness distribution present in the sample.

Fig. 2.5 is a typical L-TA result for the as-supplied material, showing the L-TMA and L-DTA traces. No mathematical smoothing (see below) has been applied to the curves. The heating rate was 10°Cs⁻¹ (a discussion of the effects of heating rate and the other machine variables is given below). It is immediately apparent that the onset of melting is considerably more abrupt than in the equivalent DSC result, particularly in the probe deflection (L-TMA) trace. The melting peak in the derivative power (L-DTA) signal is significantly narrower than that in the DSC curve. This is due to the localised nature of the measurement, which is confined to a few cubic micrometres of material. The range of thickness of the crystalline lamellae sampled by the probe is therefore likely to be narrower. However, the excellent reproducibility of the results (discussed in detail below) would appear to indicate that the range of melting temperatures encountered at each location on the surface remained relatively constant. It is more likely, therefore, that the surface of the film contains a narrower distribution of lamellar thickness than that present in the bulk. Prior to the melting transition, the upwards probe deflection is approximately linear, as the material beneath the probe expands with increasing temperature. After the onset of melting, the probe penetrates approximately 4.8 µm into the molten material before the cantilever straightens and the
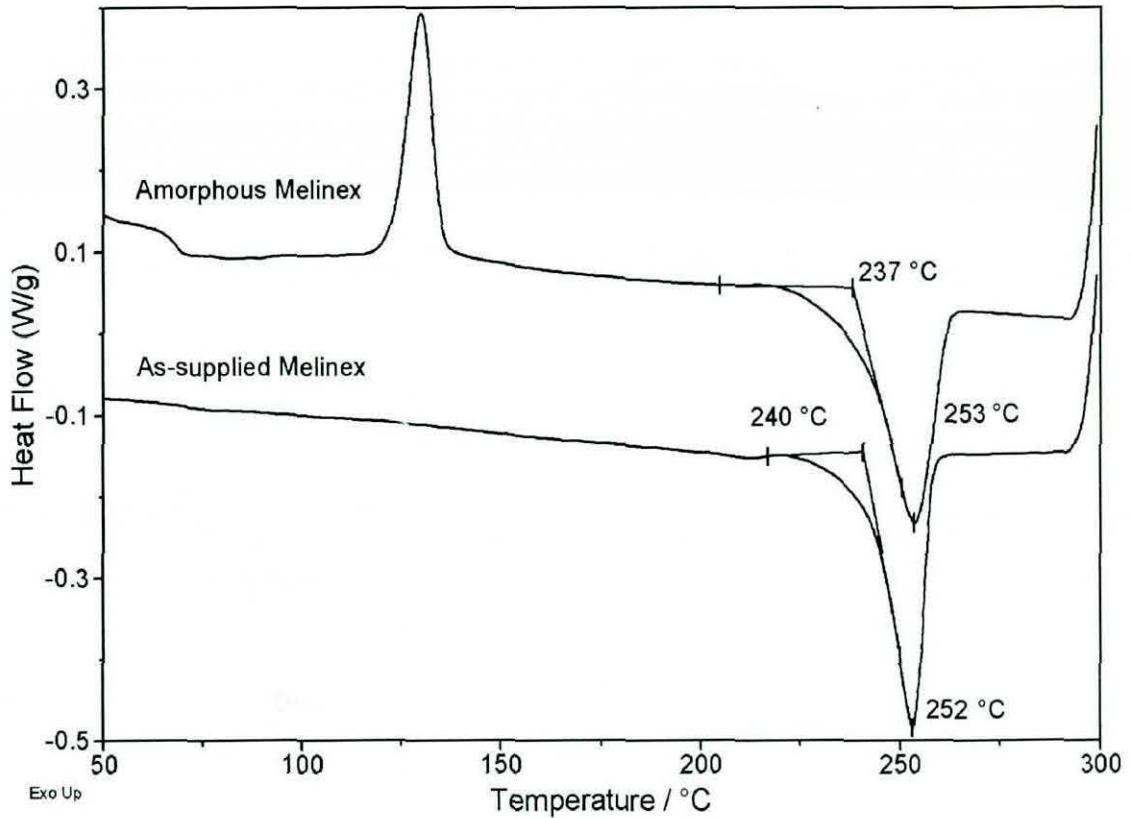
Fig. 2.4. DSC results for amorphous and as-supplied Melinex PET.

normal force tends to zero. As is discussed below, the indentation depth for a given material and heating rate is controlled by the initial probe force. As the tip sinks into the material, the contact area and hence the sample volume increases. This raises the question of how much of the equivalent response in the power signal is a direct consequence of increasing contact area. The slight difference in the onset melting temperature detected in the two traces is a possible indication that the power signal is at least to a degree independent of the probe indentation. Melting is apparently first detected in the L-DTA trace some 3°C below the temperature at which it is detected in the L-TMA signal, when the probe begins to penetrate the surface. In order to establish whether or not this is a real effect, the derivative curves from both signals need to be co-plotted. This has been done in Fig. 2.6. This reveals an almost exact match in the onset melting temperature detected in the two signals and, furthermore, in the shapes of the respective melting peaks. This would seem to indicate that, in the case of the melting of a highly crystalline polymer, the increase in power consumption through the melt is almost entirely due to the increase in contact area. This subject is explored in greater depth below.
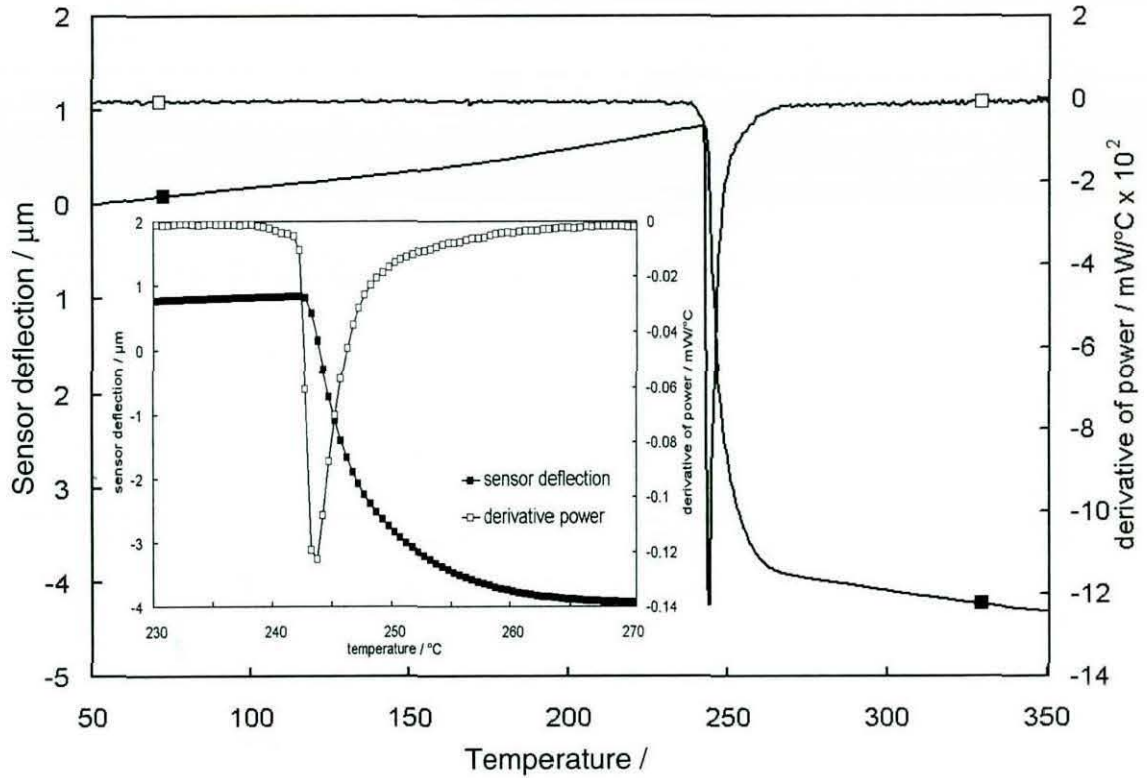
Fig. 2.5. Typical L-TMA (sensor deflection) and L-DTA (derivative power) results for as-supplied Melinex PET. For clarity, an expanded view through the melt has been inset.
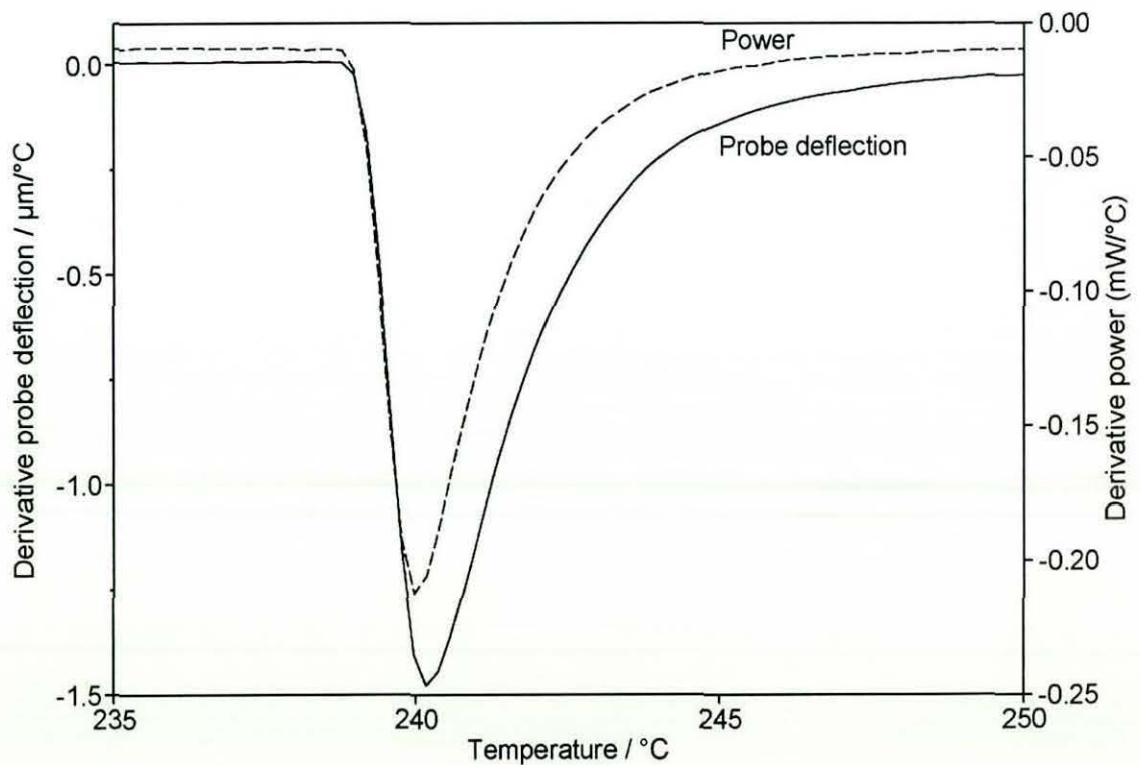
Fig. 2.6. Derivative L-TMA and L-DTA (derivative power) results for as-supplied Melinex PET.

Fig. 2.7 shows typical L-TA results for polystyrene over a temperature range of 75-225°C. Polystyrene (PS) is completely amorphous and cannot crystallise, so the only transition that should be detected is the glass transition. This is indicated by a downward deflection of probe as the material softens. In the non-derivative L-TMA signal, this appears to occur at approximately 140°C. In the derivative trace, however, indentation is shown to commence at around 130°C, although the gradual nature of the onset makes it rather difficult to be precise. In the equivalent L-DTA trace, the onset is more pronounced and occurs at approximately 125°C. This perhaps shows that here the glass transition is detected first in the power signal, before the mechanical properties of the polymer are affected to an extent that is unequivocally detected in the (derivative) L-TMA measurement. Indentation continues up to a temperature of approximately 195°C, by which time the tip has penetrated some 8.2 μm compared with its vertical position on the surface immediately prior to the glass transition. The rate of penetration is relatively modest up to a temperature of around 160°C, by which temperature the tip has indented by less than 1 μm. Above this, the rate increases rapidly to a maximum of approximately 0.36 μm/°C at around 175°C, before slowing significantly above 185°C. Above 195°C there is a rapid upward movement of the probe of around 3.5 μm which is accompanied by a corresponding exothermic peak in the L-DTA trace. The combination of temperature and exposure time at which this occurs is presumably too low for this to be a consequence of some form of thermal degradation that produces expansion of the material. There is evidence that migration of material away from the tip occurs during a L-TA experiment. This manifests itself in the form of a raised rim around the resulting crater (see Figs. 2.25 and 2.26). The mechanism behind this migration is unclear, but the driving force is presumably that it results in an increase in the entropy of the system. It may be that for PS this effect is particularly marked. The result is that, at first, the probe penetrates a considerable distance into the large void left by the removal of material from beneath the tip. Capillary forces then pull the tip further in, to the extent that the neutral position of the cantilever is passed. The resulting upward force it exerts then causes the upward movement of the probe at a temperature at which the viscosity of the material becomes too low for it to sustain the meniscus forces. The fact that the accompanying L-DTA peak is apparently exothermic is almost certainly entirely due to the reduction in probe-sample contact area.

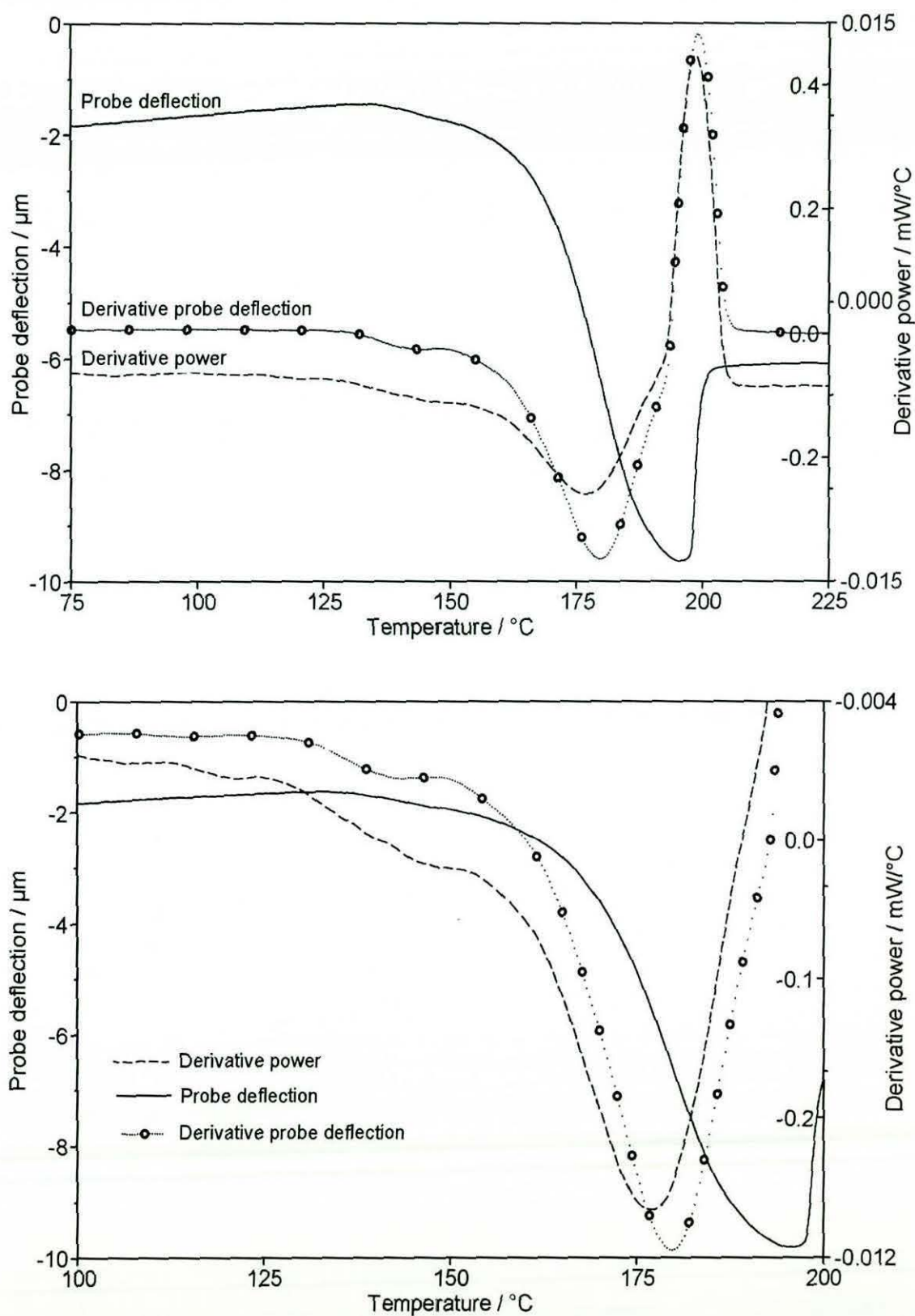Fig. 2.7. Typical L-TMA (probe deflection), derivative probe deflection and L-DTA (derivative power) for polystyrene at a heating rate of 20°Cs⁻¹. The bottom plot has been scaled to emphasise the response to softening caused by the glass transition which occurs at approximately 130°C.

The high value of the T_g, compared with what would be expected from a conventional DSC experiment, is a consequence of the relatively rapid heating rate of 20°C s^{-1}. The effects of heating rate on T_g and T_m are discussed below.

Samples that undergo a single transition over the temperature range of the experiment, such as the melt observed in this case of highly crystalline PET or a glass transition in a completely amorphous non-crystallising polymer, such as PS, display a single penetration event in the L-TMA trace. This is the simplest case for which the interaction between probe and sample can be described. As was discussed in Chapter 1, a three dimensional temperature profile exists in the material in the vicinity of the probe. Material relatively remote from the immediate contact area will therefore reach its melting temperature sometime after that which is in direct contact with the tip. Once the melting or softening temperature of the material immediately under the probe is reached, the tip will begin to penetrate into the sample propelled by the downward force imparted by the bent cantilever acting as a spring. Material that had previously been insulated from the probe will now come into direct contact with it and quickly melt or soften. Moreover, it is a consequence of the shape of the tip loop, that the contact region will increase in size both laterally and vertically. If the sample is homogeneous, this progressive melting will be detected as a single continuous process. However, even if the material has a single well-defined melting temperature, the melting event will be detected as having occurred over a finite temperature range, albeit a narrow one. The speed of penetration, and hence the width of the L-DTA melting peak, will be governed by the applied force, the shape of the tip (as this will control the rate of increase of contact area with depth of penetration) and, crucially, the viscosity of the molten material. The maximum rate of penetration will occur when the ratio of the shear stress exerted by the probe (cantilever force / contact area) to the viscosity of the material is at a maximum. If, as seems likely, the L-DTA signal is almost entirely dependent on contact area, then this will also correspond to the maximum of the transition peak detected in the L-DTA trace. For a material that contains crystallites with a distribution of melting temperatures or that has a broad glass transition, the rate of penetration will be correspondingly lower. The case of a polymer that cold-crystallises during an experiment, such as amorphous PET, is more complex and is considered below.

Before moving to the case of amorphous PET, we shall consider the information revealed in the AC signals for the as-received PET and for polystyrene. These are shown in Fig. 2.8. The frequency and amplitude of temperature modulation were 5 kHz
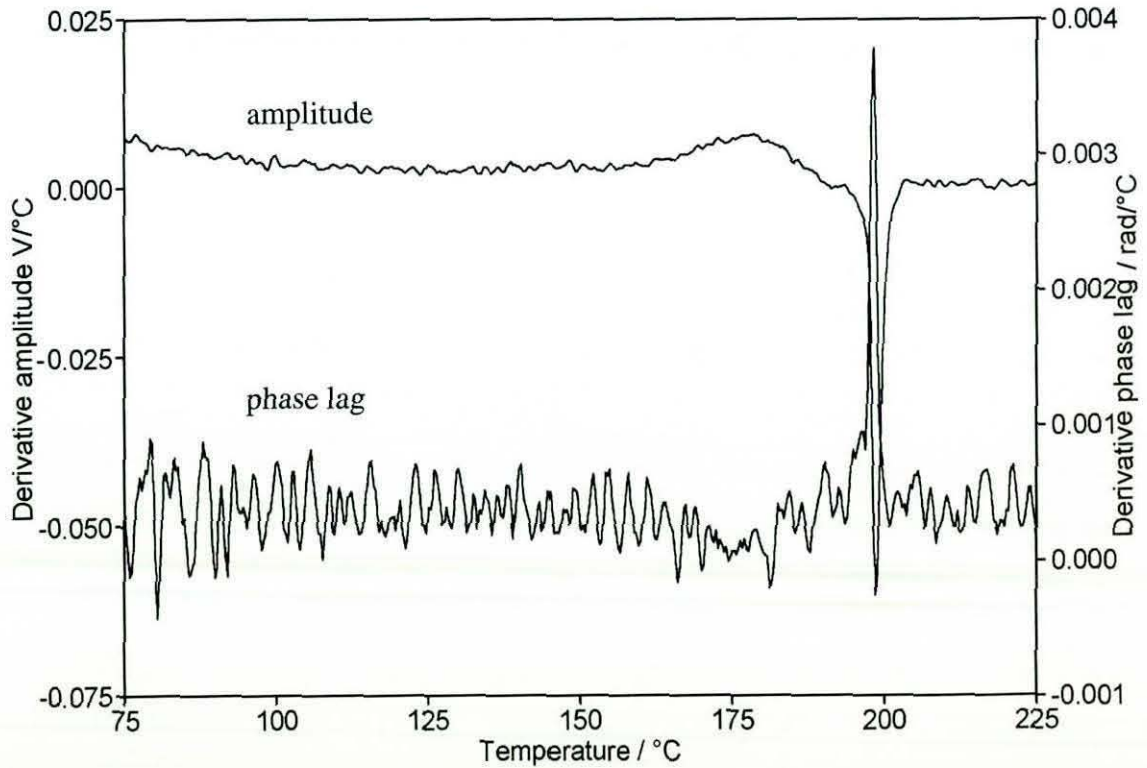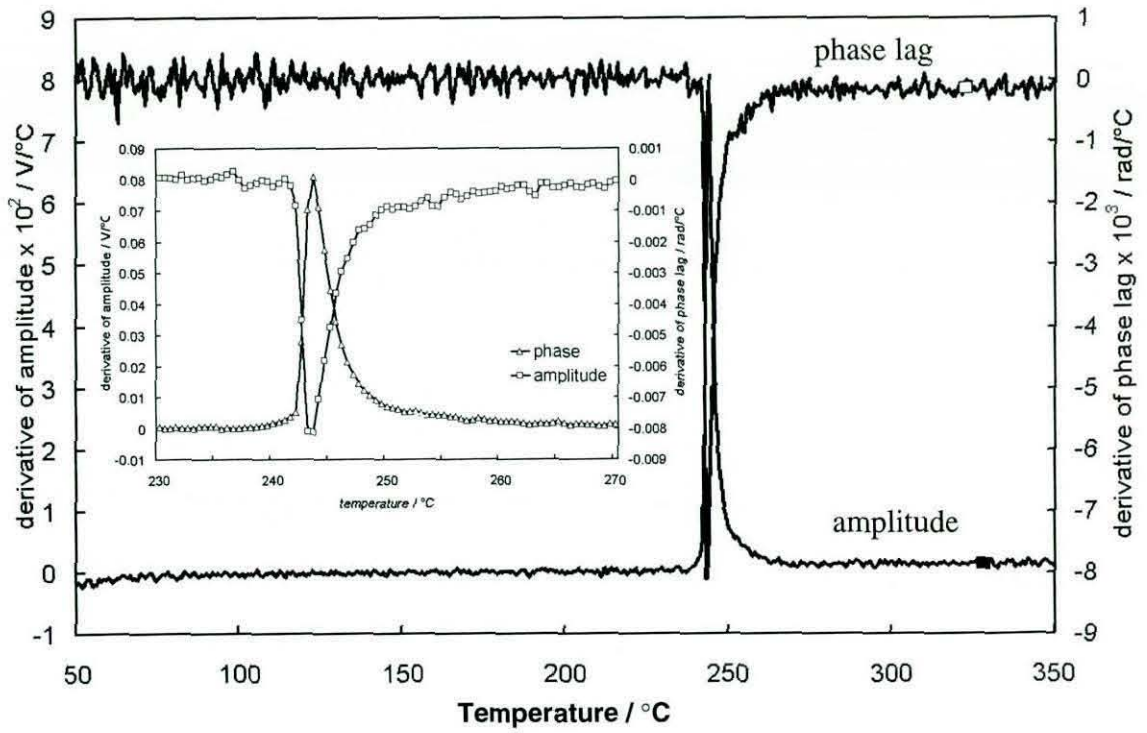
Fig. 2.8. Typical AC (derivative amplitude and phase lag) results for (top) as-supplied Melinex PET and (bottom) polystyrene. For clarity, an expanded view through the melting transition of PET has been inset.

and 6°C respectively (a discussion of the effect of these parameters on the AC results is given below). The results are displayed as first derivatives with respect to temperature, so the melting transition is shown as a peak rather than a step change. The signals are both substantially noisier than the DC signal, with the signal-to-noise ratio of the amplitude response being a factor of two or three superior to that obtained in the phase lag. In the case of the melting of PET, the relative direction of the peaks is a consequence of the amplitude of the signal increasing through the transition and the phase lag becoming increasingly negative. It is apparent, through a melting transition at least, that no information additional to that available in the DC result is produced in the AC signals.

In the case of polystyrene, the phase lag is once again substantially noisier than the amplitude signal and both fail to detect the glass transition. There is a maximum in the amplitude trace at approximately 175°C, corresponding with the maximum rate of penetration revealed in the L-TMA measurement. There is possibly an equivalent minimum in the phase-lag, although this is almost lost in the noise. The peak caused by the upward displacement of the tip is detected in both signals. It is clear from these results that for polystyrene, with this combination of parameters at least, the AC signals are insufficiently sensitive to detect the glass transition.

In a standard DSC result for amorphous PET, as illustrated in Fig. 2.2, a glass transition is detected at around 70°C, followed by cold crystallisation (shown as a large exothermic peak occurring between 115°C and 135°C) and finally a melt starting at approximately 230°C. Above the T_g, the increase in free volume in the polymer allows co-operative molecular motion to occur, which, in a "crystallisable" polymer, facilitates chain-folding and hence crystallisation from the random amorphous state. A reduction in material volume and an increase in elastic modulus accompany this release of the enthalpy of crystallisation. The reduction in volume due to crystallisation is of the order of a few percent.[211]

A typical set of L-TA results for amorphous PET is shown in Figs. 2.9 and 2.10. The untreated L-DTA signal appears to be considerably noisier than that obtained for the crystalline PET, but this is simply a consequence of the narrower signal range during the experiment compared with that required by the large melting transition of the highly crystalline material. The L-DTA signal for the amorphous sample has, therefore, also been shown in a smoothed form. The imposition of the smoothing algorithm broadens and somewhat reduces the height of transition peaks, but enables smaller transitions to be discerned more easily from background noise.
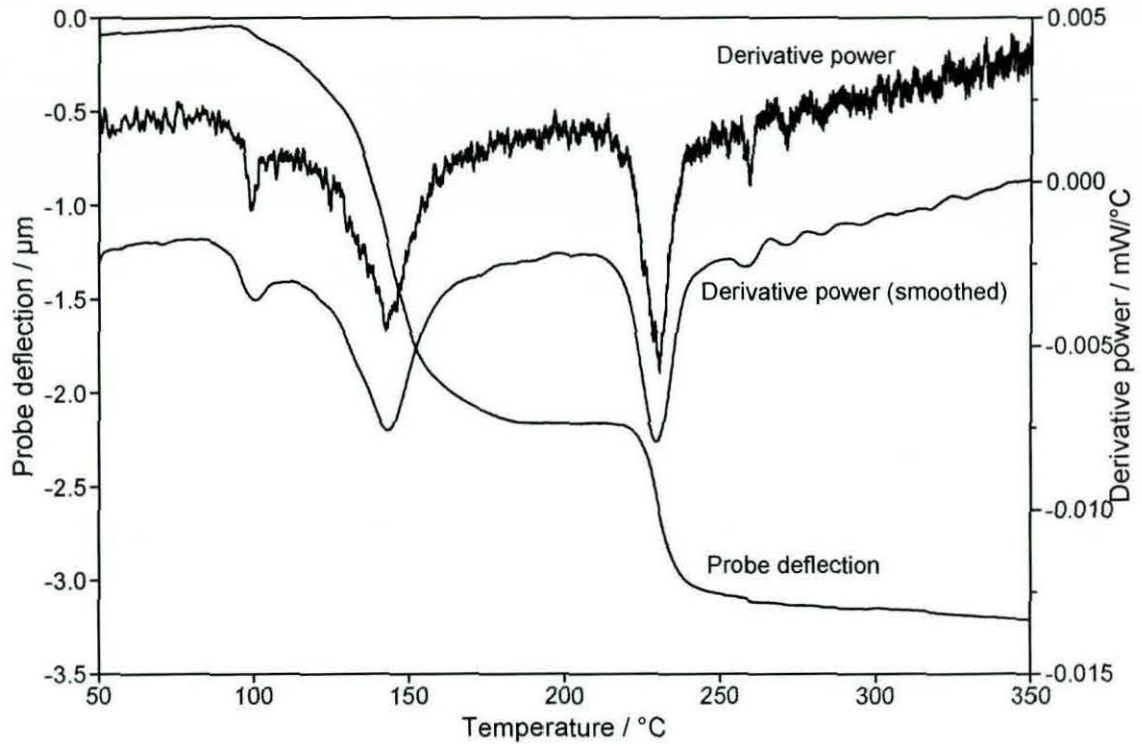
Fig. 2.9. Typical L-TMA and L-DTA results for amorphous PET. The derivative power trace has been plotted twice and shifted along the y-axis to show the effect of applying a smoothing algorithm (10°C interval) to the raw signal.
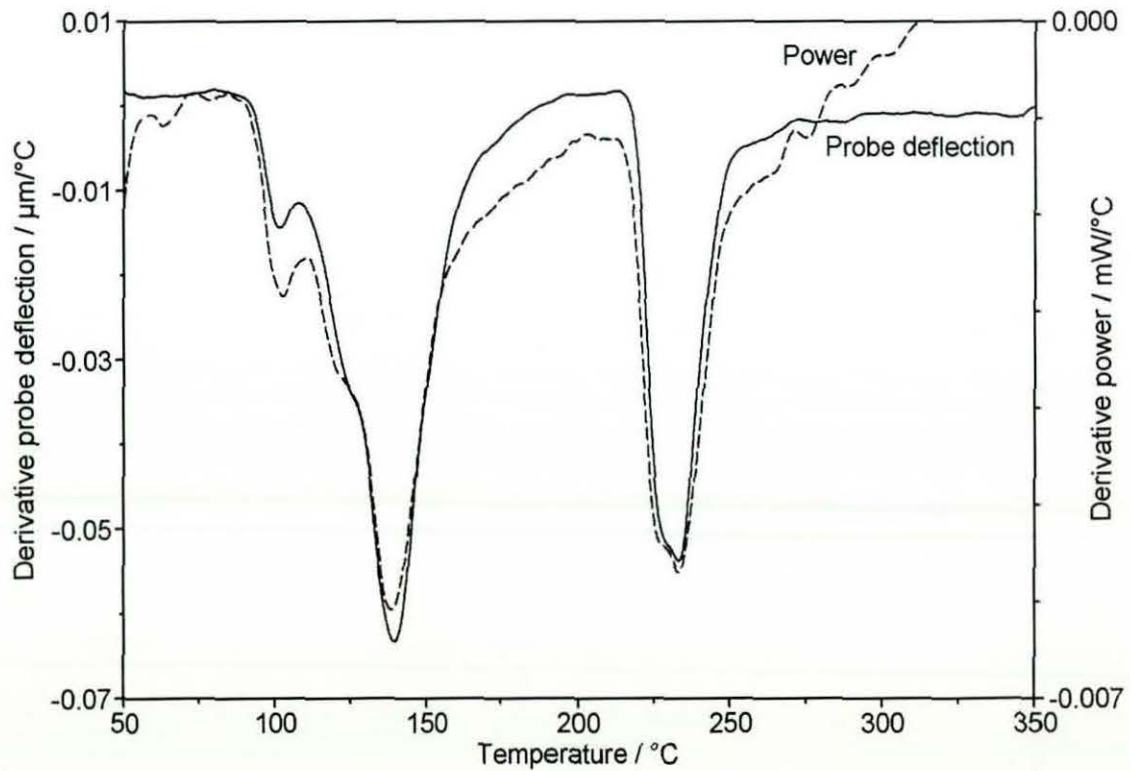
Fig. 2.10. A comparison of the derivative probe deflection and derivative power signals from a typical experimental run on amorphous PET.

The glass transition is detected at a temperature of approximately 95°C in the form of a sudden downward movement of the probe, as the tip is pushed into the softened material. This is accompanied by an increase in power consumption. As before, the latter could simply be a consequence of the increase in probe-sample contact area. Initially, the general shape of the curve is similar to that obtained for polystyrene. The maximum rate of penetration occurs in the region of 140°C and is of the order of 0.05 μm/°C, less than 20% of that observed for polystyrene. Above about 160°C, the rate of penetration slows dramatically and a plateau is reached between 180°C and 220°C at an indentation depth of 2.1 μm. This must correspond to a region in which the downward acting normal force acting on the probe is balanced by the upward force imparted by the polymer. A second obvious transition then occurs, which results in a further rapid indentation of around 1.8 μm. This can only be interpreted as the melting of crystalline material. This material could have been present in the sample before the start of the experiment; through inefficient quenching, for example. This is, however, unlikely as the preparation of amorphous PET by quenching from the melt is widely practised and documented. Moreover, the surface region is the least likely to contain crystalline material, as it would have undergone the most rapid cooling during preparation. It seems most likely, therefore, that the material responsible for the melt crystallised during the experiment, as observed in DSC result for the bulk sample. At 220°C compared with 240°C, the onset temperature is significantly lower than in the as-supplied material — a probable consequence of a decrease in the minimum lamellar thickness and/or state of crystalline perfection. The melting peak is perhaps somewhat broader for the initially-amorphous sample, which is indicative of a larger range in the lamellar thickness distribution present in the cold-crystallised material. Moreover, there is a smaller melting peak in the L-DTA trace that occurs just below 260°C. This perhaps indicates the presence of a small distinct population of crystallites with a relatively high melting temperature or lying at a greater depth within the sample. There may also be a second, smaller, subsidiary melting peak at approximately 270°C, although it is difficult to be certain that this is truly distinct from the noise. The area under the primary melting peak in the power signal is much smaller than the corresponding peak area for the as-supplied material. This is an indirect consequence of the much lower local degree of crystallinity immediately prior to melting. The considerable indentation that occurs between the T_g and the $T_{m \text{ (onset)}}$ means that the degree of bending of the cantilever and hence the probe force are substantially lower at

the start of the melting process. The effect of degree of crystallinity on melting peak area is addressed in a more quantitative manner below.

There is a point of inflection in the (non-derivative) L-TMA signal, indicating a slowing of the rate of penetration. This occurs at approximately 5°C above the temperature at which the probe first begins to sink into the sample (95°C). This could be caused, for example, by an asperity at the apex of the tip loop causing an initially rapid rate of penetration, which slows somewhat when the main body of the wire loop comes into contact with the surface. A similar feature is also apparent in the result for polystyrene.

In the absence of crystallisation, it would be expected that the form of the L-TA curves would generally follow that obtained for polystyrene, until either thermal degradation occurred or the force exerted by the cantilever tended to zero. Other factors being equal, the magnitude and rate of the indentation for a particular polymer would depend on its mechanical properties and how they changed with temperature. However, if crystallisation occurs around the tip, the viscosity of the softened material will progressively increase, resulting in the plateau observed for the initially-amorphous PET. The shrinkage due to crystallisation is likely to be a secondary effect.

Unlike in the DSC result for the bulk sample, it is not possible to discern a discrete transition peak due to cold crystallisation in the L-DTA trace. The lack of such a peak could be a consequence of the signal being dominated by the steadily increasing probe-sample contact area above the T_g. On the other hand, it may be that the sensitivity of the calorimetric measurement is simply insufficient to detect an enthalpic event that is not associated with a significant change in probe indentation and hence contact area. The close match between the L-DTA trace and the derivative L-TMA signal tends to support the conclusion that there is little independent detection of the latent heats of crystallisation or melting in the calorimetric signal.

It will be noted that the difference in total indentation observed between the as-supplied material and the amorphous PET (almost 5 μm compared with 3.1μm) is another possible consequence of probe geometry or inclination of the scanner with respect to the sample. This difference is too large to be accounted for by, for example, drift in the top-bottom photodetector signal affecting the initial probe force, so another explanation is required. Although these experiments were conducted with the same probe, a large number of experiments were conducted first on the as-received material before moving to the amorphous sample. It is possible, therefore, that the tip became blunter with use, resulting in a significant increase in contact area and a commensurate
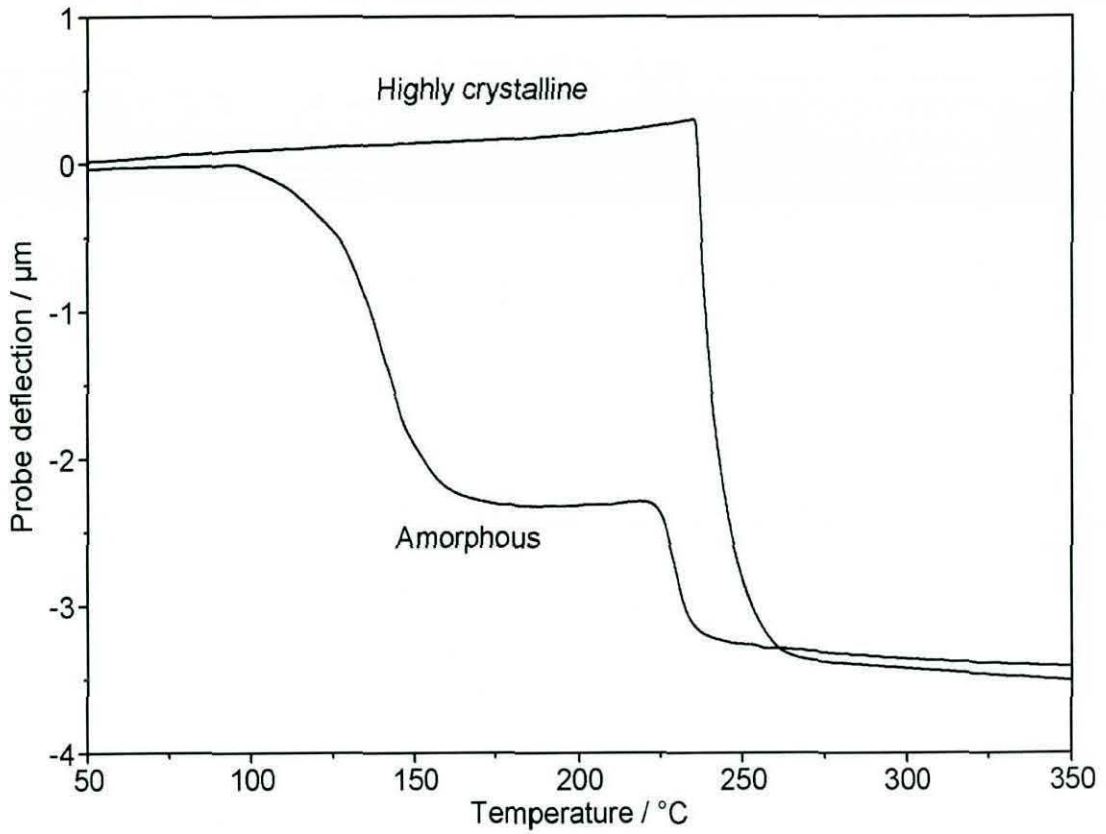
Fig. 2.11. A comparison of the L-TMA results for the as-received crystalline PET and the amorphous material acquired under identical conditions.
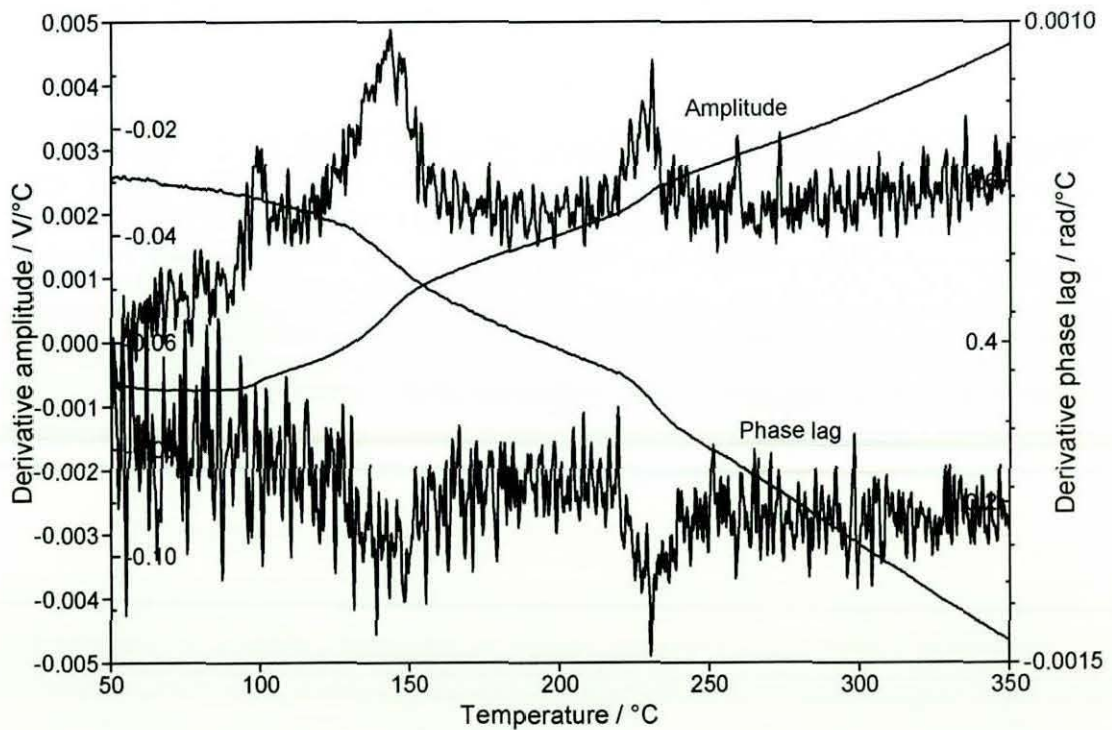

Fig. 2.12. Typical AC amplitude and phase lag results for amorphous PET, shown in linear form (inner axes) and as a first derivative with respect to temperature.

reduction in shear stress in the softened and molten material. This would in turn be translated into a reduction in the overall indentation depth. This and other possible effects of probe geometry are discussed in more detail below. Fig. 2.11 shows a direct comparison between L-TMA curves for the amorphous and as-received PET. These were conducted consecutively to ensure that the possibility of inadvertent changes occurring to the probe or other measuring conditions was minimised. The results confirm that the overall indentation depth is the same in each case. The shape of the curve for the as-supplied material is almost identical to that shown in Fig. 2.5. This means that no significant modification to the behaviour of the probe occurred in the intervening time between the experiments. There is a minor difference in the rate of upward deflection prior to the melt and the indentation through the melt is slightly greater in the first result. This probably originates from a slightly higher angle of inclination existing between the microscope (and hence the cantilever) and the sample surface. This leaves us with the conclusion that the initial force applied to the probe must have been significantly higher in the batch of experiments from which the result in Fig. 2.5 is taken. The most likely explanation for this is operator error, in that there must have been a significant discrepancy between the T–B photodetector signal and/or the set-point used between the two sets of experiments. This does not, however, undermine the validity of this part of the study and the conclusions that can be drawn from the results. A further observation from Fig. 2.11 is that the increased coefficient in thermal expansion of the crystalline material compared with the amorphous sample is apparent in the curves between 50°C and the T_g.

The corresponding AC signals for the initially amorphous PET are shown in Fig. 2.12. As with the as-supplied Melinex, the derivative traces are considerably noisier than the DC power signal. The signal-to-noise ratio of the amplitude signal is again superior to that of the phase lag. Transitions are detected in the non-derivative results as a step increase in both amplitude and negative phase lag. The small peak just above the T_g apparent in the DC L-DTA result is detected in the amplitude response but not in the phase lag. Otherwise, and in contrast to the result for polystyrene, all the transitions are apparent, but no additional information is available from the AC signals.

2.3.2 Probe-to-probe variations and the effect of probe geometry

Before considering the reproducibility of L-TA measurements, it is necessary to examine the potential effects of variations in the shape of the tip surface on the results obtained for a given sample. Results for five different probes obtained on highly
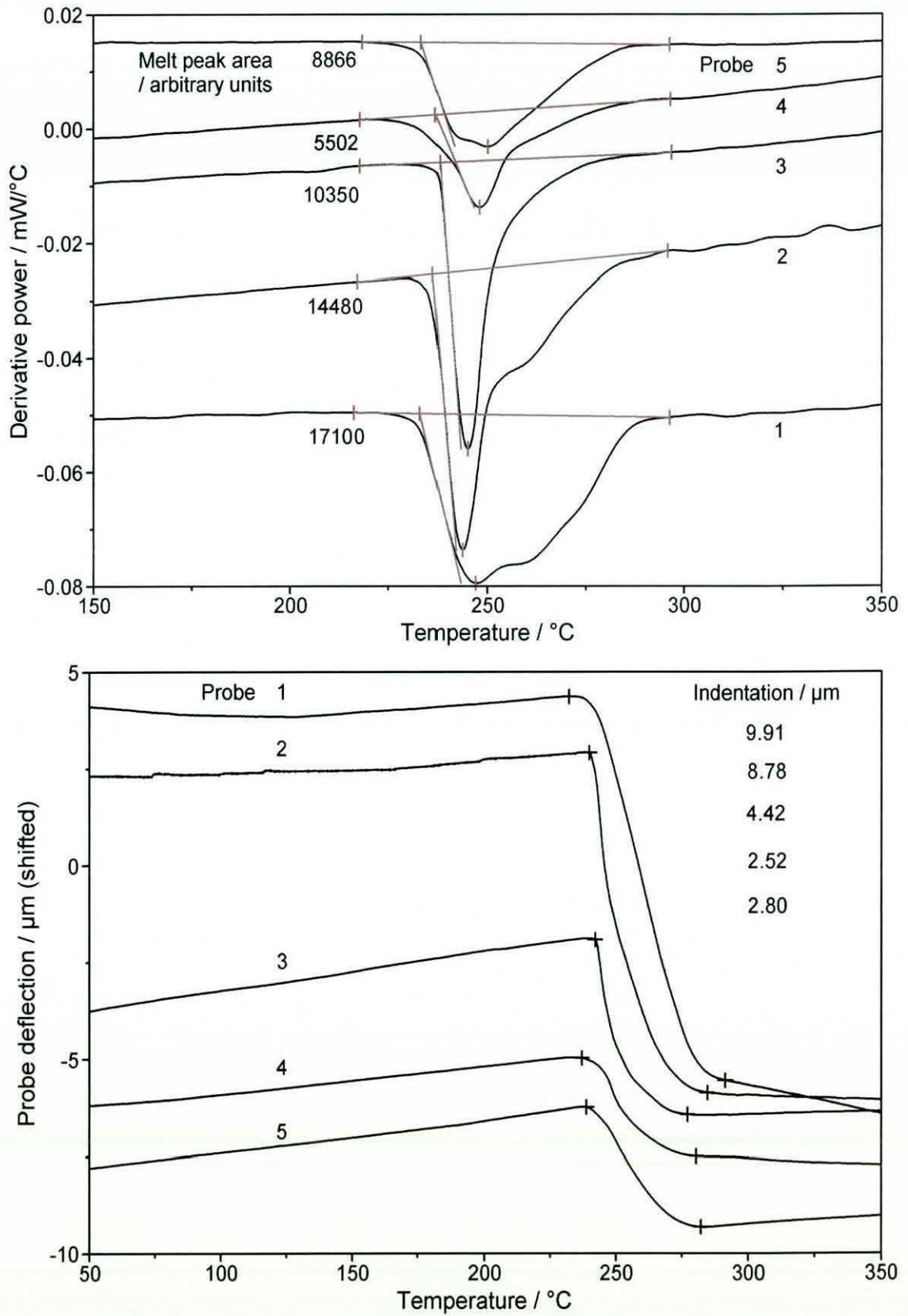
Fig. 2.13. Probe-to-probe variation in the (top) L-DTA and (bottom) L-TMA results for as-supplied Melinex PET film.
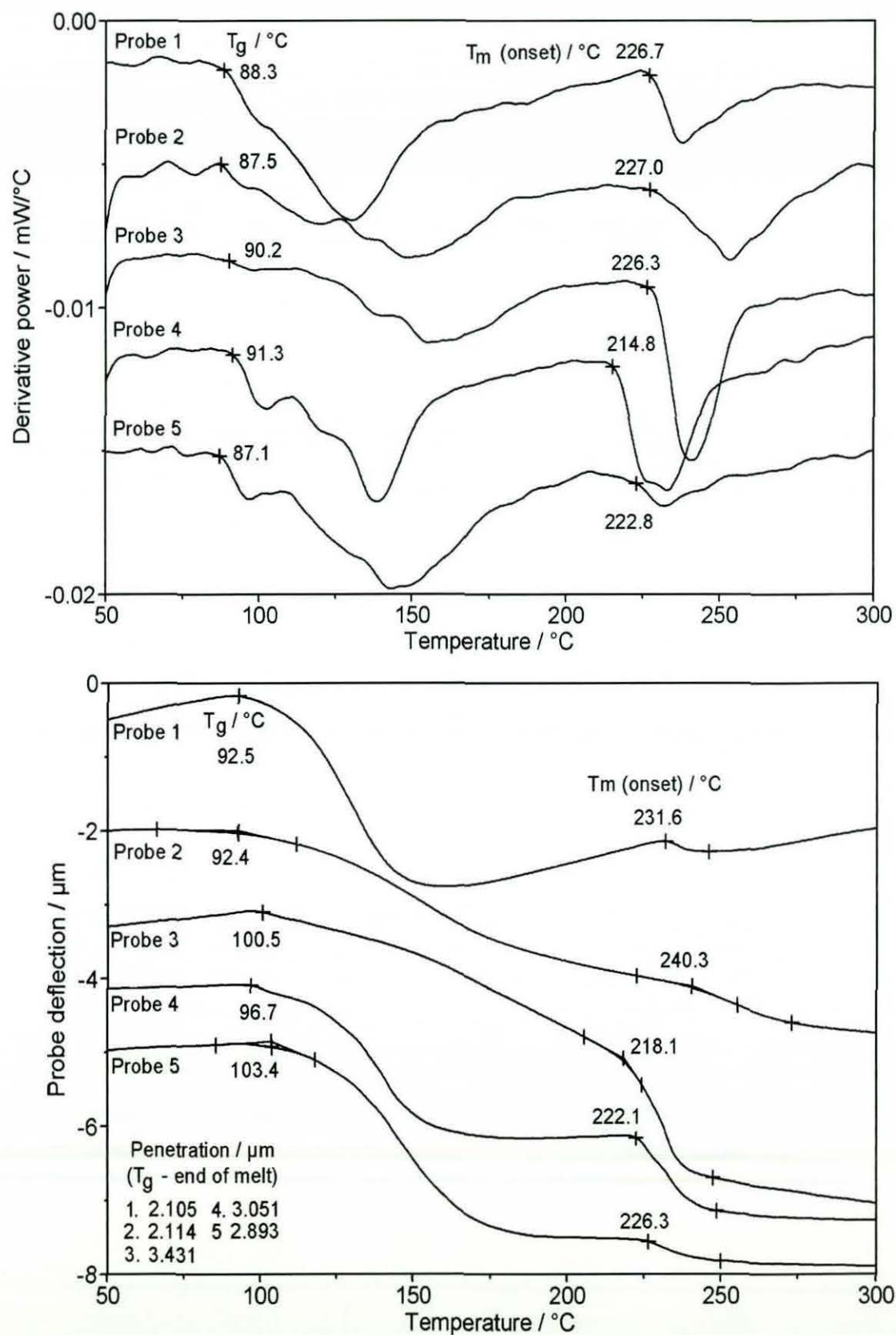
Fig. 2.14. Probe-to-probe variation in (top) L-DTA and (bottom) L-TMA results for amorphous PET. *Note: In this and subsequent figures, the precision with which the transition temperatures are displayed is a result of the particular software program used. It is not claimed that the T_g or T_m can be measured to within 0.1°C.*

crystalline and amorphous PET are shown in Figs. 2.13 and 2.14 respectively. It can be seen that, for the as-received Melinex, there are dramatic probe-to-probe differences in the shape and area of L-DTA melting peaks and the associated L-TMA indentation occurring through the melt. The maximum peak area and indentation obtained (probe1) are at least a factor of three greater than the corresponding results for probe 5. Perhaps of more significance, is the fact that only probe 3 detects the melt as a single well-defined monomodal peak. The others to a greater or lesser extent, show more complex melting behaviour. It is difficult to see how a probe could act to suppress a real melting peak, but relatively easy to understand how imperfections in the tip-loop could give rise to additional peaks. Such artefacts would result from erratic indention behaviour caused by sudden changes in contact area. This is illustrated in Fig. 2.15(b). It can also be seen that there is significant variation in the gradient and linearity of the signal between 50°C and the onset of melting. Probe 1 even exhibits a downward deflection in the initial stages of heating, which naturally should result in upward movement due to thermal expansion of the sample.

The results for the amorphous sample were conducted at a later date with a different set of probes and so are not directly comparable with the results for the as-received PET. They again show considerable variation in the shape of the curves obtained with, for example, probes 4 and 5 showing very well defined glass and melting transitions. The results for these two probes would seem to be representative of something approaching ideal performance. The results for probe 2, on the other hand, show much more gradual transitions indicative of poorer signal-to-noise, probably resulting from a blunter tip. Interestingly, probe 1 would seem to be considerably more sensitive to thermal expansion in the sample. The significant variation in the melting temperature detected by different probes is perhaps to be expected, because the inherent differences in contact area will lead, presumably, to different cold-crystallisation conditions within the sample.

All these variations must originate in differences in the shape of the tip. These can occur in two ways. The first and most obvious is the variability inherent in the manufacturing process. Wollaston probes are essentially "handmade" and variations can exist in the sharpness of the loop and in its angle relative to the cantilever as illustrated in Fig. 2.15. For a given microscope orientation relative to the sample surface and assuming a perfectly flat sample, the angle at which the tip approaches the sample surface is largely determined by the angle between the plane of the cantilever and the plane parallel to the sensor loop. There is also some variation in the angle
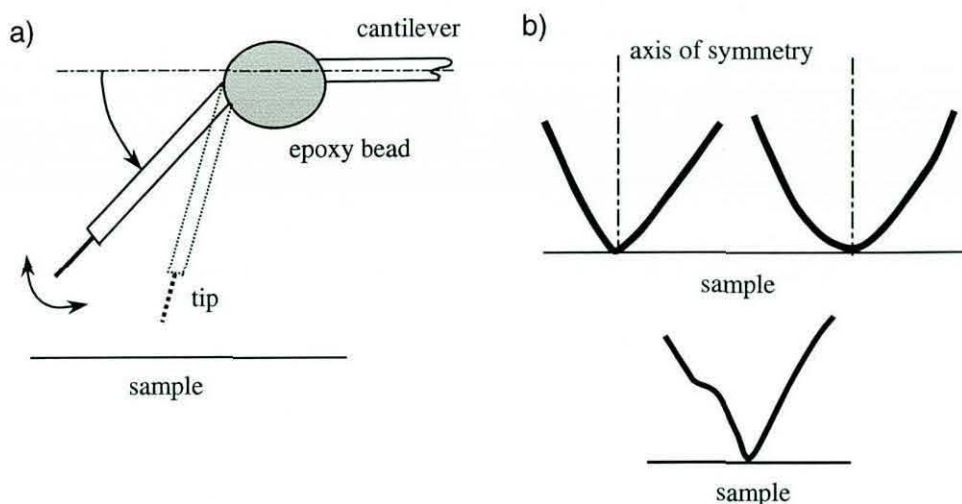
Fig. 2.15. (a) Probe-to-probe variability of the angle of the tip relative to the sample surface. (b) Variability in the shape and symmetry of the tip loop, illustrating the difference between a relatively sharp (top left) and blunt (top right) tip. A bent tip (bottom centre) will cause artefacts in the L-TA signals.

between the "half-moon" mounting plate and the cantilever. In addition, variability can exist in the angle between the plane of the sensor loop itself and the line of the downward legs of the main Wollaston wire, particularly with heavy use, as the junction between the tip and the non-etched wire can readily act as a hinge. Fig. 2.15(b) illustrates that the shape of the loop itself can vary from probe to probe, producing significant variations in initial tip-sample contact area and hence the compressive stress imparted on the sample for a given cantilever force. For a given loop-shape, the closer the tip is to being perpendicular to the sample, the sharper will be the onset of melting and the narrower will be the melt peak in both the L-DTA and L-TMA signals. Furthermore, the indentation depth through the melt will be maximised. The shape of the tip, particularly the sharpness of the apex, has the most significant effect on the form of the signals obtained through the melting transition. A sharp tip will generally produce a sharp melting onset in both signals, a narrow melting peak in the L-DTA trace and a high penetration depth, compared with a more gently curving loop. An asymmetrical loop, or one that has been bent or twisted during use, can produce artefacts of the form apparent in the melting peaks shown in Fig. 2.13. The detection of differences, in crystallinity for example, between a surface and the sub-surface region is a potentially important application of L-TA. It is therefore essential that the behaviour of a probe is checked periodically on a known homogeneous sample, in order to avoid confusing tip-related artefacts with real sample behaviour.

Differences in the linearity and rate of upward movement of probes during heating prior to the T_m result from variability in the quality of the cantilever wires (e.g. their straightness and alignment) and the position of the mirror along the cantilever. If the cantilever is in a poor condition; where one or both of the wire "arms" are distorted, for example, non-linear or in certain cases negative deflection behaviour may result as the tip is heated. This will also inevitably lead to poor imaging behaviour.

The second source of variability is wear and damage occurring to the probe with use. The probes are fragile and can be damaged in a number of ways, such as imaging too rough a sample or through collisions with the sample surface caused by operator error. As the probes are relatively expensive (about five times the cost of a standard AFM probe), it is often worth attempting to repair minor damage. This can be effected by, for example, indenting a bent tip into a crystalline polymer, cooling it to below the T_m and gently moving the sample stage until the loop is brought back to something approaching its original orientation. The probe can then be released from the sample by initiating the standard disengagement procedure. However, this is an inexact process and the shape and hence the characteristics of the probe will inevitably change as a result. This is not a fundamental problem, providing the operator is aware of the change in performance and the modifications do not lead to the production of misleading artefacts in the L-TA signals, in which case the probe must be discarded. Until mass-produced micro-fabricated probes become widely available, it is prudent to check the performance of each new probe on a simple well-characterised sample, such as the highly crystalline PET used here.

2.3.3 Reproducibility of results

During the time of the study, the reproducibility of the results was investigated for a number of probes and batches of material. The two sets of results for the as-supplied and amorphous PET film presented here are indicative of the performance that can routinely be achieved. It is vital, however, that the potential for damage to the tip is borne in mind and that drift in the temperature calibration of the probe is checked for regularly. Figs. 2.16 and 2.17 show L-DTA and L-TMA results for the melting transition of the as-supplied film, acquired over ten runs using two different probes. The onset melting temperature [$T_{m \, (onset)}$] for each signal and the area under the L-DTA melting peak and the depth of penetration of the probe through the melt are shown in each plot and summarised in Table 2.1. The run numbers are in chronological order and have
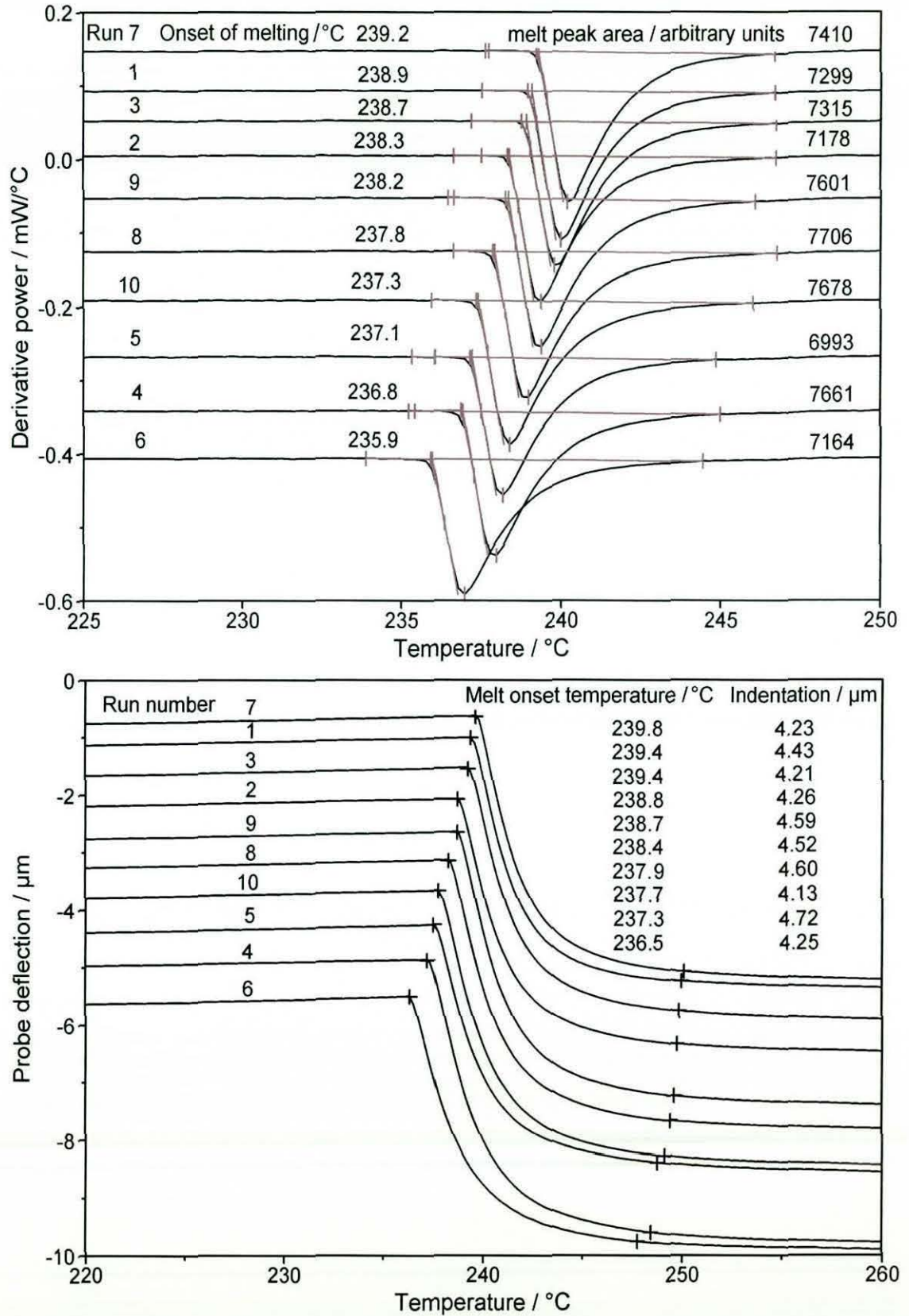
Fig 2.16. Run-to-run variation (probe 1) through the melting transition of as-supplied Melinex PET film. Top: L-DTA signals showing the calculated melt peak area and $T_{m\ (onset)}$. Bottom: the equivalent L-TMA traces showing the probe penetration through the melt and $T_{m\ (onset)}$.
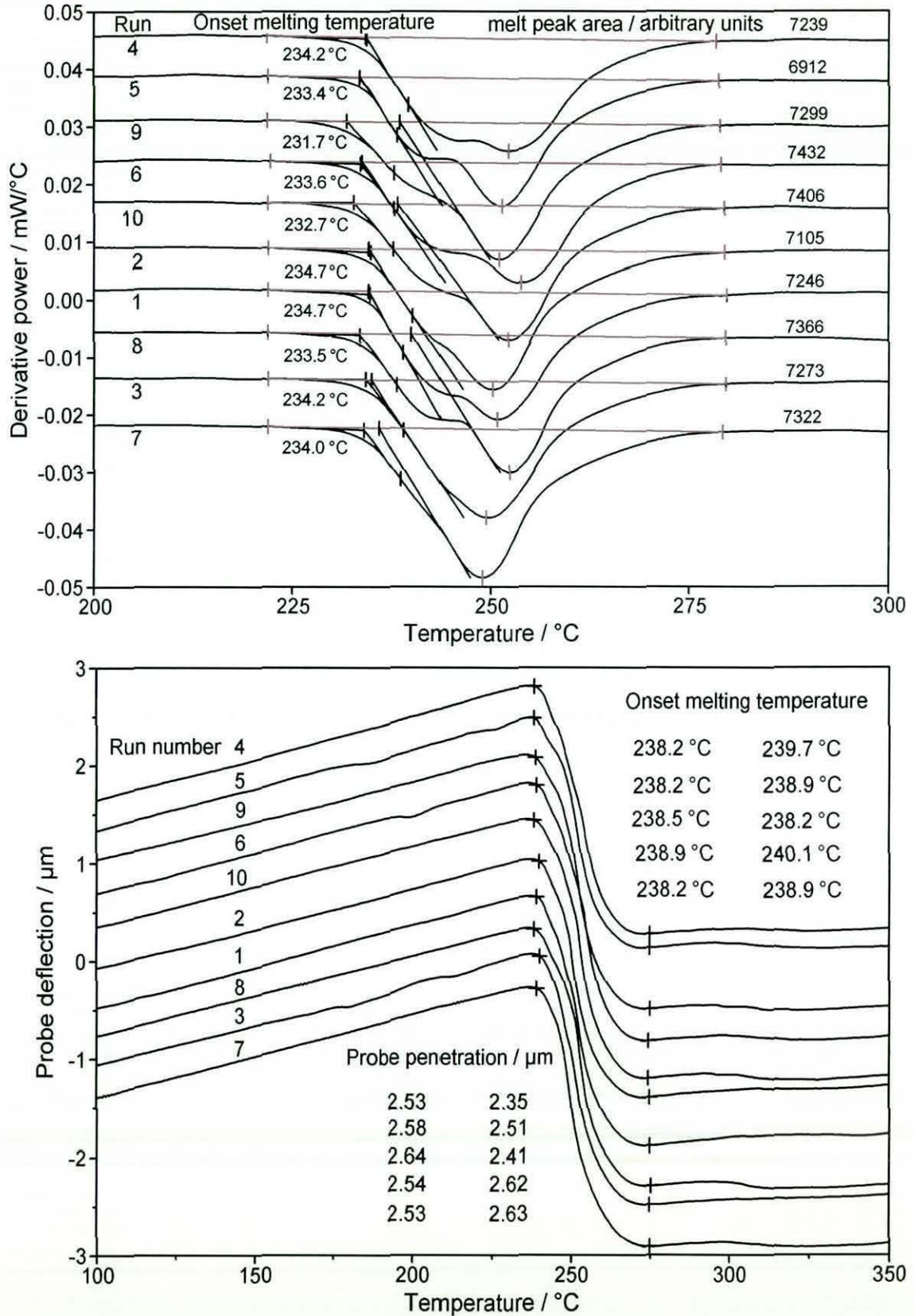
Fig. 2.17. Run-to-run variation (probe 2) through the melting transition of as-supplied Melinex PET film. Top: L-DTA signals showing the calculated melt peak area and $T_{m\ (onset)}$. Bottom: the equivalent L-TMA traces showing the probe penetration through the melt and $T_{m\ (onset)}$.

Run nº	Probe 1				Probe 2			
	L-TMA		L-DTA		L-TMA		L-DTA	
	T_m/°C (onset)	Indent^n / μm	T_m/°C (onset)	Peak area / arbitrary units	T_m/°C (onset)	Indent^n/ μm	T_m/°C (onset)	Peak area / arbitrary units
1	239	4.43	239	7299	239	2.51	235	7246
2	239	4.26	238	7178	240	2.35	235	7105
3	239	4.21	239	7315	240	2.62	234	7273
4	237	4.72	237	7661	238	2.53	234	7239
5	238	4.13	237	6993	238	2.58	233	6912
6	237	4.25	236	7164	239	2.54	234	7432
7	240	4.23	239	7410	239	2.63	234	7322
8	238	4.52	238	7706	238	2.41	234	7366
9	239	4.59	238	7601	239	2.64	232	7299
10	238	4.60	237	7678	238	2.53	233	7406
Mean	238.4	4.39	237.8	7401	238.8	2.53	233.7	7260
S. D.	1.0	0.20	1.0	251	0.7	0.09	0.9	154

Table 2.1. L-TA results taken through the melting transition of highly crystalline PET film over ten runs for two different Wollaston probes. The corresponding curves are shown in Figs. 2.16 and 2.17.

been inserted to show that the variations in the results are not due to, for example, calibration or other forms of systematic measurement drift.

The results for probe 1 generally show excellent reproducibility, with a $T_{m\ (onset)}$ ranging from 236–239°C and 237–240°C in the L-DTA and L-TMA results respectively. The mean L-DTA value, at 237.8°C is 0.6°C below the mean L-TMA value. This is negligible and would disappear if the derivative L-TMA signal were used. The standard deviation of the melting peak areas is 3.4% of the mean value. The depth of penetration of the probe through the melt varies from 4.13–4.72 μm and the mean value is 4.39 μm. The standard deviation, at 0.20 μm, is 4.6% of the mean. The shape of the single asymmetric melting peak obtained in the power signal is a near-mirror image of that in the DSC result shown in Fig. 2.2. The onset of melting is much more

abrupt and the melting range, at approximately 10°C compared with 30°C, is much narrower than for the bulk sample. The sharpness of the onset, as mentioned above, is a consequence of a narrow lamellar thickness distribution likely to be present at the surface of the film. The onset point in the corresponding L-TMA results is even more abrupt and with this probe occurs soon (within half a degree or so) after melting is detected in the power signal. The performance of this probe, in terms of the sharpness, width and size of the L-DTA melting peak is excellent. The good performance is confirmed by the smooth indentation event. As discussed above, the L-DTA performance is in fact likely to be almost entirely dictated by the indentation behaviour.

For probe 2, the results are if anything even more reproducible, but there are some important differences compared with those for probe 1. Firstly, the shapes of the L-DTA melting peaks are markedly different, in that in most of them there is a substantial point of inflection, which could be interpreted as being indicative of a bimodal distribution of melting temperatures. The temperature range over which melting occurs is much greater, with the high temperature tail in the peak finishing at around 280°C. The total peak areas are nevertheless comparable with, though somewhat lower than, those obtained with probe 1. The shape of the melting peaks is reflected in the corresponding L-TMA results through the melt, in that the indentation traces indicate a greater degree of fluctuation in the rate of indentation compared with the results for probe 1. Moreover, the average indentation depth is less than 60% of that obtained with probe 1. As discussed above, these differences in behaviour are a consequence of variations in the shape of the sensor loop and its orientation with respect to the sample surface. Despite these potential pitfalls, for a given probe and set of operating parameters, excellent reproducibility is achievable in the measurement of the onset and peak melting temperatures, in both signals and in the peak shape and area in the L-DTA trace. The latter, however, can be directly correlated to the area of the melting peak in the corresponding derivative L-TMA trace.

Figs. 2.18 and 2.19 show the run-to-run variation for amorphous PET, achieved under the same experimental conditions using two different probes. These sets of results have been chosen because of the significant differences in characteristics exhibited by the two probes, which cover the extremes in behaviour that may be exhibited by Wollaston probes in general. Their behaviour may be contrasted with the result shown in Fig 2.7 for a different probe, whose performance characteristics are in certain respects intermediate to those exhibited by the probes being considered here.
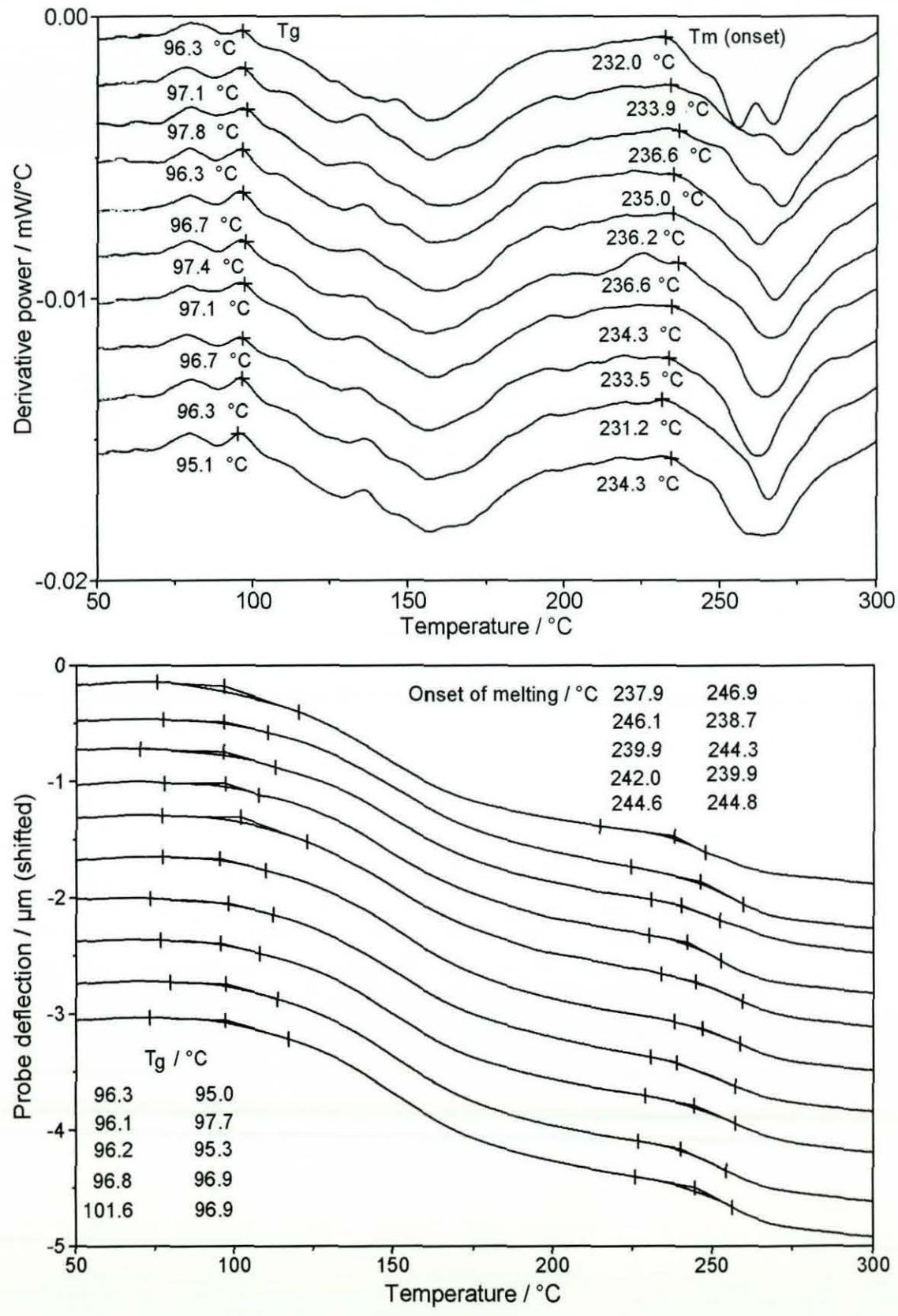
Fig. 2.18. Probe 1. Run-to-run variation for amorphous PET. Top: L-DTA; bottom: L-TMA.
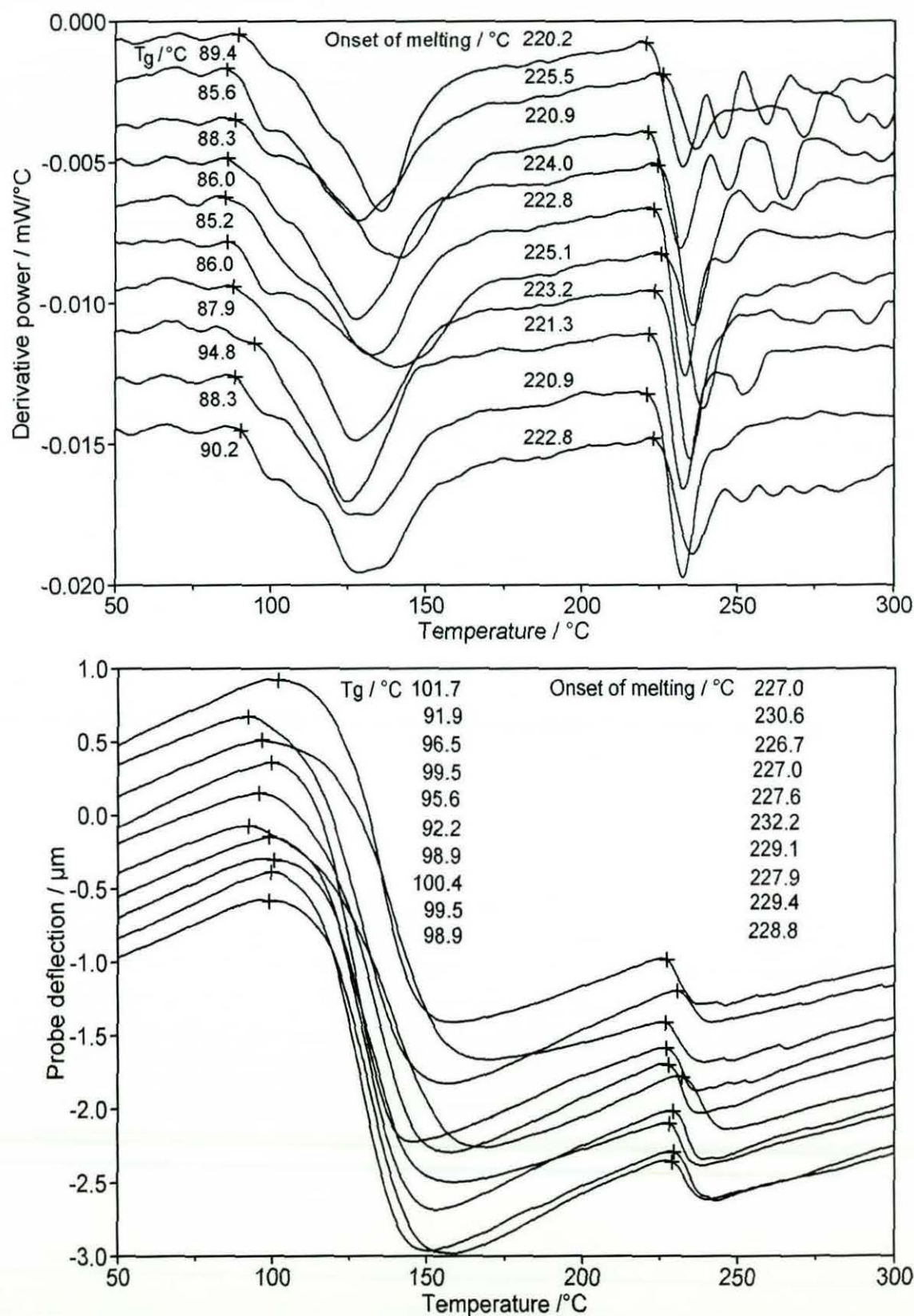
Fig. 2.19. Probe 2. Run-to-run variation for amorphous PET. Top: L-DTA; bottom: L-TMA.

Run n°	Probe 1				Probe 2			
	L-TMA		L-DTA		L-TMA		L-DTA	
	$T_g/$ °C	$T_m/$ °C (onset)	$T_g/$ °C	$T_m/$ °C (onset)	$T_g/$ °C	$T_m/$ °C (onset)	$T_g/$ °C	$T_m/$ °C (onset)
1	96	238	96	232	102	227	89	220
2	96	246	97	234	92	231	86	226
3	96	240	98	237	97	227	88	221
4	97	242	96	235	100	227	86	224
5	102	244	97	236	96	228	85	223
6	95	247	97	237	92	232	86	225
7	97	239	97	234	99	229	87	223
8	95	244	97	234	100	228	95	221
9	97	240	96	231	100	229	88	221
10	97	245	95	234	99	229	90	222
Mean	96.9	242.5	96.7	234.4	97.5	228.6	88.2	222.7
S.D.	1.8	3.2	0.8	1.8	3.4	1.8	2.9	1.8

Table 2.2. L-TA results for amorphous PET film over ten runs for two different Wollaston probes. The corresponding curves are shown in Figs. 2.18 and 2.19.

The glass transition temperature and the onset melting temperature results for each run are summarised in Table 2.2. The reproducibility within each set of results is good, although the scatter apparent in the values of T_g and $T_{m\ (onset)}$ is greater than that achieved for the as-supplied material in the measurement of $T_{m\ (onset)}$. There is a considerable discrepancy between the results for the two probes, both in the values and in the general shape of the L-DTA and L-DTA curves (the latter is particularly striking). It should, however, be noted that different height scales have been used in order to best display the L-TMA results for each probe. This has accentuated the more gradual nature of the indentation profile typically exhibited by probe 1. The mean values of T_g detected in the L-DTA signal by the two probes, at 96.9 °C and 97.5°C, are in good agreement. However, with a standard deviation of 3.4% of the mean compared with 1.8%, probe 2 displays significantly more scatter than probe 1. The shapes of the L-TMA curves through the transition are significantly different, with probe 2 showing a

precipitous indentation profile after a relatively wide maximum. Probe 1 displays a much smoother profile, indicative of a poorer signal-to-noise ratio, probably caused by a blunter tip. A further significant difference is that the L-TMA measurement from probe 2 is much more sensitive to thermal expansion. This is especially apparent after melting in that, unusually, there is upward movement of the probe. The reason for this is unclear, but is likely to originate in the configuration of the cantilever, rather than the tip.

In the results for probe 2 the difference between the apparent values of the T_g as derived from the two different measurements (discussed above) is particularly marked, with those from the L-DTA signal apparently up to10°C lower than in the equivalent L-TMA trace. This is because the shape of the (non-derivative) L-TMA curve through the onset of penetration of the tip into the sample makes it particularly difficult to assign a precise onset temperature. As before, this is not the case if the derivative L-TMA signal is used. There is a difference of over 10°C in the average T_m measured in the L-DTA signal by the two probes. The scatter within each data set, however, is very good, with a standard deviation of less than 1% of the mean in each case. The large discrepancy in the measured melting temperature is too large to be accounted for by, for example, by drift in the probe temperature calibration. It is possible that it originates in different conditions for cold crystallisation imparted by each probe as a result of differences in tip geometry.

2.3.4 The effect of instrument operating variables

Heating rate. The effect of heating rate on the T_g and T_m of polymers, as measured in a conventional DSC experiment is well documented.[20-22] The glass transition is a kinetically-controlled process and the temperature at which it occurs therefore increases with increasing heating rate. On the other hand, the melting temperature of an individual polymer crystal with a given thickness, in the absence of superheating, is invariant with heating rate. With a typical value of approximately 90°C, the T_g detected in the L-TA experiments conducted on amorphous PET at a heating rate of 10°Cs^{-1} is considerably above that measured in a conventional DSC experiment at a heating rate of 10°C min^{-1} (see Fig, 2.2). However, if a L-TA experiment is carried out at a heating rate similar to those used in conventional DSC, the results obtained for the T_g should be comparable. Fig. 2.20 shows the effect of heating rate on the results obtained for amorphous and the as-supplied PET (the plots are the average of four runs). For the
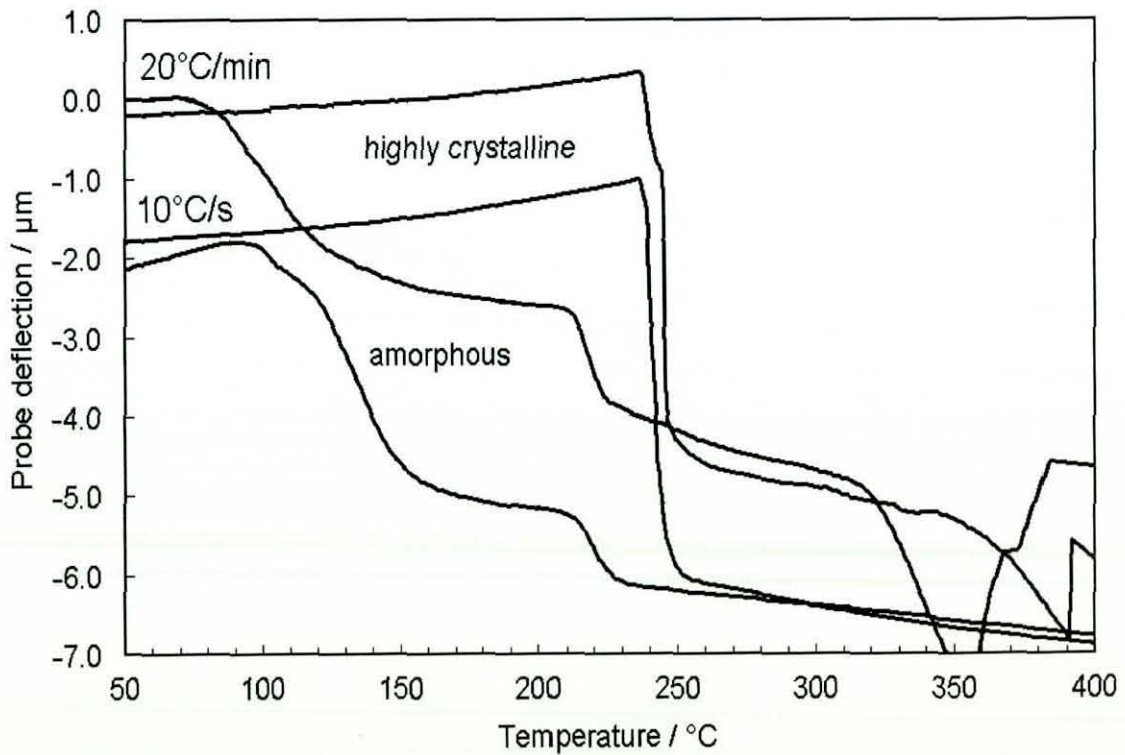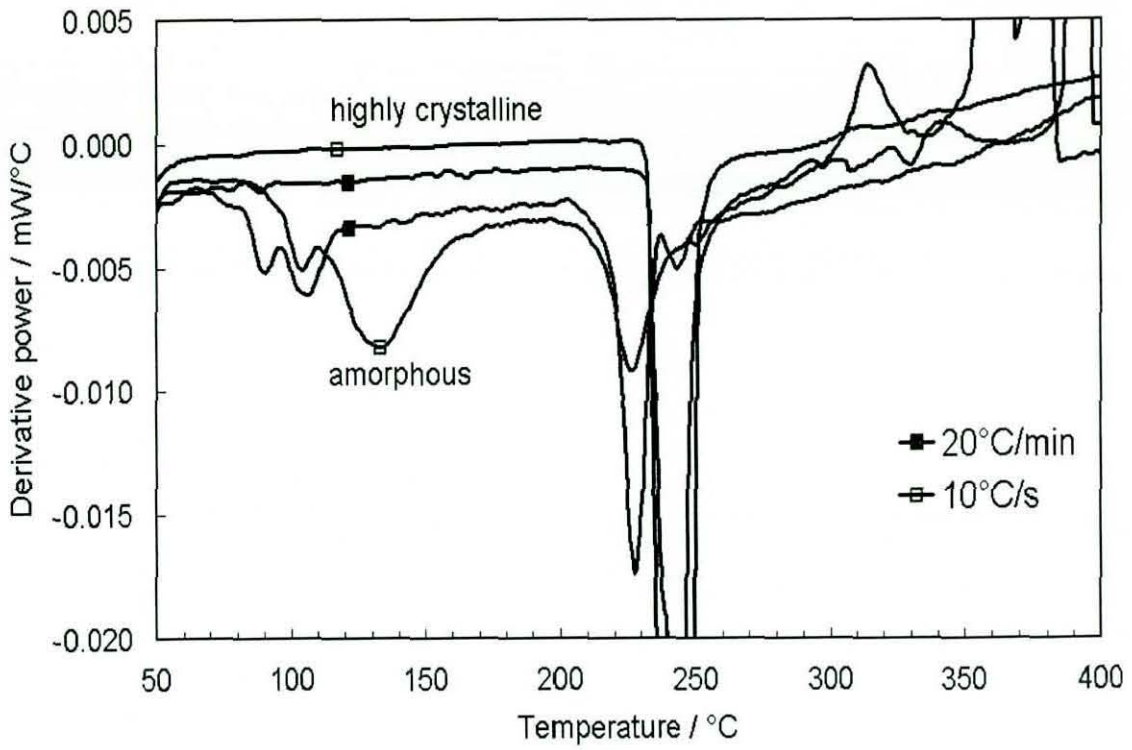
Fig 2.20. The dependence of (top) L-DTA and (bottom) L-TMA results on heating rate for amorphous and highly crystalline PET. The plots are the average of four individual runs.
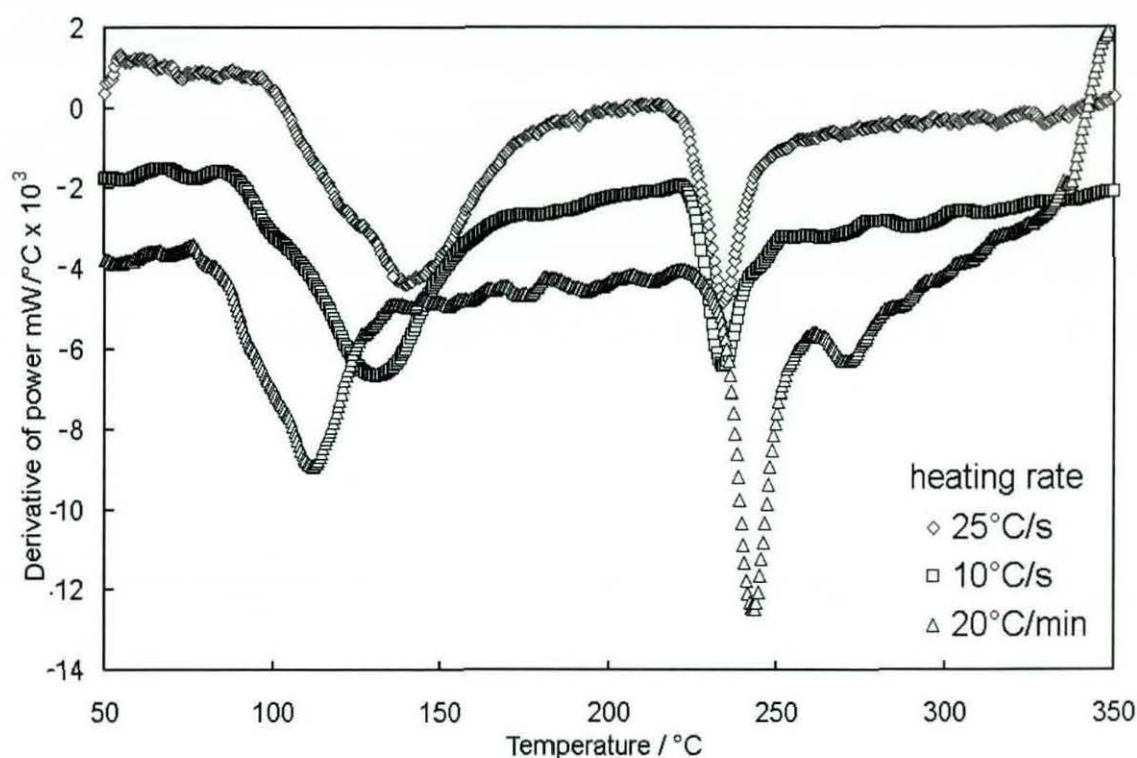
Fig 2.21. The dependence of L-DTA results on heating rate for amorphous PET. The plots are the average of four individual runs.

amorphous material, the T_g as detected in the L-DTA signal at $20°\text{Cmin}^{-1}$ and $10°\text{Cs}^{-1}$ is approximately 75°C and 90°C respectively. The melting temperature, however, remains constant within the range obtained in previous runs conducted on the amorphous material. The invariance of the melting temperature is confirmed by the averaged results for the as-supplied material carried out at $20°\text{Cmin}^{-1}$ and $25°\text{Cs}^{-1}$. The major difference between the results occurs at around 380°C, indicated by a peak, at the lower heating rate, in the L-DTA trace and a further indentation followed by a retraction in the L-TMA curve. This must be caused by thermal degradation of the polymer, which is a kinetically controlled process and therefore occurs first at the lower heating rate.

Fig. 2.21 shows in more detail the effect of three different heating rates on the L-DTA result for the amorphous material. This series of experiments was conducted with a different probe, which accounts for the slightly different shape of the curves. The heating rates were $20°\text{C min}^{-1}$, $10°\text{C s}^{-1}$ and $25°\text{C s}^{-1}$ (the fastest rate obtainable with the current implementation of the instrument). The values of T_g observed are approximately 75°C, 85°C and 100°C, respectively. The melting temperature remains roughly constant at around 220°C. There is, however, a significant increase in the area

under the melting peak as the heating rate is reduced; a consequence of the additional heat input producing a greater degree of crystallinity in the vicinity of the tip. Moreover, at 20°C min⁻¹ a significant secondary melting peak is observed between approximately 260°C and 280°C. This implies that a secondary population of thicker or more perfect crystallites was formed during the run. Thermal degradation is once more observed at this heating rate, beginning at around 330°C.

Probe force. The normal force acting between the probe and sample is determined by the degree of bending of the cantilever with the system under force-feedback control. This can readily be varied by adjusting the magnitude of the T-B photodetector signal with the probe out of contact and/or the set-point. The former is accomplished by rotating a mirror positioned in the optical path between the probe mirror and the photodetector. The latter determines the position of the laser spot on the photodetector at which the optical feedback mechanism ceases vertical motion of the z-actuator during the "probe approach" phase. Both of these parameters are measured in nA. When the T–B signal and the set-point are equalised the probe force is zero (i.e. there is no bending of the cantilever), although it is difficult to achieve stable feedback control under these conditions. In most of the experiments reported in this chapter, unless otherwise stated, the T–B signal was set at approximately –25 nA and the set-point at –10 nA. This gave a nominal net "force" of 15 nA. Because of the inherent difficulties that would be involved in carrying out an accurate calibration, no attempt was made to convert this signal into an actual force measurement. For comparative measurements this is in any case unnecessary, assuming that the relationship between the raw signal and the probe force is linear. It should be noted, however, that at high values it is possible that elastic deformation of the sample could lead to an increased initial tip-sample contact area and hence a somewhat lower compressive *stress* in the sample than would otherwise be the case. It was also assumed that for a given smooth sample, such as the as-supplied Melinex PET film used here, the contact area remained approximately constant between measurement locations (a fact supported by the reproducibility of the L-TMA results under a fixed set of conditions).

A typical set of results is shown in Fig. 2.22, the data from which have been plotted in Figs. 2.23 and 2.24. Neglecting the somewhat unreliable measurement at zero force, there is, within the limits of experimental error, a linear relationship between the probe force and both the indentation depth through the melt and the area under the melting peak in the derivative power signal. It follows that a linear relationship should exist between the L-DTA melting peak area and the L-TMA indentation depth. This is shown
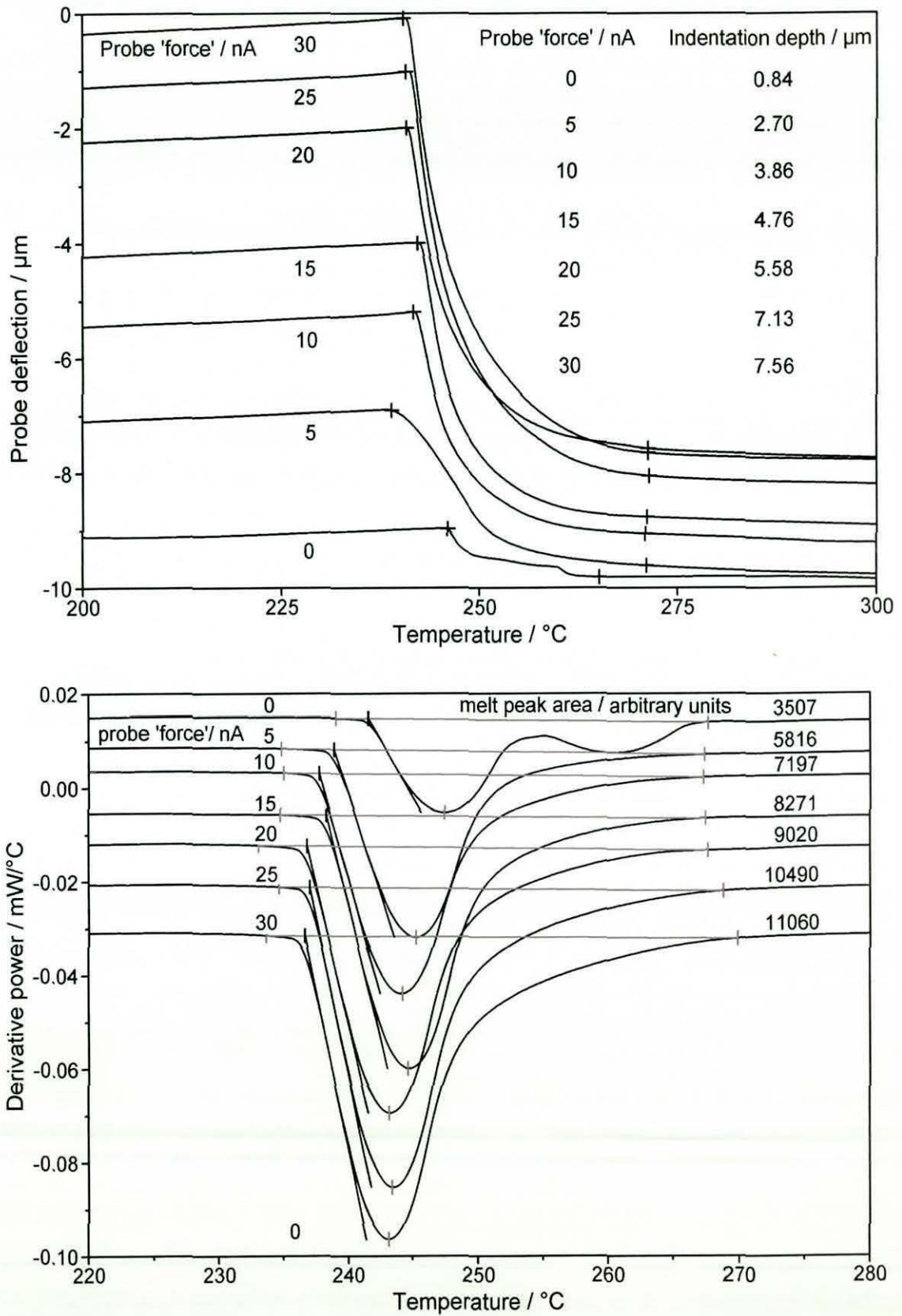
Fig. 2.22. The dependence of indentation depth (top) and melt peak area (bottom) on probe force for as-supplied Melinex PET film.
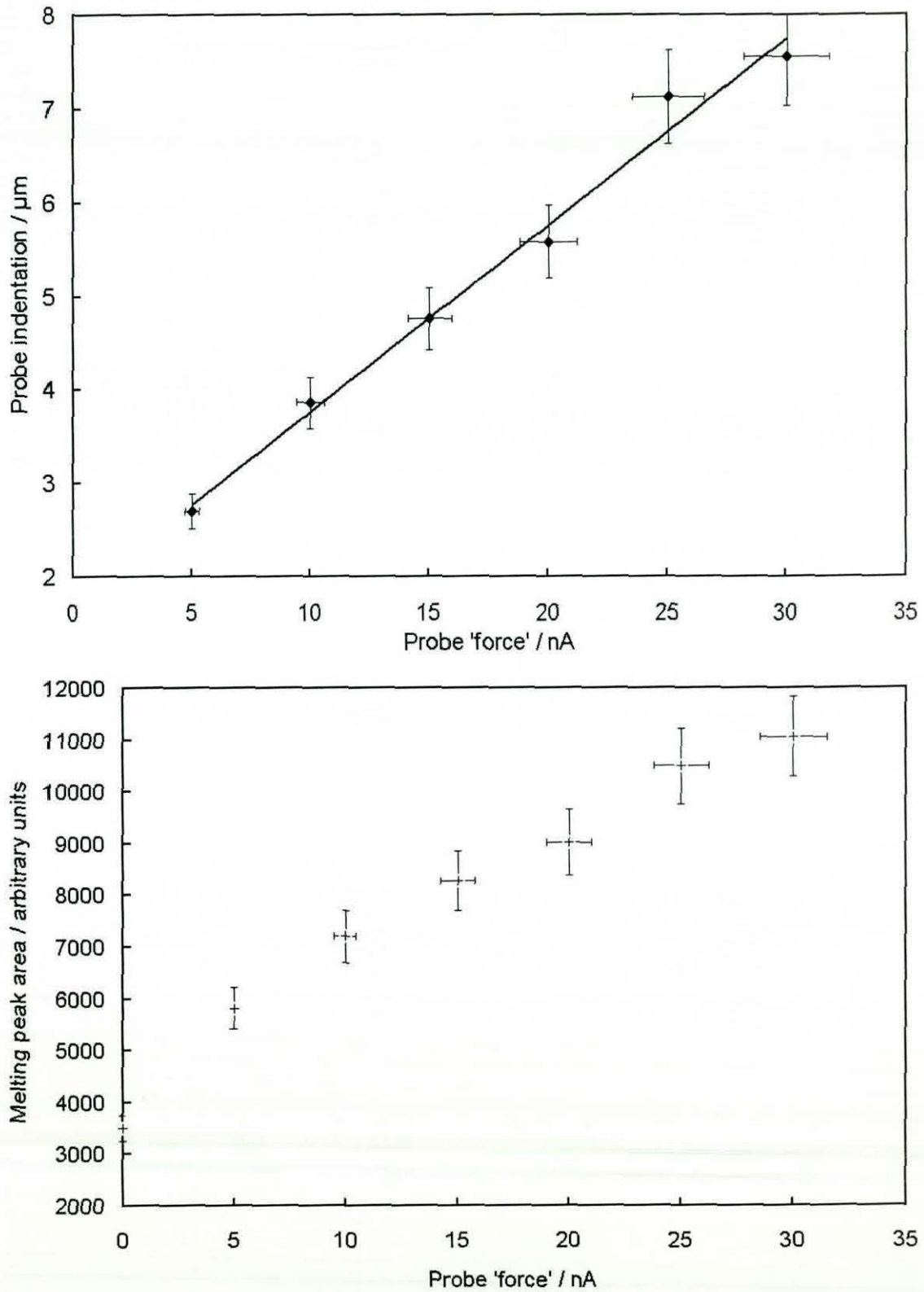
Fig. 2.23. Graphs of (top) indentation depth through the melt and(bottom) L-DTA melt peak area versus probe force for as-supplied Melinex PET film. The y-axis error bars have been constructed using the data obtained on run-to-run reproducibilty. The error in the probe force has been estimated from the percentage drift in T–B signal routinely encountered during a set of experiments.
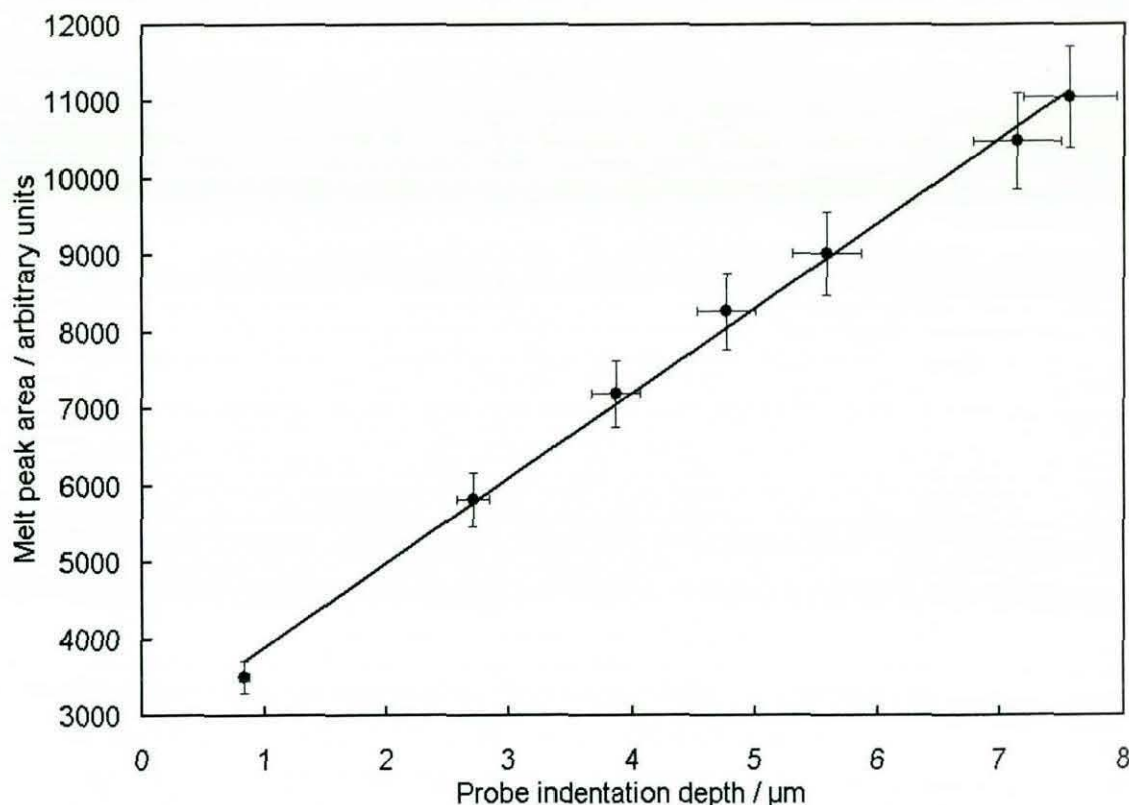
Fig. 2.24. *Graph of L-DTA melt peak area versus probe indentation depth for as-supplied Melinex PET film.*

in Fig. 2.24. While it is unsurprising that the indentation depth should vary linearly with force, it might be expected that the power signal would show a more complex relationship. It would seem, however, that the power consumption of the probe is dominated by the probe-sample contact area, which for this tip-shape must be proportional to indentation depth. This is supported by the fact that, as discussed above, even when cold crystallisation must be occurring, the power signal shows no features that are independent of the equivalent L-TMA measurement.

Topographic images were acquired of the holes or craters produced in the sample surface by L-TA, carried out at "force" values of 0 nA and 15 nA. These are shown in Figs. 2.25 and 2.26. The general shape of the holes is a flattened ellipsoid, which could perhaps be predicted from the shape of the tip-loop and the angle with which it contacts the surface. Surrounding each hole is a raised rim of material whose height is comparable with its maximum depth, as revealed in the line profiles taken from the 2-d images shown in Fig. 2.26. In the case of the crater produced at a force of 15 nA, the height of the rim, at roughly 2 μm, is approximately equal to the depth (as compared with the original height of the surface). For the 0 nA hole, the elevation of the rim, at

(a)

(b)
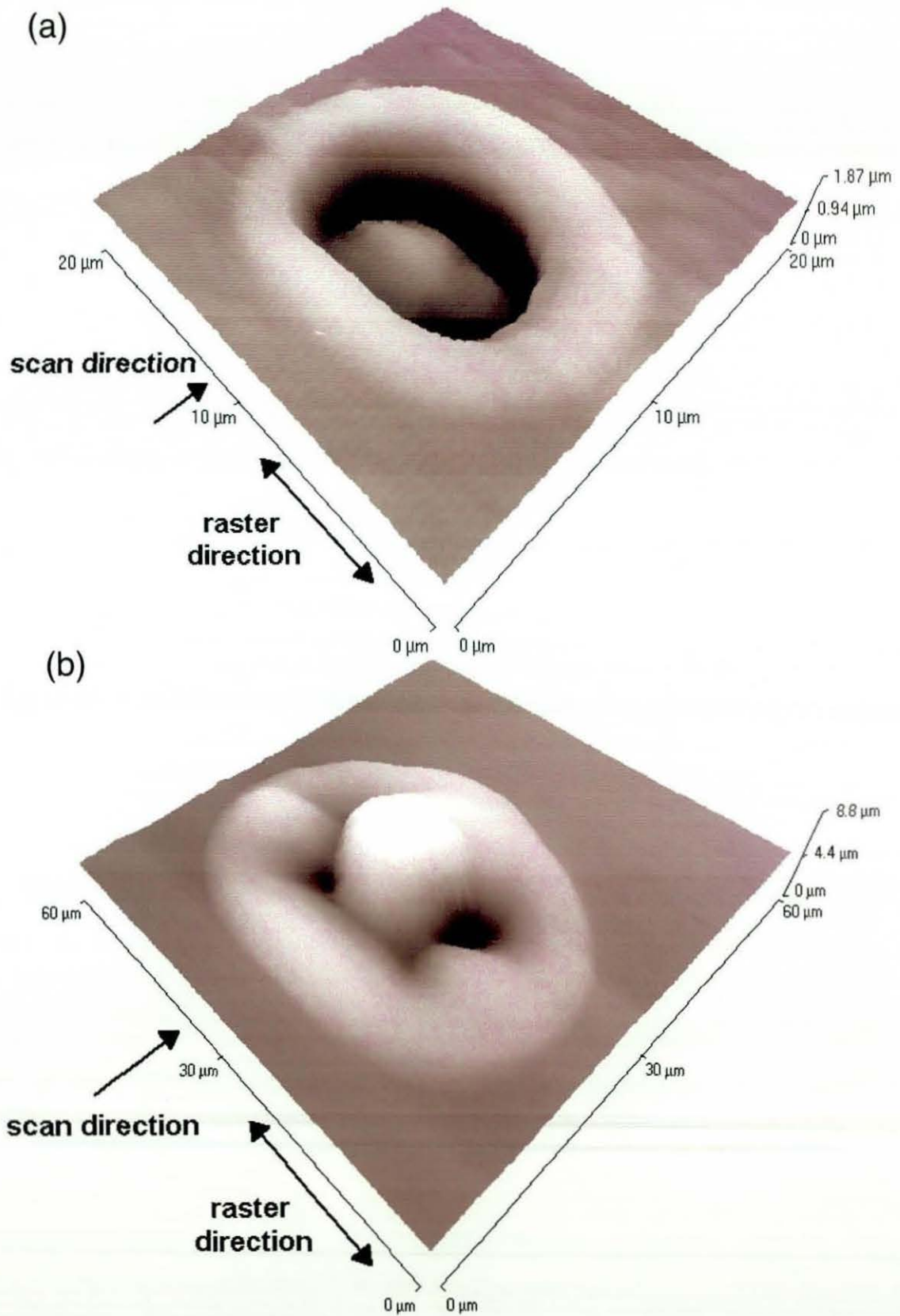
Fig. 2.25. 3-d topographic images of L-TA craters formed at a probe force of (a) 0 nA and (b) 20 nA.

orientation of the tip
(in plan)
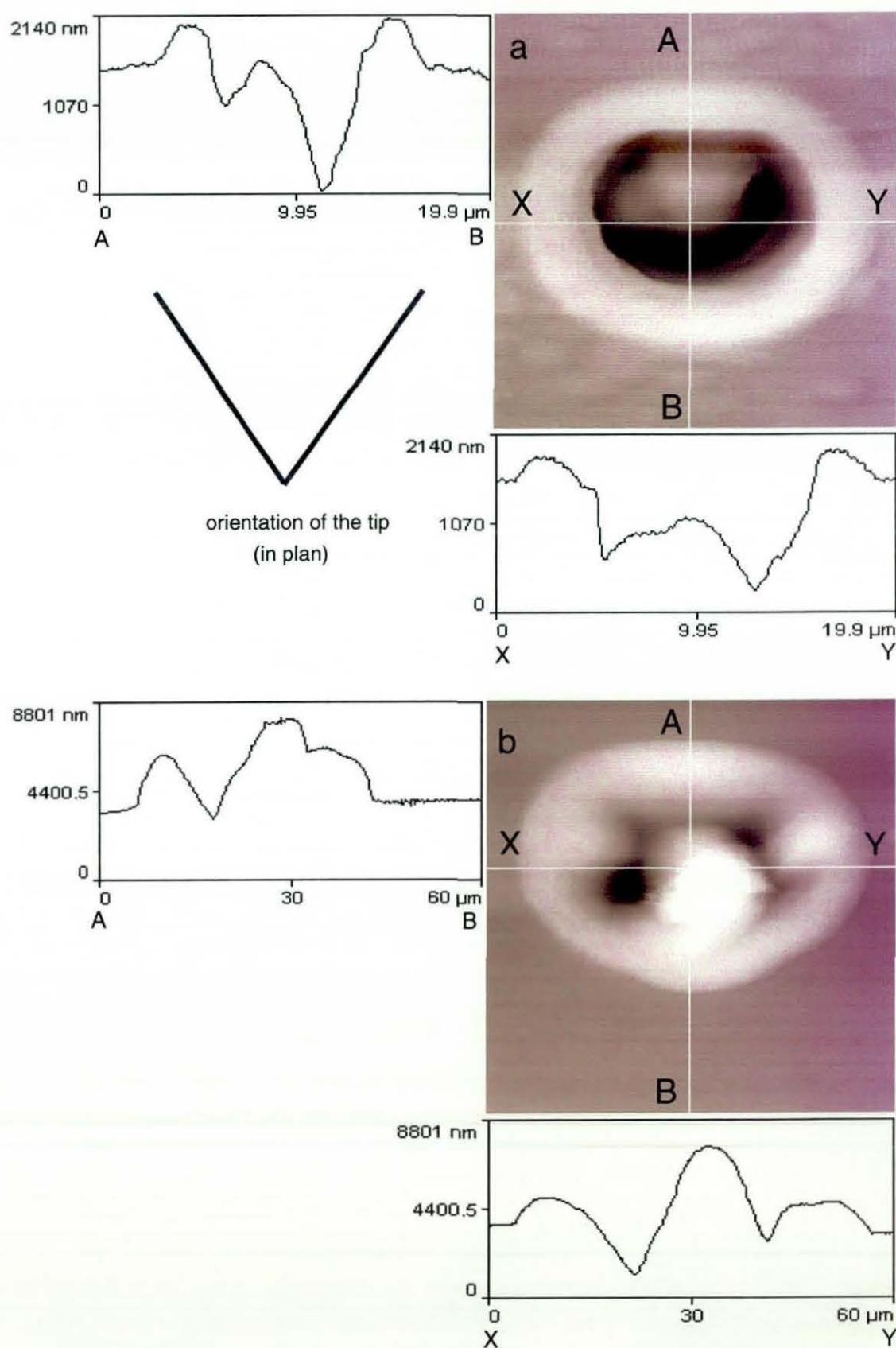
Fig. 2.26. 2-d topographic images and selected line profiles of L-TA craters formed at a probe "force" of (a) 0 nA and (b) 15 nA.

around 0.5 μm, is roughly half the depth. In both cases there is a raised mound of material inside the hole. This is a consequence of the tip-shape and material adhering to the probe as it pulls clear of the surface after the run is finished (disengagement of the probe is accomplished automatically by heating the tip back to 400°C and simultaneously energising the z-actuator). At a force of 15 nA, this plug of material fills most of the hole and projects clear of the original level of the surface by around 4 μm. It is not possible, therefore, to gain an accurate picture of the precise shape of the melt pool produced during the measurement, particularly as attempting to disengage the probe with the tip at room temperature would involve a high risk of it sustaining unacceptable damage. The maximum outside diameter of the 0 nA crater is approximately 18 μm compared with a width of the order of 50 μm at 15 nA.

Resistance of the reference element. The probe forms part of a differential measuring circuit, which allows its resistance at any temperature either to be compared with that of a suitable reference resistance maintained at room temperature or to be measured independently. In the early stages of instrument development, it was thought that to obtain meaningful AC results, the reference probe approach had to be adopted. The resistance of a Wollaston probe is typically in the range 2.5-3.5 Ω. In early experiments, the reference consisted of another Wollaston probe, but this was replaced subsequently by a 1-10 Ω variable resistor and all the results reported in this chapter were obtained using this arrangement. In order to optimise the reference resistance for a particular probe, its effects on the DC power and the AC amplitude and phase signals were investigated.

The resistance of the probe used here was 2.8 Ω, as measured using a standard multimeter. Fig. 2.27 shows the variation in the response of the DC power signal through the melting transition of the as-supplied Melinex PET, as the reference resistance is varied from 2.8 -5.0 Ω. The most striking feature is that with the reference resistance set between 2.8 and 3.4 Ω, the transition is not detected at all. In fact, it is not until the reference reaches a resistance of 5.0 Ω that the sensitivity reaches an acceptable level. Increasing the reference resistance beyond this produced excessive curvature of the baseline (obtained with the probe out of surface-contact). For all subsequent experiments, therefore, the resistance of the reference was set at a value approximately 50% greater than that of the particular probe being used.

The effect of the reference resistance on the AC amplitude and phase signals is shown in Fig. 2.28. The runs here were conducted with the probe held in air. The
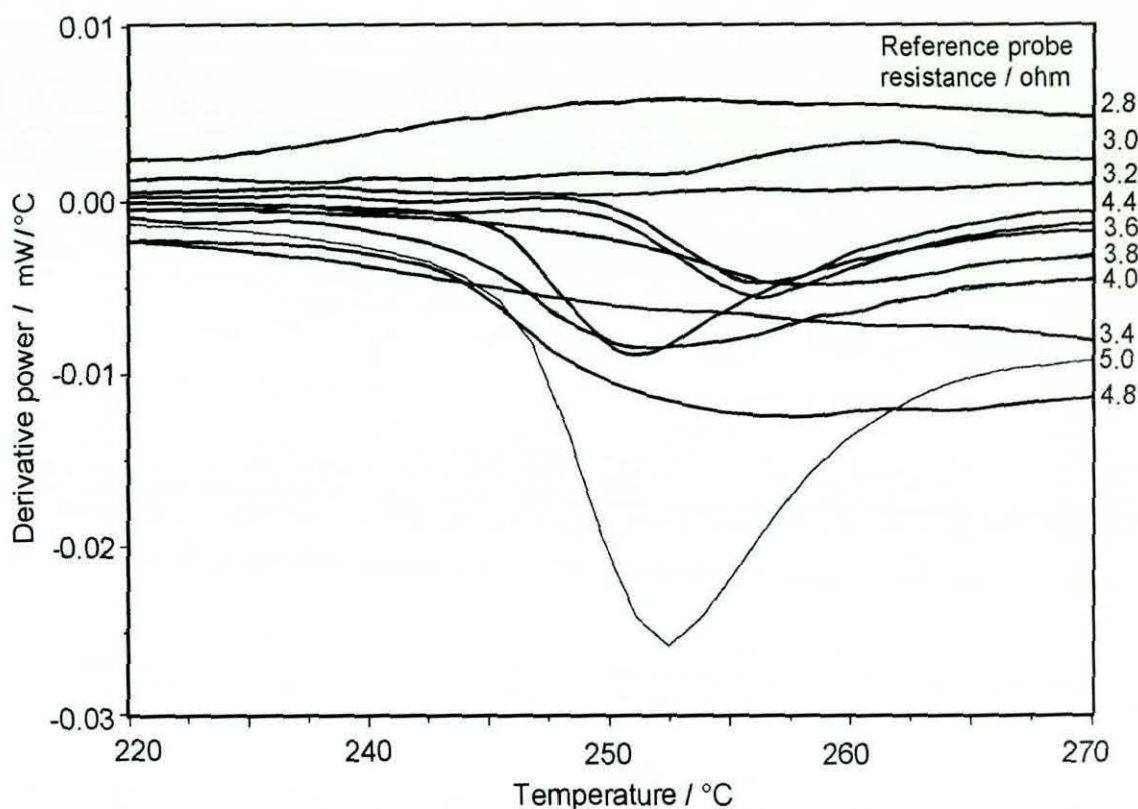
Fig. 2.27. Variation in the L-DTA melting peak with reference resistance for as-supplied Melinex PET. Resistance of the probe = 3.2 Ω.

modulation frequency was 5 kHz and the amplitude was 6°C. It should be stated that, up to this point, a great deal of time and effort had been spent on investigating the source of artefacts or saturation in the AC signals. The artefacts typically took the form of false peaks and the original aim of replacing the reference probe with a variable resistor was to investigate whether the magnitude of the reference resistance had a bearing on the appearance of such artefacts (its effect on the DC power signal was unexpected). For the amplitude signal it can be seen that with the reference resistance set at 2.0 Ω, there are artefacts in the form of peaks occurring between 50°C and 150°C and another between 200°C and 300°C. The scaling of the plot is such that the lower temperature peaks go well off-scale. Over most of the rest of the temperature range the signal is saturated, apart from between 220°C and 250°C. With the resistance set at between 2.8 Ω and 5.0 the signal is "live" over the whole temperature range, although at a resistance of 2.8 Ω there is an artefact, in the form of an upward curve, above 350°C that appears to be a prelude to a peak. At a resistance of 6.9 Ω and 10.0 Ω, signal saturation and artefacts are once again prevalent. The appearance
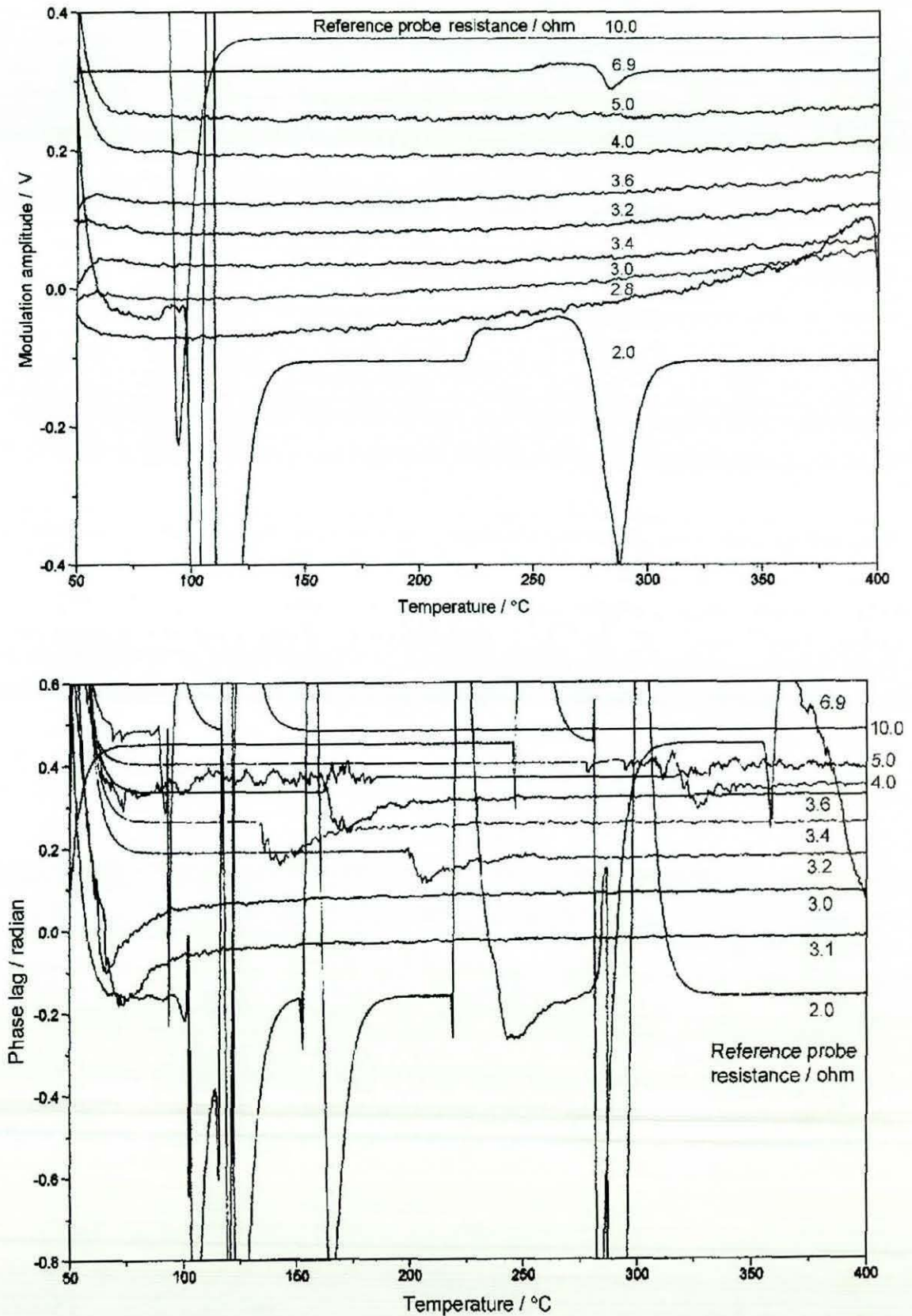
Fig. 2.28. Variation in the (top) AC amplitude and (bottom) phase lag with reference resistance with the probe held in air. Resistance of the probe = 3.2 Ω.

of artefacts and saturation in the phase response is even more marked, with only the signals obtained with the resistor set at 3.0 and 3.1 Ω completely free of artefacts and saturation over the whole temperature range. It is apparent from these results that, at the time, the requirements for an artefact-free phase signal and an optimised DC power response were incompatible. Relatively recent modifications to the control software have, however, greatly improved performance in this respect.

The effect of modulation frequency and amplitude on the AC amplitude and phase lag response. Once a reliable method had been found to obtain consistent artefact-free AC signals, the effect of the modulation frequency and amplitude on the signals was investigated. The aim was to maximise the sensitivity of the AC response and to ascertain whether a set of parameters existed under which cold crystallisation, in particular, could be detected in amorphous PET. Results using the earliest prototype instrument had suggested that this was possible. Representative plots from a series of ten runs conducted at each frequency are shown in Figs. 2.29 (amplitude) and 2.30 (phase lag). For purposes of comparison, typical L-TMA and L-DTA results are shown in each case.

The frequency was varied from 3-100 kHz at a fixed amplitude of 5°C. It can be seen that the glass transition is detected in the amplitude signal (at around 90°C) at all frequencies with the exception of 100 kHz. Above the T_g, the shape of the traces taken between 3 and 60 kHz reflects, to a greater or lesser extent, the main features in the L-DTA signal. At 80 and 100 kHz, however, the form of the curves departs somewhat from that of the DC response. The greatest sensitivity would appear to be obtained at 5 kHz, although in none of the traces is information obtained that does not appear in the L-DTA trace.

The modulation amplitude was varied from 2-10°C at a frequency of 5 kHz. Again, in none of the results is information acquired additional to that available in the DC power signal. The glass transition is detected at all but the lowest amplitude, although at an amplitude of 4°C the response is relatively weak and above the T_g the trace remains comparatively featureless, compared with those acquired at higher amplitudes and the equivalent L-DTA result. The greatest sensitivity would appear to occur at an amplitude of 6°C.

The results in Fig. 2.30, show the phase lag to be less sensitive to the glass transition (and other features present in the L-DTA trace) than the amplitude response and in none of the results can a T_g be unequivocally assigned. For this reason, in all
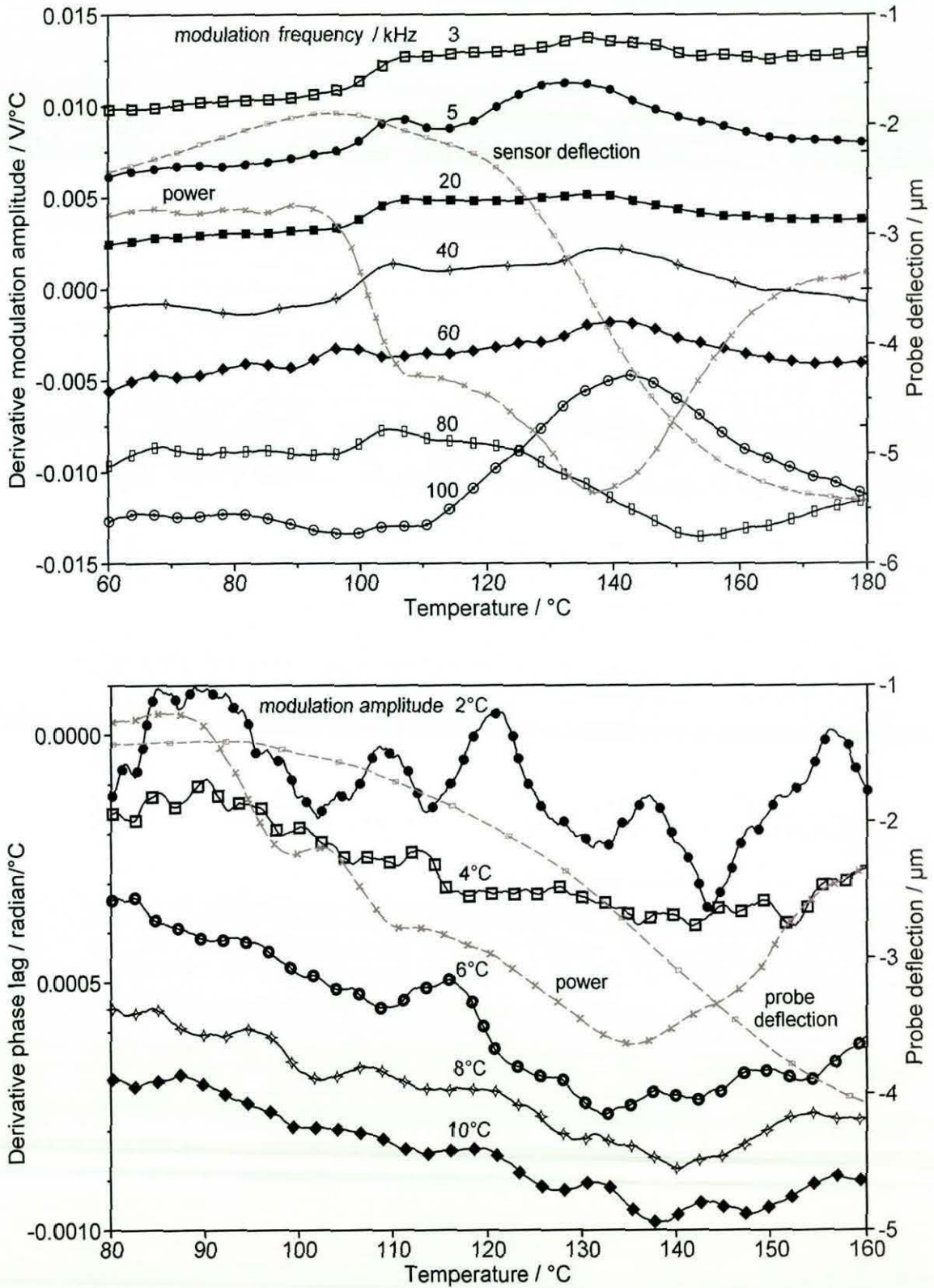
Fig. 2.29. Variation in the AC amplitude response with (top) modulation frequency and (bottom) modulation amplitude. Amorphous PET. Typical L-TMA and L-DTA results are shown for comparison.
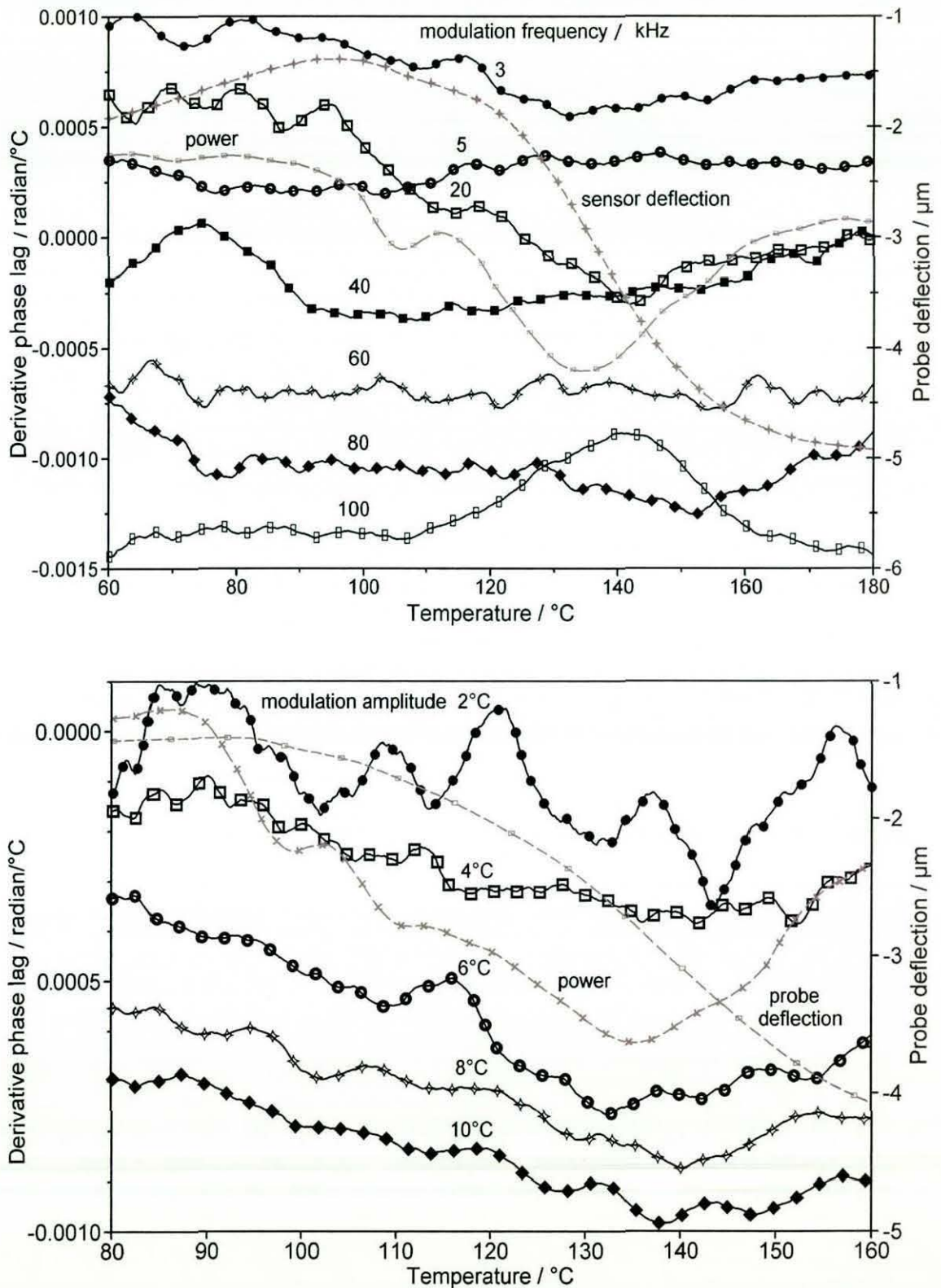
Fig. 2.30. Variation in the AC phase lag with (top) modulation frequency and (bottom) modulation amplitude. Amorphous PET. Typical L-TMA and L-DTA results are shown for comparison.

subsequent experiments, the modulation frequency and amplitude were optimised to give the best amplitude response, at 5 kHz and 6°C, respectively.

The reasons for the comparative insensitivity and poor signal-to-noise ratio of the AC signals remain unclear, but is most probably rooted in the fact that the DC calorimetric response itself seems insufficiently sensitive to detect events in a sample that produce no change in probe-sample contact area. There would appear to be no fundamental reason why this should be the case and it is therefore likely that there is considerable scope for improving the AC and DC calorimetry by modification of the electronic hardware. The same problem could perhaps account for the vulnerability of the AC signals to artefacts. Although the implementation of a recent software fix has all but eliminated such artefacts, it is unlikely that it has solved the more fundamental problem that rendered the instrument prone to them in the first place.

2.3.5 The study of a semi-crystalline polymer coated with an inert layer

In order to investigate further the degree of dependence of the calorimetric signal on variations in tip-sample contact area, it was decided to subject a fluorocarbon-coated PBT injection moulded component to analysis. The thickness of the coating (as determined by AFM) was of the order of tens of nm. It was thought that if such an inert coating was thin and yet mechanically robust, the substrate could well start to melt before the structural integrity of the coating was lost and, hence, the probe began to penetrate into the sample. If this was the case then, if the signal was sufficiently sensitive, it could be expected that the onset of melting would be detected unequivocally in the power signal before any response was detected in the L-TMA trace. This component therefore seemed to offer an ideal sample with which to determine whether at least some proportion of the L-DTA measurement was independent of the L-TMA signal.

L-TA results for the individual polymers and the coated component are shown in Fig. 2.31. The onset melting temperature of the pure PBT is approximately 220°C, while PTFE undergoes no transitions over the same temperature range of 100-400°C. In the coated component, the occurrence of the maximum of the melting peak is delayed by approximately 100°C. A weak melting onset is, however, detected in the power signal at 235°C, some 15°C above the $T_{m\ (onset)}$ of the pure PBT. There is no corresponding response in the derivative probe deflection trace and it is not until a temperature of approximately 270°C is reached that appreciable probe penetration begins. This presumably occurs when the volume of molten polymer beneath the
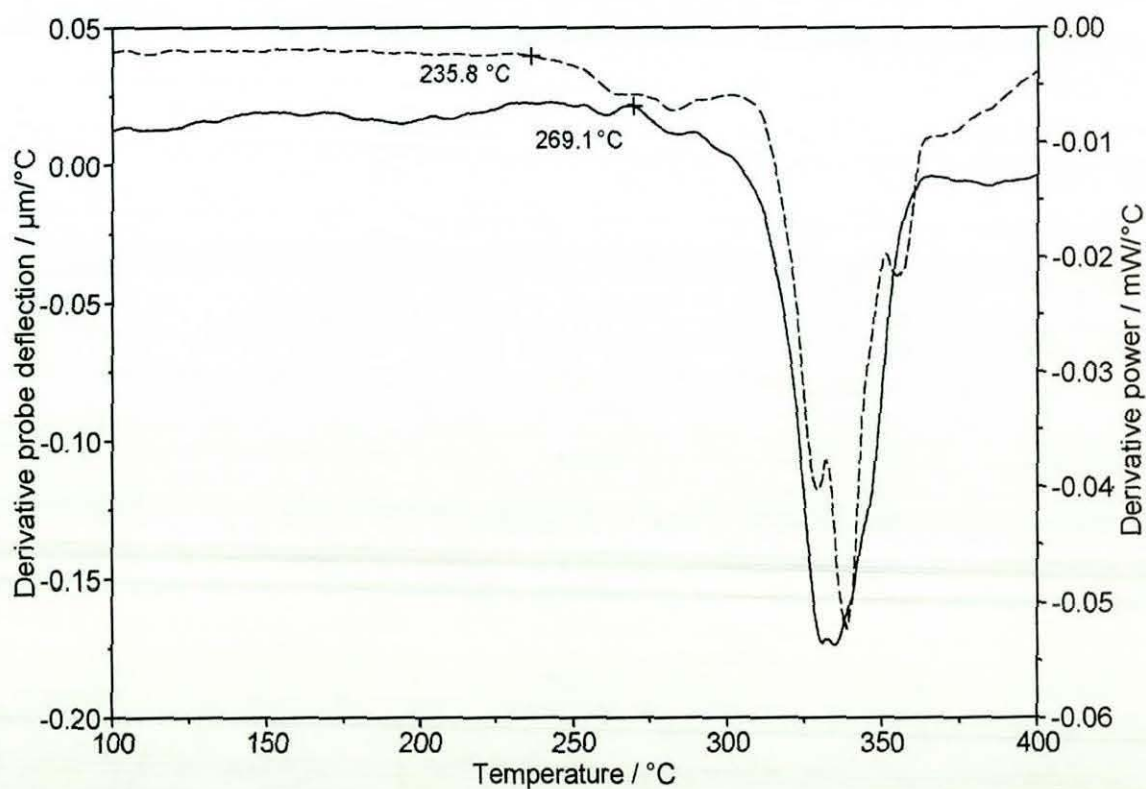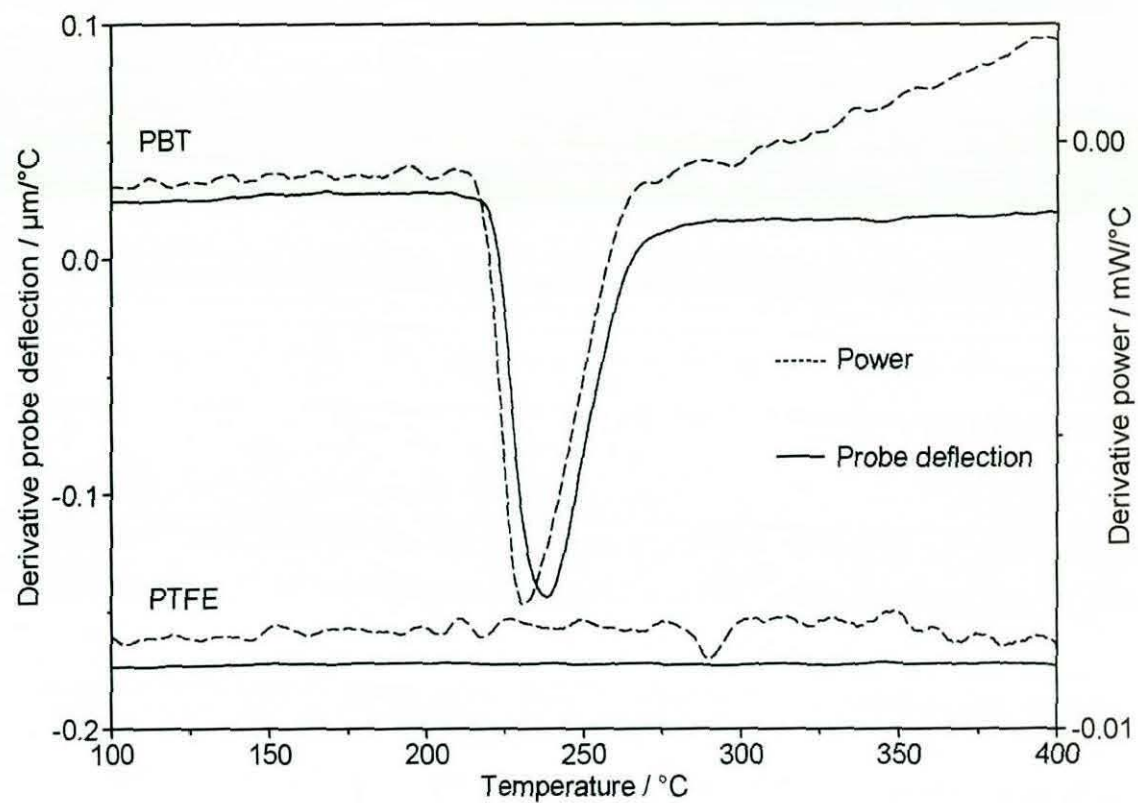
Fig. 2.31. Microthermal analyses of (top) PBT and PTFE and (bottom) a fluorocarbon-coated PBT injection moulding.

coating reaches a critical point at which the coating can no longer support the downward force exerted by the probe. This would seem to indicate that, during a melting transition, an increase in contact area does not necessarily have to occur in order to produce a response in the power signal. The effect here as a proportion of the power consumed through the main melting event is, nevertheless, very small. This result would seem, therefore, to confirm the conclusion that the sensitivity of the calorimetric response of the current instrument is not optimised.

2.3.6. Localised thermal analysis of PET with differing degrees of crystallinity - a comparison with MTDSC and micro-Raman spectroscopy.

The measurement or even just the detection of spatial variations in crystallinity (either laterally or with depth) at the micrometre scale is problematic. Up until now, one of the very few practical methods available has been micro-Raman spectroscopy.[210] For PET, the full-width half-maximum of the 1728 cm^{-1} carbonyl (C=O) Raman scattering band can be correlated to degree of crystallinity.[212] It is, however, known that confocal Raman spectroscopy is limited by the optical properties of the material and the sampled volume can be significantly larger than the theoretical minimum.[213] Furthermore, the Raman response can be very sensitive to molecular orientation and is generally a means for determining properties of, for example, uniaxially- and biaxially-oriented polymers. Localised thermal analysis, on the other hand, should be unaffected by optical properties or orientation.

The work on the reproducibility of the L-DTA melting peak area exhibited by the highly crystalline Melinex PET lent encouragement to the idea that this parameter could be used to acquire at least a qualitative picture of variations in crystallinity within a sample and between different samples. Work by Hammiche and co-workers [57] also supports this conclusion. Here, different L-TA results were obtained between the quenched surface of a PET pellet, a region of the surface that had cooled more slowly and, thirdly, the sectioned interior of the pellet, that had cooled more slowly still.

The aims of this part of the work were therefore as follows: (a) to confirm whether L-TA could be used as a qualitative tool to detect even relatively subtle variations in crystallinity across a surface or between, for example, surface and bulk; (b) to carry out L-TA on samples of known (bulk) crystallinity, as determined by DSC or MTDSC, and compare the results in order to ascertain if L-TA could be used, after carrying out suitable calibration using an independent technique, as a semi-quantitative method of
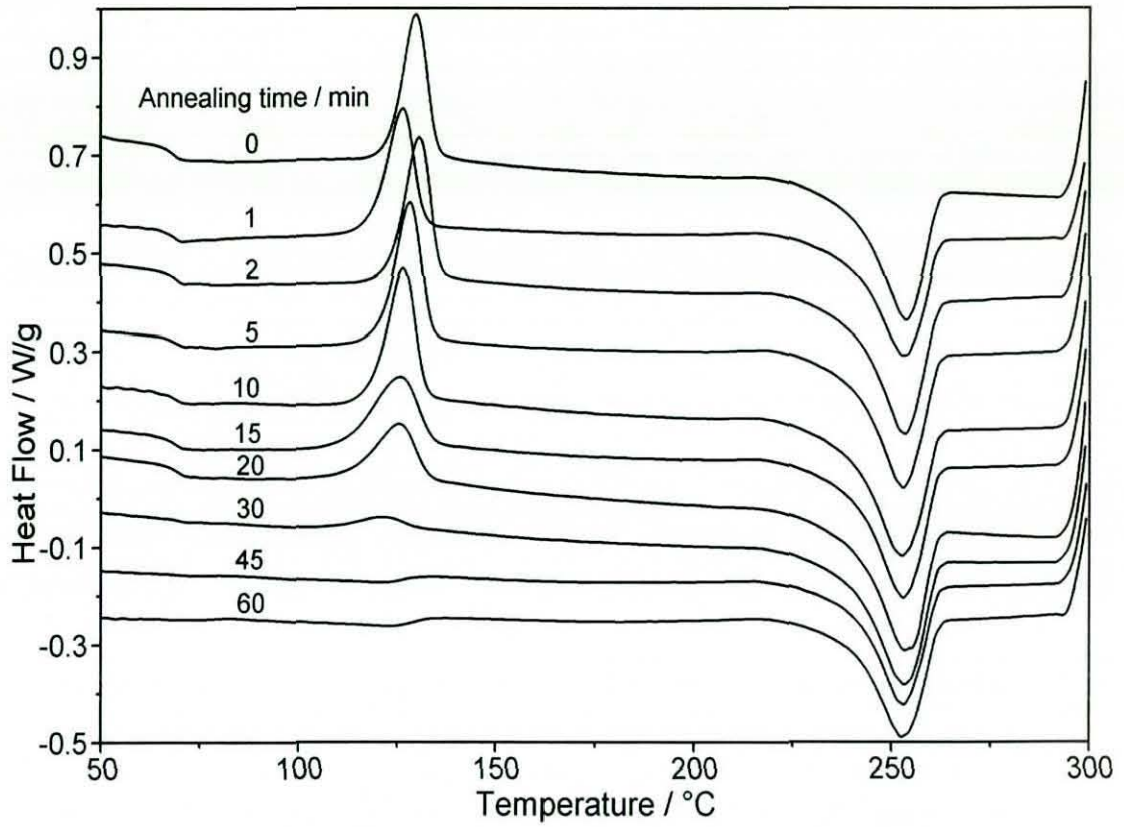
Fig. 2.32. MTDSC results (total signal) for amorphous PET and material annealed for various times at 110°C.
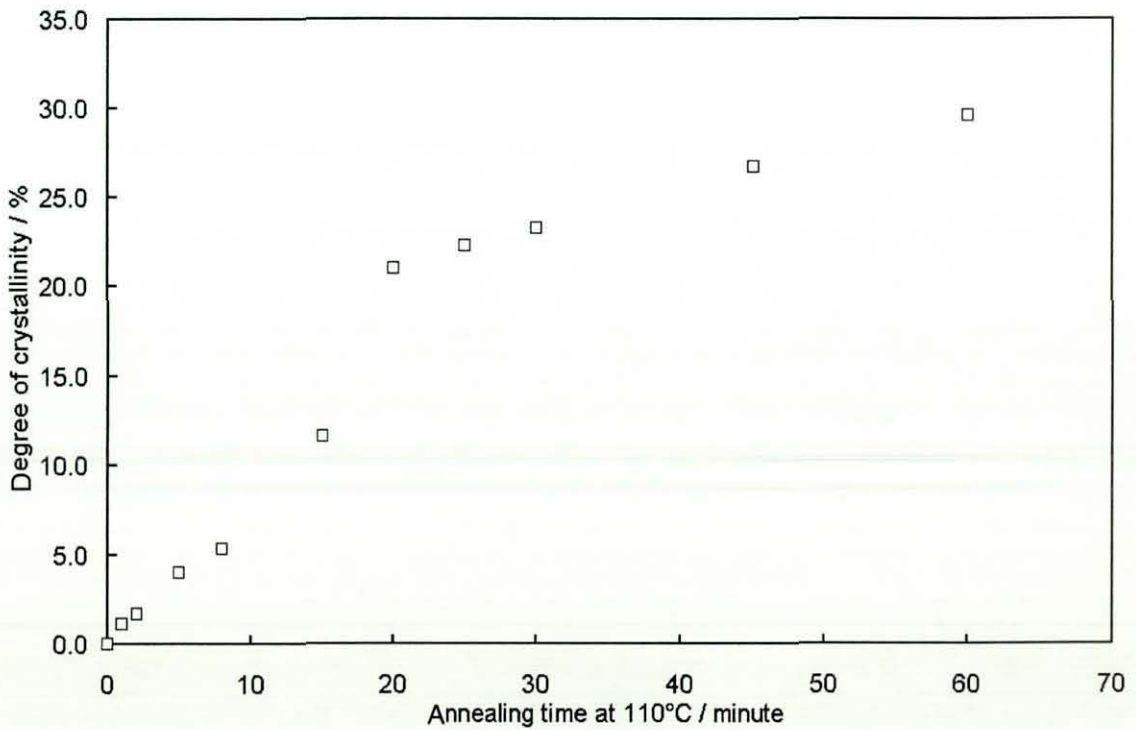
Fig. 2.33. Degree of crystallinity of annealed PET samples, as determined by MTDSC, versus annealing time.

determining local crystallinity; (c) to investigate the limit of detection of L-TA with respect to local crystallinity and compare it with that of micro-Raman spectroscopy.

The MTDSC results, here showing the total heat flow only, for the amorphous and annealed samples are shown in Fig. 2.32. The main features shown are an exothermic cold-crystallisation peak occurring between 110°C and 130°C and a melting peak between approximately 230°C and 260°C. At an annealing time of 30 minutes, the crystallisation peak has become very weak and by 45 minutes it has disappeared altogether. This shows that after annealing for 30 minutes, there is very little "crystallisable" amorphous material left in the sample. This is reflected in the attenuation of the glass transition at high annealing times. These results were used to calculate the initial degree of crystallinity of each sample using the method described by Reading et al.[214] To facilitate this, values for the heat capacity of amorphous and 100% crystalline PET were obtained from the online University of Tennessee Advanced Thermal Analysis System (ATHAS) database.[215] The calculated crystallinity values have been plotted against annealing time in Fig. 2.33 and are shown in Table 2.3.

L-DTA and L-TMA results for the amorphous and annealed samples are presented in Figs. 2.34 and 2.35, respectively. The curves have been averaged from the results of five experiments. For clarity, the results have been split into sections that emphasise separately the response in the region of the glass transition (2.34) and the melt (2.35). Taking the effect of annealing time on the glass transition first; it can be seen that up to and including an annealing time of 10 minutes, a glass transition is clearly shown in both signals at around 100°C. At annealing times of 15 minutes and above there is no glass transition detected. This is in contrast with the MTDSC results in Fig. 2.32, which show a glass transition and crystallisation peak in the bulk samples up to and including an annealing time of 30 minutes (albeit weak in the last case). The most obvious explanation for this is that the sensitivity of L-TA with respect to the glass transition is significantly inferior to that achieved by M-TDSC of bulk samples Alternatively, it could be that the degree of crystallinity at the surface of the annealed films was significantly higher than the average value measured by M-TDSC. The results for the same samples over the temperature range 200-250°C show an increasingly large melting peak as the annealing time is increased. The area under the melting peak for the material annealed for 60 minutes is at least a factor of 12 larger than the peak for the amorphous material, which must be associated entirely with material that crystallised during the experiment. An interesting feature that the samples annealed for 45 and 60
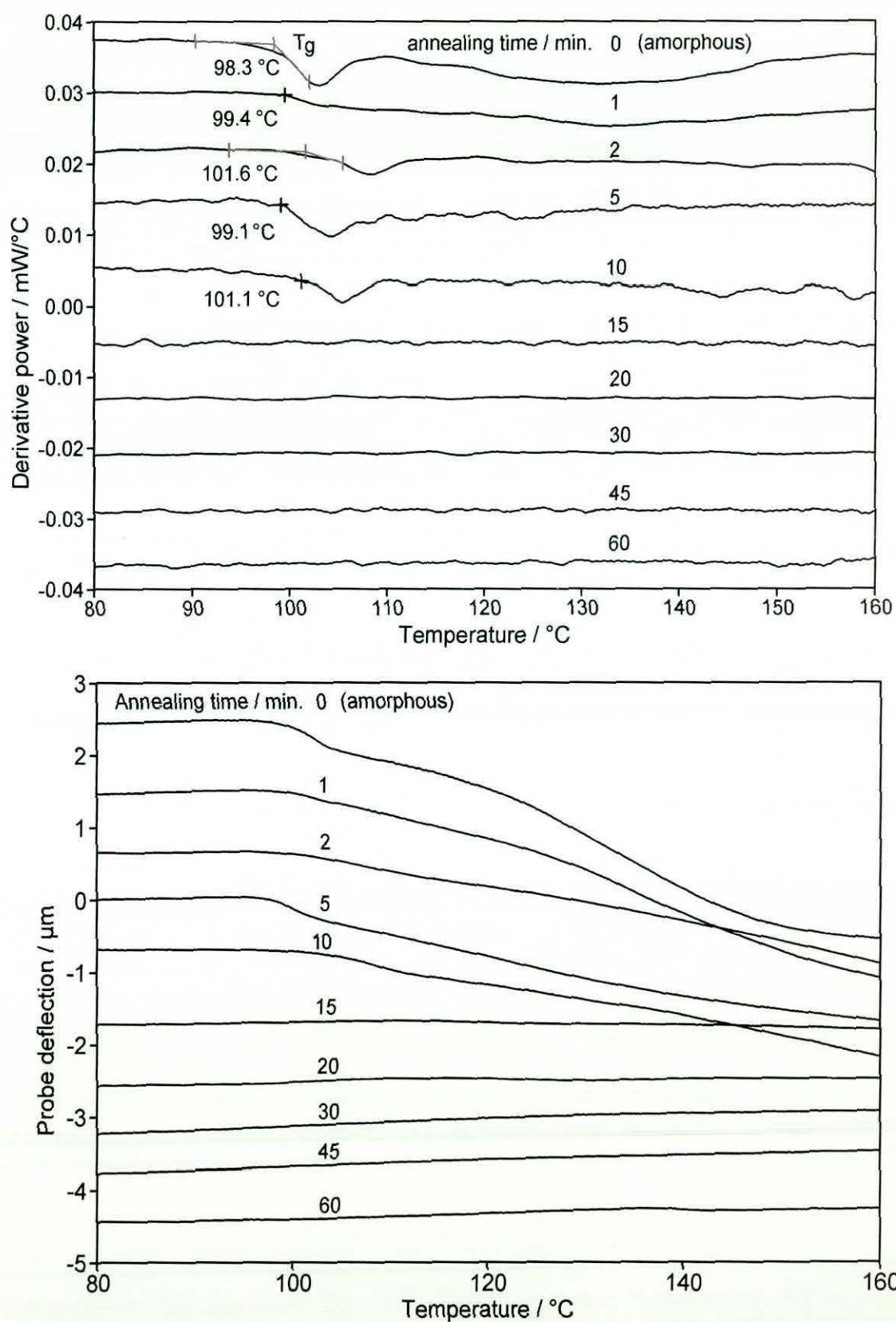
Fig. 2.34. L-TA results for annealed PET samples through the glass transition (mean of five measurements). Top: L-DTA; bottom: L-TMA.
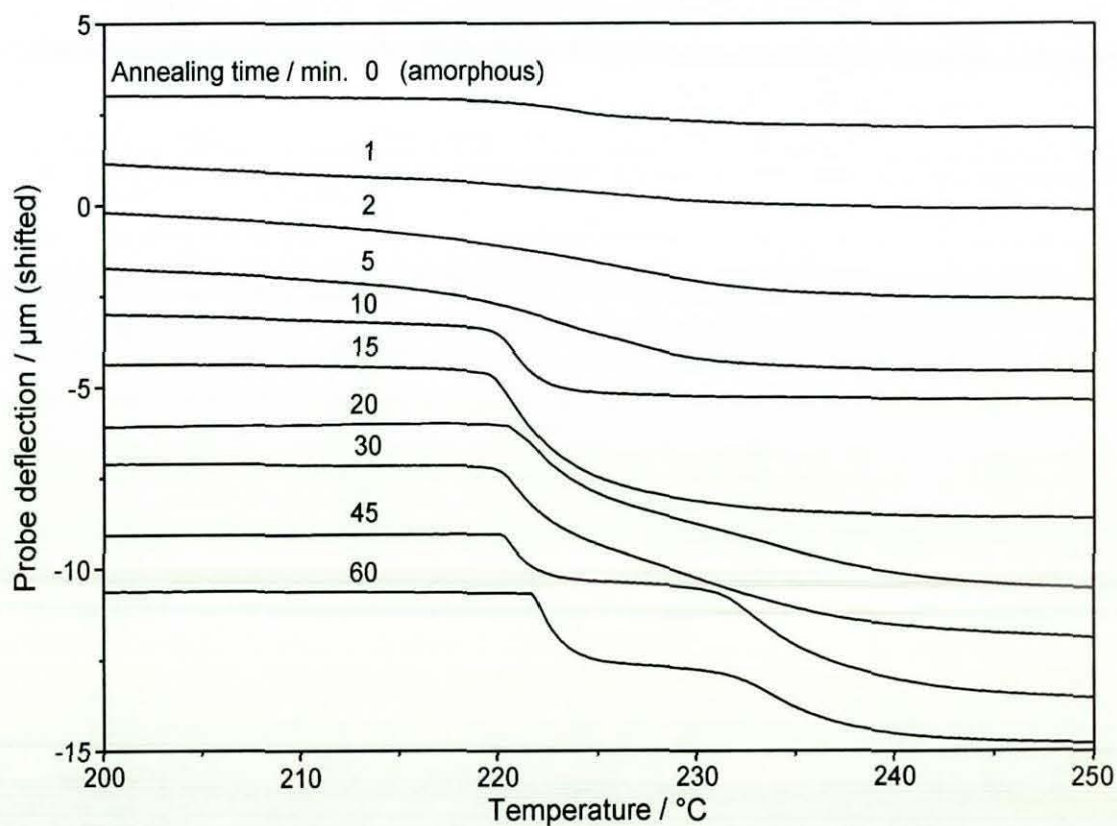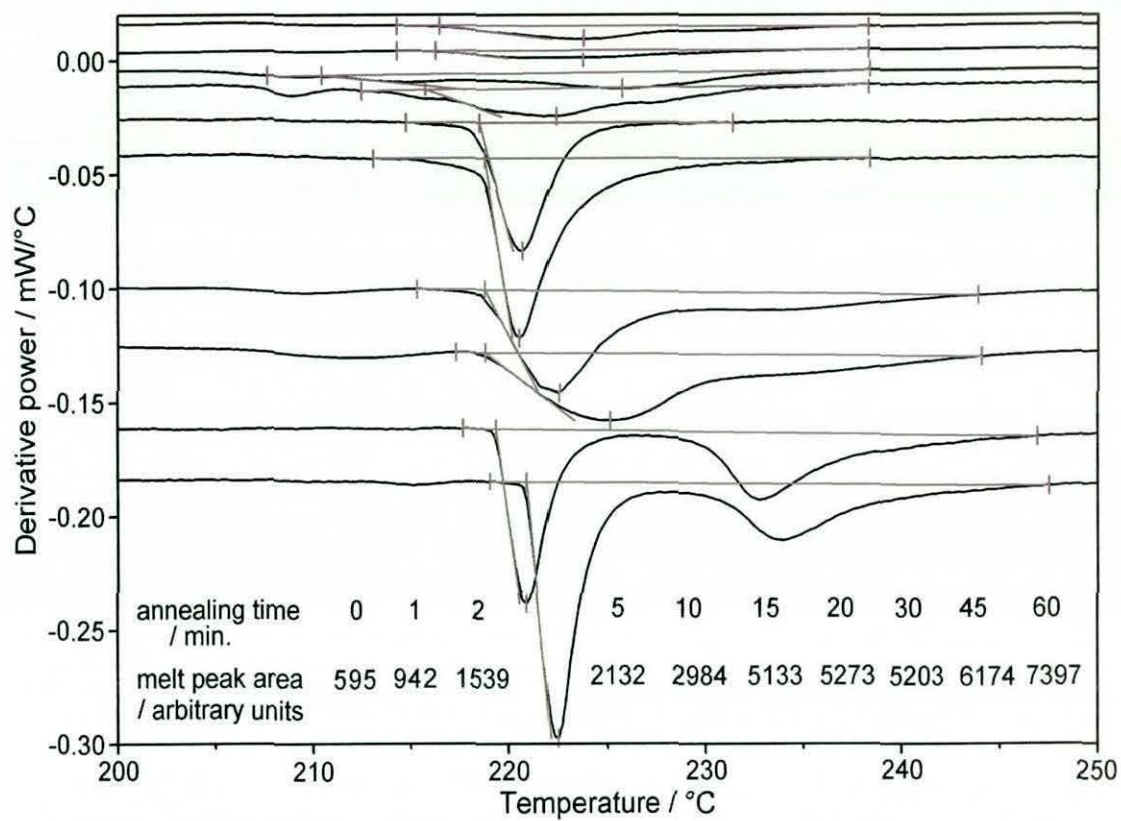
Fig. 2.35. L-TA results for annealed PET samples through the melting transition (mean of five measurements). Top: L-DTA showing melting peak areas. Bottom: L-TMA.

minutes show is the occurrence of a second, smaller, melting peak in the L-DTA trace between 230 and 240°C. This behaviour is reflected in the equivalent L-TMA results, which show that the probe penetrates into the film in two distinct stages. In both cases the total penetration occurring between 220 and 240°C is approximately 4 μm. For the 60 minute sample, this is split into two approximately equal steps, with the one at the higher temperature being the more gradual of the two. In the case of the 45 minute sample, the first penetration, at approximately 1.5 μm, is the smaller but more rapid one. It will be noted also that the L-DTA melting peaks for the samples annealed for 20 and 30 minutes are broader than those obtained at shorter annealing times. The associated L-TMA indentations through the melt are also more gradual. It seems therefore that the appearance of the bimodal behaviour exhibited at the two longest annealing times is the result of progressive changes within the material with increasing annealing time. In order to confirm that the appearance of bimodal melting behaviour was not an artefact arising from, for example, damage to the probe, a sample of the as-supplied material was subsequently tested and found to exhibit a normal single melting peak. The reason for the behaviour of the samples subjected to the longest annealing times must, therefore, be associated with a real physical phenomenon. The most likely explanation is the formation of two distinct populations of crystalline lamellae with, for example, different lamellar thickness. Considering these results in isolation, it is impossible to be certain whether the two populations are differentiated by melting temperature alone or a combination of melting temperature and depth within the sample, though the latter would seem to be the more likely scenario. The reason for the difficulty in interpreting the results is that two distinct populations of crystallites undifferentiated by depth could still produce a two-step indentation in the L-TMA trace, as well as a double melting peak. Moreover, in the case of a material that consisted of a discrete surface layer with a melting temperature higher than that of the sub-surface region, the melting temperature of the sub-surface material would still appear to be several degrees higher than that measured at the surface. In such cases, the only way of determining accurately the melting temperature of the bulk by L-TA would be to carry out successive experiments at the same location, thus gradually increasing the starting depth of the measurement relative to the original surface.

Table 2.3 contains the L-DTA melting peak areas obtained at the various annealing times, together with the corresponding values for degree of crystallinity as determined from the MTDSC results obtained for identical samples. The total peak areas include the contribution of both the primary and secondary melting peaks for the

Annealing time at 110°C / min	Mean L-DTA peak area / mW	Mean corrected L-DTA peak area / mW	% crystallinity (M-TDSC)
0	0.104	0.000	0.0
1	0.140	0.036	1.1
2	0.146	0.042	1.7
5	0.199	0.095	4.0
8	0.187	0.083	5.4
10	0.230	0.126	7.4
15	0.303	0.199	11.6
20	0.392	0.288	21.0
25	0.415	0.311	22.3
30	0.440	0.336	23.3
45	0.440	0.336	26.7
60	0.507	0.403	29.7

Table 2.3. Micro-DTA melting peak areas at various annealing times and the corresponding values for the degree of crystallinity measured by MTDSC for identical samples. The L-DTA peak areas are the mean values from five experiments.

samples annealed for 45 and 60 minutes. Column 3 contains the L-DTA melting peak data from which the offset due to the cold-crystallisation of the initially-amorphous has been subtracted. This is an approximation, as the contribution from cold crystallisation will progressively decrease with increasing annealing time. However, because of the relative sizes of the melting peaks, at high annealing times the percentage error will be relatively small. Consequently, no attempt has been made to adopt a more sophisticated data treatment based on, for example, the rate of attenuation of the glass transition with increasing annealing time. Fig. 2.36 contains both a graph of the corrected L-DTA melting peak area versus degree of crystallinity and a histogram showing the variation in peak area and degree of crystallinity with annealing time. The correlation between degree of crystallinity and the L-DTA melting peak area is shown to be very close. At low or moderate values, however, L-TA would seem to overestimate the degree of crystallinity compared with the average value obtained by MTDSC. This could well be because, at short annealing times, the degree of crystallinity produced in the region of the surface is greater than that in the bulk of the
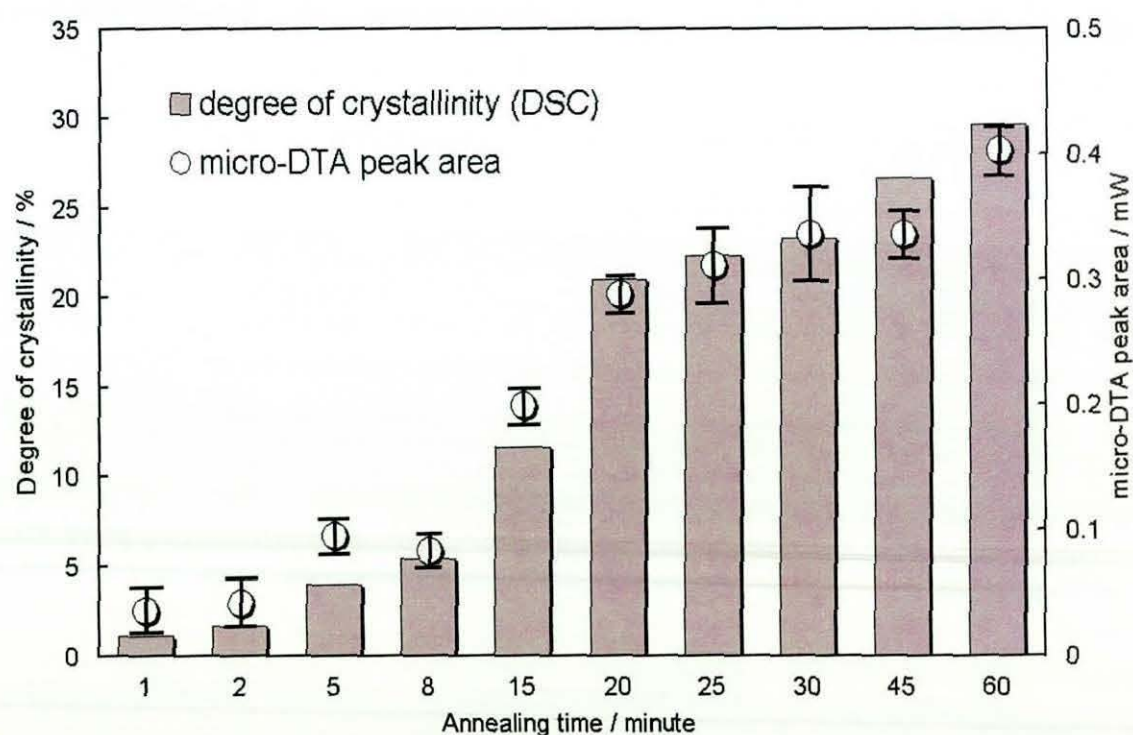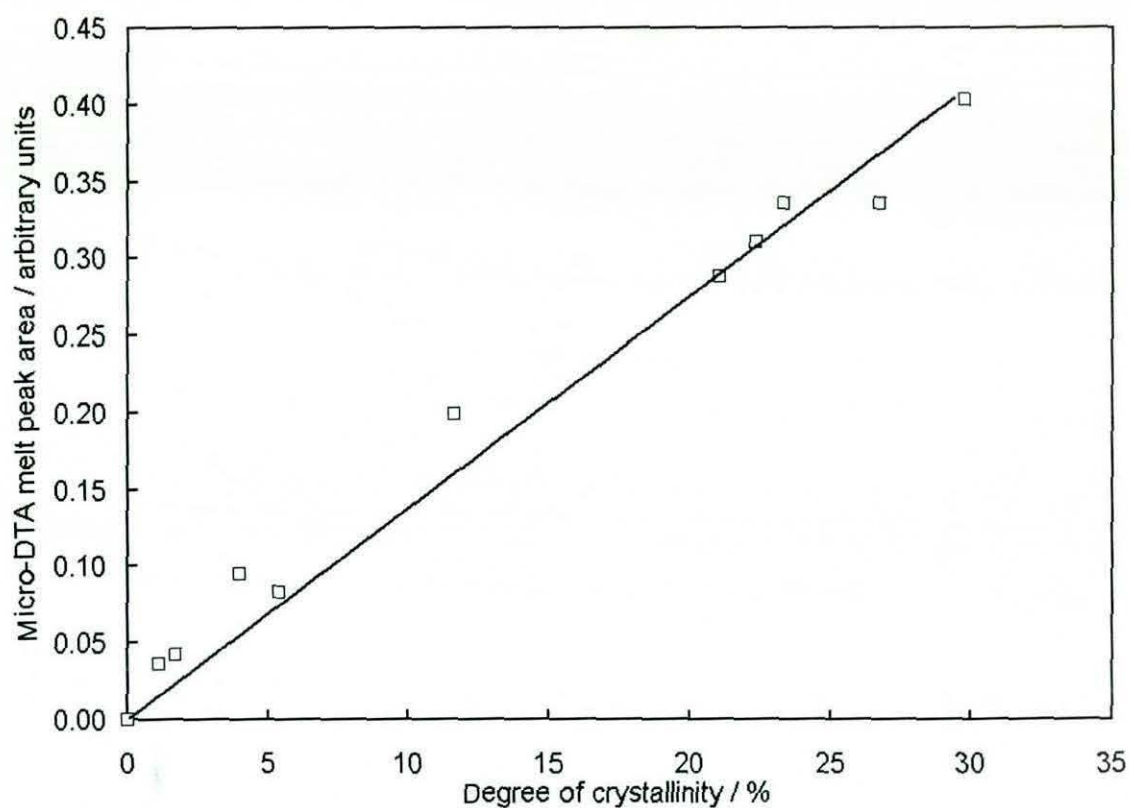
Fig. 2.36. L-TA melting peak areas for annealed PET samples compared with their bulk degree of crystallinity as determined by M-TDSC.

film. These results would seem to confirm that L-TA can readily be used to map relative spatial variations in crystallinity. Moreover, provided a rigorous calibration procedure has been carried out for a particular polymer, it can also be used to indicate absolute values of crystallinity within a reasonable margin of error. It must be noted that, for the reasons cited elsewhere, the area under the peak in the derivative L-TMA signal could have been used to equal effect. This would produce a more accurate measurement of the indentation through the melt than would be possible from the non-derivative curve.

In the absence of a calorimetric measurement sensitive enough to detect variations in crystallinity directly through the heat of melting, we must consider how the L-TMA measurement through the melt appears to be so sensitive to crystallinity. In fact, it is the amount of indentation that occurs between the glass and melting transitions that determines the depth of penetration through the melt and hence the area under the L-DTA melting peak. If the material is largely amorphous at the start of the experiment, then we have seen that considerable indentation occurs above the T_g.

In the case of a non-crystallising polymer, such as PS, the rate and depth of penetration is determined largely by the initial probe force and the how the viscosity of the material changes with temperature. For amorphous PET, the rate of penetration is reduced by crystallisation occurring in the vicinity of the tip. This effectively increases the viscosity of the material and hence the upward force that it can exert on the probe. When the melting temperature is reached, the degree of further penetration is determined by the probe force at the onset of melting. This in turn is controlled by the amount of curvature remaining in the cantilever. If substantial indentation has taken place prior to the melt, the probe force will be low. When a sample having a moderate initial degree of crystallinity is tested, the depth of penetration between T_g and T_m will be reduced by the crystalline material already present as well as by crystallites that form during the experiment. Consequently, when T_m is reached, the probe force will be higher than for the amorphous material and a larger penetration will result. Finally, for a sample that is substantially crystalline and cannot crystallise any further under the conditions of the experiment, no reduction in probe force occurs as a result indentation taking place above the T_g. On the contrary, the force will instead continue to increase due to thermal expansion of the material increasing the bend on the cantilever. This is a consequence of the AFM force-feedback mechanism being disabled during a L-TA run. The effect of thermal expansion is, however, relatively small, in that the upward deflection is typically less than 10% of the total indentation that takes place from the start to the finish of the experiment. The effect of the high probe force when the T_m is

reached is to produce a substantial degree of penetration compared with amorphous or low crystallinity samples.

It may be expected that for highly crystalline samples, L-TA will tend to underestimate or become insensitive to increases in the degree of crystallinity. It can be seen from the L-TMA curves in Fig. 2.34, that no detectable glass transition occurs above an annealing time of 20 minutes. If our hypothesis is correct, then this means that there should be no significant increase in L-DTA melting peak area above a degree of crystallinity of about 20%. The comparison between degree of crystallinity and L-DTA peak area in Fig. 2.36 is inconclusive in this respect. Although the peak area appears to follow the upward trend in crystallinity that occurs between annealing times of 20 and 30 minutes, the increase is small and the L-TMA measurement error may account for the increase in peak area. Perhaps of more significance is the fact that there is no increase in peak area between the measurements made on the samples with annealing times of 30 and 45 minutes. MTDSC, on the other hand, shows an increase in crystallinity of over 3% between the same samples. Finally, for the sample annealed for 60 minutes, the L-TA result does show an increase in melting peak area, although the increase is proportionately less than the measured increase in crystallinity that occurs between annealing times of, say, 30 and 60 minutes. The increase in L-DTA peak area between annealing times of 45 and 60 minutes could be due to experimental error, or it could be a result of a small calorimetric contribution to the measurement. It is clear that further work is required, preferably on a range of semi-crystalline polymers, to gain a full understanding of the relationship between L-TA measurements and crystallinity.

The crucial effect of initial probe force on the subsequent penetration through the melt and the L-DTA melting peak area, means that careful attention must be paid to the T–B signal prior to each measurement. Movements of the cantilever caused by, for example, air currents, can easily cause this to drift by a several percent. It is therefore recommended that the experimenter checks that the total indentation from the start to the finish of a run remains constant between samples with different degrees of crystallinity.

The spatial resolution that can routinely be achieved is somewhat difficult to quantify accurately, due to the effect, discussed above, of the probe retraction step on the crater size. However, with care a probe can be removed from the surface with the tip either at room temperature (provided the probe penetration is kept as low as possible) or just sufficient to melt the polymer. The results of such an experiment are
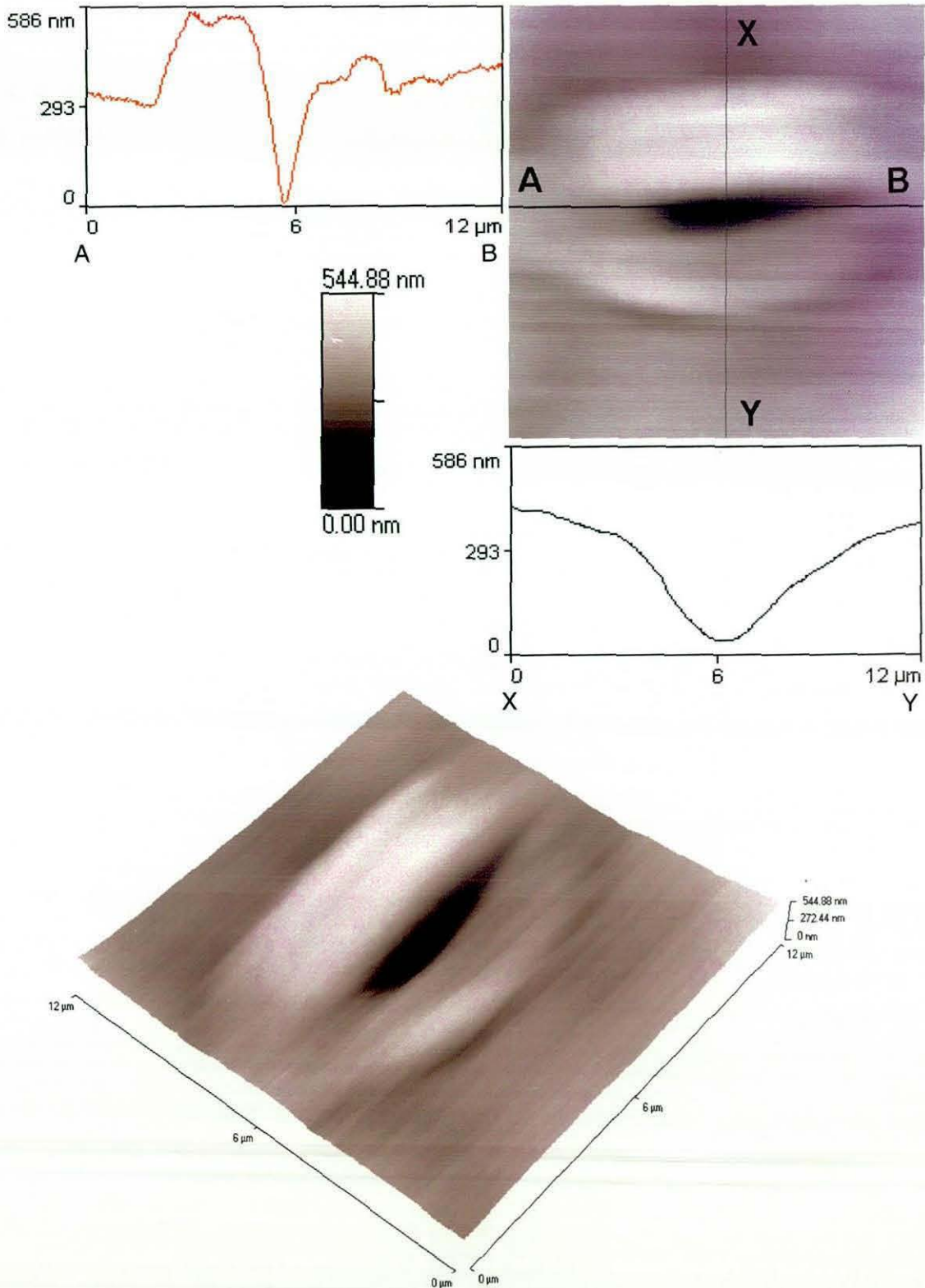
Fig. 2.37. A typical L-TA crater made in semi-crystalline PET at a probe "force" of 0 nA. Disengagement of the probe was achieved in this case with tip at room temperature. This is an example of the smallest sample size that can routinely be achieved using a Wollaston probe.

shown in Fig. 2.37, which contains images and line profiles of the resulting crater. The sample was again the as-supplied PET, the probe "force" was 0 nA and retraction was achieved with the tip at 250°C. It can be seen that, although a raised rim of material is still present, it is much smaller than that obtained at with the probe retracted at 400°C, shown in Fig. 2.25(a) and 2.26(a). It is therefore much easier in this case to make an estimate of the actual size of the hole and therefore the size of the sample. It would appear that, for PET at least, the smallest sample size is of the order of 5 µm × 2 µm × 200 nm. The smallest lateral dimension occurs in the direction perpendicular to the plane of the tip loop (along XY). This is not necessarily the same as the highest spatial resolution achievable, as the heat affected zone will extend beyond this. This means that the nearest adjacent measurement that could safely be made would be of the order of 5 µm in the direction perpendicular to the loop and 10 µm parallel to the loop. On the other hand, if all that is required is an indication of the general spatial variation in surface crystallinity, this could be achieved at a scale in the region of 5 µm × 2 µm.

As discussed above, it is largely the rheological properties of the material between the T_g and T_m, together with probe force, that determine the indentation that occurs through the melt and hence the L-DTA peak area. This means that at low values of probe force, the sensitivity and accuracy of the technique will be compromised. On the other hand, high forces will increase the sample volume and therefore have a deleterious effect on spatial resolution. Further work would be required to investigate further the nature of the trade-off between initial probe force, the reliability of the measurement and spatial resolution.

The Raman carbonyl group absorption bands for the amorphous material and samples annealed for 2.5 and 10 minutes are presented in Fig. 2.38. It can be seen that up to a degree of crystallinity of 7.4% (10 minute anneal), there is no significant change in bandwidth. In fact, the error in the analysis is of the order of the spread of crystallinity in this sample set. It must be concluded, therefore, that at these low levels of crystallinity, micro-Raman spectroscopy does not have the same sensitivity as micro-thermal analysis. It can neither detect differences between crystalline and amorphous material nor differentiate between materials, or regions within the same sample, possessing different degrees of crystallinity. The inability of the technique to distinguish between an amorphous material and one that is over 7% crystalline is surprising. The reported sensitivity of micro-Raman spectroscopy is of the order of 2%. Further work would be required to ascertain the reasons for its failure in this case. One possible reason is that the order present in these low crystallinity samples is an
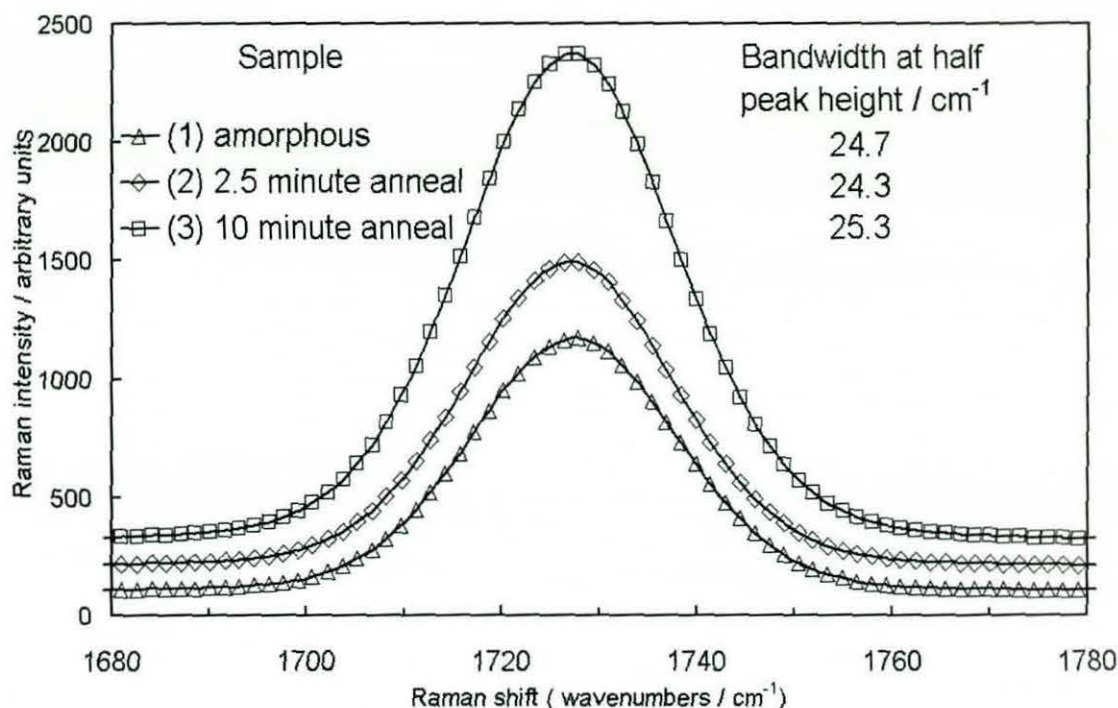
Fig. 2.38. Micro-Raman spectra, showing the carbonyl band, for amorphous PET and samples annealed for 2.5 and 10 minutes.

imperfect precursory state that affects the enthalpy of melting but not the scattering behaviour of the carbonyl group.

2.4 Conclusions

It has been shown that localised thermal analysis can readily and reproducibly detect glass and melting transitions in typical amorphous and semi-crystalline polymers, in this case PET and polystyrene. However, in a sample that cold-crystallises, the effects of the crystallisation cannot be separated from the results of, for example, increasing probe-sample contact area above the T_g. The reproducibility with which glass transition and melting temperatures are measured is well within the ±2°C claimed by the manufacturer. However, this can be achieved only with the aid of careful and frequent calibration of the resistance/temperature characteristic of the probe. The reproducibility of the area under the peak in the L-DTA signal and the rate and magnitude of probe penetration through the melting transition has been shown to be excellent. This can be achieved at a typical heating rate in the range 10-25°Cs^{-1}, which is roughly two orders of magnitude faster than in a conventional bulk DSC experiment.

Probe geometry has been shown to exert a powerful influence over the shape of the melting peak detected in both the derivative power and derivative probe deflection signals. In extreme cases, defects such as bends or twists in the wire forming the sensing tip, can produce artefacts such as double melting peaks. The performance of a probe must therefore be checked regularly by carrying out a run on a polymer whose melting behaviour has already been well characterised and preferably shows a single well defined melting peak when tested on a homogeneous crystalline polymer.

The L-DTA (derivative power) signal appears to be almost entirely dependent on the rate of change of probe-sample contact area. This is best illustrated by co-plotting the derivative power and derivative probe deflection data. If this is done, then the shape of the resulting curves are remarkably similar. This must bring into question the sensitivity of the calorimetric measurement.

The T_g of a material as measured by L-TA increases with increasing heating rate, whilst the crystalline melting temperature is unaffected. If L-TA is carried out at a heating rate comparable with that used in a typical DSC experiment, then similar values for the T_g are obtained.

For a given semi-crystalline polymer, the area under the melting peak in the L-DTA signal and the corresponding probe indentation through the melt are, to a first approximation, linearly dependent on the probe-sample contact force.

When using the instrument with the reference circuit active, for a particular sample probe, careful tuning of the resistance of the reference element is required in order to find the best compromise between sensitivity of the power signal and curvature of the baseline. This typically occurs with the reference resistance set at around 50% higher than that of the probe.

The AC phase lag and amplitude signals have been shown to have a significantly inferior signal-to-noise ratio than the DC power signal, with the amplitude response being a factor of two or three less noisy than the phase lag signal. On the evidence garnered in this study, no information is acquired in the AC signals that is not available in the DC L-DTA measurement. Furthermore, the AC signals are vulnerable to saturation and the appearance of false peaks or artefacts over a wide range of instrument parameters. It is possible to tune the reference resistance and, for example, the internal signal amplification to obtain "live" AC signals over a wide temperature range, but such efforts may be counter-productive, as no advantage over the DC measurement is obtained and the sensitivity of the L-DTA signal may be reduced by optimising the reference resistance for the AC measurements. The succession of

modifications to the operating software have improved the situation, but have not addressed the fundamental problem in the hardware that would appear to be the most likely source of the problems in the AC detection and, perhaps, the less than optimal sensitivity in the general calorimetric response.

L-TA is able to detect low concentrations of crystalline material (of the order of a few percent) and, therefore, similar small spatial variations in the degree of crystallinity present across a surface. Good correlation between the L-DTA melting peak area and the bulk degree of crystallinity, as measured by MTDSC, has been demonstrated. At very low levels of crystallinity, however, the L-DTA measurement may produce a significant overestimate compared with the bulk value. On the other hand, the technique may simply be detecting genuine variation in crystallinity between surface and bulk. Further work would be required to elucidate this. It is probable that the ability to detect variations in crystallinity is a consequence of the attenuation of the effect of the glass transition on the probe indentation with increasing degree of crystallinity. This decrease in the depth to which the probe penetrates between T_g and T_m means that the probe force is reduced to a lesser extent immediately prior to the melt. The resulting higher penetration that occurs through the melting transition produces a commensurate increase in the L-DTA melting peak area.

L-TA has superior sensitivity, for PET at least, than micro-Raman spectroscopy in the detection of low levels of crystallinity. The best spatial resolution is achieved in the direction perpendicular to the plane of the probe (or the normal fast-scan direction) and is the order of 2 μm, although the diameter of the heat affected zone is at least twice this. The minimum sample depth is of the order of 200 nm.

2.5 Recommendations for further study

An important area for further work involves further investigation of the sensitivity of both the AC and DC calorimetric response of the instrument. In MTDSC, a glass transition is detected as a peak in the phase lag signal. However, such a result has never been observed in the equivalent L-TA signal. Furthermore, the calorimetric response through the melting of PET, discussed in this thesis, is clearly dominated by the tip-sample contact area. There is every reason to believe that a significant contribution to the total response arising from the enthalpy of melting. Very recent work [236] has shown exothermic peaks associated with secondary curing in epoxy resins which are not accompanied by a significant change in contact area. There would seem, therefore, that there is every reason to believe that this aspect of the performance of the

instrument can be improved. However, this requires careful investigation of the hardware responsible for the calorimetric performance.

Its less than optimal calorimetric response notwithstanding, the instrument is still perfectly capable of producing very useful data and, in certain applications, data that would be very difficult to obtain by any other means. The study of variations in surface crystallinity is a case in point. Further work in this area would be fruitful. In particular, more time needs to be devoted to understand the reasons why Raman spectroscopy failed to detect any crystallinity in PET samples that DSC had shown to have a bulk degree of crystallinity of several percent. It would also be useful to carry out L-TA work on other semi-crystalline polymers, and to study, for example, variations in crystallinity between the surface and bulk of sectioned thick films.

As has been mentioned, a major problem associated with the Wollaston probe is its relatively poor spatial resolution compared with conventional AFM tips. Whilst the development of smaller thermal probes is in the hands of the specialist manufacturer, it is possible that the performance of the Wollaston probe could be improved. A possible method of achieving this has already been demonstrated and involves producing a sharp asperity at the apex of the tip loop by ion beam machining. The performance of such a probe, in terms of imaging resolution and L-TA requires investigation.

Chapter 3

Micro-thermal analysis of heterogeneous polymer systems using conventional high resolution AFM probes in conjunction with a variable temperature microscope stage

3.1 Introduction

As has been mentioned, the highest lateral spatial (or thermospatial) resolution achievable by Wollaston wire thermal probes used for scanning thermal microscopy (SThM) is in excess of one micrometre. The morphologies of many heterogeneous polymer systems, such as semi-crystalline polymers, blends and copolymers, contain discrete features, domains or phases that are too small to be resolved by this type of probe. Furthermore, even if the domain size in the sample is relatively large, the difference in thermal conductivity between phases is often insufficient to be distinguished in a thermal property image. In the majority of practical applications encountered and reported so far, thermal images have been dominated by the effects of topography. It is often the case, therefore, that little information is revealed in a thermal image that cannot be inferred from the corresponding topographic image. In the characterisation of heterogeneous polymer systems, even nanometre scale resolution elevation maps of the surface topography of a sample rarely reveal the underlying morphology of the material. It can be the case that in the preparation of certain materials by, for example, casting from solution, surface energy, viscosity or other effects do produce consistent and measurable height contrast between phases. However, the phase boundaries in such materials, rather than taking the form of vertical or near-vertical "cliffs" are instead likely to lie within gradually sloping regions from one phase to another. Even in these cases, therefore, height images may not produce an accurate picture of the size and shape of domains.

Images of heterogeneous surfaces constructed from variations in a physical property are much more likely to reveal the true morphology of the material. As was discussed in chapter 1, AFM imaging modes based on mechanical or other property-related measurements are well established. In the absence of a suitable high resolution thermal probe, it was decided to pursue one or more of these methods as a route to achieving micro-thermal analysis in a high spatial resolution. Thermally-based information was to be contributed by imaging at different temperatures. The choice of imaging temperature(s) for a particular sample would be informed either by prior knowledge of the thermal properties of the candidate materials, particularly the glass transition temperature(s), or by carrying out conventional thermal analysis, notably MTDSC.

In the first part of the study a model system, a blend of polystyrene (PS) and poly(methyl methacrylate) (PMMA), is used to explore the concept of using changes in temperature to aid the elucidation of structure when making local property

measurements by IC-AFM. A significant number of polymer systems are stable over a wide range of temperatures and so are amenable to study in this way. One such material is the blend chosen here. It is completely phase-separated and remains so at elevated temperatures. Domain sizes can be of the order of tens of nanometres; well below the resolution of the Wollaston thermal probes currently available commercially. The T_g of both polymers is of the order of 100°C, so it was envisaged that imaging at elevated temperatures would potentially reveal useful information concerning the morphology of the blend. In the process, the relationship between AFM mechanical property measurements and temperature would be explored thoroughly, with the effect of the glass transition being of particular interest.

In the second part of the work, three elastomeric segmented polyurethane (SPU) copolymers are investigated. The morphology of these industrially-important materials has been the subject of investigation in numerous studies.[216-230] These have typically revealed, by small angle X-ray scattering (SAXS) and other methods, a microstructure that is phase-separated into so-called hard- and soft-segment domains or *nanophases*. The term hard segment refers to that section of the SPU molecule that contains the rigid urethane linkages, often separated by a so-called chain extender to increase their size and modify their properties. The soft segment is made up of a much more flexible part of the copolymer chain, often a polyol. The domain size is typically of the order of 5-25 nm, although much larger-scale order has also been revealed. In an IC-AFM (PDM) study of a solution-cast SPU elastomer, McLean and Sauer [161] obtained results showing separate hard- and soft-segment domains. A phase image is shown, revealing a relatively uniform distribution of hard-segment domains 5-10 nm in diameter. Optical microscopy and small angle light scattering (SALS), on the other hand, have identified phase separation on the scale of several micrometres.[222, 227] Characterisation of their morphology through more established microscopy techniques, the most obvious being transmission electron microscopy (TEM), is difficult, because the different domains produce little contrast in electron-density, even after staining.[231] A method of overcoming this problem is through the use of element-specific electron microscopy.[232] This is, however, not universally applicable to phase separated polymers, as it requires that a particular element is present in one phase and not the other(s).

It was known through the work of Sykes [233] that the soft segment of the materials selected for study have a T_g in the region of –30°C to –50°C. It was thought, therefore, that imaging at both ambient temperature and below this T_g would potentially reveal

useful morphological information. It would also thoroughly test the low-temperature capabilities of the variable temperature microscope stage developed for the instrument.

The principal AFM technique chosen for the work was pulsed force mode (PFM-AFM). There were a number of reasons for this. Initial studies had indicated that the use of phase detection microscopy (PDM) would be problematic at elevated temperatures, at least with the set-up used here. Furthermore, PFM-AFM is a relatively recent development and it was intended that the study make a significant contribution in evaluating its potential benefits in the characterisation of heterogeneous polymers. In PFM-AFM, the frequency of oscillation of the cantilever is held constant, irrespective of the temperature. In PDM, the driving frequency requires tuning for each different imaging temperature, as the stiffness and hence resonance frequency of the cantilever changes. Although this is not an insurmountable problem in itself, it nevertheless introduces another variable into the experiment. Moreover, the time taken to initiate imaging at low temperatures was of particular concern, because the liquid nitrogen flask in the temperature stage could not be replenished with the microscope *in-situ*. This gave a limited time in which to carry out an experiment, so any time saved during set-up was valuable. It was expected that in avoiding a re-tuning step, PFM-AFM would give more time in which to acquire an image at low temperature. It was also thought that the PFM-AFM micro-mechanical property measurements would be particularly sensitive to thermally-induced transitions in the sample. Another factor was that it was expected that the images produced would be easier to interpret than, for example, IC-AFM phase images, as the nature of the image contrast generated is somewhat complex (as discussed in chapter 1). The accuracy of these assumptions was to be investigated by carrying out a direct comparison of the two techniques on the same sample over the same temperature range.

In an additional part of the study, it was hoped to use a micro-machined bowtie thermal probe in pulsed force mode. As was discussed in chapter 1, the use of a *heated probe has potential advantages compared with the strategy of changing the temperature of the whole sample. If it proved possible to control the temperature of the probe and operate it in PFM, it was intended to use the model PS-PMMA blend as a means of comparing the utility of the two approaches.*

The principal aims were therefore as follows.

1) To determine the feasibility and the effects of carrying out pulsed force mode AFM at temperatures substantially above and below room temperature.

2) To investigate the effects of temperature and in particular the glass transition on PFM-AFM results for a model system and whether the behaviour could be used to elucidate structure and identify phases.

3) To investigate the ability of variable-temperature PFM-AFM to characterise phase-separated segmented polyurethane elastomers.

4) To compare the information produced by PFM-AFM on the morphology of SPUs with that published in the literature for similar materials obtained by other modes of AFM or unrelated techniques, such as SAXS.

5) To carry out a direct comparison of variable temperature PFM-AFM and resonance IC-AFM modes

6) To investigate the possibility of using a bowtie thermal probe to carry out highly localised variable-temperature PFM-AFM.

3.2 Experimental

3.2.1 Variable temperature stage

Photographs of the TAI temperature stage both on its own and with the microscope in place are shown in Fig 3.1. In order to carry out sub-ambient temperature imaging, the integral Dewar flask is filled with liquid nitrogen. A thermoplastic shield is fitted to the underside of the microscope so that, once the microscope is on the stage, the scanner head and cantilever are effectively isolated from the surrounding atmosphere. Nitrogen boiling off from the Dewar flask through vents around the sample stage effectively purges this sealed environment, maintaining a dry atmosphere at the sample surface and thus preventing icing. For high temperature work, the shield must be removed. For all the experiments, the stage was positioned on an anti-vibration air table.

The temperature of the stage was regulated by the Linkam TP 93 temperature controller, which maintained the stub temperature to within ±1°C. As has been mentioned, at the time of writing, for imaging purposes at least, the effective operating temperature range of the stage was approximately –70-250°C. At temperatures lower than this, there was generally insufficient time after the sample temperature had stabilised, to obtain images with reasonable resolution (i.e. one having a minimum of 300 × 300 pixels), before temperature control was lost and the flask required replenishment. It is envisaged that a semi-automatic filling system will solve this problem in the near future.

130

180

To stage
temperature
controller

z translator

Coolant
reservoir

x-y
translators

Sample
stub

x-y clamp

Nitrogen
gas vent

z clamp

144 mm

Liquid
nitrogen
filler hole

Space
envelope of
nitrogen gas
shield
(25 mm dia.)
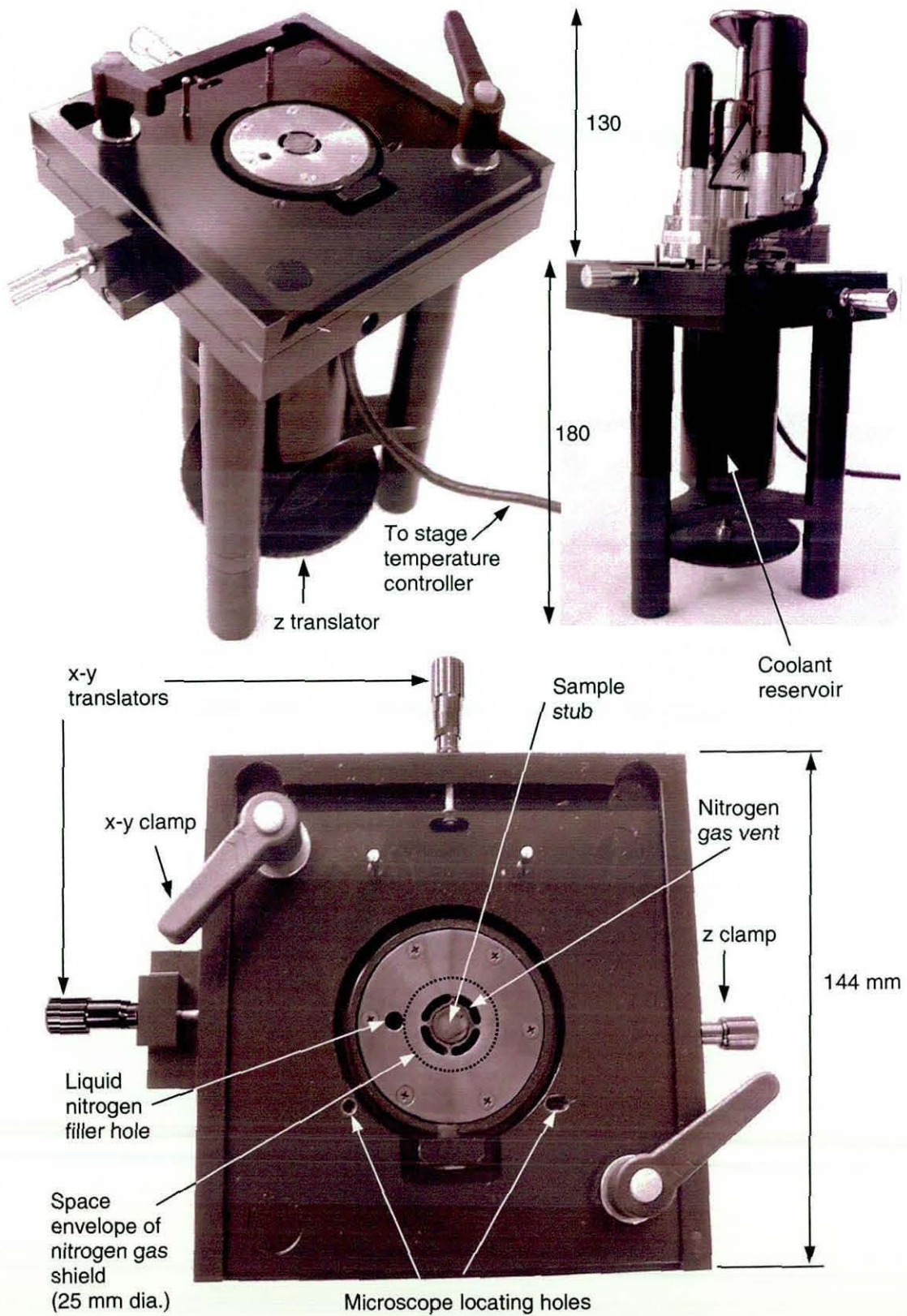
Microscope locating holes

Fig. 3.1. Various views of the TA Instruments / Linkam variable-temperature microscope
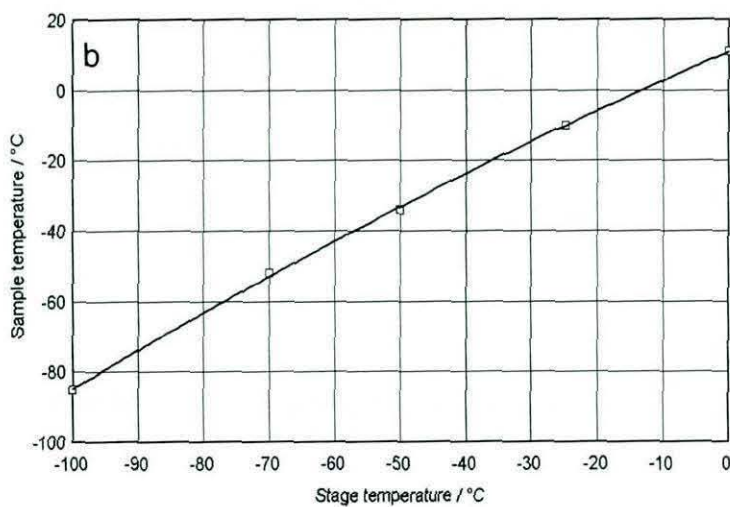stage.

At elevated temperatures, the temperature of the surface of a sample is inevitably somewhat lower than that of the stage below it. Conversely, with the stage held at sub-ambient temperatures, the temperature of the surface of the sample is somewhat higher than the temperature of the stage. Therefore, if a direct comparison is required between the results of experiments conducted on different samples, the temperature of the sample needs to be measured at each stage temperature. This was achieved using a calibrated (see chapter 2) Wollaston thermal probe. The probe was brought into contact with the sample and the temperature at which the onset of thermal feedback occurred was recorded. A calibration curve of stage versus sample temperature was then constructed — see Tables 3.1 and 3.2. In order to produce an accurate calibration the probe must itself be calibrated using the temperature stage and not by melting standard samples. As discussed in chapter 2, the two approaches produce substantially different results. Calibration of the probe was carried out with the tip just out of contact with the copper sample stub. A difficulty arises for work at high temperatures, in that a standard Wollaston probe begins to lose structural integrity above150°C or so (200°C is possible for a very short time and with care). This means that the temperature-versus-resistance calibration curve must be extrapolated to temperatures above this. The errors involved in this extrapolation are likely to be small and consistent between samples, so the important conclusions that can be drawn from the work are unaffected. The high and sub-ambient temperature sample calibration curves are shown in Figs. 3.2(a) and (b), respectively. The calibration curve of the thermal probe used is shown in Fig. 3.2(c).

In the study of the SPU materials, imaging at a stage temperature of –50°C or lower was often required. Once the stage temperature was set there was a substantial delay before imaging could begin. With the 100 µm × 100 µm × 10 µm tripod scanner used for most of the experiments, this was approximately 5-10 minutes. The temperature of the stage first had to stabilise after ballistic cooling and then gross spatial drift of the sample had to cease. Furthermore, vibration in the sample (indicated by noise in the AFM internal sensor signal) generated by the boiling nitrogen coolant had to decrease to an acceptable level. However, to save time, an initial targeting scan could usually be carried during this stabilisation period. With the high resolution 2 µm × 2 µm × 0.8 µm tube scanner installed, the delay could be substantially longer, as it is much more sensitive to drift and transmitted noise. However, over small sample areas the scanning frequency could be increased considerably, producing a substantial reduction in acquisition time. A further complication was caused by the fact that,
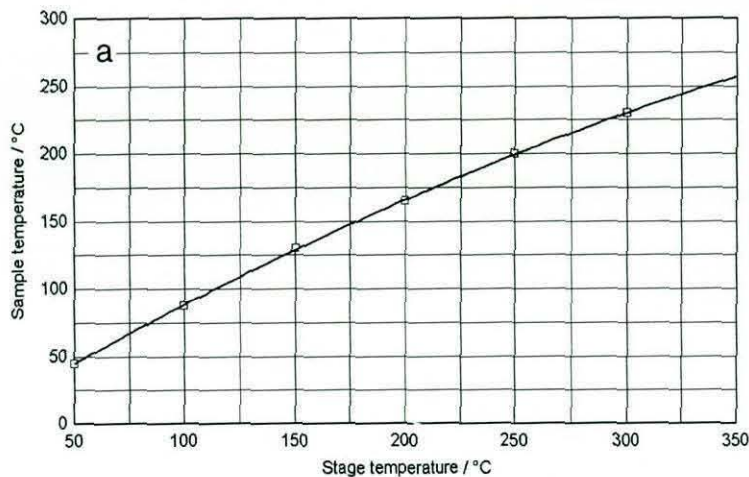
Stage temperature / °C	Sample temperature / °C (PS-PMMA)
50	45
100	88
150	130
200	165
250	200
300	230

Table 3.1. Sample temperature versus stage temperature calibration – hot stage.

Stage temperature / °C	Sample temperature / °C (polyurethane)
-100	-85
-70	-47
-50	-34
-25	-10
0	11

Table 3.2. Sample temperature versus stage temperature calibration – cold stage.
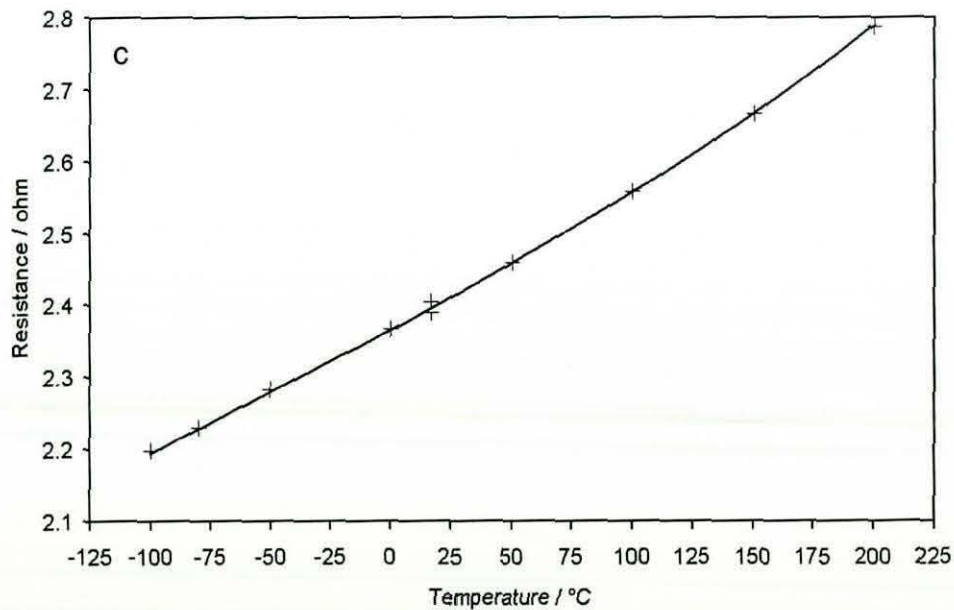
Fig. 3.2. Temperature calibration curves. Plots of sample surface temperature (as measured by a Wollaston thermal probe) versus the stage temperature at (a) elevated temperature and (b) sub-ambient temperature. (c) The resistance versus stage temperature calibration curve for the Wollaston probe.

between room temperature and −50°C, the sample could easily drift beyond the maximum lateral range of this scanner. This made it extremely difficult to obtain very high magnification images of precisely the same areas at the different temperatures.

3.2.2 Pulsed force mode AFM

A *Witec pulsed force module* was used, (Wissenschaftliche Instrumente und Technologie GmbH, Albert-Einstein-Allee 15, D-89081 Ulm, Germany) *coupled to the* TA Instruments (TAI) 2990 Micro-Thermal Analyzer. A Tektronix TDS 210 digital oscilloscope was used to monitor the *modulated force versus time signal* and to set the measurement points.

TM Microscopes silicon probes were used throughout. Initially, these were FIS silicon probes, having a resonant frequency of 23-38 kHz, a nominal force constant of 0.2 Nm^{-1} and a tip radius of approximately 10 nm. These were later discontinued and replaced by model 1950-00 probes, which have very similar characteristics. Both these probes feature a single "diving board" cantilever. Unless stated otherwise, the instrument parameters were set as follows: a modulation frequency of 500 Hz; an amplitude at 5% of maximum; an indentation "force" signal (set point) of 5 nA; a scan frequency of 0.5-1.0 Hz.

The PS, PMMA and blend samples were all relatively smooth. Suitable areas for imaging were selected using the optical microscope and television camera, which are integral parts of the microscope. Imaging was carried out at 20°C intervals, from room temperature up to a stage temperature in excess of 300°C. At high temperatures, condensation was sometimes observed on the cantilever. No detrimental effect on the measurements was encountered, beyond the need to reposition the laser from time to time to recover a signal from the photodetector. However, in order to be able to make absolute comparisons between results, it is important that the total photodetector signal remains approximately constant throughout a series of experiments.

The SPU samples were rougher, requiring an initial 50 μm × 50 μm scan to identify areas smooth enough for analysis. Once this was achieved, a higher resolution (300 or 400 line) 10 μm × 10 μm scan was carried out. This, in turn, was used to select increasingly smaller and smoother areas down to a minimum of 1 μm × 1 μm. The original area was then scanned again to check for physical damage to the surface caused by the tip. In cases where comparisons of the same area at different temperatures were required, the sub-ambient temperature scan was carried out first. Care was taken to incorporate a distinctive landmark in the image, so as to enable the

same area be located after heating back to room temperature and the inevitable movement of the sample that subsequently took place relative to the scanner. Such direct comparisons enable the effects of topography on other images to be evaluated.

3.2.3 Intermittent contact AFM (phase detection microscopy)

With the exception of the probes and the Witec control unit, the same equipment was used for IC-AFM phase and amplitude imaging as for PFM-AFM (it was found that the relatively large and soft cantilevers used for PFM-AFM produced unsatisfactory results when used for PDM). The type of probe used, unless stated otherwise, was the TM Microscopes 1660-00 silicon low resonance frequency (LRF) probe. This has a resonance frequency in the range 160-220 kHz and a nominal force constant of 48 Nm^{-1}. Occasionally, a high resonance frequency (HRF) probe was required (for samples with high adhesion, for example). This has a frequency range of 240-420 kHz and a nominal force constant of 42 Nm^{-1}. The LRF type was preferred, because of the higher sensitivity afforded by its softer cantilever.

Imaging was generally carried out with the driving frequency set a few percent lower than the frequency of the maximum of the resonance peak, so that it lay on the shoulder of the peak. Amplitude attenuation was generally 40-55% of the free amplitude. Line scans were used to optimise this and other instrument parameters, such as the driving amplitude, scan speed and the feedback loop P.I.D. values (potential; integral; derivative). Re-tuning of the driving frequency was performed at each imaging temperature, with the cantilever as close as possible to the sample surface, but out of range of attractive forces. It was ensured that the selected frequency was at the same position relative to the resonance peak at each temperature.

3.2.4 Modulated temperature differential scanning calorimetry (MTDSC).

MTDSC was carried out on the SPU samples using a TAI 2920 instrument. Each material was heated from $-70°C$-$200°C$ at a rate of 3°C/minute. The modulation applied was $\pm0.5°C$ with a period of 40 seconds. A two-point temperature calibration of the cell was carried out using the onset of melting of indium and room temperature as references.

3.2.5 Materials.

PS-PMMA system. Polystyrene and poly(methyl methacrylate) were obtained from the Aldrich Chemical Company Ltd. Their weight average molecular weight (M_w), and polydispersity index (M_w/M_n) were determined by gel permeation chromatography (GPC) to be as follows. PS: $M_w = 2.40 \times 10^5$ g mol^{-1}, $M_w/M_n = 4.9$; PMMA: $M_w = 1.03 \times 10^5$ g mol^{-1}, $M_w/M_n = 2.5$. A 50/50, by weight, blend of PS and PMMA was spun-cast from solution in chloroform onto a glass cover slip. Thin films of the individual polymers were prepared in the same way. The samples were conditioned in a vacuum oven at 40°C for one week to remove residual solvent.

Segmented polyurethanes. Sykes [233] covers the syntheses of the materials in detail. 4,4′-methylenebis(phenyl isocyanate) (MDI) of 98% purity was obtained from the Aldrich Chemical Company Ltd. Poly(tetramethylene oxide) glycol (PTMG, Terathane® 1000) with an average molecular weight of approximately 1000 was supplied by Du Pont Chemicals. Three different chain extenders were used: (1) 1,3-dihydroxybenzene (98% purity); (2) 1,4-butanediol (99% pure, as confirmed by ^{1}H NMR spectroscopy) and (3) cis-but-2-ene-1,4-diol (95% purity). These were all supplied by the Aldrich Chemical Company Ltd. The material chain-extended with 1,4-butanediol was prepared by a two-shot process, the other two via a one-shot route. The cure temperature was 80°C in each case. The materials were cast in an open mould to form a sheet approximately 3mm thick. The materials are translucent, strong, high modulus elastomers. Material 1 was somewhat more opaque than the other two materials. The free surface, which was relatively smooth and glossy to the naked eye, was used for imaging. This could readily be distinguished from the other surface by the absence of mould lines.

3.3 Results and discussion

3.3.1 PS-PMMA system.

In these experiments, the amplitude and frequency of modulation of the cantilever remained constant at 5% of maximum and 500 Hz respectively. It is not necessarily the case, however, that these were the optimum imaging conditions for each temperature. At low temperatures, for example, when a material is generally harder and less adhesive, it is often possible to use a significantly lower amplitude. This generally increases the sensitivity of the technique. In this case, however, it was vital that the imaging conditions remained constant so that direct comparisons could be carried out

between results at each temperature. It is therefore prudent to carry some preliminary imaging at, say, the two extremes of the temperature range being considered. This is to ascertain the values of operating parameter that will be suitable throughout the temperature range. As can be seen from the results, it was also the case here that, at high temperature, the adhesion signal became saturated. It was therefore necessary to reduce the total signal by moving the laser spot slightly to one side of the cantilever to ensure that the measurement remained responsive to changes in adhesion over the whole temperature range. This inevitably reduced the sensitivity of the pull-off force measurement at moderate temperatures.

A collection of 300 line 10 μm × 10 μm images obtained from PFM-AFM pull-off force measurements of the same region of the PS-PMMA blend obtained with the sample at various temperatures between 25°C and 250°C is shown in Fig. 3.3. The pull-off force range detected in each scan is shown by the shaded scale bar inset into each image. In these experiments, the pull-off force signal is not calibrated to give a reading in absolute units of force; it remains expressed in volts. Each image has been treated to maximise the grey-scale contrast and hence the amount of detail available at each temperature. An alternative strategy would have been to shade each image over the maximum pull-off force range encountered in this set of experiments (1.8-10.0 V). This would have drastically reduced the detail in the images, apart from those from the scans that produced the highest measurement range.

At room temperature there is little indication of the morphology of the blend and the pull-off force range is narrow (1.8-2.1 V). At 90°C, the pull-off force range has increased slightly to 0.6 V and shifted substantially (3.5-4.1 V). There is now a faint indication of the phase-separated microstructure. Roughly circular occluded domains, ranging from approximately 0.2-0.5 μm in diameter, are revealed by being slightly brighter (of higher pull-off force) than the surrounding continuous phase. At 100°C (the approximate T_g of both polymers), the measurement range has increased to 1 V. This is made up of an increase of 0.3 V in the maximum adhesion and a reduction of 0.2 V in the minimum value. This trend continues to 125°C, by which temperature the signal range is 1.5 V and the microstructure is revealed clearly. Between 125 and 135°C there is a large increase in the maximum adhesion to 7.1 V, but the minimum remains approximately constant, producing a signal range of approximately 4 V. By 160°C, both the maximum and minimum values have increased substantially and the measurement range is now 4.7 V. The occluded domains now appear to be substantially smaller than before and the interfacial regions are somewhat blurred. At 180°C, the maximum pull-
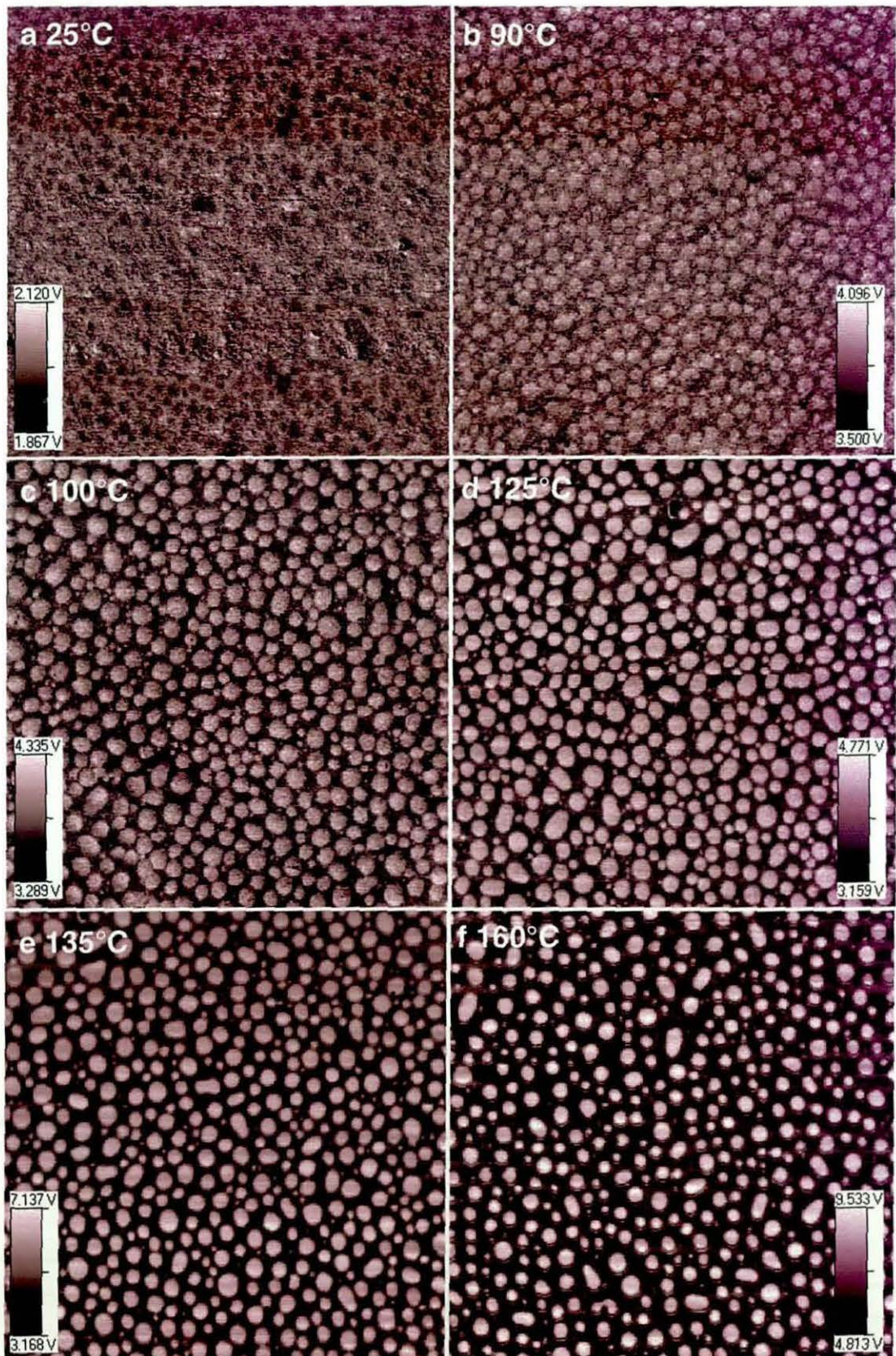
Fig. 3.3. 10 μm × 10 μm PFM-AFM pull-off force (adhesion) images, with scale bars, of a PS-PMMA blend acquired at various sample temperatures. Brighter means higher pull-off force.
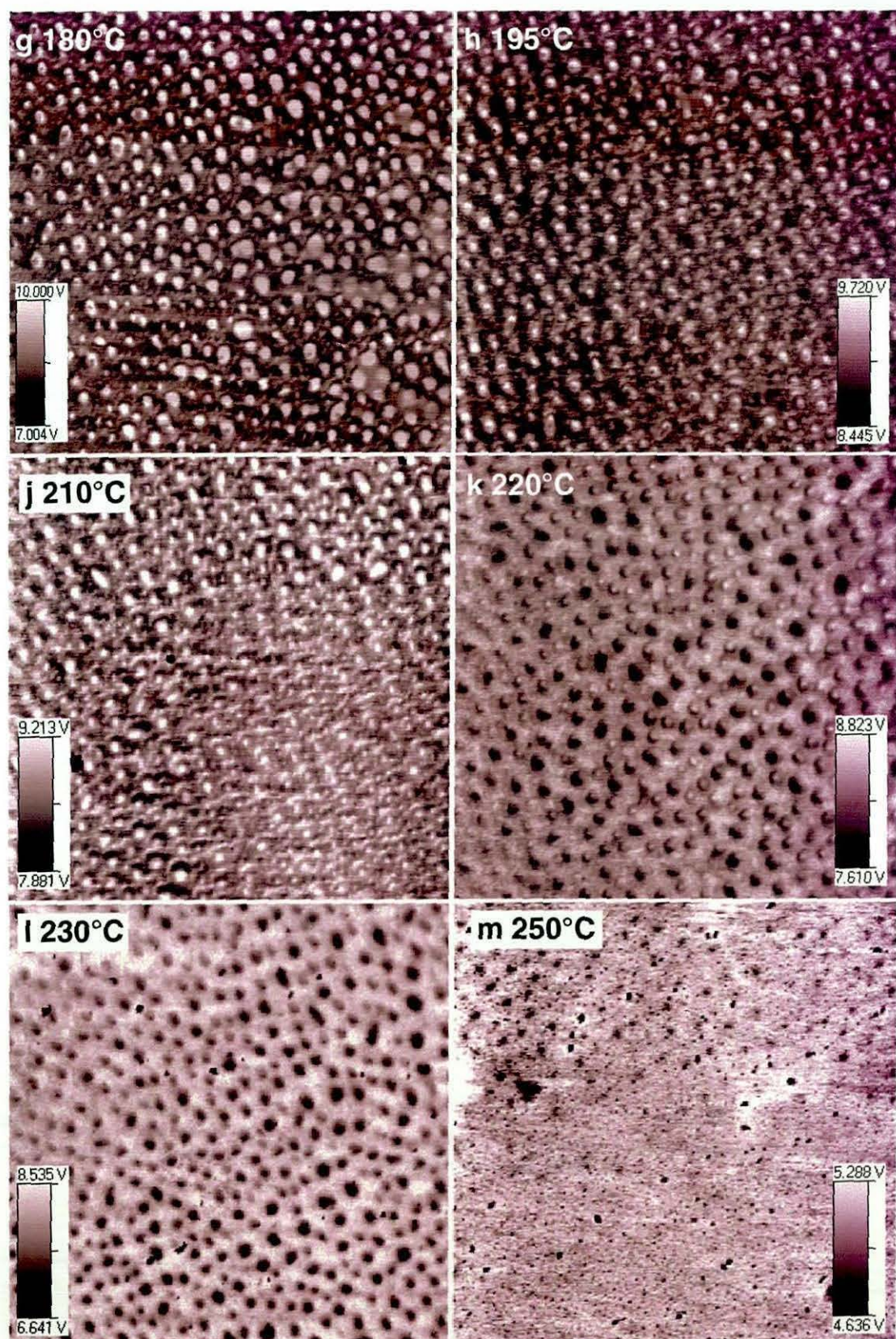
Fig. 3.3 (cont'd). 10 μm × 10 μm PFM-AFM pull-off force (adhesion) images of a PS-PMMA blend acquired at various sample temperatures. Brighter means higher pull-off force.

off-force signal saturates at a value of 10.0 V and the minimum increases to 7.0 V. The morphology now appears somewhat distorted. By 195°C the maximum signal has decreased to 9.7 V, whereas the minimum has continued to increase to 8.5 V. The phase contrast has now all but disappeared, but the occluded phases are still just about discernible as being of higher adhesion than the surrounding material. The same is true of the 210°C image, though both the maximum and minimum signal have begun to fall. Between 210°C and 220°C, *contrast reversal* occurs and the occluded phase becomes the less adhesive of the two. The effect is even more marked at 230°C. Indeed, between 210 and 230°C, the maximum adhesion signal associated with the occluded phase diminishes from 9.2 to 6.6 V. Finally, by 250°C, the adhesion of the whole surface decreases dramatically and the phase-separated morphology becomes completely invisible. At these elevated temperatures, both polymers are in a liquid state.

The variation in the adhesion behaviour of the blend with temperature revealed by these results is somewhat complex. However, between room temperature and approximately 160°C, it is clear that it is only the occluded phase that undergoes a significant increase in adhesion. In principle, therefore, characterising the responses of the individual polymers over this temperature range gives us a way of identifying the different phases.

The corresponding indentation or stiffness images acquired at four selected temperatures are shown in Fig. 3.4. Unlike in the equivalent pull-off image [Fig. 3.3(a)], at 100°C the morphology of the blend is not revealed at all. At 135°C, however, the occluded phase is revealed as darker (lower stiffness or higher compliance) features. The result is not simply a mirror image of the corresponding adhesion result [Fig. 3.3(e)], as the domains appear to be significantly smaller and the phase boundaries are much less well defined. This is probably a consequence of the much poorer signal-to-noise ratio generally obtained in the indentation signal throughout this study. This is evident in the total signal range of less than 0.3 V in a possible full scale range of 10 V. Indeed, the judicious use of noise filtering was required to produce all the indentation images shown. At 160°C, the occluded phases appear to be smaller still, reflecting the trend in the corresponding adhesion images. By 220°C contrast reversal has occurred, with the occluded phase now detected as being less compliant than the continuous phase. Again, this reflects the behaviour of the equivalent adhesion measurement [shown in Fig. 3.3(k)], although this may be a rare case in which the indentation image
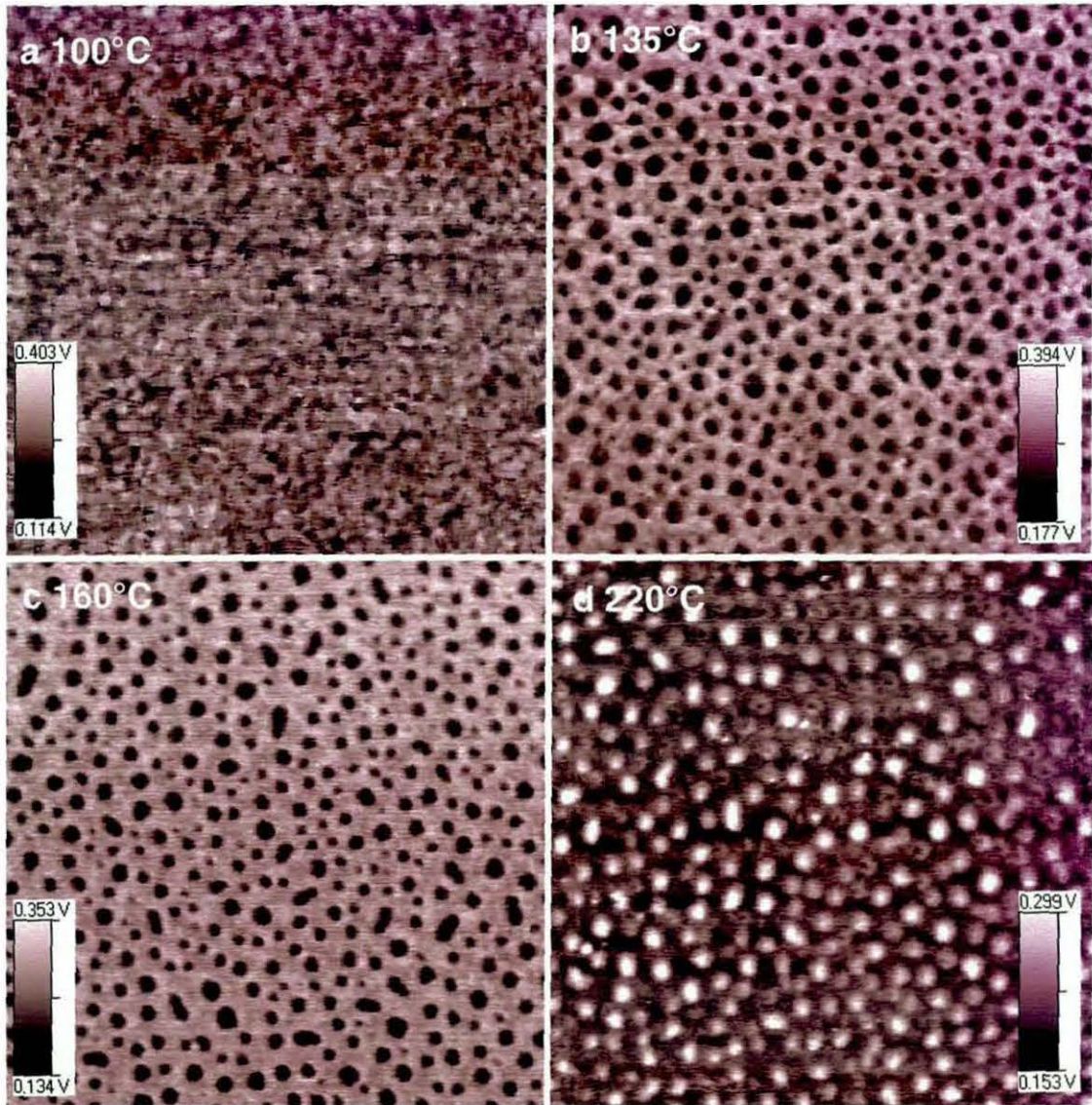
Fig. 3.4. PS-PMMA blend. PFM-AFM 10 μm × 10 μm indentation (stiffness) images at selected temperatures. Brighter means lower compliance. All these results are from the same scans that produced the pull-off force images at the corresponding temperatures in Fig. 3.3.

reveals the size and distribution of phases with greater sensitivity than the corresponding pull-off force measurement.

Topographic images from the scans carried out at room temperature, 100, 135 and 220°C are shown in Fig. 3.5, together with height profiles selected from all but the 100°C image. At 100°C and below, the occluded phase is higher than the surrounding continuous phase. The room temperature line profile shows the discontinuous domains to be a few nm higher than the surrounding material. The images acquired at 135 and 220°C, however, show that the occluded phase has become the lower of the two phases. The line profiles reveal that, at 135°C, its surface is typically a few nm below
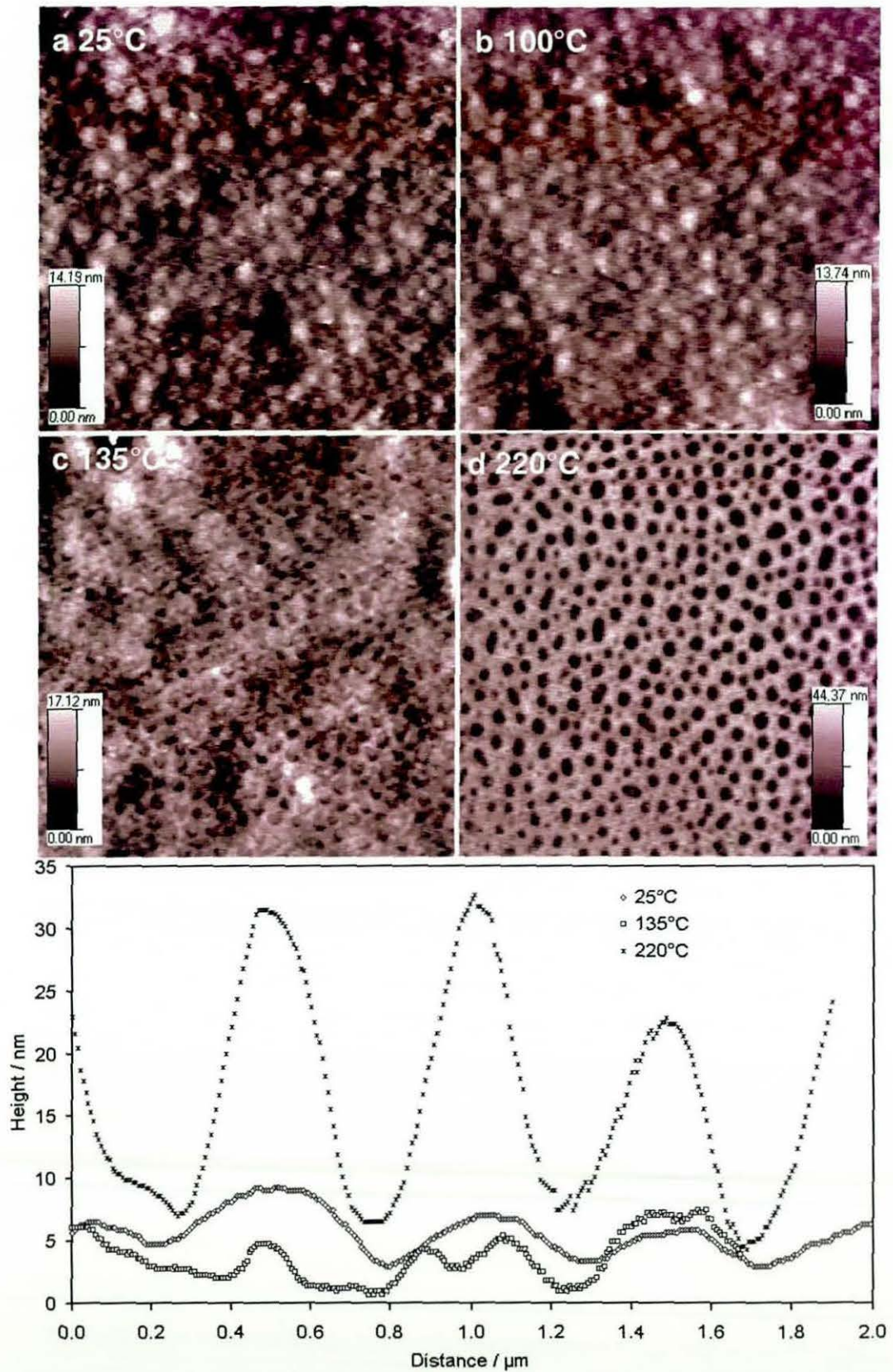
Fig. 3.5. PS-PMMA blend. PFM-AFM 10 μm × 10 μm topographic images at selected temperatures. All these results are from the same scans that produced the pull-off force images at the corresponding temperatures in Fig. 3.3. Also shown are height profiles along 2 μm lines selected from the images acquired at 25°C, 135°C and 220°C.

that of the continuous phase. By 220°C, the height difference has grown to over 20 nm. One possible cause of this behaviour is that relative changes to the viscosity of the materials cause the occluded phase to flow and thus reduce in height. However, it is difficult to see how this could account for the fact that it ends up at a lower level than that of the continuous material. A much more likely mechanism is that, as the occluded phase softens relative to the surrounding material, it is pushed into the surface by the action of the tip. If we assume that the level of the continuous phase remains approximately constant with temperature, at 220°C, the occluded material must be being pushed into the surface by over 30 nm compared with its position at room temperature.

The fact that the morphology of the blend can be discerned in the pull-off force measurement before significant changes occur in the corresponding topographic images indicates that the measurement it is not merely an artefact of topography. The same cannot be said of the indentation measurement, at least at moderate temperatures. It is not until the surface softens to an extent that significant deformation can occur (in this case, at a temperature in the region of 135°C) that the heterogeneous morphology is detected in this signal. At 220°C, however, although the topographic image still shows that the occluded domains are substantially lower than the continuous phase, the indentation measurement now indicates that it is less compliant or, more accurately, has higher viscosity. This result is difficult to explain; it could be that some or all of the deformation induced by previous scans of the same area at lower temperature was still present at the surface. A much more likely explanation is that, the probe is now penetrating through the film to the glass substrate.

That the pull-off force measurement is independent of probe-induced changes in topography can be confirmed by imaging at a nominal indentation "force" of 0 nA. Results from such a scan made at 160°C are shown in Fig. 3.6. The nature of the heterogeneous microstructure is still clearly visible in the pull-off force image, but no longer in the indentation image. The occluded phase has a maximum pull-off force value of over 8 V, whereas that of the continuous phase is of the order of 2 V. The topographic image and selected line profile reveal that regions corresponding to the high-adhesion domains are substantially higher than the surrounding material. This confirms that, unlike at a probe force of 5 nA, no significant deformation of the material was occurring at this temperature. It will be observed that the range of the pull-off force values is significantly different to that obtained at 160°C at 5 nA. This is because the total photodetector signal did not require reducing in order to take account of the higher

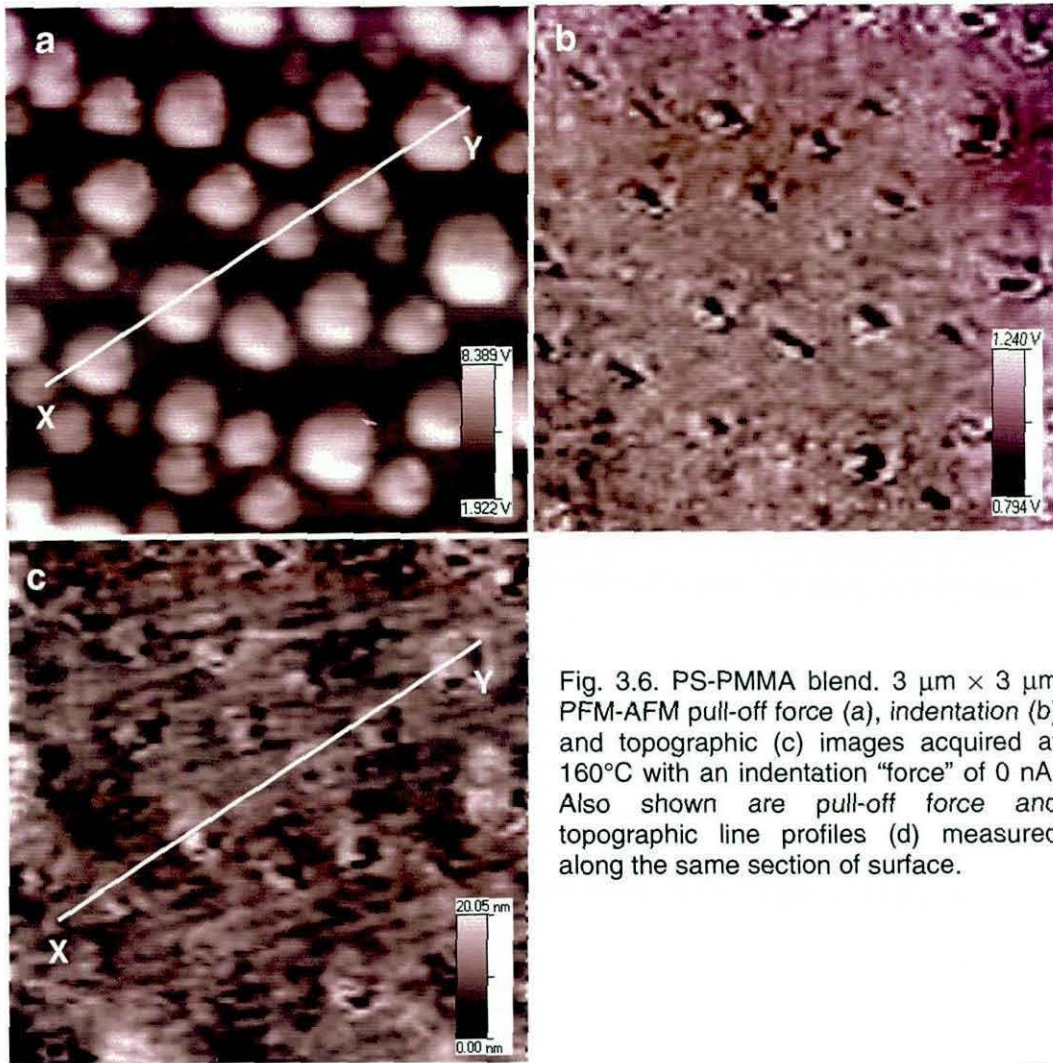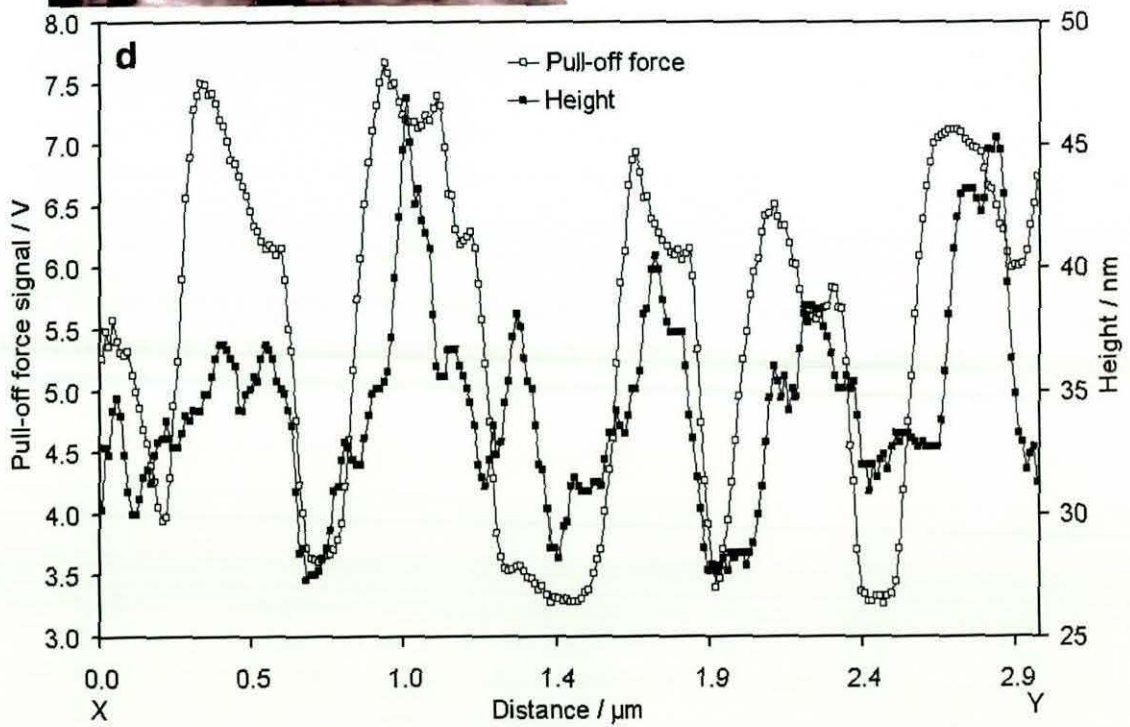Fig. 3.6. PS-PMMA blend. 3 μm × 3 μm *PFM-AFM pull-off force* (a), *indentation* (b) and topographic (c) images acquired at 160°C with an indentation "force" of 0 nA. Also shown are *pull-off force* and topographic line profiles (d) measured along the same section of surface.

adhesion encountered above 160°C. Another contributing factor was that a different probe was used in this experiment which would inevitably have had somewhat different characteristics from those of the first probe. Factors that affect the relationship between voltage and force include the spring constant of the cantilever, the radius and shape of the tip (which has a profound effect on contact area), the cleanliness of the tip, the reflectivity of the top of the cantilever and alignment of the laser. Any of these factors could, therefore, explain the change in the range of observed pull-off force measurements. Calibrating these measurements and allowing for changes in tips due to damage or wear is a problem yet to be solved. In comparing results from different probes, we must assume that comparisons of absolute values between different series of experiments are unreliable and we must rely instead on the *trends* in behaviour as a function of temperature.

A series of 3-d pull-off force images for polystyrene on glass, conducted between room temperature and 180°C is shown in Fig. 3.7. These were acquired by imaging an isolated particle on the glass slide. It is apparent that a substantial increase in adhesion occurs over this temperature range. By 160°C, there has been an approximately four-fold increase in pull-off force, compared with the signal at 25°C. The equivalent results for PMMA on glass, shown in Fig. 3.8, reveal no corresponding increase in adhesion over the same temperature range. It is not until a temperature of 180°C is reached that the pull-off force of the PMMA becomes higher than that of the glass. It then increases steadily until the signal saturates at 230°C. It will be noted that between 90 and 180°C, the highest adhesion is obtained in the region of the edge of the PMMA particle (indicated by the bright "spikes"). This is almost certainly due to an increase in contact area and hence frictional forces as the tip moved up the slope. The striking disparity between the behaviour of PS and PMMA allows the conclusion to be drawn that *the occluded phase in the blend must be polystyrene.*

In the approach that is illustrated by these results, we rely on the influence of the temperature dominating other possible influences, such as sample and tip topography. In this way, informed by the knowledge of how individual components behave with temperature, it is possible to identify phases even though other factors may influence the results and complicate the interpretation of images.

The reasons why the temperature dependence of the responses of the individual polymers differs so widely are unclear. The nature of the interactions between a polymer surface and probe tip at the nanometre scale is not yet well understood. Work has been done on lower molecular weight organic materials showing good correlation

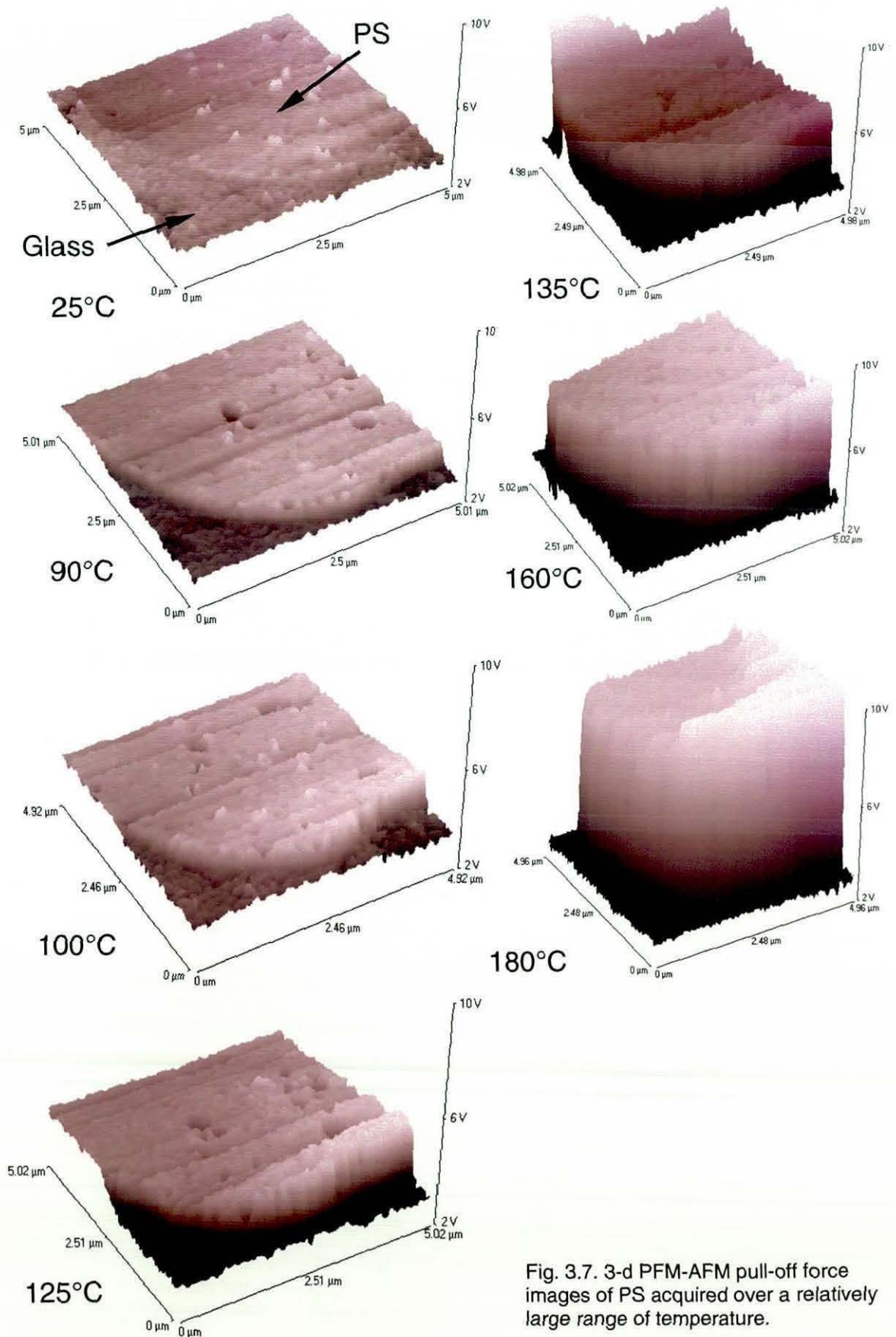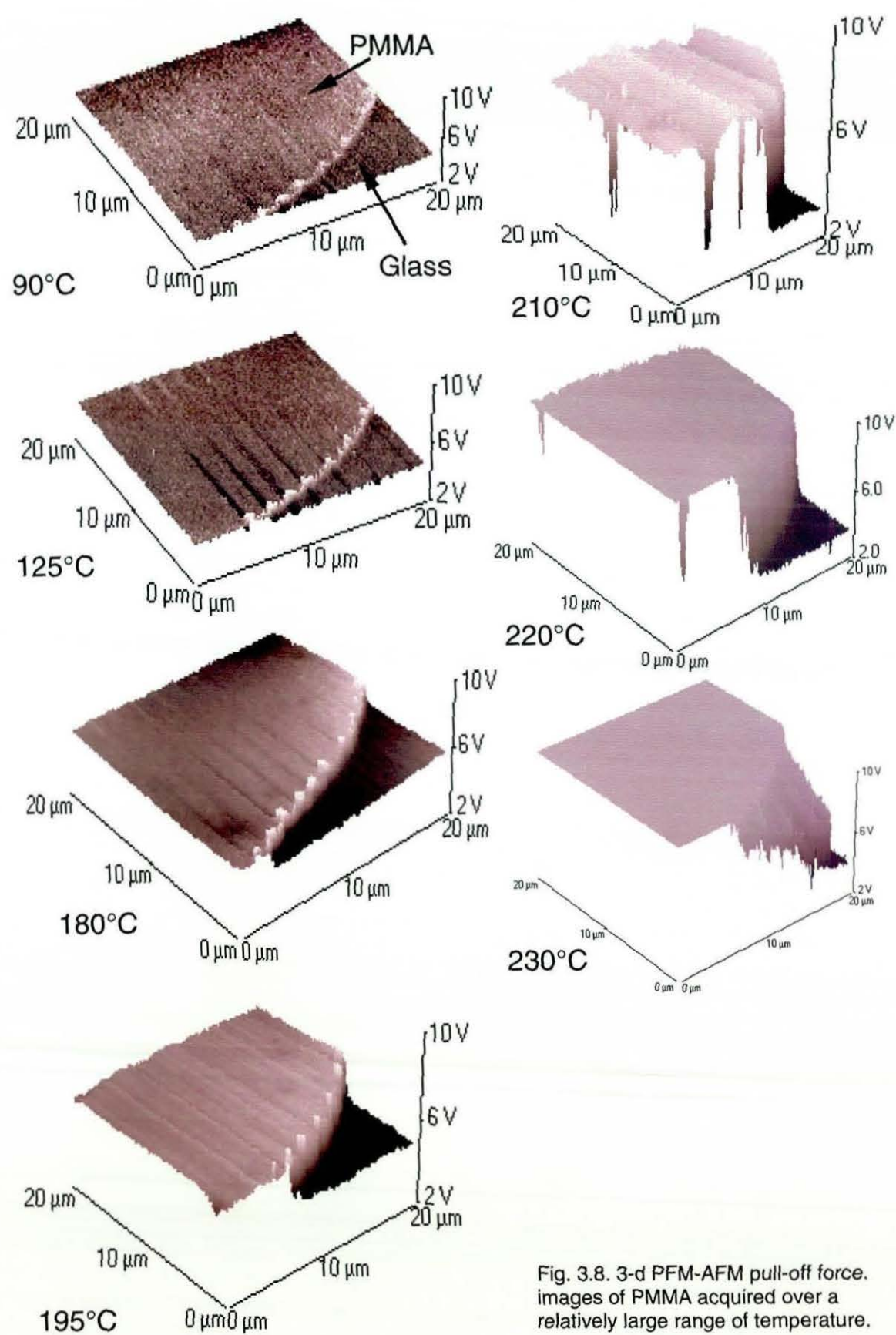Fig. 3.7. 3-d PFM-AFM pull-off force images of PS acquired over a relatively *large range* of temperature.

90°C

125°C

180°C

195°C

210°C

220°C

230°C

Fig. 3.8. 3-d PFM-AFM pull-off force. images of PMMA acquired over a relatively large range of temperature.

151

between pull-off force and adhesive force.[168] Krotil *et al.*[183] have made an initial study of the effect of the molecular weight of PS on pull-off force and its dependence on temperature. A tentative conclusion from this work is that pull-off force reduces with increasing molecular weight. The distribution of molecular weight across a surface is indeed one factor that may play a role in the form of the distributions obtained in pull-off force values (see below). At lower temperatures, hydrophilic surfaces have been shown [169, 170] to exert higher adhesive forces on a chemically neutral tip, than hydrophobic materials. If such a mechanism was at work in our study, it may be expected that PMMA, because it is a more polar than PS, would exert greater adhesion on the hydrophilic tip. Our results support no such conclusion. Another factor that will affect the pull-off measurement is the viscoelastic nature of the material. This is consistent with the observation that it changes greatly immediately above the T_g for polystyrene, but again raises the question of why no such effect is seen with the PMMA. It is likely that the rheological properties of the polymers are likely to play a major role. It could be that immediately above its T_g the viscosity of polystyrene becomes sufficiently low for capillary forces to pull material up the sides of the tip. This would greatly increase the contact area and hence pull-off force. In the case of PMMA, the same effect may not occur until a temperature of 180°C or so is approached. It must be concluded that many mechanisms could affect pull-off force and that further work is required to elucidate the effects of factors such as molecular weight and the temperature dependence of viscosity. Nevertheless, the observation that PS and PMMA have very different behaviours as a function of temperature, enable images to be created that, at an appropriate temperature, allow the different phases to be clearly differentiated and individual phases to be identified. *The goal of using temperature to elucidate structure and identify phases on a small scale has thus been achieved in this case.*

These results for PS and PMMA are presented as histograms of the number of pixels as a function of pull-off force in Fig. 3.9. These enable us to see clearly the numerical distribution of measurements de-coupled from their location on the sample. The mean of the peak for PS steadily increases with temperature, from under 4 V at 25°C to approximately 9.5 V at 160°C. PMMA, on the other hand, shows a similar pattern of behaviour, but over a temperature range shifted upwards by approximately 60°C. To illustrate this, a plot of the mean value of the peak against temperature is also shown in Fig. 3.9. An important point to note is that a single phase has a distribution of responses, rather than a single value. These distributions are approximately Gaussian.
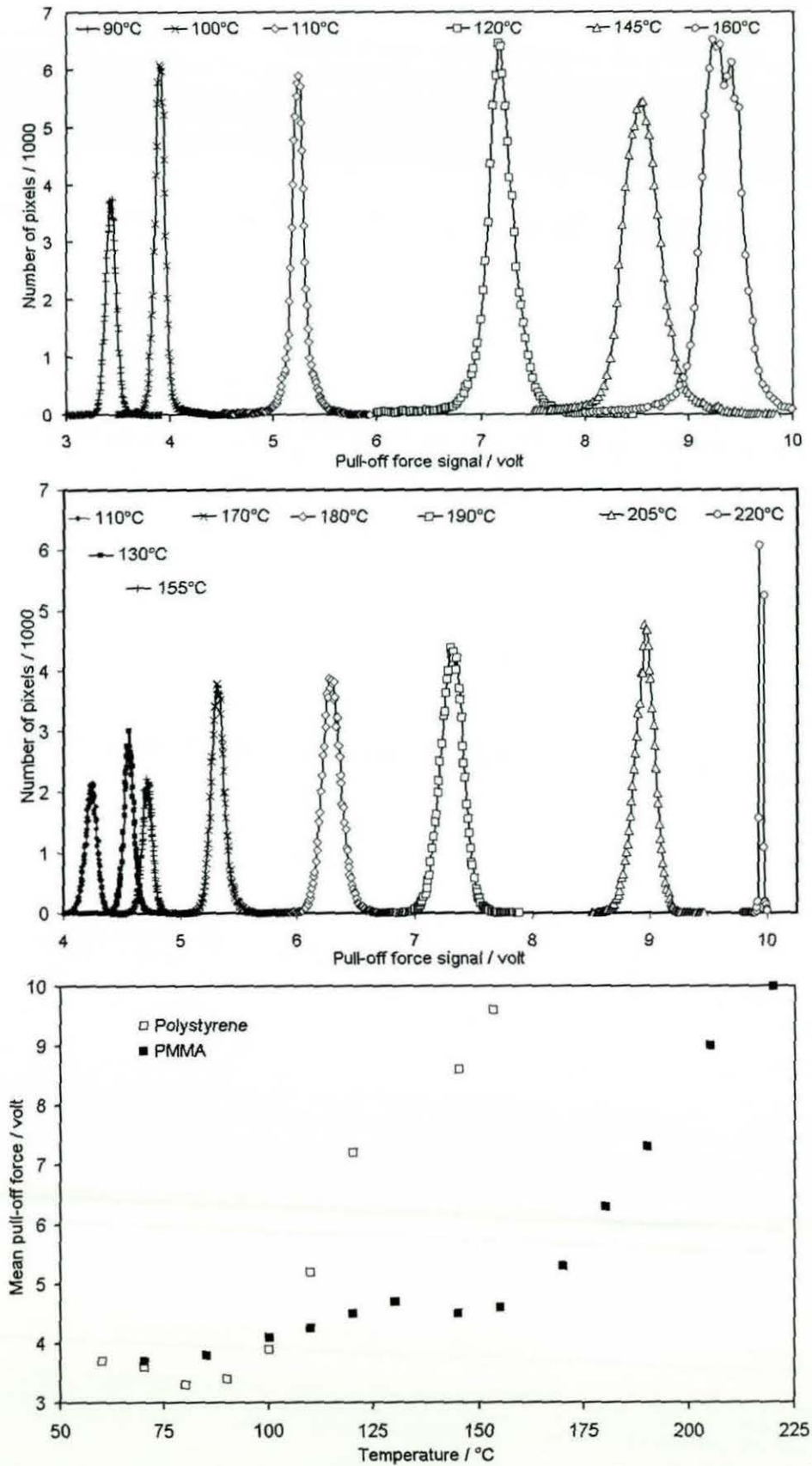
Fig. 3.9. Pull-off force intensity histograms at various temperatures for polystyrene and PMMA. These are from the same series of scans that produced the images shown in Figs. 3.7 and 3.8. Also shown is a plot of mean pull-off force against temperature for the two polymers.
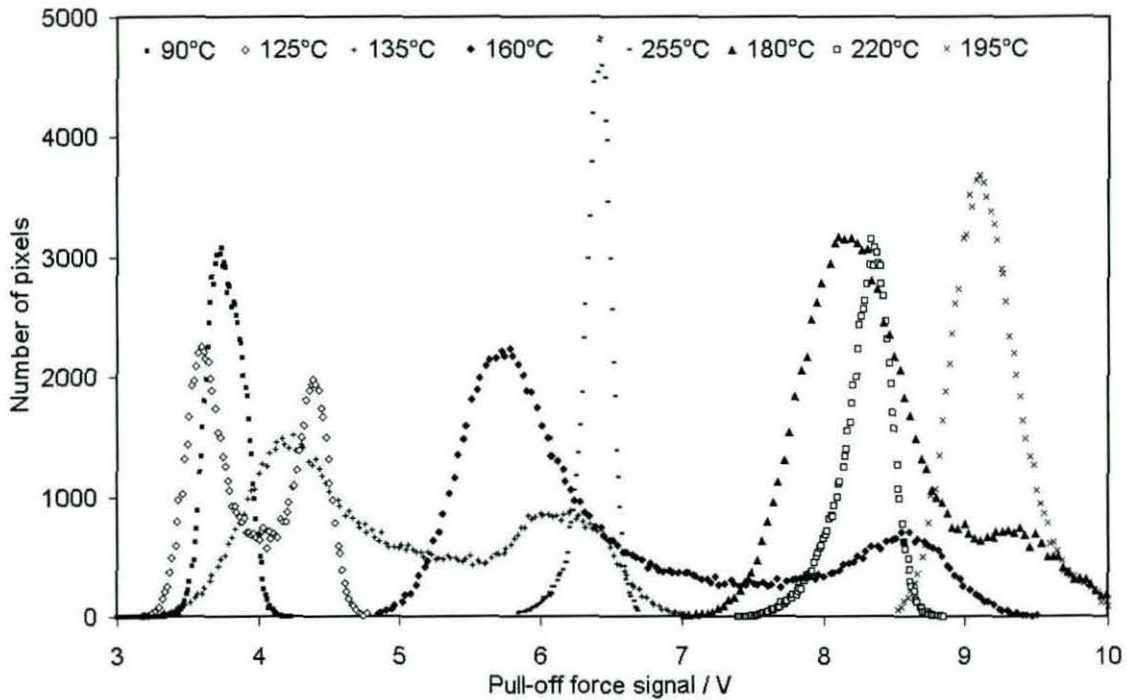
Fig. 3.10. Pull-off force intensity histograms at various temperatures for the PS-PMMA blend. These are the results of the same 10 μm × 10 μm scans that produced the images in Fig. 3.3.

A distribution of some form is to be expected, as all measurements contain error. It is not clear, however, whether these distributions arise from normal measurement errors. It is likely to be the case that polymeric surfaces have an inherent heterogeneity for this parameter. Regardless of the origin of these distributions, it is important to note that a single phase gives only one peak. While such a peak may or may not shift significantly with temperature, it will remain mono-modal in character. Histograms for the PS-PMMA blend are shown in figure 3.10. As the temperature is increased, there is a very clear transformation from a single, approximately mono-modal, peak at 90°C and below to an approximately bimodal distribution. At 125°C the two peaks in the distribution are relatively narrow and close together. Increasing the temperature by 10°C causes the peak attributable to the PS phase to shift upwards by 2 V, whilst the PMMA peak shifts by much less. This has the effect of significantly broadening the bimodal distribution. The broadest distribution is obtained at 160°C, by which temperature the PS peak has shifted to around 8.5 V and the PMMA peak has also shifted upwards to nearly 6 V. As the temperature is increased further, the distribution narrows as the mean of the PMMA begins to "catch up" with that of the polystyrene. By 195°C the distribution is substantially mono-modal once more. This corresponds to image (h) in Fig. 3.3, in which very little phase contrast is apparent. At 220°C, the mean pull-off force has decreased to just over 8 V and the distribution is a skewed single peak. This is the

region where the pull-off force of the PMMA is greater than that of the PS. The corresponding image [Fig. 3.3(k)], shows a weak reversal of phase contrast compared with the images acquired below 200°C or so. At 250°C and above the mean pull-off force decreases rapidly to around 6.5 V and the distribution becomes narrow and mono-modal once more.

The nature of the distribution of a PFM-AFM measurement at a particular temperature has a profound effect on the resulting image. If it is genuinely a single well-defined Gaussian peak, then no phase contrast will be generated, no matter how many phases are present in the material. In other words; the materials display identical behaviour to each other and cannot be differentiated. If, on the other hand, the bimodal distribution consists of completely separated-peaks, the resulting phase contrast will be strong. However, as Fig. 3.10 indicates, intermediate types of behaviour are possible. One such example is the bimodal distribution obtained at 125°C. Although the two peaks are well defined and evenly balanced, it is clear that there is still some overlap between them. The pixels that correspond to the values of pull-off force that lie within this region cannot therefore be assigned to a particular phase. The greater the area of overlap, the greater will be the degree of uncertainty in the resulting image. Another type of case in which interpretation is not straightforward is illustrated by the broad distributions obtained at 135 and 160°C. Although the peaks appear to be well differentiated, there is a wide plateau between them containing a significant proportion of the data points. We shall now examine such a distribution in more detail. Fig. 3.11 shows 2 µm × 2 µm pull-off force images of the blend acquired at 60°C and 135°C. The inset histograms show a clear transformation from a monomodal distribution to a more complex distribution over this temperature interval. In fact, Fig. 3.12 reveals that at least three separate Gaussian distributions are required to provide an adequate fit to the data set obtained at 135°C. The obvious conclusion is that there are more than two phases in this system, whereas it is believed that there can only be two. To help explain this, a series of images of the blend is shown in Fig. 3.13. The first (a) is a "conventional" pull-off force image produced with a greyscale graduated over the whole voltage range. Image (b) was derived by assuming the existence of a two-phase structure and imposing a threshold, a "decision boundary", at 5.2 V. This lies in the intermediate region above the highest value in the low adhesion population (PMMA) and below the lowest in the high pull-off force population (PS). All measurements below this value are, therefore, assigned to the PMMA phase and produce black pixels whilst all those above are assigned to the PS phase and give white pixels. No grey is

a) 60°C

b) 135°C

Fig. 3.11. High resolution (300 lines over 2 μm × 2 μm) PFM-AFM 3-d pull-off force images of the PS-PMMA blend acquired at (a) 60°C and (b) 135°C. Also shown are the corresponding intensity histograms.
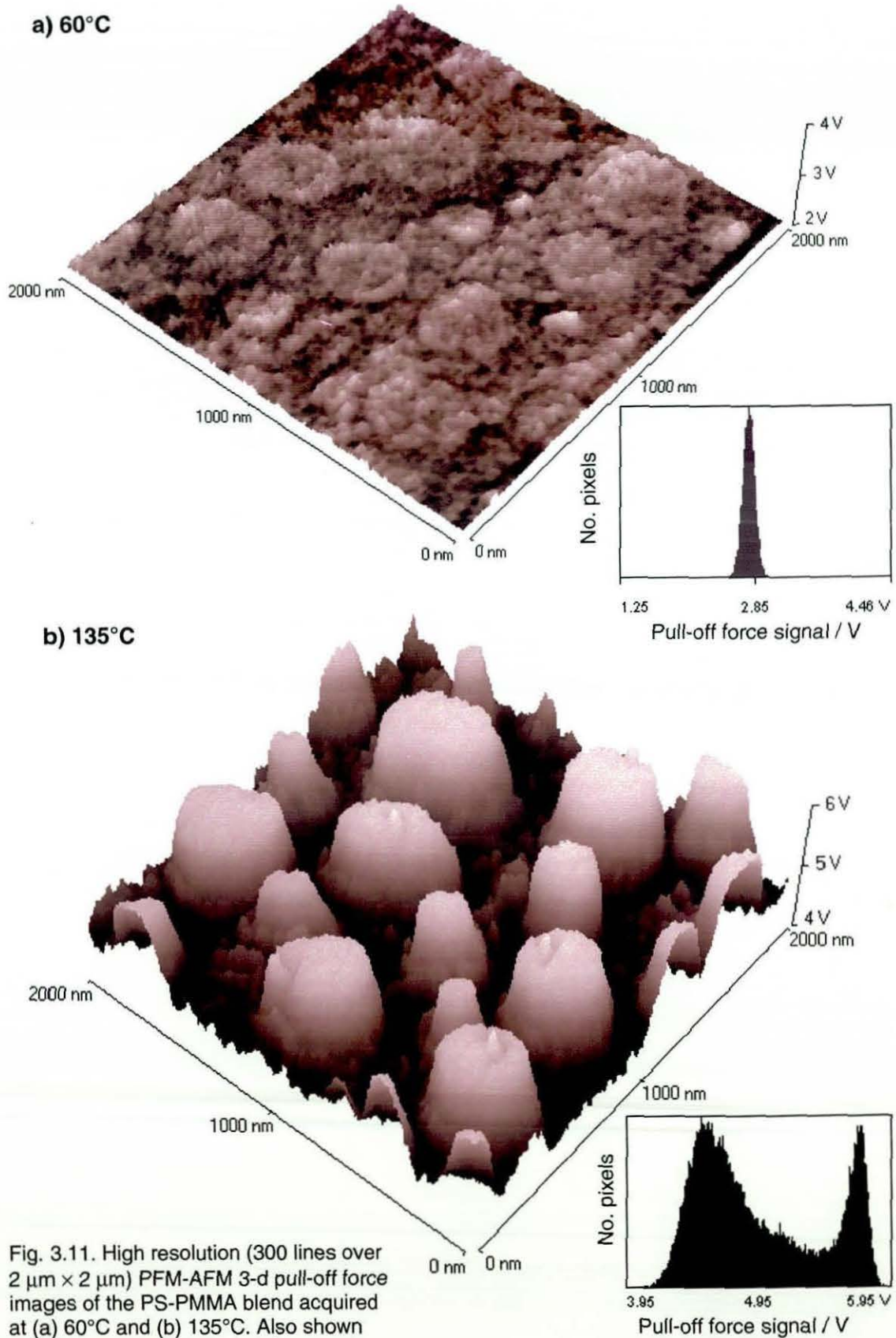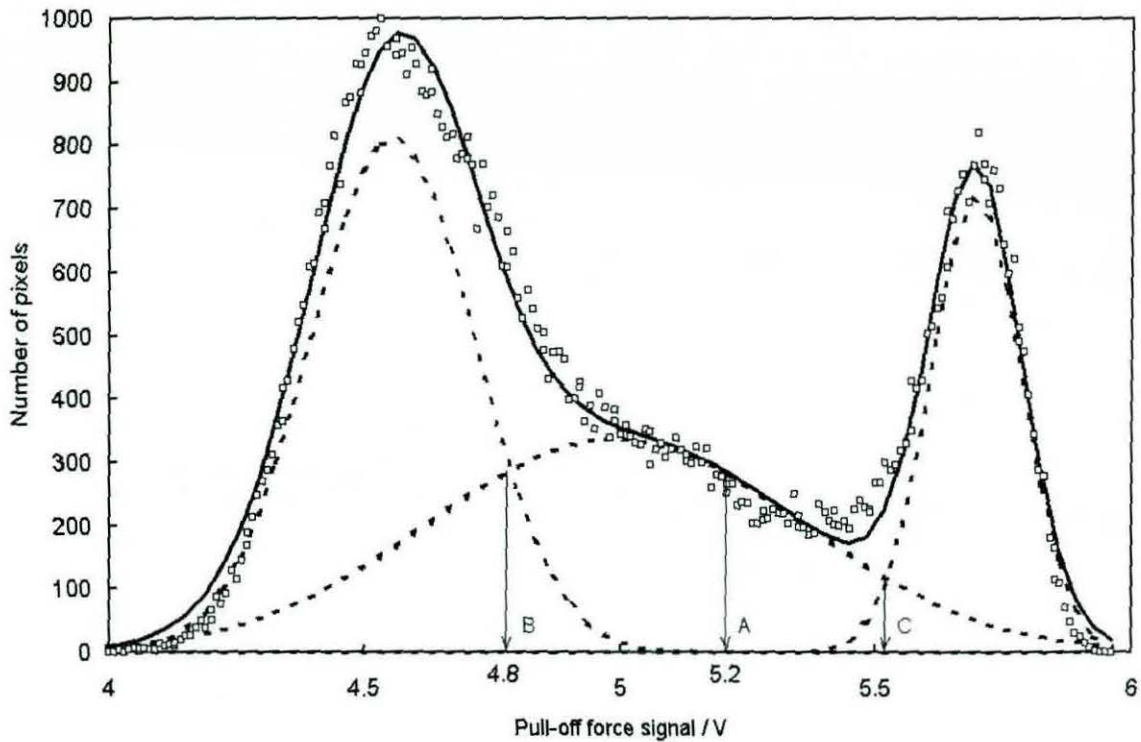
Fig. 3.12. The intensity histogram of the 2 μm × 2 μm pull-off force image shown in Fig. 3.4(b) of the PS-PMMA blend acquired at 160°C. The result of curve-fitting to the data is shown by the solid line. Three separate Gaussian distributions are required to achieve the fit and these are shown by the broken lines. Threshold or *decision boundary* values used to reprocess the (2-d) image [Fig. 3.13(a)], are indicated by the arrows [see Fig. 3.13(b) and (c)].

allowed. The final pull-off force image (c) was again constructed with the information in Fig. 3.12, but in this case the intermediate peak was assumed to represent a real phase and two thresholds were imposed. All those data points that lie in the region in which the Gaussian distribution with the lowest mean value has the highest intensity (≤ 4.8 V) have been processed to give black pixels. Those where the Gaussian peak with the intermediate mean is most intense are grey (4.8 V ≤ pull-off force ≤ 5.5 V). Finally, those data points where the Gaussian peak with the highest mean is dominant are white (≥ 5.5 V). In effect, we are assigning the probable phase to each value of pull-off force, commensurate with the phase that has the highest probability of being correct at that value. The resulting image shows that the "intermediate phase" appears primarily around the occluded phase and therefore has the appearance of being an interphase with a width of between 50 and 100 nm. The presence of such a phase can be discounted in this case, because these polymers are known to be highly immisible. The topographic image of this region [Fig. 3.13(e)] contains no corresponding features. It is unlikely, therefore, that this intermediate phase is a topographic artefact. The proposed
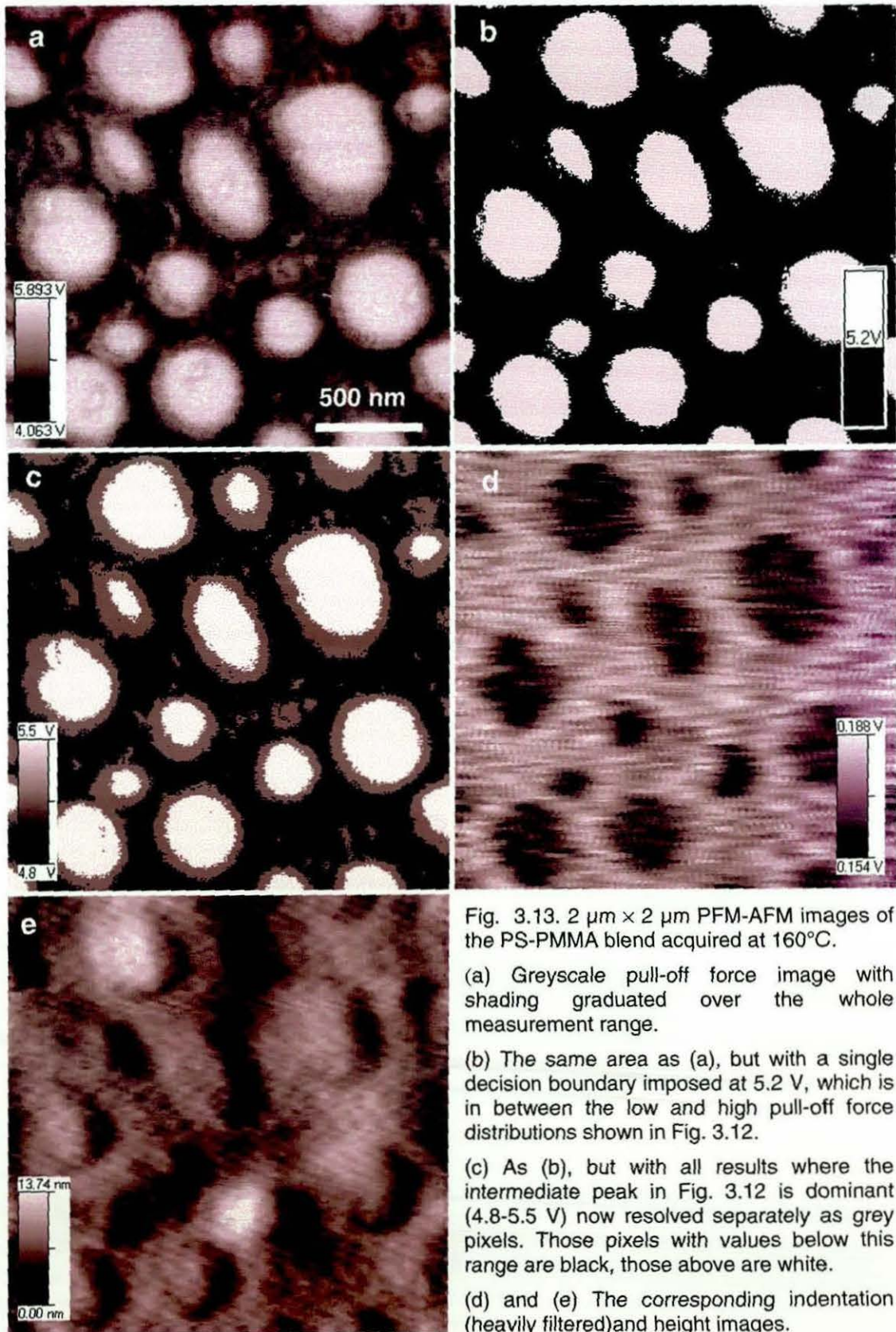
Fig. 3.13. 2 µm × 2 µm PFM-AFM images of the PS-PMMA blend acquired at 160°C.

(a) Greyscale pull-off force image with shading graduated over the whole measurement range.

(b) The same area as (a), but with a single decision boundary imposed at 5.2 V, which is in between the low and high pull-off force distributions shown in Fig. 3.12.

(c) As (b), but with all results where the intermediate peak in Fig. 3.12 is dominant (4.8-5.5 V) now resolved separately as grey pixels. Those pixels with values below this range are black, those above are white.

(d) and (e) The corresponding indentation (heavily filtered) and height images.
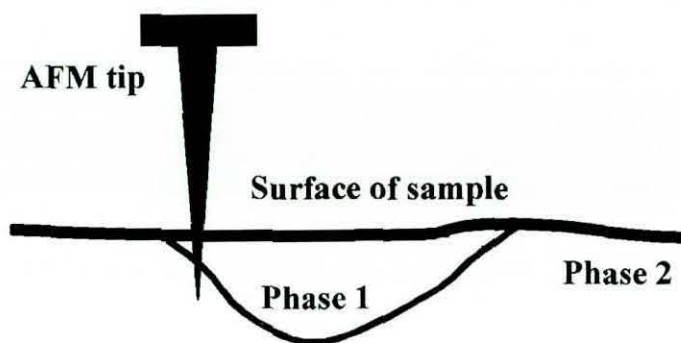
Fig. 3.14. Schematic diagram showing how the sub-surface structure of an immiscible phase-separated binary polymer blend could give rise, in PFM-AFM pull-off force images, to an apparent third phase surrounding the occluded domains.

explanation is that the structure of the blend changes with depth in the manner shown in Fig. 3.14. At the edges of the occluded domains, as it penetrates the surface, the tip comes into contact with both phases. Because of this, we observe a response that is intermediate to that of the two pure materials. The possible influence of three-dimensional structure on the pull-off force images must, therefore, be borne in mind when interpreting them. It should be noted that any interphase cannot realistically be represented by a single Gaussian distribution; at best it is a rather crude approximation. However, in the absence of other information with which to construct an alternative distribution, the fitting of Gaussian peaks would seem to be a reasonable starting point in interpreting pull-off force histograms and enabling the construction of the most meaningful images from them.

It is clear from this exercise that, for the PS-PMMA blend, there must be an optimum temperature (or temperature range) at which the size, shape and distribution of phases is detected with the greatest degree of certainty. This is the *minimum* temperature at which the phases are detected as discrete Gaussian peaks having little or no overlap. At this temperature, the plateau region between the peaks is also minimised. The physical significance of this is that the viscosity of the two materials must still be sufficiently high to minimise the sampling of the underlying phase through surface material. In this study, this temperature lies between 125 and 135°C. By 160°C the edges of the occluded domains are significantly blurred because the reduced local viscosity increases the width of the regions around each domain boundary within which both materials are sampled. The width of this region will also increase with probe force.

High temperature IC-AFM phase imaging was also carried out on the PS-PMMA blend to compare the suitability of the two techniques for this application. A typical
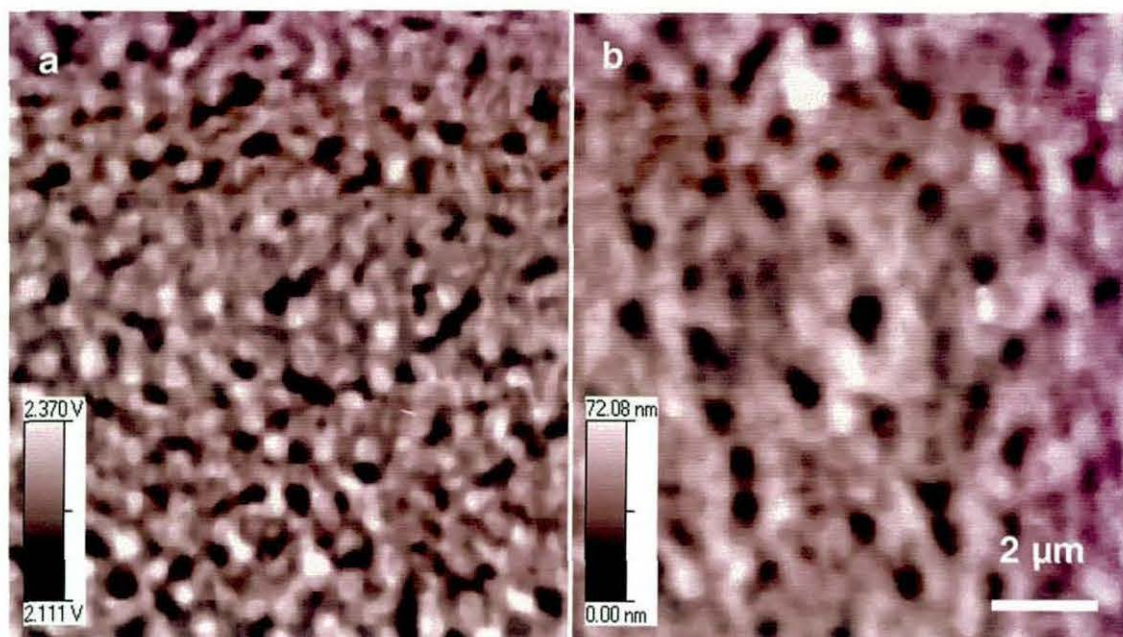
Fig. 3.15. PS-PMMA blend. 10 μm × 10 μm IC-AFM images acquired at 150°C. (a) Phase lag. (b) Topography.

result, obtained at a sample temperature is shown in Fig. 3.15. The phase-separated morphology of the blend is revealed neither in the phase nor the topographic image. In our study, the signal-to-noise ratio in both height and mechanical property-based IC-AFM images deteriorated rapidly with increasing temperature. This is not to say that this imaging mode could not be used successfully for this type of elevated-temperature experiment. However, with the set-up used here, PFM-AFM proved to be a much more robust technique.

3.3.2 Segmented polyurethanes

SPU with 1,3-dihydroxybenzene chain extender. Figure 3.16 shows images obtained at room temperature and a stage temperature of −50°C for the material incorporating 1,3-dihydroxybenzene as a chain extender. The topographic images confirm that the same area was scanned at the two temperatures and that changes in topography are not responsible for the changes in the other images. Excellent contrast is apparent in the room temperature pull-off force image. A high concentration of occluded domains or phases is revealed, with relatively low surface adhesion (dark), embedded in a relatively high-adhesion continuous phase (bright). The domains range in diameter from under 100 nm to over 400 nm. This morphology is also reflected in the indentation force image, although with less contrast and detail. This sample provided
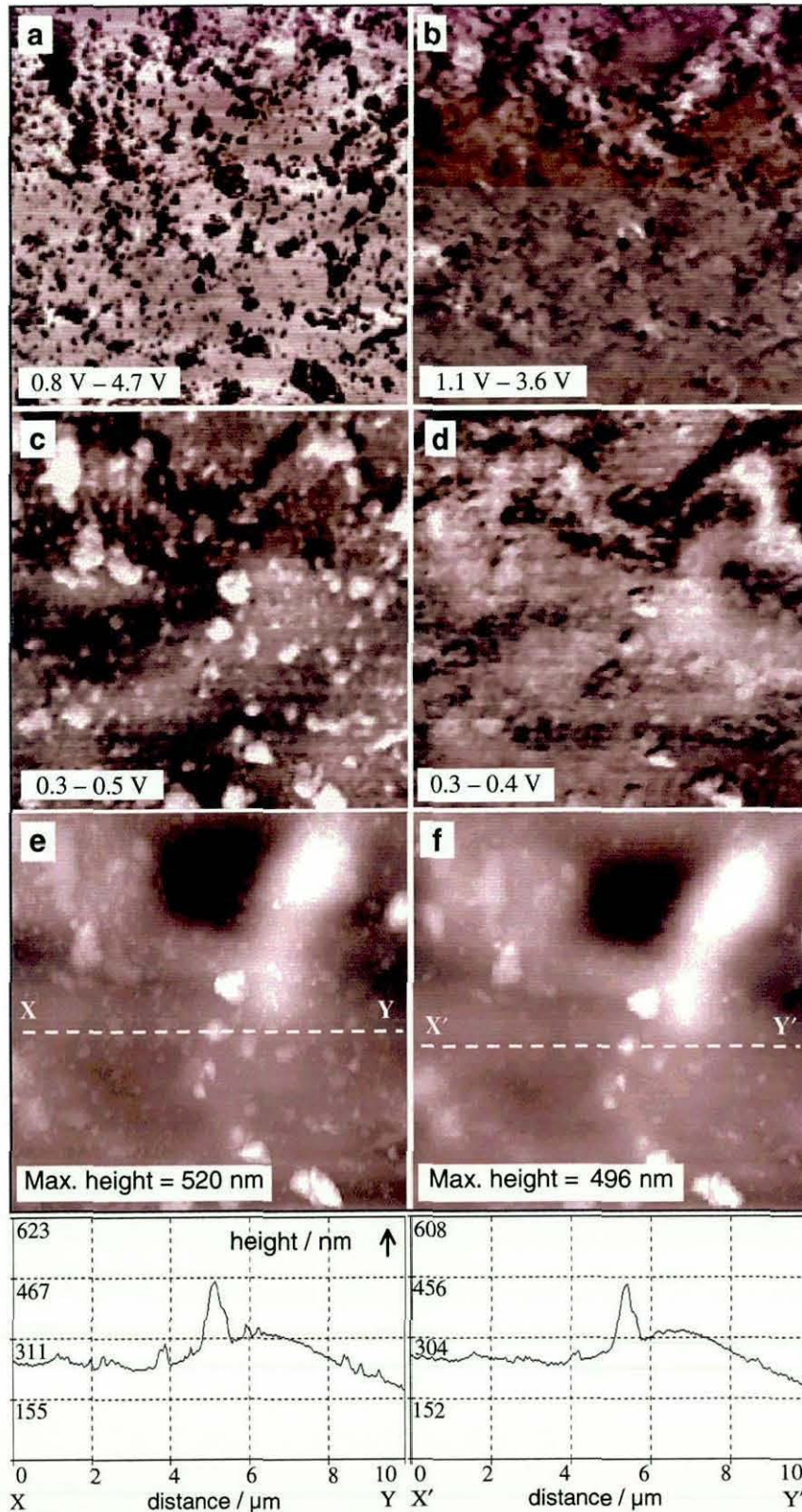
Fig. 3.16. Segmented polyurethane. Chain extender: 1,3-dihydroxybenzene.
10 μm × 10 μm PFM-AFM scans of the same area at room temperature (left) and −50°C (right). (a) and (b) show spatial variation in pull-off force at the two temperatures, (c) and (d) are constructed from the indentation force, (e) and (f) show topography. Below are topographical sections. Dark areas indicate low values in each case.

161

the best indentation image encountered in the SPU study, but careful filtering was still required to optimise image contrast and remove noise. The occluded low adhesion phases appear as bright relatively low compliance or hard structures. These presumably incorporate predominantly hard segment material, in the surface layer at least. Their size, however, is at least an order of magnitude greater than that expected for individual hard-segment domains in this type of SPU. As far as the author is aware, this is the first time that such high-contrast images have been obtained using a thermally-based technique, which show clearly the phase-separated microstructure of a SPU at a scale substantially larger than that of the smallest possible individual domains. At a stage temperature of −50°C, the contrast all but disappears, because the now glassy continuous phase exhibits much less adhesion towards the tip. There is, however, a feature towards the top of the image with relatively high pull-off force (though still lower than that of the continuous phase at room temperature). Inspection of figure the corresponding topographic image shows that this area is related to a raised feature surrounding a depression. The high pull-off force region is therefore likely to be a topographic artefact. The fact that this artefact is swamped by the effect of changing temperature is evidence that supports the utility of the approach advocated here.

The MTDSC results in Fig. 3.17 show that, on heating, this material undergoes a glass transition that finishes at approximately −42°C. This is the only transition occurring between −50°C and room temperature and is known to take place in the soft segments of the polyurethane chains. This result, combined with the images at above and below the onset of the glass transition, therefore serves to identify the phase that is bright at room temperature as being soft segment-rich.

For this material and all of those dealt with in this part of the study, at the lower stage temperature of −50°C, the sample surface was typically at −35°C or so. This means that the soft segment was typically not beneath the start-point (on cooling) of its glass transition, but only part way into it as measured by MTDSC. However, the MTDSC measurement was carried out at a temperature-modulation frequency of 0.025 Hz, whereas the PFM-AFM measurements were made at 500 Hz. This difference in frequency will tend to make the glass transition, as detected by PFM-AFM, significantly higher than that detected by MTDSC. This should, therefore, enhance our ability to detect the effect of the transition on PFM-AFM measurements. IC-AFM resonance imaging is conducted at frequencies of the order of hundreds of kilohertz. It was thought, therefore, that the effect of the glass transition would be detected at a
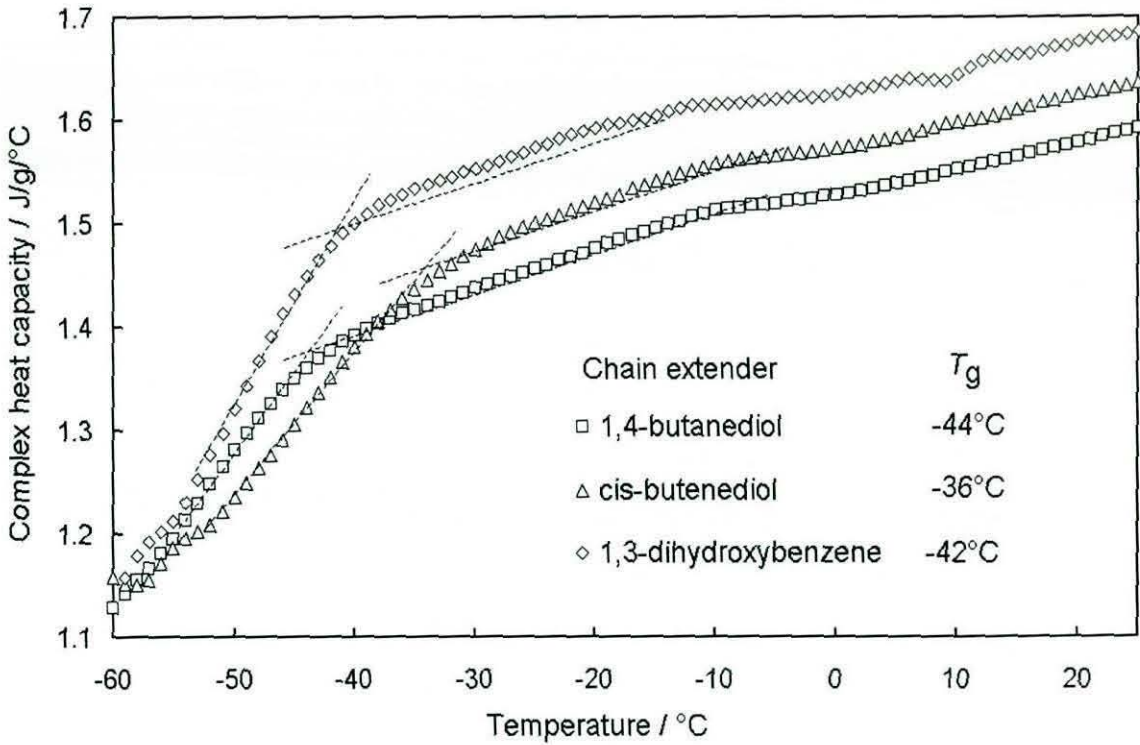
Fig. 3.17. *Segmented polyurethanes. Modulated differential scanning calorimetry results showing complex heat capacity as a function of temperature. The onset (on cooling) of the glass transition of the soft segment is shown for each material.*

significantly higher temperature than in PFM-AFM, thus increasing the effective low temperature range of the instrument. This is explored below in a direct comparison of the two techniques.

The occluded hard domains are shown in the topographic images to be higher than the surrounding continuous phase. The line measurement selected from the room temperature image shows that they range in height from approximately 20 nm to 150 nm above the average level of the continuous phase. Some topographical contrast is lost at –50°C. A possible explanation for this is that the, now glassy, soft segment material is no longer deformed to the same extent by the compressive stresses imparted by the tip during the indentation part of the measurement cycle. This would be consistent with the indentation images.

The intensity histograms of the pull-off force images are shown in Fig. 3.18. There is a virtually mono-modal distribution at low temperature changing to a well-differentiated bimodal distribution at room temperature. The material that has formed the higher pull-off force peak at room temperature is presumably the material that has passed through its glass transition. This corresponds to the continuous phase. This
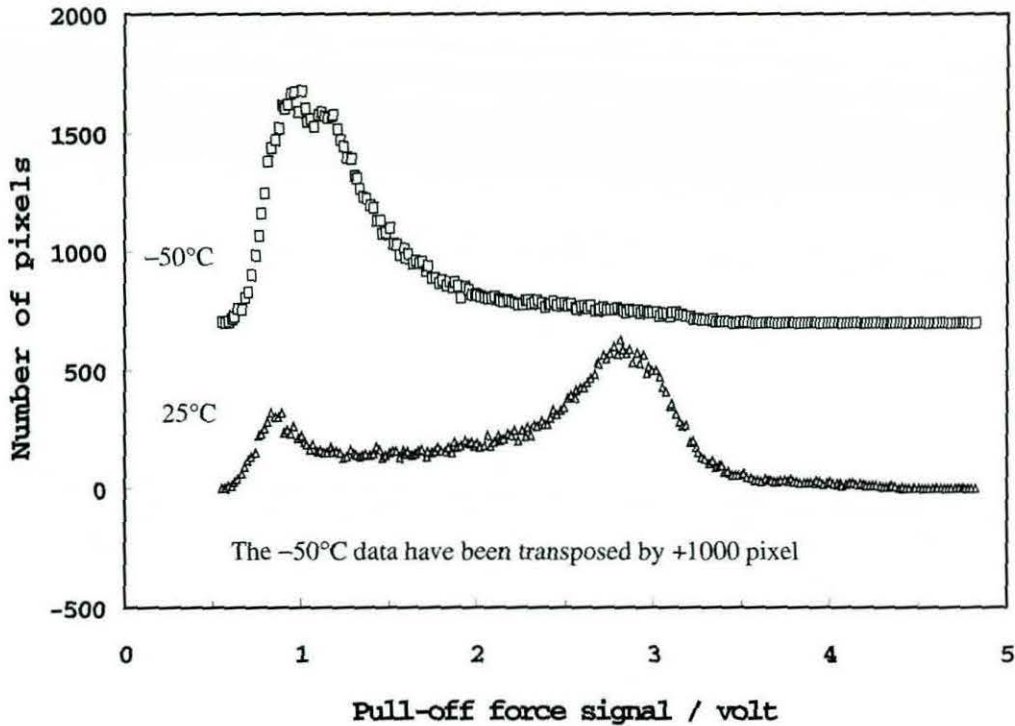
Fig. 3.18. Segmented polyurethane. Chain extender: 1,3-dihydroxybenzene. Intensity histograms of the PFM-AFM pull-off force images shown in Fig. 3.13, acquired at room temperature and −50°C.

behaviour echoes that seen for the PS-PMMA blend, except the differentiation between the two phases at higher temperatures is even more marked.

SPU with 1,4-butanediol chain extender. Figure 3.19 shows 4 μm × 4 μm images selected from a 10 μm × 10 μm scan of the material chain-extended with 1,4-butanediol. Even at this higher level of magnification, the structure is too fine to be able to make realistic estimates of the size and distribution of phases. This indicates that the phase-separated morphology is on a finer scale than in the first material. This is in agreement with the observation that this material was significantly less opaque than the first, indicative of phase separation at a smaller scale. The topographic images confirm that substantially the same area of the sample was scanned at each temperature. It will be noted, however, that equivalent features in the sub-ambient temperature image appear truncated in the slow-scan (top-to-bottom) direction. This is presumably a consequence of *sample-drift* towards the advancing tip. It was mentioned above that, at the time the work was carried out, the time available for low-temperature imaging was strictly limited. Consequently, it was not always possible to ensure that the sample had fully-stabilised before scanning had to commence. This problem will be
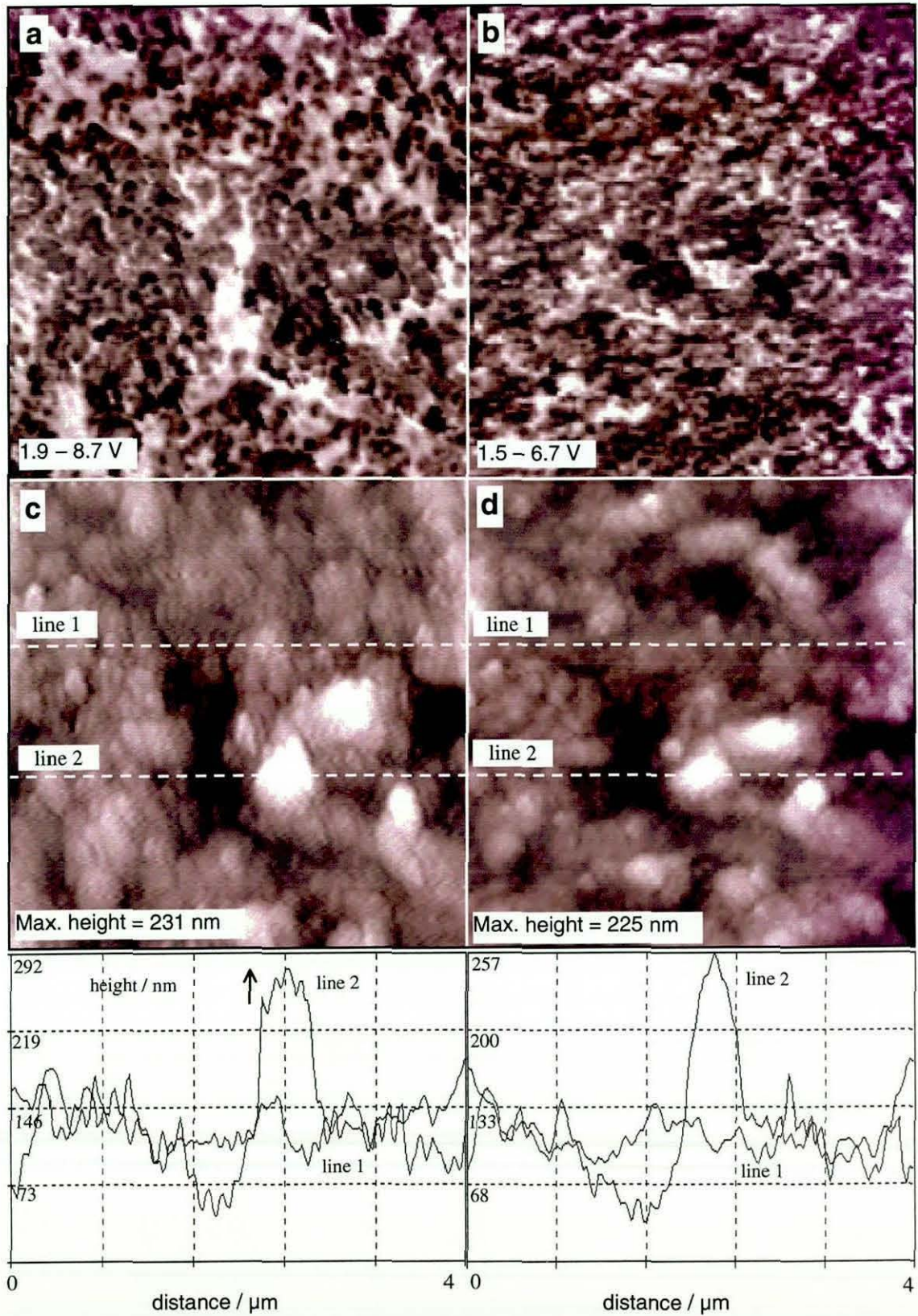
Fig. 3.19. Segmented polyurethane. Chain extender: 1,4-butanediol. 4 µm × 4 µm details of the *same area* of a 10 µm × 10 µm image, showing pull-off force (a) and (b) and topography (c) and (d) at room temperature (left) and –50°C (right).

Fig. 3.20. Segmented polyurethane. Chain extender: 1,4-butanediol. Intensity histograms from a 10 μm × 10 μm scan, showing the pull-off force distribution at room temperature and –50°C. The results of curve-fitting are shown for the bimodal distribution obtained at room temperature.

solved in the future by modifications to the temperature stage to allow replenishment of the coolant reservoir with the microscope *in-situ*.

There is an increase in the maximum pull-off force signal, from 6.7 V at –50°C to 8.7 V at room temperature. This again shows that the adhesion properties of at least part of the surface undergo a marked change at some intermediate temperature. MTDSC shows (Fig. 3.17) that this sample has a glass transition finishing, on heating, at –44°C. When we examine the pull-off force histogram, shown in figure 3.20, we again see a shift from a near mono-modal distribution to a clear bimodal distribution, as a consequence of passing through the transition temperature.

There is more detail in the topographic image taken at room temperature than that taken at –50°C. This is confirmed in the equivalent line measurements. This observation is again most likely to be associated with the increase in compressive modulus of the softer phase below its T_g (in most polymers, increases of two orders of magnitude may be expected [20]). This is consistent with the observations made above on the sample with the 1,3-dihydroxybenzene chain extender.

1.2 -10.0 V

250 nm

Max. height=78 nm
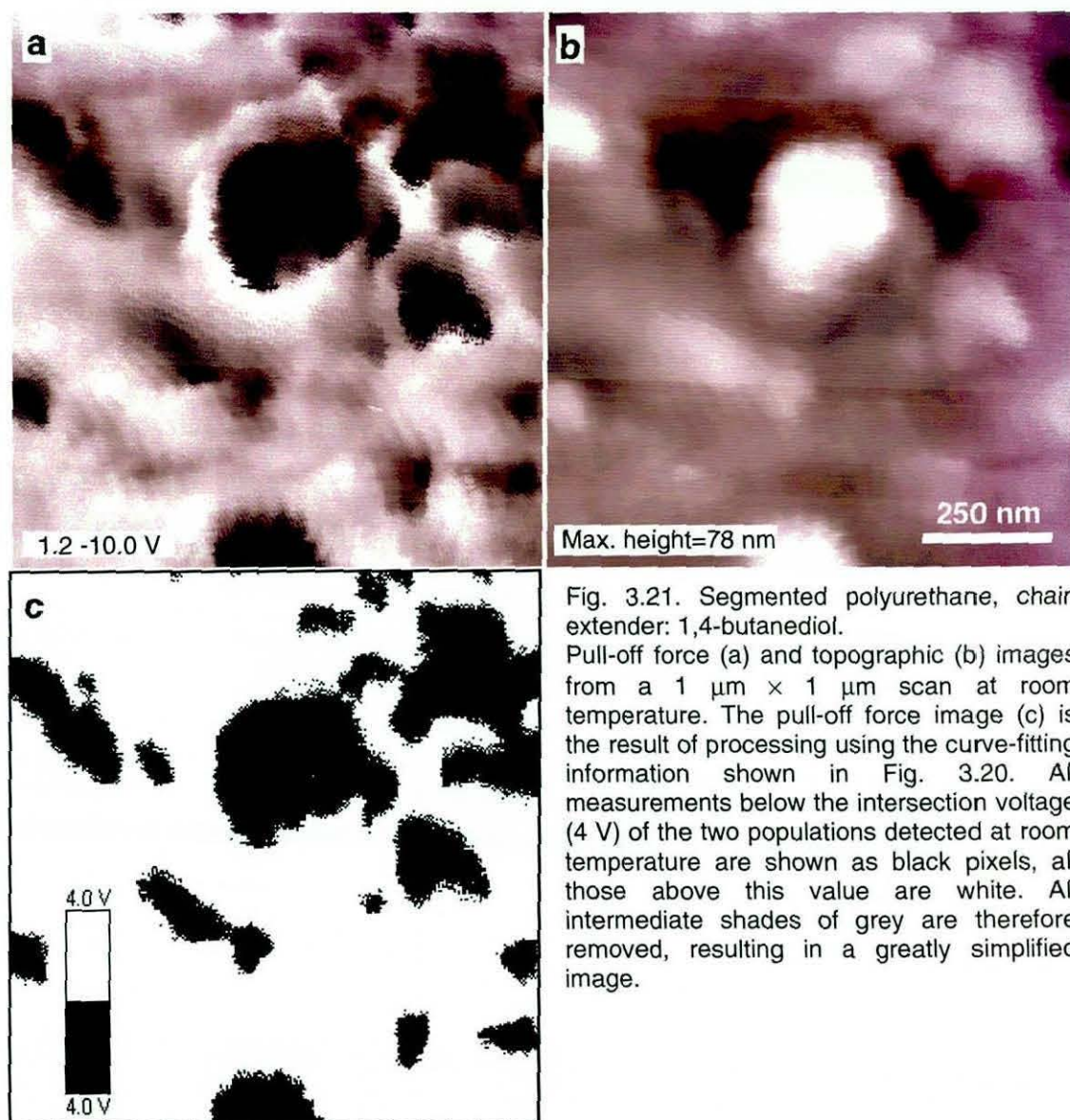
Fig. 3.21. Segmented polyurethane, chain extender: 1,4-butanediol.
Pull-off force (a) and topographic (b) images from a 1 μm × 1 μm scan at room temperature. The pull-off force image (c) is the result of processing using the curve-fitting information shown in Fig. 3.20. All measurements below the intersection voltage (4 V) of the two populations detected at room temperature are shown as black pixels, all those above this value are white. All intermediate shades of grey are therefore removed, resulting in a greatly simplified image.

Because of the fine structure apparent in this material, a series of 1 μm × 1 μm scans were carried out. Typical adhesion and topographic images are shown in figure 3.21(a) and (b), respectively. A complex morphology is apparently revealed. Low adhesion (dark) lobe-shaped phases are distributed through a high adhesion (light to grey) continuous phase and typically range in diameter from 100-300 nm. The lobe-like shape of the phases is unlikely to be an artefact, because it was reproduced in scans of the same area at different magnifications. The occluded low adhesion phases are higher than the surrounding continuous phase. At the time these experiments were conducted, a 1 μm × 1 μm scan was at the limit of the capabilities of the AFM scanner

used. For this reason, no attempt could be made to resolve any structural detail within individual phases.

The grey (intermediate adhesion) regions in the high magnification pull-off force image will be formed, in part, by the overlap in the pull-off force distributions for the two populations of domains present in this sample, as shown in figure 3.20. It was noted above, in the discussion of the PS sample, that even a 'pure' phase gives an approximately Gaussian distribution of responses. This sample displays incompletely separated Gaussian peaks, although, unlike the PS-PMMA blend sample, two Gaussian distributions are all that are required to achieve a good fit to the data. It follows that, in the overlapping region of pull-off force, this parameter cannot be used to distinguish between the different phases, because of the distribution inherent in the measurement. This is true even if there are, in reality, only two distinct, completely spatially separated phases. Consequently, a detailed interpretation of the images is complicated. It will depend on whether the distribution is purely random, arises as a consequence of topography (at worst, a second order effect here), the quality of feedback control (itself dependent on topography), a "real" spatial distribution of adhesion properties at the surface and possibly many other factors. While it is possible that more sophisticated methods of image analysis could be used to separate the two phases in the region of overlap, here the simple approach adopted above for the PS-PMMA blend is again used. All those data points with values in the area where the Gaussian peak with the lower mean has the higher value are shown as black, all others as white. This treatment is applied to the pull-off force image in Fig. 3.21(a) to produce Fig. 3.21(c).

To summarise: the intensity histogram suggests that there are only 2 phases present at the surface of this sample, whereas inspection of the pull-off force image in Fig. 3.21(a) gives the impression that many phases might be present, because shapes with various shades of grey can be discerned. We propose that the latter observation is an illusion that arises from the inherent distribution in pull-off force produced even by a pure phase. When these distributions overlap, some strategy is required to interpret the image correctly. Here a very simple strategy has been employed to obtain Fig. 3.21(c), but this map of the distribution of the phases will be approximately correct.

SPU with *cis*-but-2-ene-1,4-diol chain extender. Fig. 3.22 shows 4 µm × 4 µm "zoom images" selected from a 10 µm × 10 µm scan of the material chain-extended with *cis*-but-2-ene-1,4-diol. Once more, there is insufficient magnification to reveal precise morphological information. However, changing the temperature results in a
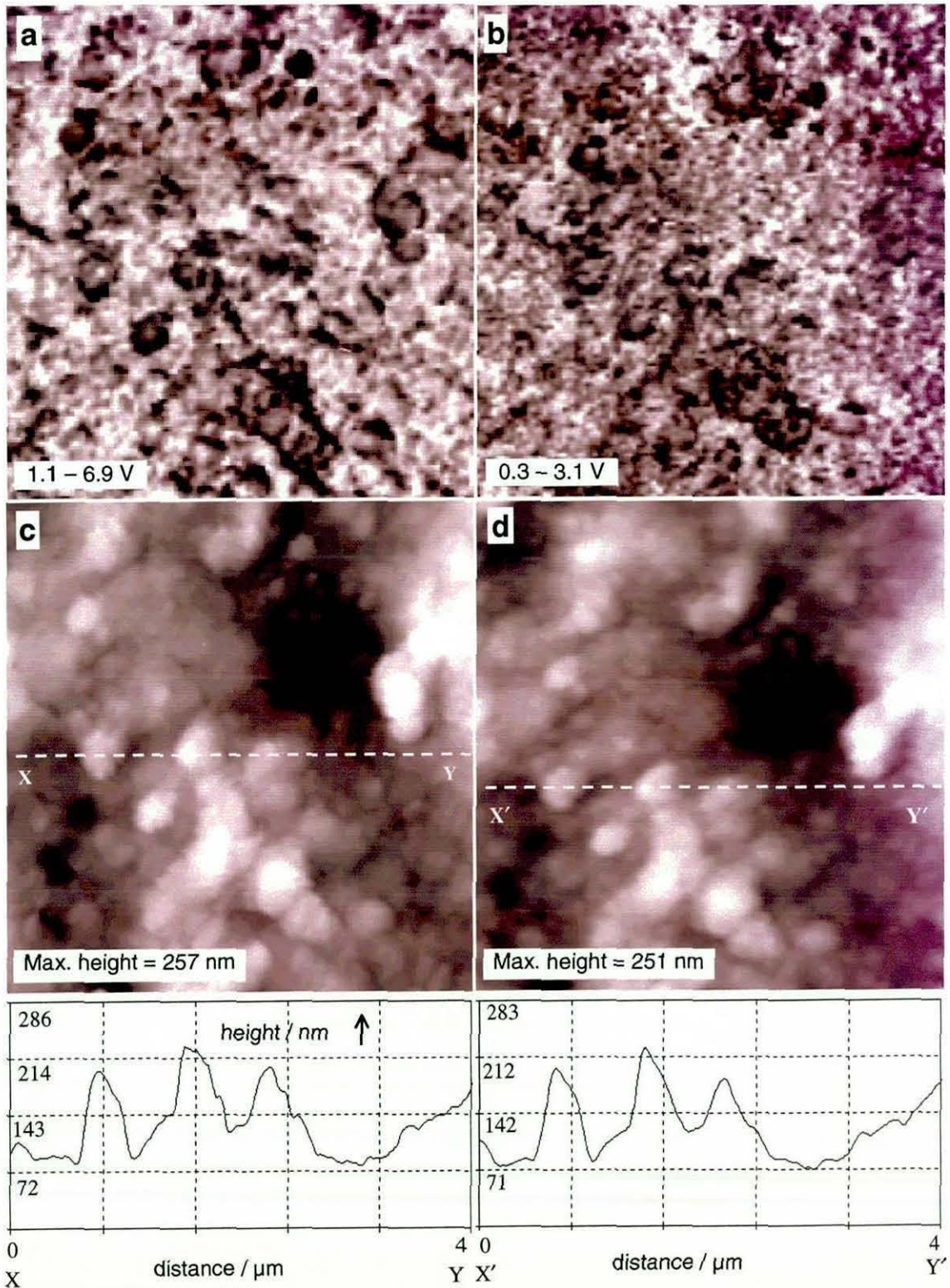
Fig. 3.22. Segmented polyurethane, chain extender: *cis*-but-2-ene-1,4-diol. 4 µm × 4 µm details of the same area of a 10 µm × 10 µm image, showing pull-off force (a) and (b) and topography (c) and (d) at room temperature (left) and –50°C (right).

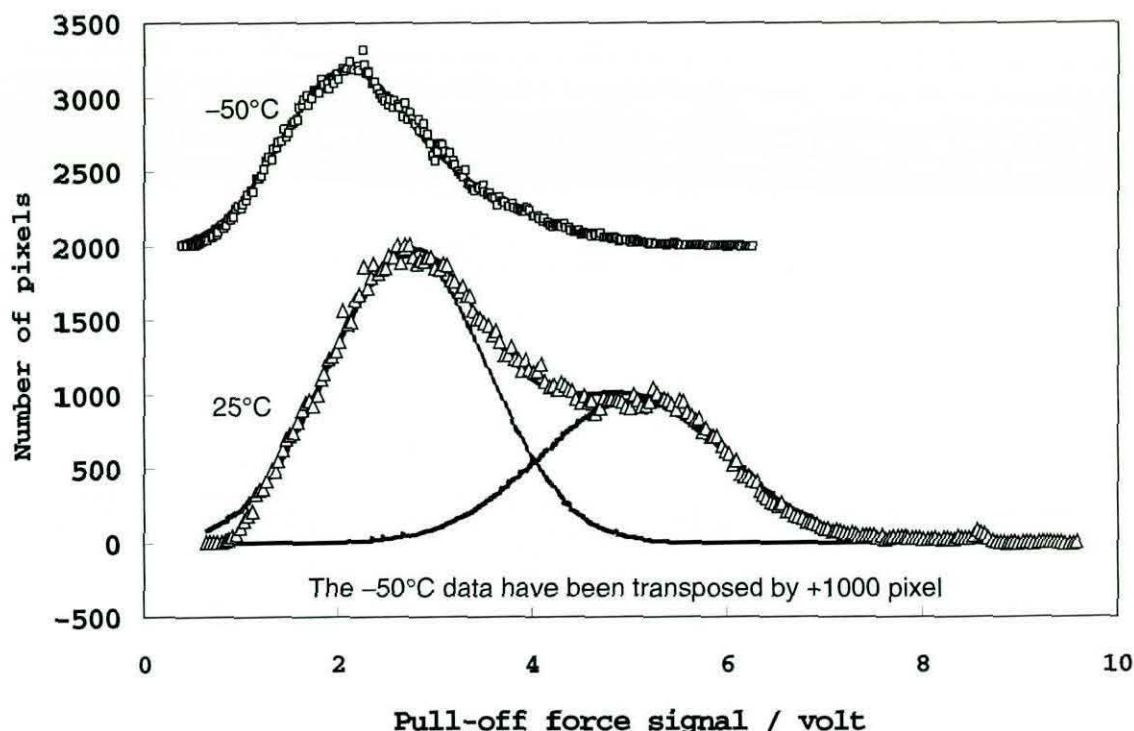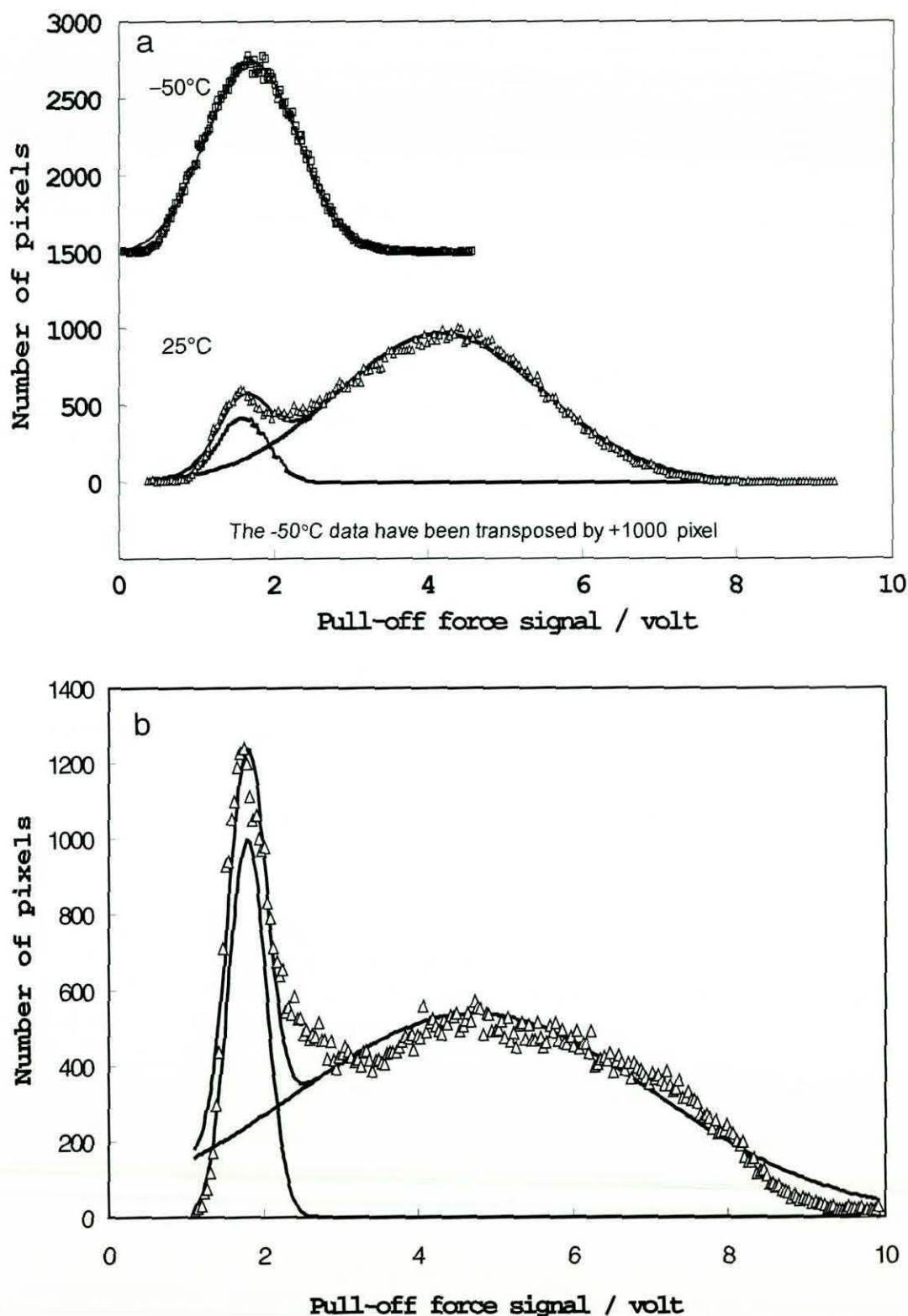Fig. 3.23. Segmented polyurethane, chain extender: *cis*-but-2-ene-1,4-diol. (a) Intensity histograms from a 10 μm × 10 μm scan, showing the pull-off force distribution at room temperature and –50°C. (b) Intensity histogram from a room temperature 1 μm × 1 μm scan. The results of curve-fitting are shown for the bimodal distributions obtained at room temperature in each case.

shift in maximum pull-off force range from 3.1 V to 6.9 V. Similarly, the histograms for the 10 µm × 10 µm sample in Fig. 3.23(a), show a transformation from a near mono-modal peak at low temperature to a clear bimodal distribution at room temperature. As before, this indicates that part of the material undergoes a transition within this temperature range. The MTDSC result for this material (Fig. 3.17) is consistent with this, as it shows that the glass transition finishes, on heating, at around –36°C. This is somewhat higher than for the material chain-extended with butanediol, which could account for the larger reduction in maximum pull-off force. It is interesting that, although this scan has insufficient magnification to clearly show the structure, the pull-off force measurement still shows the two-phase nature of the sample, as revealed in the intensity histograms.

The topographic images show that roughly the same areas were scanned at the two temperatures. Minor topographic differences are, as before, apparent. These are again the result of a change in compliance rather than the cause of the change in adhesion-related contrast.

It will be noted that in the adhesion histogram from the 10 µm × 10 µm scan [Fig. 3.23(a)], the low pull-off force "tail" of the higher adhesion population completely overlaps the lower pull-off force (hard segment rich) distribution. An important consequence of this is that at no location within the image can we unequivocally assign a pixel to this phase. Conversely, all pixels with a value above approximately 2.4 V must belong to the soft segment rich phase.

Fig. 3.24(a) and (b) show adhesion and topographic images resulting from a 1 µm × 1 µm scan. There is an artefact, indicative of difficult scanning conditions, towards the end (bottom) of the pull-off force image. This was caused by the combination of a deep narrow valley, lying parallel to the raster or fast-scan direction, being bisected by the highest region in the scanned area. Consistent spatial resolution of adhesion properties was, however, maintained. The histogram of pull-off force distribution shown in Fig. 3.23(b) is from this 1 µm × 1 µm scan. It shows that an area had been selected with a more even balance between the two phases, although the lower pull-off force phase is still completely overlapped by the higher one. The point at which the two populations intersect corresponds to a pull-off force of 2.2 V. This threshold value can once more be imposed on the image so that each value of pull of force, and thus each corresponding pixel, is assigned to the phase that it most probably represents and no grey area is allowed. This produces the result shown in figure Fig. 3.21(c).

a

b

250 nm

1.2–10.0 V

Max. height=70 nm

c

2,2 V

2,2 V
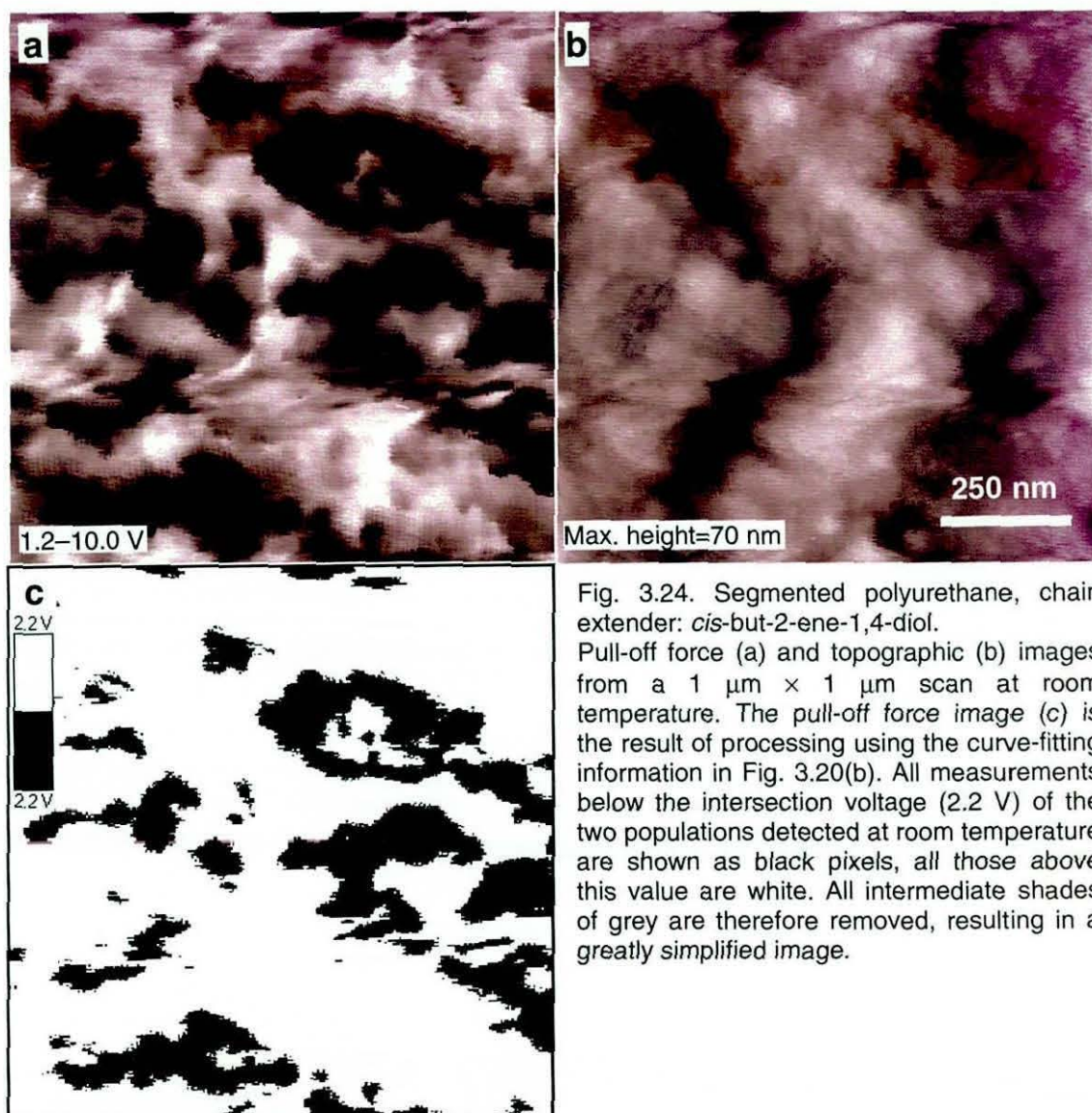
Fig. 3.24. Segmented polyurethane, chain extender: *cis*-but-2-ene-1,4-diol.
Pull-off force (a) and topographic (b) images from a 1 μm × 1 μm scan at room temperature. *The pull-off force image (c) is the result of processing using the curve-fitting information in Fig. 3.20(b). All measurements below the intersection voltage (2.2 V) of the two populations detected at room temperature are shown as black pixels, all those above this value are white. All intermediate shades of grey are therefore removed, resulting in a greatly simplified image.*

Overview. Overwhelming evidence that the features we observe in the pull-off force images of the polyurethanes do not stem from topographical contrast is provided in Fig. 3.24. This shows topographical histograms from the 10 μm × 10 μm scans of the SPU chain-extended with 1,3-dihydroxybenzene at both room temperature and –50°C. It can be checked whether topography is responsible for spatial variations in pull-off force by comparing the respective distributions of the two measurements. It is evident that there is no significant shift in height distribution with temperature, whereas the pull-off force moves from a bimodal to monomodal distribution on cooling.

These results reveal a morphology that is far removed from the widely accepted structural model of these materials, having phases at least an order of magnitude
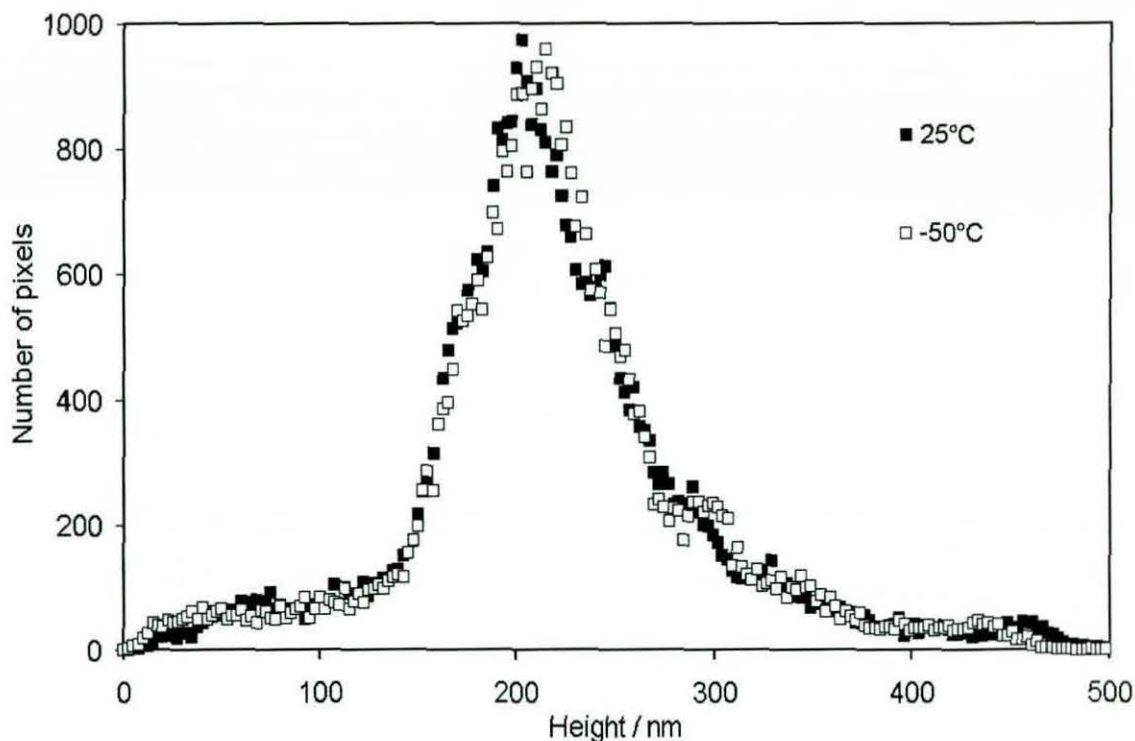
Fig. 3.25. Segmented polyurethane. Chain extender: 1,3-dihydroxybenzene. Intensity histograms of the topographic images shown in Fig. 3.13 acquired at room temperature and –50°C.

larger than that of individual hard and soft segment domains.[161, 216-230] If the results indicate real morphology, then we must be detecting structures, whose growth results from the co-operative behaviour of a large number of individual hard or soft domains. If the hard and soft segment domains present at the surface reflect bulk phases, then the nature and size of the individual segmented copolymer molecules dictate that the hard phases must contain a high proportion of soft segment material and vice-versa. It is unclear as to what mechanism or structural geometry could account for this behaviour. It is likely that the surface of a phase differs markedly from its interior. It seems plausible, therefore, that the two individual bulk phases could consist of similar proportions of hard and soft-segment domains, while simultaneously exhibiting very different surface properties. Surface energy and, therefore, adhesion will be particularly dependent on which type of domain dominates the surface. The form of the samples makes this hypothesis more likely. All were free surfaces imaged in the as-cast condition. Had they been microtomed sections, for example, the images would have been dependent on the "bulk" mechanical properties of individual phases. It is indeed possible that high-magnification scans on such samples could distinguish between the bulk and the surface. Thin films cast from solution could also be expected to produce

very different results. In addition to any effect that this may have on the structure of the bulk material, it has been shown that a sub-nanometre soft segment-rich layer forms at the surface of such films.[234, 235] The possible existence of different surface layers on otherwise similar phases could explain the relative insensitivity of the indentation force measurements. Such ultra-thin layers are less likely to produce significant differences in the local stiffness beneath the tip. That we are detecting a real phenomenon is supported by the reproducibility of the results. A large number of scans were carried out for each material and the change in properties at different temperatures was consistent, while consecutive scans of the same area would invariably produce the same morphology.

3.3.3. A comparison of the effectiveness of pulsed force mode and intermittent contact phase detection microscopy for ambient and sub-ambient temperature imaging of segmented polyurethanes

As has been mentioned above, for high-temperature work on the PS-PMMA system, PFM-AFM proved to be much more useful than IC-AFM phase imaging. Indeed phase imaging proved to be so prone to noise at high temperature that it proved fruitless to carry out a direct comparison of the two techniques on the same area of sample. However, this was not the case for ambient and sub-ambient temperature imaging of the polyurethane samples. It was therefore decided to attempt, for the first time as far as the author is aware, to carry out imaging of precisely the same areas of the same material at different temperatures using the two techniques. In doing so, it was hoped that direct comparisons could be made of the nature of the phase contrast produced by each imaging mode and, for example, the sensitivity and signal-to-noise ratio that could be expected in each case.

Fig. 3.26 shows a comparison between images of the same 4 µm × 4 µm area of the SPU chain-extended with 1,3-dihydroxybenzene obtained using the two imaging modes at room temperature. The scan speed was 4 µm s^{-1} in each case. The IC-AFM phase image (a) displays excellent phase contrast, with occluded domains revealed as dark (low phase) against a light (higher phase) background. It will be noted that, like the pull-off force, the phase signal is expressed as a voltage rather than an actual phase angle. This is a characteristic of the instrument used. However, for purposes of comparison, this is unimportant. With the parameters used here, a low phase lag between the driving signal and the response of the sample indicates harder or less compliant material. This is confirmed by the PFM-AFM pull-off force adhesion (c) and
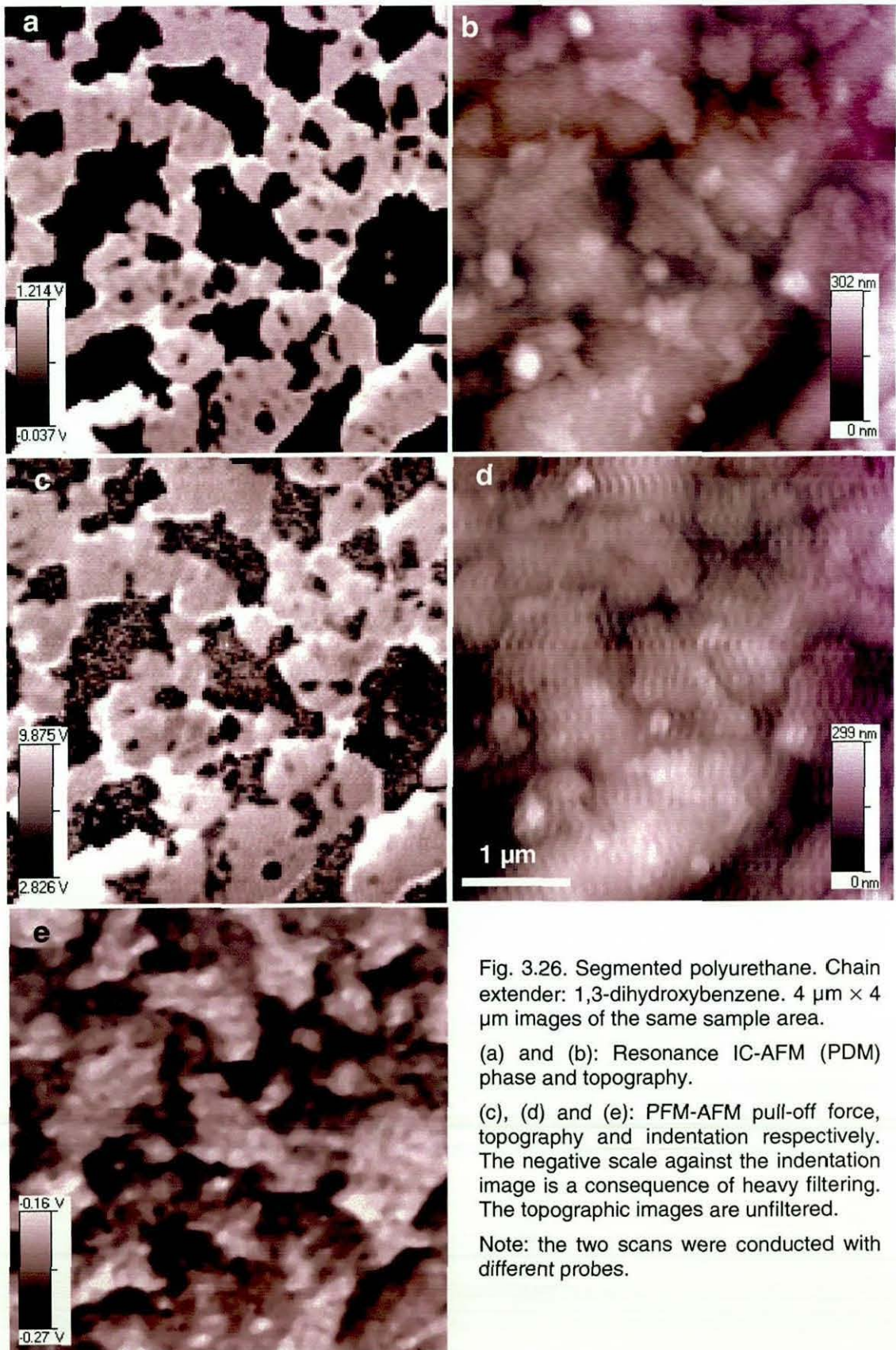
Fig. 3.26. Segmented polyurethane. Chain extender: 1,3-dihydroxybenzene. 4 μm × 4 μm images of the same sample area.

(a) and (b): Resonance IC-AFM (PDM) phase and topography.

(c), (d) and (e): PFM-AFM pull-off force, topography and indentation respectively. The negative scale against the indentation image is a consequence of heavy filtering. The topographic images are unfiltered.

Note: the two scans were conducted with different probes.
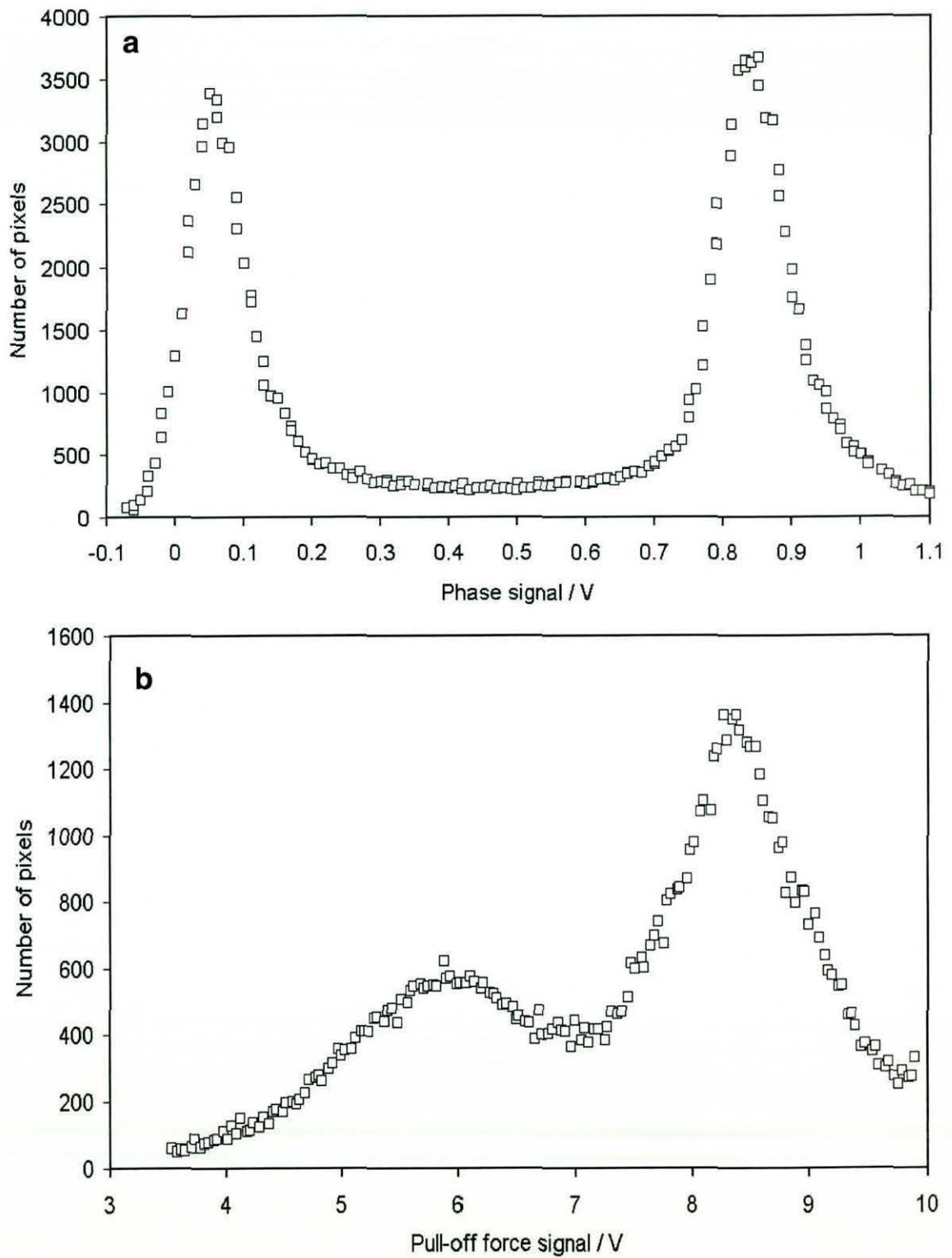
Fig. 3.27. Segmented polyurethane. Chain extender: 1,3-dihydroxybenzene. Intensity histograms of the phase (a) and pull-off force (b) images shown in Fig. 3.26 acquired at room temperature.

indentation (d) images, which, as before, show the occluded phase to be harder and less adhesive than the surrounding material. As expected, the signal-to-noise ratio in the indentation image is much poorer than that in the other two images. The differences between the phase and adhesion images are less clear cut. Certainly, the contrast between the domains appears to be superior in the phase image and several small (< 100 nm) occluded domains are detected that do not appear in the adhesion image. On the other hand, the pull-off force measurement appears to distinguish between two different types of occluded domain. The dominant colour is dark grey, however there are several black particles which may be impurities (they are shown as being higher than the other occluded domains in the corresponding topographic images). In the phase image, these particles are not differentiated from the rest of the occluded domains. The difference between the topographic images is more obvious, in that there is considerably more noise in the PFM-AFM image (both images are unfiltered). It will be noted that, with a maximum peak-to-valley height of around 300 nm in a 4 μm square, the sample is relatively rough. In PFM-AFM, the topographic image is acquired by keeping the maximum compressive force constant. It was noted throughout the study that, unless the scan speed was very low, for rough samples the feedback mechanism was not responsive enough to achieve this. This is probably the source of the noise apparent in this particular case.

Further information can be gained by comparing the intensity histograms of the phase and pull-off force images. These are shown in Fig. 3.27. The major difference between the two measurements is now apparent; the IC-AFM phase image completely separates the two phases into two very similar peaks, whereas the adhesion measurement consists of two dissimilar and overlapping peaks. This strongly implies that the phase imaging mode is superior to PFM-AFM in characterising this morphology, at least at room temperature on this relatively rough sample. It will be noted that, even though the peaks are extremely well separated, the plateau region between them contains relatively few data points. This is in contrast to the PFM-AFM pull-off force results for the PS-PMMA blend at elevated temperatures. Both SPU phases at room temperature must therefore be less compliant than PS and PMMA above their T_g. Consequently, there will be relatively few measurements made at locations where both phases are detected.

Fig. 3.28 contains 4 μm × 4 μm IC-AFM phase and PFM-AFM pull-off force images of the same area of the SPU at ambient and sub-ambient temperatures. Three phase images are shown, acquired at room temperature and stage temperatures of −50 and

a 0.6- 2.4 V

b 0.7- -0.5 V

c -0.9- -0.7 V   1 μm

d 1.0- 8.7 V

e 0.8- 5.9 V

f Max. height = 139 nm

g Max. height = 146 nm

Fig. 3.28. Segmented polyurethane. Chain extender: 1,3-dihydroxybenzene.

(a), (b) and (c): 4 μm × 4 μm IC-AFM phase images acquired at a (stage) temperature of 25°C, −50°C and −75°C respectively.

(d) and (e): PFM-AFM pull-off force images of the same area obtained at 25°C and −50°C respectively.

(f) and (g): IC-AFM and PFM-AFM topography at 25°C.

(h): The corresponding intensity histograms of the phase images acquired at a range of stage temperatures between room temperature and −75°C.

−75°C. The latter two correspond to sample temperatures of approximately −35 and −50°C, respectively. As before in the room temperature image, dark low-phase domains are clearly visible against a high-phase background. The domain size ranges from approximately 100 nm to several hundred nm. The signal range decreases from 1.8 V at 25°C to 0.2 V in both of the sub-ambient temperature scans. However, the microstructure is still visible at room temperature, albeit with less image-contrast. Despite the signal range being the same in the two low temperature images, significant differences are visible between them. At −75°C, fewer occluded domains are revealed and they are less well defined. This presumably indicates that the mechanical properties of the hard- and soft-segment material are now a significantly closer match. The fact that most of the hard-segment domains are visible at this temperature would seem to indicate that the soft-segment material is still not fully below its T_g. Moreover, there is no evidence that the effect of the glass transition is detected at a higher sample temperature in the phase images. Further work would, however, be required to confirm this. Topographic artefacts are apparent at low temperature, particularly at −50°C, in the form of bright (high phase) areas surrounding certain relatively high features. Such artefacts occur only rarely at room temperature.

The intensity histograms from these images are plotted in Fig. 3.28(h). Histograms from scans made at −60 and −70°C are also shown. At room temperature, there is a clear bimodal distribution. However, its nature is much more reminiscent of a pull-off force distribution, in that the distribution is asymmetric and the peaks are incompletely separated. This is in contrast to the well-defined balanced distribution shown in Fig. 3.27(a). The reason for this difference is unclear, as it is exactly the same material. The domains here are, however, somewhat smaller and more numerous than the area shown in Fig. 3.26. This means that there is a much greater proportion of interface, which, as was seen with the PS-PMMA system, can give rise to such "uncertain" intensity histogram distributions. Another possible reason is that significant wear of the tip had occurred in the interim or that the machine parameters were less well set up. All the low temperature scans show a mono-modal distribution and they are all shifted well below the measurement range of the room temperature result. The physical significance of the absolute measurement range is unclear, although, as has been mentioned, the mechanism of contrast generation in phase imaging is somewhat complex and that temperature-induced changes in resonance frequency may affect the resulting images.

The corresponding pull-off force images acquired at room temperature and –50°C are in many respects very similar to the phase images. However, significant differences do exist, particularly at room temperature. Fewer (low adhesion) occluded domains are visible than in the phase image. Furthermore, they are significantly smaller and the interfaces are less well defined. This may be a consequence of the higher driving amplitude and contact time in PFM-AFM. At –50°C, the pull-off force image is much more like the corresponding phase image. The degree of contrast between the phases is perhaps inferior, but, on the other hand, there are no obvious topographic artefacts in the pull-off force image.

These results show that it is perfectly possible to carry out low temperature phase imaging and in certain respects, the resulting images are superior to equivalent PFM-AFM adhesion images. This may reflect a superior overall signal-to-noise ratio in the resonance IC-AFM (PDM) technique than is obtainable in the current implementation of PFM-AFM, in which a much smaller number of individual measurements are made per scan. However, there is no doubt that PDM results are much more susceptible to small changes made to the various operating variables.

An interesting observation from these pull-off force results is that significantly more occluded domains are visible in the image acquired at –50°C than at room temperature. This behaviour was apparent in several sets of results and with phase-separated materials other than polyurethanes. It was therefore decided to investigate the phenomenon further. Fig. 3.29 contains 5 μm × 5 μm PFM-AFM images of the same SPU acquired at room temperature and stage temperatures of –40 and –50°C. The topographic images confirm that the same area was scanned at each temperature. As before in the pull-off force images of these materials, low adhesion occluded domains are visible at room temperature, although their shape is somewhat ill-defined. In the –40°C image, the definition of the domains is sharper, they appear in greater concentration and they are in general somewhat larger. The apparent increase in definition may be a consequence of the continuous soft segment material becoming more rigid. At –50°C the phase contrast has diminished, despite having somewhat larger measurement range. A significant number of hard-segment domains now appear to be smaller than at –40°C. In order to illustrate these effects more clearly, the same 2 μm × 2 μm area of the pull-off force images has been selected for more detailed analysis and are shown in Fig. 3.30. Although the image resolution is somewhat low at this magnification, some interesting differences are apparent. On the left hand side of the images is a chain of dark domains running top to bottom in a chevron shape. The
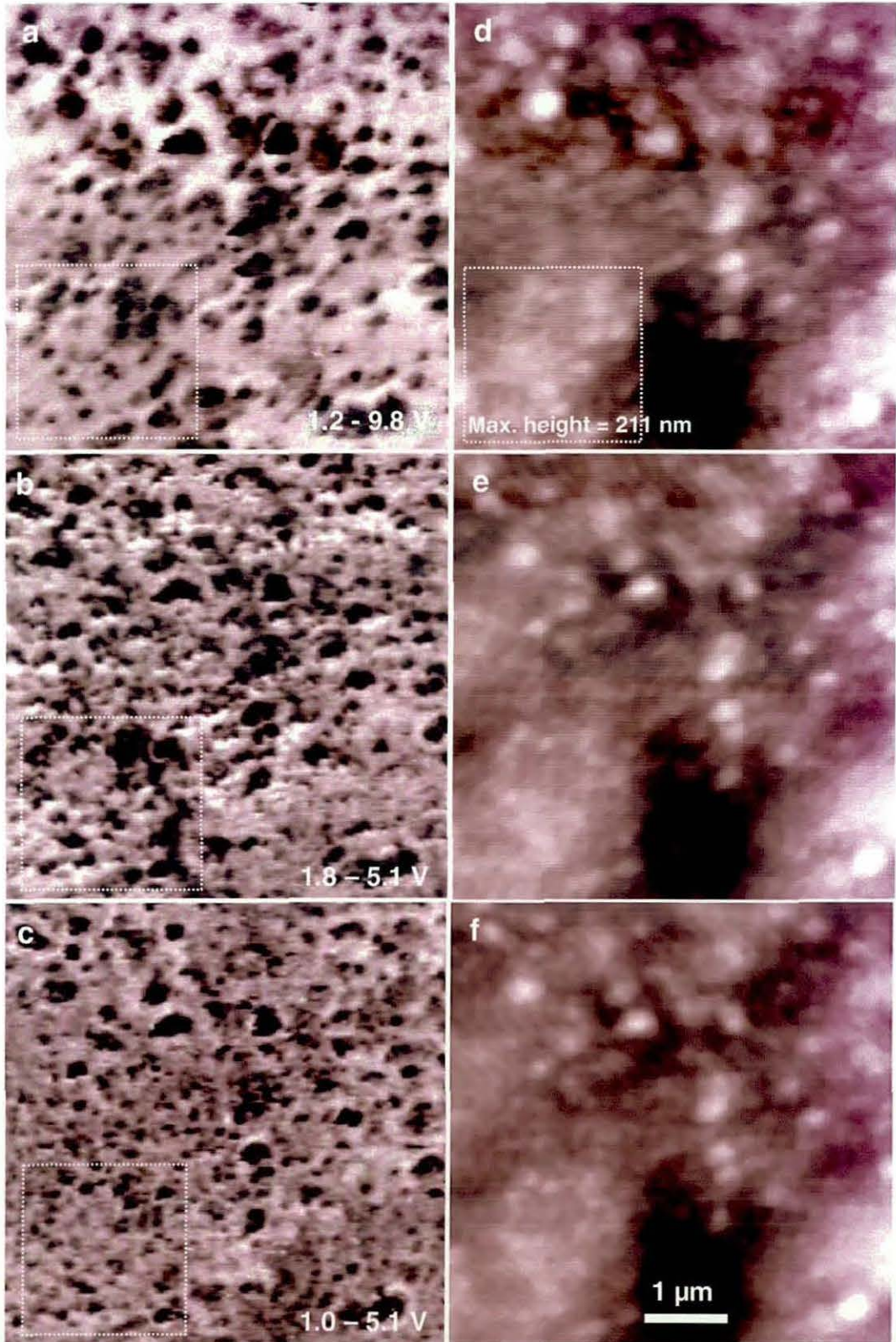
Fig. 3.29. Segmented polyurethane. Chain extender: 1,3-dihydroxybenzene. 5 μm × 5 μm PFM-AFM pull-off force images at room temperature (a) and at a stage temperature of −40°C (b) & −50°C (c). The corresponding topographic images (d-f) confirm that the same area was imaged in each case. The squares marked in the pull-off force and room temperature topographic images show the location of the 2 μm × 2 μm "zoom" images in Fig. 3.30
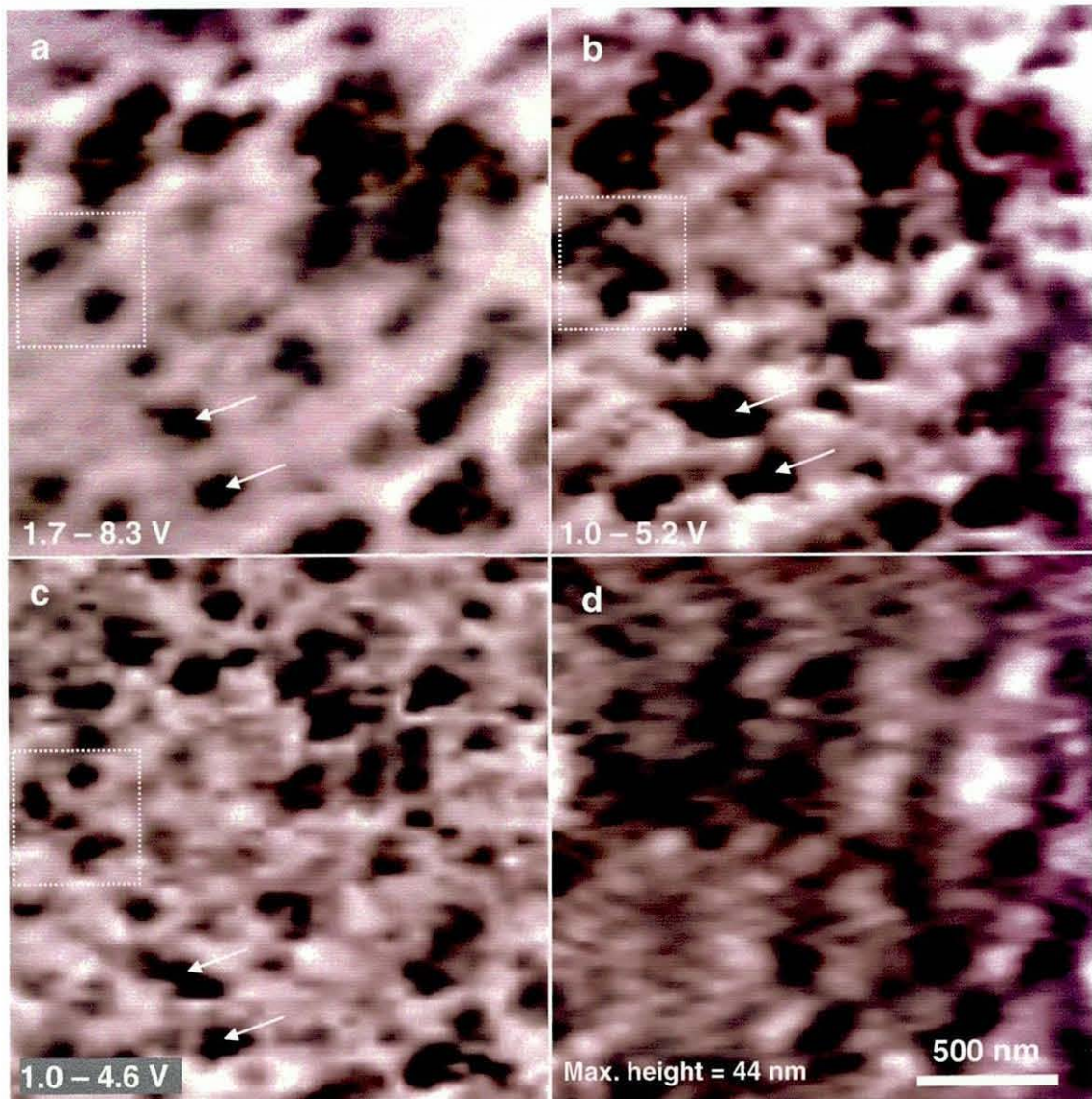
Fig. 3.30. Segmented polyurethane. Chain extender: 1,3-dihydroxybenzene. 2 μm × 2 μm PFM-AFM pull-off force (a-c) and topographic (d) images. These are "zoom" images of the areas marked in Fig. 3.29 acquired at room temperature (a) and at a stage temperature of –40°C (b) & –50°C (c).
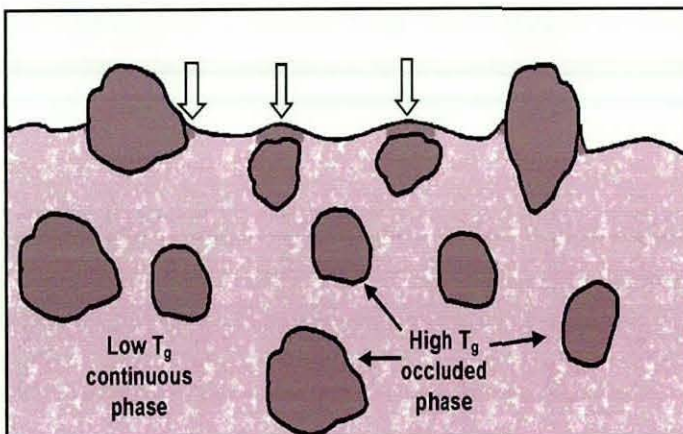
Fig. 3.31. A schematic illustration of the proposed mechanism for the apparent increase in the number and size of hard segment domains in low temperature PFM-AFM adhesion images of segmented polyurethanes, compared with the corresponding room temperature images. Thin constrained layers of soft-segment material (arrowed) lying either above sub-surface hard segment domains, or in an interfacial region, pass through the T_g before the bulk of the phase.

domains forming its apex are marked by a square in the pull-off force images. At room temperature, there appears to be three dark particles within the square. At −40°C there is a cluster of six or so, whilst at −50°C there are three or perhaps four. Two domains towards the bottom of the chain have been highlighted by arrows. These appear to be significantly larger at −40°C than at either room temperature or −50°C. Fig. 3.31 illustrates a possible mechanism to account for these observations. At a stage temperature of −40°C, the sample surface is at around −25°C. The MTDSC results showed that this material does not commence its glass transition until −42°C. As has been mentioned, the relatively high frequency of the PFM-AFM measurement will act to increase this. Even so, it is likely that the soft segment material is above its glass transition at this temperature. However, material lying in thin layers over shallow sub-surface hard domains or around partially buried hard domains could well behave as a constrained layer. These are often in found in, for example, composite materials in areas of resin in close proximity to well-bonded glass or other fibres. These regions often have a T_g significantly higher than that of the bulk resin matrix.[26, 90] Similarly, the soft-segment material here may have a higher T_g than material relatively remote from any hard-segment domains. If this is indeed the case, then such soft-segment rich material would be detected first as the temperature of the pull-off force measurement is decreased. This would explain the apparent increase in the concentration of hard domains at −40°C compared with room temperature, because shallow sub-surface domains have now become visible. It also explains the apparent increase in observed domain size. At a stage temperature of −50°C, the sample is likely to be at least part way through the glass transition of the soft segment-rich phase. It would be expected, therefore, that sub-surface domains would become invisible once more, as the pull-off force of the rubbery phase proper decreased to match that of any thin constrained layers. This accounts for the reduction in the number of dark phases in the selected area. The apparent domain size decreases as the stage is cooled to −50°C. This would seem to indicate that, although the pull-off force of the rubbery phase proper now matches that of any constrained layer, there is still sufficient adhesion contrast between the two phases to be resolved in the resulting image.

A potential advantage imbued to the technique if such a mechanism is indeed at work, is that over a certain narrow temperature range, sub-surface domains or particles become visible in the resulting images. A disadvantage is that, over the same temperature range, any potential measurement of domain size could not be relied upon. It is clear that further work is required to study this phenomenon.

3.3.4 Pulsed force mode AFM of a PS-PMMA blend using a micro-machined thermal probe

In the final part of the study, PFM-AFM of the PS-PMMA blend was carried out using the micro-fabricated "bowtie" thermal probe developed at Glasgow University. This was achieved by using one E.C.U. to regulate the probe temperature and a second E.C.U. to carry out the imaging functions. Temperature calibration was carried out using the variable temperature stage in exactly the same way as has been described for the Wollaston probe. Melting standard calibrants would have given a more accurate calibration for this application, but, as has been mentioned, it is impossible to remove this type of probe from such a sample once it has penetrated into it. For the purposes of this study, a knowledge of the precise temperature of the tip was not essential. It should be noted that, even had the precise probe temperature been known, the temperature of the material in the locality of the tip would have been lower by a small but unknown amount.

It was observed that the adhesion exhibited between sample and tip when at high temperature tended to increase steadily over time. It was thought that this was due to material transfer to the pyramid from the sample surface. This gave a fairly limited time before the pull-off force signal saturated and the probe had to be solvent-cleaned. For this reason there was little time to optimise the operating parameters for a particular probe (of which there was a strictly limited supply). As a consequence of the high levels of adhesion and the significantly shorter and stiffer cantilever, the amplitude was set to 20 % of maximum, in order to bring the tip out of contact with the surface. The frequency of modulation was kept at 500 Hz.

A preliminary set of results is shown in Fig. 3.32. This shows pull-off force, indentation and topographic images obtained with the probe in a passive state (at room temperature) and at a nominal temperature of 150°C. It is immediately apparent that, with the probe at 150°C, excellent phase contrast is achieved in the pull-off force image. At room temperature, there is little trace of this morphology. As was the case with the whole of the sample at this temperature, occluded, high-adhesion polystyrene phases are clearly visible. The corresponding intensity histograms again show the transformation from a mono-modal to bimodal distribution. Because the probe has a larger contact area than a conventional AFM tip, the quality of the image is somewhat inferior, with reduced edge definition, increased noise and so on. Little information is revealed in the indentation images, although it seems that at 150°C, the polystyrene phase is apparently harder than the PMMA. The topographic images are also
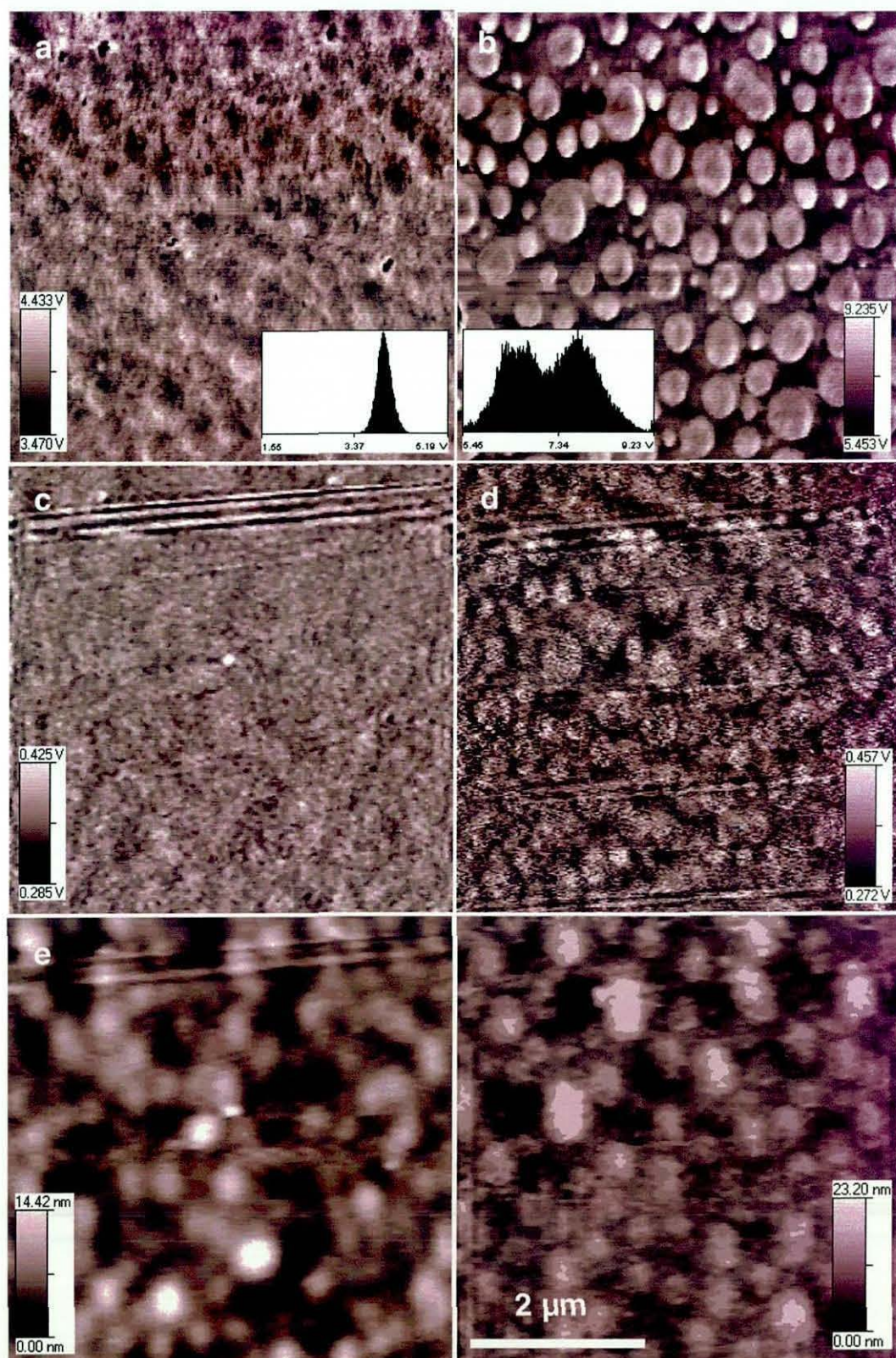
Fig. 3.32. 5 μm × 5 μm PFM-AFM images of the PS-PMMA blend acquired using a micro-machined "bowtie" thermal probe held at (left) 30°C and (right) 150°C. (a) and (b) are pull-off force images with the corresponding intensity histograms inset. (c) and (d) are indentation images and (e) and (f) show topography.

somewhat inferior to those obtained with a conventional probe. Nevertheless, *the principle of using a heated probe in an intermittent contact AFM mode for the characterisation of heterogeneous polymers has been established.*

3.4 Conclusions

The ability to carry out PFM-AFM experiments at sample temperatures as low as –50°C and as high as 250°C has been demonstrated as a practicable method of carrying out micro-thermal analysis of materials. Furthermore, variable temperature PFM-AFM has proved to be a potentially powerful technique for characterising the morphology of heterogeneous polymer systems. The adhesion-related pull-off force measurement has been shown to be much more sensitive to changes in surface properties than the stiffness-related indentation force. The results for the PS-PMMA system demonstrate that, in order to facilitate absolute comparisons between different sets of data obtained, for example, using different probes, some form of reliable calibration procedure is required for the pull-off force measurement. In the absence of such a calibration procedure, meaningful conclusions may still be drawn from *trends* that occur as a function of temperature. In analysing such trends it is important to consider that, at a given temperature, single phases give an approximately Gaussian distribution of pull-off force and a single peak is observed regardless of temperature changes. Different polymers may show different trends in the relationship between the mean value and form of their pull-off force distributions and temperature. These trends may serve to identify phases in blends.

The analysis of histograms that show the intensity distribution of pull-off force results can provide a powerful tool to aid the interpretation of images and, furthermore, is essential in the construction of more meaningful images. This is applicable to all AFM techniques that are based on the measurement of a physical property. The fitting of Gaussian peaks to these histograms may serve to indicate how many phases are present, but caution must be used in interpreting this type of data. Where a surface consists of two or more phases having overlapping property distributions, it is impossible to achieve a complete separation of the phases in any image constructed from spatial variations in that property. However, it has been shown that, by changing the imaging temperature, complete or near-complete separation of the peaks is possible. This strategy is not without risk, because it has also been shown that pull-off force images may be affected by the three-dimensional (sub-surface) structure of a material and this can manifest itself in a loss of edge-definition or the detection of

erroneous interphases. This is true even for materials in which a completely phase-separated morphology exists and the individual property distribution curves show no overlap at a given temperature. The risk of generating such interphases is greatest with very soft materials, such as the PS-PMMA blend at elevated temperature, because the ultra-sharp AFM tip can readily sample both materials for a significant distance either side of the real phase boundary. It is important, therefore, that the minimum imaging temperature is chosen at which separation of the peaks is achieved, but without softening the materials (or decreasing their viscosity) unduly. It is also the case that optimising the AFM operating parameters at a given sample temperature will minimise the percentage of pixels in a pull-off force image associated with any apparent interphase. Notable amongst these are the set point, which controls the maximum downward tip-sample force, and the amplitude of the cantilever vibration. Both should be minimised to optimise the adhesion image. However, minimising the tip-sample force will result in a deterioration of the signal to noise ratio in the corresponding indentation or stiffness measurement. A consequence of this is that separate scans will be required in order to obtain both optimised pull-off force and indentation images of the same sample.

Another approach that may bring potential benefits is through the use of more sophisticated data and image analysis techniques that are applied in other imaging fields. These may well facilitate a more quantitative interpretation of the multi-modal histograms that multiple phase materials have been shown to produce. This will, in turn, enable more accurate and useful images to be constructed.

The work on the PS-PMMA blend and the individual polymers shows that significant differences exist between them in terms of the variation in pull-off force with temperature. Polystyrene exhibits a large step increase above its T_g, whilst poly(methyl methacrylate) is relatively insensitive to changes in temperature up to approximately 160°C, when it too experiences a similar increase. Although this allows the phase-separated morphology of this system to be characterised by selecting a sample temperature within this interval, before the technique can be applied more generally as a characterisation tool, further investigation of the factors influencing the pull-off force and its relationship with temperature is required. These principally include the type of polymer (amorphous, or semi-crystalline, polar or non-polar etc.), the molecular weight distribution and the relationship between temperature and viscosity. The effects of instrument variables, such as the frequency and amplitude of modulation, the

maximum compressive force (set point) and probe-geometry also warrant further investigation.

PFM-AFM proved to be a much more robust technique at elevated temperature than IC-AFM phase imaging. The deterioration in the quality of phase images at even moderately high temperature is likely to be attributable to the particular instrument used or that insufficient time was spent optimising the operating parameters and/or type of probe. That this is the case is proved by the fact that a considerable number of elevated temperature IC-AFM studies have been published (as was discussed in chapter 1). Indeed, in a recent paper, Fasolka et al. [237] have replicated the basic approach used here in the PFM-AFM study of PS-PMMA. TappingMode™ is used successfully at temperatures up to 100°C on selected diblock copolymers that remain stable over the temperature range of the experiment and a similar improvement in phase contrast is demonstrated above the T_g of one of the phases.

It has been shown that, at room temperature, PFM-AFM is able to produce high contrast images revealing the phase-separated morphology of segmented polyurethanes. The results indicate that these materials have a complex structure, with phases an order of magnitude larger than the domain or nanophase size usually obtained with other techniques, notably SAXS. Further work is clearly required to establish the nature of the morphology revealed by PFM-AFM and its relationship with that of individual hard and soft-segment domains. In particular, it may be the case that *the presence of phase separation at different scales is indicative of a fractal structure. The relatively large (and variable) domain size obtained must mean that both the high and low pull-off force material contains substantial volume fractions of both hard- and soft-segment nanophases.*

By cooling the samples and examining the response of the different phases, it was demonstrated that the different domains could be identified. This was the case despite the fact that, with the current design of the temperature stage, it was impossible to obtain images at a temperature low enough to guarantee that the sample was substantially below the T_g of the soft segment rich material.

It was shown that IC-AFM resonance imaging could also be used successfully to characterise the polyurethane materials, both at ambient and sub-ambient temperatures. In some ways, this proved to be a superior method, in that the signal-to-noise ratio in the phase shift (and topography) signal(s) was higher than that obtained in the pull-off force measurement. However, for the PS-PMMA system, which required imaging at elevated temperatures, phase imaging proved to be ineffective, at least with

the instrument used in this study. An additional advantage of PFM-AFM is that the effect of temperature on the absolute value of the measurements produced can be interpreted in a more intuitive manner than a corresponding variation in phase lag in IC-AFM resonance mode.

In carrying out low-temperature imaging, it was observed that pull-off force images of certain materials often had improved definition than at room temperature. This was the case even when no transition had occurred over the temperature interval. This may simply be attributable to materials becoming more rigid as their temperature is reduced. In the case of the polyurethanes, it was shown that at a temperature close to the onset temperature of the glass transition (on cooling) it may well be possible to achieve sub-surface imaging of hard-segment domains. At the same temperature, the size of exposed domains may appear to be somewhat larger than they really are. Both of these observations may be attributable to the possible presence of a constrained layer of rubbery material close to the rigid domains. This phenomenon warrants further investigation by carrying out a study on several materials with a range of glass transition temperatures.

It has been shown that it is possible to carry out variable-temperature PFM-AFM using a micro-machined thermal probe and achieve results similar to those obtained by changing the global sample temperature. This holds out great promise for the time when thermal probes with even higher spatial resolution become available.

3.5. Recommendations for further study

There would appear to be considerable scope for further study in the area of micro-thermal analysis through variable-temperature AFM. The variable temperature stage used in this study has proved itself to be versatile and relatively easy to use and pulsed force mode AFM has been shown to be amenable to both sub-ambient and elevated temperature work.

The relationship between pull-off force and temperature, through the glass transition and above the T_g of amorphous polymers requires further investigation. The effects of, for example, polarity, molecular weight and viscosity all merit in-depth exploration. The role of material transfer from the sample to the tip in controlling local adhesion is another area of interest. An experimental programme can be envisaged in which the affinity of a range of polymers for a silicon tip would be investigated using, for example, secondary ion mass spectrometry (SIMS) to detect material on the tip surface after PFM-AFM imaging.

Further work is required in the application of the technique to the characterisation of polymer blends. It would be useful to study a partially miscible system that is known to produce a mixed interphase. A study similar to that carried out on the immiscible PS-PMMA blend could be undertaken. Particular areas of interest would be the effect of temperature on the apparent thickness of an interphase (if it could indeed be detected) and whether spurious interphases were generated at interfaces, in a manner similar to that encountered with the PS-PMMA blend. The use of Gaussian curve-fitting to image intensity histograms would again be useful here.

It is also possible that variable temperature PFM-AFM could be used to study the actual process of phase separation and its dependence on temperature. For this, a suitable candidate blend would need to be identified in which phase separation (or, conversely, mixing) was slow enough to allow meaningful imaging to be carried out in real time. The use of samples quenched at different stages of morphological development is unlikely to succeed, because it was shown, for the PS-PMMA system at least, that the pull-off force measurement could not discriminate between the phases below their T_g.

The indentation or "stiffness" measurement acquired during a PFM-AFM scan has proven to have a much lower signal-to-noise ratio than the pull-off force signal. This is probably a consequence of the current method of extracting the measurement, in which only two points are extracted from the indentation part of the measurement cycle This includes the maximum force peak, which is itself vulnerable to fluctuations originating in local topography. If a method could be found of fitting to all intermediate points (by digitising the whole curve, for example), this would presumably result in a considerable improvement. Generally, in the experiments reported in this thesis, the indentation force was minimised to reduce the risk of damaging or distorting the samples and introducing excessive frictional or shear forces into the pull-off force measurement. It would be perfectly possible to increase the maximum indentation force to optimise the indentation measurement. A meaningful comparison could then be made between optimised pull-off force and indentation measurements obtained from separate scans conducted on the same sample area. The work on the PS-PMMA blend has already highlighted interesting differences between, for example, the size of phases detected in the two types of mechanical property image acquired during the same scan.

The morphology of the segmented polyurethanes requires further investigation in order to determine the mechanism underlying the production of the large-scale

structure encountered in this study. In this context, it would be useful to conduct imaging on microtomed sections and compare the results with those obtained from as-cast surfaces, for example. Higher resolution imaging of the hard segment domains could usefully be carried out to determine whether the relatively large structures are, indeed, agglomerations of smaller individual domains. Comparison of AFM results with those from, for example, SAXS, would also be very useful.

The effect of low temperature on both PFM-AFM and IC-AFM phase images warrants further study. In particular, the apparent detection of sub-surface domains or particles in a multiphase material over a relatively narrow temperature range requires verification on at least one other material.

It is clear that the use of a suitable thermal probe in pulsed force and perhaps other IC-AFM modes will open up a fruitful area of research when such probes routinely become available. Given the necessary developments to the instrument control unit and software, it should be possible to synchronise the probe temperature control with the scanner modulation signal. This would allow, for example, high temperature cleaning to be carried out with the tip out of contact with the sample surface, so that each measurement cycle is guaranteed to be conducted with a clean tip.

Chapter 4

Overall conclusions

4. Overall conclusions

This study, along with others, has shown that there is no reason in principle that micro-thermal analysis will not become an increasingly powerful addition to the range of techniques available in the field of polymer characterisation. In this study it has been shown that useful information can be gathered from a range of polymer systems, both when using active thermal probes or inert AFM probes in conjunction with a variable temperature sample stage. It is likely that the two approaches will remain essentially complementary in the short to medium term. However, developments in the semi-conductor and computer industries will lead to the advent of thermal probes with much higher spatial resolution than the Wollaston probes used currently. This should mean that the use of conventional AFM probes will become unnecessary except for work requiring the highest possible spatial resolution (it is unlikely in the foreseeable future that thermal probes will be able to be manufactured as small as inert tips). Naturally, a comprehensive experimental programme will be required to investigate the performance of such probes.

Once such probes are available, the ability to be able to produce high-resolution thermal images and mechanical property-based images at different probe temperatures will come into its own. Localised thermal analysis will be able to be carried out on all but the smallest individual domains in multi-phase polymer systems and should be able to detect variations in crystallinity within, for example, spherulites. Furthermore, L-TA experiments will be able to be conducted at extremely high heating rates with a single run being completed in perhaps a fraction of a second.

The use of high-resolution probes as infrared detectors and to pyrolise small volumes of material as a precursor to GC-MS, will enable chemically-based characterisation to be conducted at high spatial resolution. In particular, the fact that the near-field infrared technique is not diffraction limited should produce a step change in the spatial resolution available to the infrared spectroscopist.

Finally, it should be noted that all these complementary techniques can be carried out using the same instrument and on the same area of sample material.

References

1. Binnig, G., Quate, C. F., Gerber, C., *Phys. Rev. Lett.*, **12**, 930 (1986).

2. Binnig, G. and Rohrer, H., *Helv. Phys. Acta*, **55**, 355 (1982).

3. Almond, D. P. and Patel, P. M., *Photothermal Science and Techniques*, Chapman and Hall, London (1996).

4. Oesterschulze, E., Stopka, M., Ackerman, L., Sholtz, W. and Werner, S., *J. Vac. Sci. Technol. B*, **14**, 832 (1996).

5. Balk, L. J., Maywald, M. and Pylkki, R. J., *9th Conf. on Microscopy of Semiconducting Materials (Inst. Phys. Conf. Ser. 146)*, Oxford, pp655-658 (1995).

6. Forster, R. and Gmelin, E., *Rev. Sci. Instrum.*, **67**, 4246 (1996).

7. Smallwood, R., Metherall, P., Hose, D., Delves, M., Pollock, H. M., Hammiche, A., Hodges, C. S., Mathot, V. and Willcocks, P., *Thermochim. Acta*, (2002) (in press).

8. Metherall, P., Barber, D. C., Smallwood, R. H. and Brown, B. H., *Nature*, **380**, 509 (1996).

9. Depasse, F., Gomès, S., Trannoy, N. and Grossel, P., *J. Phys. D: Appl. Phys.*, **30**, 3279 (1997).

10. Gomès, S., Depasse, F. and Grossel, P., *J. Phys. D: Appl. Phys.*, **31**, 2377 (1998).

11. Gomès, S., Trannoy, N., Depasse, F. and Grossel, P., *Int. J. Therm. Sci.*, **39**, 526 (2000).

12. Gomès, S., Trannoy, N., Grossel, P., Depasse, F., Bainier, C., Charraut, D., *Int. J. Therm. Sci.*, **40**, 949 (2001).

13. Grandy, D. B., Hourston, D. J., Price, D. M., Reading, M., Goulart Silva, G., Song, M. and Sykes, P. A., *Macromolecules*, **33**, 9348 (2000).

14. Jähne, B., *Digital Image Processing, Concepts, Algorithms and Scientific Applications*, 4th ed., p76, Springer- Verlag, Berlin (1997).

15. Varesi, J. and Majumdar, A., *Appl. Phys. Lett.*, **72**, 37 (1998).

16. Hammiche, A., Price, D. M., Dupas, E., Mills, G., Kulik, A. J., Reading, M., Weaver, J. M. R., and Pollock, H. M., *J. Microsc.*, **199**, 180 (2000).

17. Lawson, N.S., Ion, R. H., Pollock, H. M., Hourston, D. J. and Reading, M., *Physica Scripta*, **T55**, 199 (1995).

18. Hammiche, A., Pollock, H. M., Song, M. and Hourston D. J., *Meas. Sci. Technol.*, **7**, 142 (1996).

19. Hammiche, A., Hourston, D. J., Pollock, H. M., Reading, M. and Song, M., *J. Vac. Sci. Technol. B*, **14**, 1486. (1996).

20. Haines, P. J. (Ed.), *Thermal Methods of Analysis: Principles, Applications and Problems*; Blackie: London (1995).

21. Brown, M. E., *Introduction to Thermal Analysis - Techniques and Applications*, Chapman and Hall, London (1988).

22. Mathot, V. B. F. (Ed.), *Calorimetry and Thermal Analysis of Polymers*, Hanser, Munich (1994).

23. Tian, M.-W., Loos, J. and Fisher, H., (2002) (in preparation).

24. Reading, M., *Trends Polym. Sci.*, **1**, 248 (1993).

25. Jones, K. J., Kinshott, I., Reading, M., Lacey, A. A., Nikolopoulos, C. and Pollock, H. M., *Thermochim. Acta*, **305**, 187(1997).

26. Häßler, R. and zur Müehlen, E., *Thermochim. Acta*, **361**, 113 (2000).

27. Blaine, R. L., Slough, C. G. and Price, D. M., in: Williams, K. R. and Kociba, K. (eds.), *Proc. 27th NATAS, Savannah, Georgia*, North American Thermal Analysis Society/Omnipress pp691-696 (1999).

28. Oulevy, F., Burnham, N. A., Gremaud, G., Kulik, A.J, Pollock, H. M., Hammiche, A., Reading, M., Song, M. and Hourston, D. J., *Polym. Commun.*, **41**, 3087 (2000).

29. Dransfeld, K, and Xu, J., *J. Microsc.*, **152** 35 (1988).

30. Xu, J-B., Laeuger, K., Moeller, R., Dransfeld, K. and Wilson, I. H., *J. Appl. Phys.*, **76**, 7209 (1994).

31. Gomès, S., Depasse, F. and Grossel, P., *Meas. Sci. Technol.*, **10**, 805 (1998).

32. Gorbunov, V. V., Fuchigami, N., Hazel, J. L. and Tsukruk, V. V., *Langmuir*, **15**, 8340 (1999).

33. Ruiz, F., Sun, W. D., Pollak, F. H. and Venkatraman, C., *Appl. Phys. Lett.*, **73**, 1802 (1998).

34. Gorbunov, V. V., Fuchigami, N. and Tsukruk, V. V., *Probe Microsc.*, **2**, 65 (2000).

35. Callard, S., Tallarida, G., Borghesi, A. and Zanotti, L., *J. Non-Crystalline Solids*, **245**, 203 (1999).

36. Majumdar, A., *Ann. Rev. Mat. Sci.*, **29**, 505 (1999).

37. Moon, I. K., Jeong, Y. H. and Kwun, S. I., *Rev. Sci. Instrum.*, **67**, 29 (1996).

38. Cahill, D. G., *Rev. Sci. Instrum.*, **61**, 802 (1990).

39. Moon, I., Androsch, R., Chen, W. and Wunderlich, B., *J. Therm. Anal. Cal.*, **59**, 187 (2000).

40. Fiege, G. B. M., Altes, A., Heiderhoff, R. and Balk, L. J., *J. Phys. D: Appl. Phys.*, **32**, L13 (1999).

41. Williams, C. C. and Wickramasinghe, H. K., *Appl. Phys. Lett.*, **49**, 1587 (1986).

42. Williams, C. C. and Wickramasinghe, H. K. in: *Proc. Ultrasonics Symposium* (McAvoy, B. R., ed., IEEE, New York), p393 (1986).

43. Williams, C. C. and Wickramasinghe, H. K., *J. Vac. Sci. Technol. B*, **9**, 537 (1991).

44. Nonnenmacher, M. and Wickramasinghe, H. K., *Appl. Phys Lett.*, **61**, 168 (1992).

45. Majumdar, A., Carrejo, J. P. and Lai, J., *Appl. Phys. Lett.*, **62**, 2501 (1993).

46. Gimzewski, J. K., Gerber, C., Meyer, E., and Schlittler, R. R., *Chem. Phys. Lett.*, **217**, 589 (1994).

47. Nakabeppu, O., Chandrachood, M., Wu, Y., Lai, L. and Majumdar, A., *Appl. Phys. Lett.* **66**, 694 (1995).

48. Luo, K., Shi, Z., Lai, J., and Majumdar, A., *Appl. Phys. Lett.*, **68**, 325 (1996).

49. Pohl, D. W., Denk, W. and Lanz, M., *Appl. Phys. Lett.*, **44**, 651 (1984).

50. Betzig, E., Trautman, J. K., Harris, T. D., Weiner, J. S. and Kostelak, R. L., *Science*, **251**, 1486 (1991).

51. Goodson, K. E. and Asheghi, M., *Microscale Thermophys. Eng.*, **1**, 225 (1997).

52. Dinwiddie, R. B., Pylkki, R. J., and West, P. E. in: Tong, T.W. (ed.), *Thermal Conductivity 22*, Technomics, Lancaster PA, 668 (1994).

53. Pylkki, R. J., Moyer, P. J., West, P.E., *Jpn. J. Appl. Phys. 1*, **33**, 784 (1994).

54. Zhou, H., Midha, A., Mills, G., Thoms, S., Murad, S. K. and Weaver, J. M. R., *J. Vac. Sci. Technol. B*, **16**, 54 (1998).

55. Mills, G., Zhou, H., Midha, A., Donaldson, L. and Weaver, J. M. R., *Appl. Phys. Lett.*, **72**, 2900 (1998).

56. Zhou, H., Mills, G., Chong, B. K., Midha, A., Donaldson, L. and Weaver, J. M. R., *J. Vac. Sci. Technol. A*, **17**, 2233 (1999).

57. Hammiche, A., Bozec, L., Conroy, M., Pollock, H. M., Mills, G., Weaver, J. M. R., Price, D. M., Reading, M., Hourston, D. J. and Song, M., *J. Vac. Sci. Technol. B*, **18**, 1322 (2000).

58. Chui, B. W., Stowe, T. D., Kenny, T. W., Mamin, H. J., Terris, B. D. and Rugar, D., *Appl. Phys. Lett.*, **69**, 2767 (1996).

59. Chui, B. W., Stowe, T. D., Ju, Y. S., Goodson, K. E., Kenny, T. W., Mamin, H. J., Terris, B. D., Ried, R. P. and Rugar, D., *J. Microelectromechanical Syst.*, **7**, 69 (1998).

60. Binnig, G., Despont, M., Drechsler, U., Häberle, W., Lutwyche, M., Vettiger, P., Mamin, H. J., Chui, B. W. and Kenny, T. W., *Appl. Phys. Lett*, **74**, 1329 (1999).

61. Mamin, H. J. and Rugar, D., *Appl. Phys. Lett.*, **61**, 1003 (1992).

62. Chui, B. W., Mamin, H. J., Terris, B. D., Stowe, T. D., Rugar, D. and Kenny, T. W., *Appl. Phys. Lett.*, **69**, 2767 (1996).

63. Chui, B. W., Mamin, H. J., Terris, B. D., Ried, R. P., Rugar, D., Stowe, T. D., Soh, H. T., Minne, S. C., Quate, C. F., Ju, Y. S., Goodson, K. E. and Kenny, T. W., in: *Proc. Solid-State Sensor and Actuator Workshop*, Hilton Head, SC, pp219-224 (1996).

64. Pollock, H. M., Hammiche, A., Song, M., Hourston, D. J., and Reading, M., *J. Adhesion*, **67**, 217 (1998).

65. Price, D. M., Reading, M., Hammiche, A. and Pollock, H. M., *Int. J. Pharm.*, **192**, 85 (1999).

66. Hammiche, A. and Pollock, H. M., *J. Phys. D: Appl. Phys.*, **34**, R23-R53 (2001).

67. Conroy, M., Hammiche, A. and Mills, G., in: Hammiche, A. and Pollock, H. M., *J. Phys. D: Appl. Phys.*, **34**, R23-R53 (2001).

68. Conroy, M., Blanco, C., Appleyard, S., in: Hammiche, A. and Pollock, H. M., *J. Phys. D: Appl. Phys.*, **34**, R23-R53 (2001).

69. Price, D. M. and Reading, M., in: Williams, K. R. and Kociba, K. (eds.), *Proc. 27th NATAS, Savannah, Georgia*, North American Thermal Analysis Society/Omnipress pp420-425 (1999).

70. Reading, M., Price, D. M., Grandy, D. B., Smith, R. M., Pollock, H. M., Hammiche, A., Bozec, L., Mills, G. and Weaver, J. M. R. in: Tsukruk, V. V. and Spencer, N. D. (eds.), *Recent advances in scanning probe microscopy of polymers; Macromolecular Symp.*, **167**, 45 (2001).

71. McClennen, W. C., Buchanan, R. M., Arnold, N. S., Dworzanski, J. P., Meuzelaar, H. L. C., *Anal. Chem.*, **65**, 2819 (1993).

72. Price, D. M., Reading, M., Hammiche, A. and Pollock, H. M., *J. Therm. Anal. Cal.*, **60**, 723 (2000).

73. Hammiche, A., Pollock, H. M., Reading, M., Claybourn, M., Turner, P. H. and Jewkes, K., *Appl. Spectrosc.*, **53**, 810 (1999).

74. Bozec, L., Hammiche, A., Pollock, H. M., Conroy, M., Chalmers, J. M., Everall, N. J. and Turin, L., *J. Appl. Phys.*, **90**, 5159 (2001).

75. Williams, C. C. and Wickramasinghe, H. K., *Soc. Photograph. Instrum. Eng.*, **897**, 129 (1998).

76. Grafstrom, S., Kowalski, J., Neumann, R., Probst, O. and Wortge, M., *J. Vac. Sci. Technol. B*, **9**, 568 (1991).

77. Trannoy, N., Grossel, P. and Troyon, M., *Probe Microsc.*, **1**, 201 (1998).

78. Oesterschulze, E., Stopka, M. and Kassing, R., *Microelectron. Eng.*, **24**, 107 (1994).

79. Anderson, M. S., *J. Appl. Spectrosc.*, **54**, 349 (2000).

80. Rosencwaig, A., *Photoacoustics and Photoacoustic Spectroscopy*, Wiley, New York (1980).

81. Bialkowski, S. E., *Photothermal Spectroscopy Methods for Chemical Analysis*, Wiley, New York (1996).

82. Song, M., Hourston, D.J. and Grandy, D.B., *J. Appl. Polym. Sci.*, **81**, 2136 (2001).

83. Price, D. M., Reading, M. and Lever, T. J., *J. Therm. Anal. Cal.*, **56**, 673 (1999).

84. Reading, M., Hourston, D. J., Song, M., Pollock, H. M. and Hammiche, A., *Am. Lab.*, **30** (1), 13 (1998).

85. Lever, T. J. and Price, D. M., *Am. Lab.*, **30** (16), 15 (1998).

86. Song, M., Hourston, D. J., Pollock, H. M., Schäfer and Hammiche, A., *Thermochim. Acta.*, **304/305**, 335 (1997).

87. Price, D. M., Reading, M., Hammiche, A., Pollock, H. M. and Branch, M. G., *Thermochim. Acta*, **332**, 143 (1999).

88. Zur Müehlen, E., in: *Developments in Polymer Analysis and Characterisation*, Rapra Technology Seminar, 10th May, 1999.

89. Price, D. M., Reading, M., Caswell, A., Hammiche, A. and Pollock, H. M., *Microsc. Anal.*, **65**, 17 (1998).

90. Van Assche, G., Volckaerts, B. and van Mele, B., in: Pan, W-P. (ed), *Proc. 2nd Int. Symp. on Microthermal Anal.*, University of Western Kentucky, Bowling Green, KY, USA, (May 2000).

91. Reading, M., Price, D. M., Pollock, H. M., Hammiche, A. and Murray, A., *Am. Lab.*, **31** (1), 13 (1999).

92. Sanders, G. H. W., Danesh, A., Murray, A. J., Price, D. M., Roberts, C. J., Davies, M. C., Tendler, S. J. B., Williams, P. M. and Wilkins, M. J., *J. Microsc.*, **198**, 77 (2000).

93. Royall, P. G., Craig, D. Q. M., Price, D. M., Reading, M. and Lever, T. J., *Int. J. Pharm.*, **190**, 97 (1999).

94. Royall, P. G., Hill, V. L., Craig, D. Q. M., Price, D. M. and Reading, M., *Pharm. Res.*, **18**, 294 (2001).

95. Royall, P. G., Kett, V. S., Andrews, C. S. and Craig, D. Q. M., *J. Phys. Chem. B*, **105**, 7021 (2001).

96. Royall, P. G., Craig, D. Q. M. and Grandy, D. B., *Thermochim. Acta*, **380**, 165 (2001).

97. Buck, A., Jones, B. K. and Pollock, H. M., *Microelectron. Reliab.* **37**, 1495 (1997).

98. Meyers, G. F., Dineen, M. T., Shaffer II, E. O., Stokich, Jr. T. and Im, J.-H., *Polym. Prepr. (Am. Chem. Soc., Polym. Chem. Div.)*, **41**, 1419 (2000).

99. Fryer, D. S., de Pablo, J. J. and Nealey, P. F., *Proc. SPIE 3333*, 1031 (1998).

100. Price, D. M., Reading, M. and Smith, R. M., *J. Therm. Anal. Cal.*, **64**, 309 (2001).

101. Sarid, D., *Scanning force microscopy*, Oxford University Press, New York (1993).

102. Colton, R. J., Engel, A., Frommer, J. E., Gaub, H. E., Gewith, A. A., Guckenberger, R., Rabe, J., Heckl, W. M. and Parkinson, B., (eds.) *Procedures in scanning probe microscopies*, Wiley, Chichester (1998).

103. Sheiko, S. S., *Imaging of polymers using scanning force microscopy: from superstructures to individual molecules, Adv. Polym. Sci.*, **151**, pp61-174 (2000).

104. Magonov, S. N. and Reneker, D. H., *Characterization of polymer surfaces with atomic force microscopy, Annu. Rev. Mat. Sci.*, **27**, pp175-222 (1997).

105. Magonov, S. N. and Whangbo, M.-H., *Surface analysis with STM and AFM*, VCH, Weinheim (1996).

106. Howland, R. and Benetar, L., *A Practical Guide to Scanning Probe Microscopy*, Park Scientific Instruments, Sunnyvale, CA, USA (1997).

107. Albrecht, T. R., Dovek, M. M., Lang, C. A., Grutter, P. and Quate, C. F., Kuan, S. W. J., Frank, C. W. and Pease, R. F. W., *J. Appl. Phys.*, **64**, 1178 (1988).

108. Dovek, M. M., Albrecht, T. R., Kuan, S. W. J., Lang, C. A., Emch, R., Grutter, P., Frank, C. W., Pease, R. F. W. and Quate, C. F., *J. Microsc.-Oxford*, **152**, 229 (1988).

109. Quate, C. F., *Nature*, **342**, 739 (1989).

110. Patil, R., Kim, S.-J., Smith, E., Reneker, D. H. and Wiesenhorn, A. L., *Polym. Commun.*, **31**, 455 (1991).

111. Alexander, S., Hellemans, L., Marti, O., Schneier, J., Elings, V., Hasma, P. K., Longmire, M. and Gurley, J., *J. Appl. Phys.*, **65**, 164 (1989).

112. Maivald P., Butt, H. J., Gould, S. A. C., Prater, C. B., Drake, B., Gurley, J. A., Elings V. B. and Hansma, P.K., *Nanotechnol.*, **2**, 103 (1991).

113. Radmacher, M., Tilmann, R. W. and Gaub, H. E., *Biophys. J.*, **64**, 735 (1993).

114. Kajiyama, T., Takata, K., Ohki, I., Ge, S.-R., Yoon, J.-S., Takahara, A., *Macromolecules*, **27**, 7932 (1994).

115. Chen, J. T. and Thomas, E. L., *J. Mat. Sci.*, **31**, 2531 (1996).

116. Lin, H. N., Hung, T. T., Chang, E. C. and Chen, S. A., *Appl. Phys. Lett.*, **74**, 2785 (1999).

117. Motomatsu, M., Nie, H. Y., Mizutani, W. and Tokumoto, H., *Jpn. J. Appl. Phys. 1*, **33**, 3775 (1994).

118. Cuberes, M. T., Assender, H. E., Briggs, G. A. D. and Kosolov, O. V., *J. Appl. Phys. D – Appl. Phys.*, **33**, 2347 (2000).

119. Oulevy, F., Gremaud, G., Sémoroz, A., Kulik, A.J, Burnham, N. A., Dupas, E. and Gourdon, D., *Rev. Sci. Instrum.*, **69**, 2085 (1998).

120. Mate C. M., McClelland, G. M., Erlandsson, R. and Chiang, S., *Phys. Rev. Lett.*, **59**, 1942 (1987).

121. Meyer, G. and Amer, N. M., *Appl. Phys. Lett.*, **57**, 2089 (1990).

122. Marti, 0., Colchero, J. and Mlynek, J., *Nanotechnol.*, **1**, 141 (1990).

123. Liu, E., Blanpain, B., and Celis, J. P., *Wear*, **192**, 141 (1996).

124. Gibson, C. T., Watson, G. S. and Myhra, S., *Wear*, **213**, 72 (1997).

125. Pietrement, O., Beaudoin, J. L. and Troyon, M., *Tribol. Lett.*, **7**, 213 (1999).

126. Cain, R. G., Biggs, S. and Page, N. W., *J. Colloid Interf. Sci.*, **227**, 55 (2000).

127. Kendall, K., *Science*, **263**, 1720 (1994).

128. Lantz, M. A., O' Shea, S. J., Welland, M. E. and Johnson, K. L., *Phys. Rev. B*, **55**, 10776 (1997).

129. Lantz, M. A., O' Shea, S. J., Hoole, A. C. F. and Welland, M. E., *Appl. Phys. Lett.*, **70**, 970 (1997).

130. Carpick, R. W., Ogletree, D. F. and Salmeron, M., *Appl. Phys. Lett.*, **70**, 1548 (1997).

131. Yamanaka, K., Takano, H., Tomita, E. and Fujihira, M., *Jpn. J. Appl. Phys 1*, **35**, 5421 (1996).

132. Dinelli, F., Buenviaje, C. and Overney, R. M., *J. Chem. Phys.*, **113**, 2043 (2000).

133. Forster, S., Liu, G. B. and Vansco, G. J., *Polym. Bull.*, **36**, 471 (1996).

134. Vansco, G. J., Forster, S. and Leist, H., *Macromolecules*, **29**, 2158 (1996).

135. Garcia, R., Tamayo, J. and San Paulo, A., *Surf. Interf. Anal.*, **27**, 312 (1999).

136. Garcia, R. and San Paulo, A., *Phys. Rev. B*, **60**, 4961 (1999).

137. Llewellyn, J. P. and Sayers, P., *Inst. Phys. Conf. Ser. No. 163*, pp403-406 (1999).

138. Wang, L., *Surf. Sci.*, **429**, 178 (1999).

139. Wang, L., *Appl. Phys. Lett.*, **73**, 3781 (1998).

140. Whangbo, M.-H., Bar, G. and Brandsch, R., *Surf. Sci. Lett.*, **411**, L794 (1998).

141. Ancsykowski, B., Krüger, D., and Fuchs, H., *Phys. Rev. B*, **53**, 15485 (1996).

142. Ancsykowski, B., Krüger, D., Babcock, H. and Fuchs, H., *Ultramicroscopy*, **66**, 251 (1996).

143. Marth, M., Maier, D., Honerkamp, J., Brandsch, R. and Bar, G., *J. Appl. Phys.*, **85**, 1 (1999).

144. Pickering, J. P. and Vansco, G. J., *Polym. Bull.*, **40**, 549 (1998).

145. Bar, G., Thomann, Y., Brandsch, R., Cantow, H.-J. and Whangbo, M.-H., *Langmuir*, **13**, 3807 (1997).

146. Magonov, S. N., Elings, V. and Whangbo, M.-H., *Surf. Sci. Lett.*, **375**, L385 (1997).

147. Noy, A., Sanders, C. H., Vezenov, D. V., Wong, S. S. and Lieber, C. M., *Langmuir*, **14**, 1508 (1998).

148. Duborg., F. and Aimé, J. P., *Surf. Sci.*, **466**, 137 (2000).

149. Sarid, D., Hunt, J. P., Workman, R. K., Yao, X. and Peterson, C. A., *Appl. Phys. A.*, **66**, S283 (1998).

150. Pearce, R. and Vansco, G. J., *J. Polym. Sci. B.*, **36**, 2643 (1998).

151. Vansco, G. J., Beekmans, L. G. M., Pearce, R., Trifonova, D. and Varga, J., *J. Macromol. Sci.—Phys. B*, **38**, 491 (1999).

152. Ivanov, D. A., Jonas, A. M. and Legras, R., *Bull. Am. Phys. Soc.*, **41**, 395 (1996).

153. Ivanov, D. A. and Jonas, A. M., *Macromolecules*, **31**, 4546 (1998).

154. Ivanov, D. A., Nysten, B. and Jonas, A. M., *Polymer*, **40**, 5899 (1999).

155. Basire, C. and Ivanov, D. A., *Phys. Rev. Lett.*, **85**, 5587 (2000).

156. Hobbs, J. K., McMaster, T. J., Miles, M.J. and Barham, P. J., *Polymer*, **39**, 2437 (1998).

157. Godovsky, Y. K. and Magonov, S. N., *Langmuir*, **16**, 3549 (2000).

158. Magonov, S. N., Elings, V. and Papkov. V. S., *Polymer*, **39**, (1998).

159. Bar, G., Thomann, Y. and Whangbo, M.-H., *Langmuir*, **14**, 1219 (1998).

160. Bar, G., Ganter, M., Brandsch, R., Delineau L, and Whangbo, M.-H., *Langmuir*, **16**, 5702 (2000).

161. McLean, R. S. and Sauer, B. B., *Macromolecules*, **30**, 8314 (1997).

162. Sauer, B. B., McLean, R. S. and Thomas R. R., *Langmuir*, **14**, 3045 (1998).

163. Mizes, H. A., Loh, K.-G., Miller, R. J., Ahuja, S. K. and Grabowski, E. F., *Appl. Phys. Lett.*, **59**, 2901 (1991).

164. Weisenhorn, A. L., Maivald, P., Butt, H.-J. and Hansma, P. K., *Phys. Rev. B*, **45**, 266 (1992).

165. Weisenhorn, A. L., Khorsandi, M., Kansas, S., Gotzos, V. and Butt, H.-J., *Nanotechnol.*, **4**, 403 (1993).

166. Hazel, J. L. and Tsukruk, V. V., *J. Tribol.- Transact. A.S.M.E.*, **120**, 814 (1998).

167. Hazel, J. L. and Tsukruk, V. V., *Thin Solid Films*, **339**, 249 (1999).

168. Berger, C. E. H., van der Werf, K. O., Kooyman, R. P. H., de Grooth, B. G and Greve, J., *Langmuir*, **11**, 4188 (1995).

169. Frisbie, C. D., Rosznay, L. F., Noy, A., Wrighton, M. S. and Lieber, C. M., *Science*, **265**, 2071 (1994).

170. Akari, S., Horn, D. and Keller, H., *Adv. Mater.*, **7**, 594 (1995).

171. Anon., *Can. Ceram. Quart.*, **64**, 201 (1995).

172. Abbis, T. and Collins, G., *R&D Mag.*, **37**, 57 (1995).

173. Anon., *Lubr. Eng.*, **52**, 336 (1996).

174. Anon., *Topometrix Explorer Manual (ref. 85-10244 rev. A)*, pp 3.34-3.35, Topometrix Corporation, Santa Barbara, CA, USA (1996).

175. Chen, X., Davies, M. C., Roberts, C. J., Tendler, S. J. B., Williams, P. M., Davies, J., Dawkes, A. C. and Edwards, J. C., *Langmuir*, **13**, 4106 (1997).

176. Tsukruk, V. V. and Huang, Z., *Polym. Comm.*, **41**, 5541 (2000).

177. Miyatani, T., Horii, M., Rosa-Zeiser, A., Fujihira, M. and Marti O., *Appl. Phys. Lett.*, **71**, 2632 (1997).

178. Rosa-Zeiser, A., Weilandt, E., Hild, S. and Marti O., *Meas. Sci. Technol.*, **8**, 1333 (1997).

179. Luzinov, I., Minko, S., Senkovsky, V., Voronov, A., Hild, S., Marti, O. and Wilke, W., *Macromolecules*, **31**, 3945 (1997).

180. Miyatani, T., Okamoto, S., Rosa-Zeiser, A., Marti, O. and Fujihira, M., *Appl. Phys. A-Mat. Sci. Process.*, **66**, S349 (1998).

181. Hild, S., Rosa-Zeiser, A., Volswinkler, G. and Marti, O., *Bull. Microsc. Soc. Can.*, **26**, 24 (1998).

182. Marti, O., Stifter, T., Waschipky, H. Quintus, M. and Hild, S., *Colloid Surf. A*, **154**, 65 (1999).

183. Krotil, H. U., Stifter, T., Waschipky, H., Weishaupt, K., Hild, S. and Marti, O., *Surf. Interface Anal.*, **27**, 336. (1999).

184. de Pablo, P. J., Colchero, J., Gómez-Herrero, J. and Baró, A. M., *Appl. Phys. Lett.*, **73**, 3300 (1998).

185. Moreno-Herrero, F., de Pablo, P. J., Colchero, J., Gómez-Herrero, J. and Baró, A. M., *Surf. Sci.*, **453**, 152 (2000).

186. Leijala, A and Hautojarvi, J., *Text. Res. J.*, **68**, 193 (1998).

187. Okabe, Y., Fujihira, M., and Akiba, U., *Appl. Surf. Sci.*, **157**, 398 (2000).

188. Okabe, Y., Furugori, M., Tani, Y., Akiba, U. and Fujihira, M., *Ultramicroscopy*, **82**, 203 (2000).

189. Zhang, H., Grim, P. C. M., Foubert, P., Vosch, T., Vanoppen, P., Wiesler, U. M., Berresheim, A. J., Mullen, K. and De Shhryver, F. C., *Langmuir*, **16**, 9009 (2000).

190. Zhang, H., Grim, P. C. M., Vosch, T., Wiesler, U. M., Berresheim, A. J., Mullen, K. and De Shhryver, F. C., *Langmuir*, **16**, 9294 (2000).

191. Chen, X., Davies, M. C., Roberts, C. J., Tendler, S. J. B. and Williams, P. M., *Appl. Phys. Lett.*, **77**, 3462 (2000).

192. Fujihira, M., Tani, Y., Furugori, M., Akiba, U. and Okabe, Y., *Ultramicroscopy*, **86**, 63 (2001).

193. Fujihira, M., Furugori, M., Akiba, U. and Tani, Y., *Ultramicroscopy*, **86**, 75 (2001).

194. Dickson, L. E. and Berg, J. C., *J. Adhesion Sci. Technol.*, **15**, 171 (2001).

195. Schönherr, H., Hruska, Z. and Vansco G. J., *Macromolecules*, **33**, 4532 (2000).

196. Musevic, I., Slak, G., and Blinc, R., *Rev. Sci. Instrum.*, **67**, 2554 (1996).

197. Baekmark, T. R., Bjornholm, T. and Mouritsen, O. G., *Rev. Sci. Instrum.*, **68**, 140 (1997).

198. Sikes, H. D. and Schwartz, D. K., *Science*, **278**, 1604 (1997).

199. Prilliman, S. G., Kavanagh, A. M., Scher, E. C., Robertson, S. T., Hwang, K. S. and Colvin, V. L., *Rev. Sci. Instrum.*, **69**, 3245 (1998).

200. Kirk, M. D., Albrecht, T. R. and Quate, C. F., *Rev. Sci. Instrum.*, **59**, 833 (1988).

201. Giessibl, F. J., Gerber, C. and Binnig, G., *J. Vac. Sci. Technol. B*, **9**, 984 (1991).

202. Albrecht, T. R., Grütter, P., Rugar, D. and Smith, D. P. E., *Ultramicroscopy*, **42B**, 1638 (1992).

203. Hug, H. J., Moser, A., Jung, T., Fritz, O., Wadas, A., Parashikov, I. and Güntherodt, H. –J., *Rev. Sci. Instrum.*, **64**, 2920 (1993).

204. Euler, R., Memmert, U. and Hartmann, U., *Rev. Sci. Instrum.*, **68**, 1776 (1997).

205. Pelekhov, D. V., Becker, J. B. and Nunes, G., *Appl. Phys. Lett.*, **72**, 993 (1998).

206. Hug, H. J., Stiefel, B., van Schendel, P. J. A., Moser, A., Martin, S. and Güntherodt, H. –J., *Rev. Sci. Instrum.*, **70**, 3625 (1999).

207. Allers, W., Schwarz, A., Schwarz, U. D., and Wiesendanger, R., *Rev. Sci. Instrum.*, **69**, 221 (1998).

208. Rychen, J., Ihn, T., Studerus, P., Herrmann, A. and Ensslin, K., *Rev. Sci. Instrum.*, **70**, 2765 (1999).

209. Allers, W., Schwarz, A., Hölscher, H., Schwarz, U. D. and Wiesendanger, R., *Jpn. J. Appl. Phys.*, **39**, 3701 (2000).

210. Bower, D. I., and Maddams, W. F., *The Vibrational Spectroscopy of Polymers*, Cambridge University Press (1992).

211. Billmeyer, F. W. Jr., *Textbook of Polymer Science* (2nd ed.), Wiley-Interscience, New York (1971) p169.

212. Chalmers, J. M., Croot, L., Eaves, J. G., Everall, N., Gaskin, W. F., Lumsdon, J. and Moore, N., *Spectros. Int. J.*, **8**, 13 (1990).

213. Everall, N. J., *Appl. Spectros.*, **54**, 1515 (2000).

214. Reading, M., Price, D. M. and Orliac, H., *Measurement of Crystallinity in Polymers Using Modulated Temperature Differential Scanning Calorimetry* in: Riga, A. and Judovits, A. (eds.), *Material Characterization by Modulated Thermal Analytical Techniques*, ASTM STP 1402. American Society for Testing and Materials, West Conshocken, PA, pp17-31 (2001).

215. University of Tennessee, ATHAS database - http://web.utk.edu/~athas/databank/phenylen/pet/pet.html.

216. Clayden, N. J., Nijs, C. and Eeckhart, G., *Macromolecules*, **31**, 7820 (1998).

217. Valenkar, S. and Cooper, S., *Macromolecules*, **31**, 9181 (1998).

218. Chang, S. L., Yu, T. L., Huang, C. C., Chen, W. C., Linliu, K. and Lin, T. L., *Polymer*, **39**, 3479 (1998).

219. Li, Y., Ren, Z., Zhao, M., Yang, H. and Chu, B., *Macromolecules*, **26**, 612 (1993).

220. Koberstein, J. T., Galambos A. F. and Leung, L. M., *Macromolecules*, **25**, 6195 (1992).

221. Koberstein, J. T., Galambos A. F. and Leung, L. M., *Macromolecules*, **25**, 6205 (1992).

222. Xu, M., MacKnight, W. J., Chen-Tsai, C. T. Y. and Thomas, E. L., *Polymer*, **28**, 2183 (1987).

223. Li, Y., Gao, T. and Chu, B., *Macromolecules*, **25**, 1737 (1991).

224. Desper, C. R., Schneider, N. S., Jasinsky, J. P. and Lin, J. S., *Macromolecules*, **18**, 2755 (1987).

225. Koberstein, J. T. and Stein, R. S., *Polymer*, **25**, 171 (1984).

226. Koberstein, J. T. and Stein, R. S., *J. Polym. Sci: Polym. Phys. Ed.*, **21**, 1439 (1983).

227. Wilkes, G. L., Samuels, S. L. and Crystal, R., *J. Macromol. Sci. Phys. B*, **10**, 203 (1974).

228. Samuels, S. L. and Wilkes, G. L., *Polymer Lett.*, **9**, 761 (1971).

229. Samuels, S. L. and Wilkes, G. L., *J. Polym. Sci. Symposium*, **43**, 149 (1973).

230. Wilkes, G. L. and Yusek, C. S., *J. Macromol. Sci. Phys. B*, **7**, 157 (1973).

231. Sawyer, L. C. and Grubb, D. T., *Polymer Microscopy*, Chapman and Hall, New York (1987).

232. Eisenbach, C. D., Ribbe, A. and Günter, C., *Macromol. Rapid Commun.*, **15**, 395 (1994).

233. Sykes, P. A., *PhD thesis*, Loughborough University, (1999).

234. Shard, A. D., Davies, M. C., Tendler, S. J. B., Jackson, D. E., Lan, P. N., Schacht. E. and Purbrick, M. D., *Polymer*, **36**, 775 (1995).

235. Hasegawa, H. and Hashimoto, T., *Polymer*, **33**, 475 (1992).

236. Slough, G., TA Instruments Inc., Personal Communication.

237. Fasolka, M. J., Mayes, A. M. and Magonov, S. N., *Ultramicroscopy*, **90**, 21, (2001).

Publications

Grandy, D. B., Hourston, D. J., Price, D. M., Reading, M., Goulart Silva, G., Song, M. and Sykes, P. A., Micro-thermal characterisation of segmented polyurethane elastomers and a polystyrene-poly(methyl methacrylate) blend using variable-temperature pulsed force mode atomic force microscopy, *Macromolecules*, **33**, 9348 (2000).

Song, M., Hourston, D.J. and Grandy, D.B., An application of micro-thermal analysis to polymer blends, *J. Appl. Polym. Sci.*, **81**, 2136 (2001).

Reading, M., Price, D. M., Grandy, D. B., Smith, R. M., Pollock, H. M., Hammiche, A., Bozec, L., Mills, G. and Weaver, J. M. R. in: Tsukruk, V. V. and Spencer, N. D. (eds.), *Recent advances in scanning probe microscopy of polymers*; *Macromolecular Symp.*, **167**, 45 (2001).

Royall, P. G., Craig, D. Q. M. and Grandy, D. B., The use of micro-thermal analysis as a means of *in-situ* characterisation of a pharmaceutical tablet coat, *Thermochim, Acta.*, **380**, 165 (2001).

Reading, M., Grandy, D. B., Hammiche, A., Bozec, L. and Pollock, H. M., Thermally assisted nanosampling and analysis using micro-IR spectroscopy and other analytical methods, *Vibrational Spectroscopy*, **901**, 1 (2002).